AD 734248
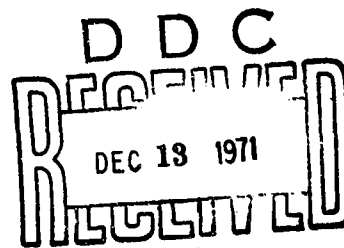
AFRPL-TR-128

EXPLORATORY DEVELOPMENT OF ADVANCED COLLOID THRUSTERS

M. Huberman, C. Lear, H. Shelton, W. Krieve and R. Kemp

TRW SYSTEMS GROUP

TECHNICAL REPORT AFRPL-TR-128

NOVEMBER 1971

D D C

DEC 13 1971

C.

Air Force Rocket Propulsion Laboratory
Air Force Systems Command
Edwards Air Force Base, California

313

AFRPL-TR-128

EXPLORATORY DEVELOPMENT OF ADVANCED COLLOID THRUSTERS

M. Huberman, C. Lear, H. Shelton, W. Krieve and R. Kemp
TRW SYSTEMS GROUP

TECHNICAL REPORT AFRPL-TR-128

NOVEMBER 1971

FOREWORD

This document was prepared by TRW Systems, Redondo Beach, California, under United States Air Force Contract No. F33615-70-C-1405. Prior to July 27, 1971, this work was sponsored and directed by the Air Force Aero Propulsion Laboratory (AFAPL), Aeronautical Systems Division, Wright-Patterson Air Force Base. During this period, Mr. Jack Geis provided program management and technical guidance to AFAPL. On July 27, 1971, management responsibility for the program was transferred to the Air Force Rocket Propulsion Laboratory (AFRPL), Air Force Flight Center, Edwards Air Force Base. At this time, Lieutenant Stanley Rosen assumed technical responsibility for AFRPL.

This report describes the work performed from May 15, 1970, to September 15, 1971, by the Electric Propulsion Department, Applied Technology Division, TRW Systems. Dr. M. N. Huberman was Program Manager.

In addition to the authors' involvement in the project, Professor A. T. Forrester of UCLA and Dr. John Brooks collaborated on the theoretical neutralization study. A. Seaton, L. G. Beck, W. Daley, N. Law, and J. Ripley provided invaluable technical support throughout the program. Managerial and technical advice was provided by Mr. E. Cohen, Manager of the Electric Propulsion Department.

This report was submitted by the authors in September 1971.

This Technical Report has been reviewed and is approved.

WALTER A. DETJEN, Chief
Engine Development Branch

ii

ABSTRACT

This report describes a program to develop high performance colloid thruster systems. An electrostatically vectorable high thrust-density colloid source was developed and endurance tested for periods up to 2000 hours. The investigation of pulsed colloid thruster technology resulted in a demonstration of a feasible concept. Also, a breadboard high voltage supply for a pulsed thruster was built and demonstrated as well as a high voltage isolation valve to electrically decouple the propellant storage system from an individual thruster. Theoretical neutralization investigations evaluated the feasibility of utilizing the electrons in the ambient space plasma at synchronous altitudes to provide colloid thruster exhaust space charge neutralization. An electron gun type neutralizer for colloid engines was developed and life tested for more than 10,000 hours. Diagnostic investigations were directed toward analytically evaluating colloid thruster performance and its interaction with the laboratory test environment.

SPECIAL NOTE

Unless otherwise stated, all results presented in this report are based on time-of-flight measurements. These measurements are used to calculate thrust, specific impulse, charge-to-mass ratios, mass flow, and thruster efficiency. The efficiency in this case is defined as $T^2/2 \, \dot{M}P$, where T and $\dot{M}$ are, respectively, the thrust and mass flow resulting from the time-of-flight calculations, and P is the product of the applied needle voltage times the current supplied to the thruster. The time-of-flight calculations neglect the effects of beam spread and an approximate 400-volt loss in the spraying process. These two effects, which are impractical to measure in each experiment, are believed to result in overestimates of the order of 5 percent on specific impulse, thrust, and efficiency, based on periodic experimental observations of beam spread.

CONTENTS

CONTENTS (Continued)

CONTENTS (Continued)

CONTENTS (Continued)

ILLUSTRATIONS

ILLUSTRATIONS (Continued)

ILLUSTRATIONS (Continued)

Page

ILLUSTRATIONS (Continued)

Page

ILLUSTRATIONS (Continued)

Page

ILLUSTRATIONS (Continued)

ILLUSTRATIONS (Continued)

Page

ILLUSTRATIONS (Continued)

Page

ILLUSTRATIONS (Continued)

Page

ILLUSTRATIONS (Continued)

Page

TABLES

TABLES (Continued)

1. INTRODUCTION AND SUMMARY

The major program goal was to advance colloid propulsion technology toward providing a capability for designing, fabricating, and testing advanced high performance thrusters. In addition to the primary goal, major efforts were expended in developing and advancing ancillary technology related to the development of total colloid thruster flight systems. These investigations included pulsed thruster operation, electrostatic thrust vectoring, propellant feed system technology, neutralization, thruster diagnostic techniques, and problems related to laboratory ground testing of colloid thrusters.

Section 2 of this report describes the experimental development of a high performance, electrostatically vectorable annular geometry source. The major task was to develop a source capable of delivering ten times more thrust than a capillary needle and to prove its ability to operate for 1000 hours or more. Most of the early work consisted of an experimental design program (in which a series of design modifications were performance tested) to determine the influence of various design factors on thruster operation. Specific design areas investigated included emitter rim design, internal meniscus cavity configuration, source impedance, vector electrode geometry, and overall thruster module design, as well as studying the influence of test chamber ambient background pressure and the effects of vertical and horizontal thruster operation.

Several extensive endurance tests were performed to prove long term operational reliability. Two of these were nominally 1000 hours in duration and one test was allowed to continue for 2000 hours. The latter test was performed with a neutralizer. Several vectoring experiments performed during this test probed the exhaust to determine the beam cross-section profile during both vectored and unvectored operation. This run was originally intended to last for only 1000 hours; but, in view of the thruster's operational stability and freedom from deterioration at that time, a decision was made to continue the run to further determine long term effects of thruster operation.

For the first 1000 hours, the thrust   ed between 20 and 30 µlb and the specific impulse between 1300 and 1700 seconds at an efficiency of the order of 70 percent. At 1100 hours, the source was throttled to approximately 15 µlb thrust at 65-percent efficiency for the remainder of the run. During the last part of the run, several facility failures caused temporary shutdown; however, it was possible to restart thruster operation without aborting the run. The electrostatic vectoring system did not attain the hoped for ±7 degrees response in all directions. It was also found that vectored operation was not stable for this source.

Investigations of the feasibility of pulsed colloid operation are described in Section 3. This work included the design, fabrication, and successful testing of a laboratory breadboard power conditioning and control unit. The unit was designed to operate a 200-µamp beam-current thruster at a typical pulsing frequency for station keeping functions on spinning satellites. Life testing and performance investigations were performed for

1

several capillary needle and annular type sources. Several successful 500-hour pulse mode tests were performed, including a single needle test at greater than 1000-second specific impulse, greater than 2-μlb thrust (during on-time), and greater than 65-percent beam efficiency. The implications of pulsed operation regarding the design of flight power conditioning systems are also discussed.

Section 4 describes the development of a high voltage isolation valve that can electrically decouple the propellant storage system from an individual thruster. At 15 kv, the valve had a leakage current of 2.5 μamp. This valve is capable of decoupling a failed thruster subsection to allow continued operation of the remainder of the system, with only minimal power drain on the high voltage supply.

Neutralization studies are described in Section 5. Normally, a neutralizer satisfies two functions: (1) maintaining zero net spacecraft potential and (2) providing point-to-point space charge neutralization within the colloid thruster exhaust beam. The feasibility of utilizing the background electrons in the ambient space plasma at synchronous altitudes was theoretically investigated. An approximate approach was developed, indicating that this idea is feasible but a more detailed solution is necessary to confirm the feasibility. The motivation for this study is that such a concept will allow an electron gun neutralizer to be used solely for maintaining zero net spacecraft potential, thus allowing it to be positioned on the spacecraft far away from the thruster to minimize potential contaminating effects caused by the thruster exhaust. Also, this repositioning offers the possibility of requiring only one neutralizer aboard the spacecraft for several thruster systems.

A second phase of the neutralization program consisted of the design, fabrication, and testing of an electron gun type neutralizer for colloid thrusters. Such a neutralizer could be placed much further from the exhaust beam than the more conventional space charge coupled source, thus eliminating contamination problems caused by the propellant exhaust and allowing the use of high efficiency cathodes, which are normally prohibited because of their high susceptibility to poisoning. The several gun type neutralizers fabricated, tested, and proven easily provided a high efficiency performance. Four of these sources are still in operation after having passed thousands of hours of successful performance. One of these has accumulated more than 10,000 hours of total on-time and 50,000 on-off cycles. It is currently producing 1.35 millamp of emission current for 0.3-watt heater input. The other three neutralizers are operating after more than 8000 hours. All three neutralizers are producing acceptable emission currents at an injection voltage of 95 volts.

The effectiveness of gun type and tungsten wire neutralizers used with an annular source was also investigated. Floating collector techniques were used to measure neutralization as a function of electron injection voltage. A tungsten wire neutralizer provided neutralization throughout the 2000-hour life test. This test also proved that neutralization eliminates a minor annoyance inherent in most long term tests; that is the charging up and sudden discharging of insulating surfaces within the test chamber.

Section 6 describes colloid thruster vacuum bombardment contamination studies. Chemical investigations were undertaken to identify particulate matter deposited on both vacuum chamber walls and the thruster during long term operation. Attempts were made to prove the feasib⁻ity of propellant additives for inhibiting the formation of particulate matter in the propellant, but were not successful. Experiments to determine the influence of collector geometry on the back-scattering of materials to the colloid thruster were able to demonstrate conclusively that a honeycomb collector configuration significantly reduces back-scattering. Microscopic visual observation of an operating source demonstrated the importance of a good operating vacuum for colloid performance. These experiments demonstrated that, as the vacuum is degraded through the 10^{-5} torr region, electron bombardment induced gas generation begins to nucleate bubbles within the emitter.

Section 7 of this report describes several diagnostic techniques developed and used during this program to understand thruster performance better. An automatic data acquisition system was developed to provide automatic readout and calculation of time-of-flight performance parameters. The angular distribution of the mass and current within the thruster beam was measured and its influence on the accuracy of time-of-flight measurements has been demonstrated to be of the order of 3 percent or less. An analytical balance method was developed for directly measuring the mass flow through a colloid thruster. These results were compared with simultaneous time-of-flight measurements. The agreement was usually within the estimated accuracy of time-of-flight data. However, because of the scatter inherent in time-of-flight measurements, this comparison is not in itself sufficient to prove that there is no significant neutral mass fraction within the thruster exhaust.

2. ANNULAR GEOMETRY

The annular emitter geometry development program objective was the development of a high thrust density, high specific impulse vectorable colloid source. As the annular geometry passed through its several development phases, performance improved and became better defined. Performance of the final design (design 6BM3) may be characterized in two ways. This design was subjected to a 2000-hour life test; the first half was accomplished with between 20 and 30 μlb (actually closer to 20 μlb after the first 400 hours) thrust, 1300 and 1700 seconds specific impulse, and 70-percent thrust efficiency. A contaminating speck appeared within the propellant meniscus after a night of unattended operation. This served as a gas generation site which made it necessary to throttle back to 15 μlb for the remainder of the test. The final design was also extensively tested for short term performance over a wide range of operating parameters. During these tests, performance was demonstrated ranging from 13 μlb and 1300 seconds at 65-percent efficiency and 13-kv source voltage to 30 μlb and 1800 seconds at 68-percent efficiency and 16-kv source voltage.

Much of the early work consisted of an experimental design program, in which a series of design modifications were performance tested to determine the influence of various design factors.

In a properly designed colloid source, the propellant must be delivered in a controlled manner into a region of the proper electric field strength so that stable electrohydrodynamic spraying of multimolecular ions, or charged droplets, can occur. Figure 1 illustrates how this is accomplished by the annular emitter geometry tested during this program. Propellant is admitted, under pressure, from some type of plenum, as shown to the left in the figure. A standard flow impedance is provided by a length of small bore tubing to provide viscous resistance to the flow, permitting regulation of propellant flow rate by the inlet pressure. The propellant then passes into a shallow cavity at the source tip (called the meniscus cavity). Here, it forms a nearly semispherical, concave meniscus. The edges of this meniscus attach to the emitting rim. Propellant flows through the meniscus to the rim, mostly across the meniscus surface where there are no viscous forces. The long, sharp edge of the emitting rim provides a region where the proper electric field is obtained for electrostatic
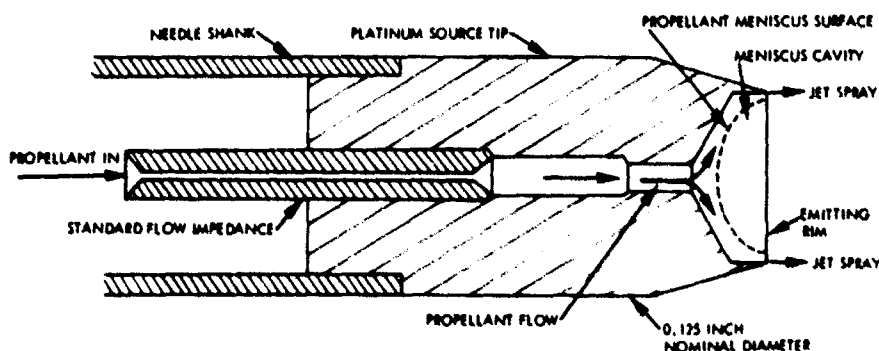
Figure 1. High Thrust Colloid Annular Source Configuration Schematic Drawing

4

spraying. This spraying occurs from many discrete sites (called jets) closely spaced around the rim circumference.

A total of 16 different emitter designs were tested throughout the program. Of these, there were three that shared the majority of the tests, all being of nearly optimal design and yielding the most fruitful results. Specific design areas investigated included emitter rim design, internal meniscus cavity configuration, propellant flow impedance, vector electrode geometry, and overall thruster module design.

Throughout the task, some 10 different electrostatic thrust vectoring experiments were run, yielding a variety of results. A thrust vectoring capability of about 7 degrees was demonstrated at least once, but this achievement was not repeatable. Difficulties were also experienced with operational stability during the vectored mode.

Two-axis time-of-flight probes were used to map the beam characteristics during both the vectored and unvectored states. With these probes, not only was thrust vectoring capability studied, but the angular distribution of beam current, mass flow, and charge-to-mass ratio were also mapped extensively (Section 7.2). The angular distribution of the beam was found to be consistently smooth and tight, with a beam cone angle of 15 degrees or less.

A test sequence was also undertaken during this task to determine if any appreciable performance differences could be realized by testing a source firing vertically rather than horizontally. No significant differences were found. The effects of test chamber ambient background pressure were also studied.

To conclude the task, several extensive endurance tests were performed to prove long term operational reliability. Two of these were nominally 1000 hours in duration and one test was allowed to continue for 2000 hours. The latter test was performed with a neutralizer. Several vectoring experiments were performed during this test, and time-of-flight probe data was obtained for the beam. The ability of the thruster to restart after several days shutdown in vacuum was demonstrated late in the test. The run was originally intended to last for only 1000 hours; but, in view of the thruster's operational stability and freedom from problems, a decision was made to extend the test for further study.

Upon completion of the experimental effort, a single source module was constructed, tested, and prepared for delivery under the contract.

The emitter configuration and geometry were first optimized through short term performance testing. After short term performance was established, a thrust vectoring capability was also established. Further testing and design modification eventually led to desirable long term stability characteristics. This was followed by life testing and more careful and exhaustive measurement of thruster performance characteristics.

Table 1 summarizes the developmental test program. The more important experiments will be discussed in appropriate subsections. The sources listed in this table are described in Table 2 and in Section 2.1.

5

Table 1. Program Experiment Log

Run No.	Date		Source No.	Vacuum System		Deflector Type	Remarks
	Start	Finish		TOF Distance (meters)	Pump Port Diameter (inches)		
No run no.	3/24/70	3/31/70	5	0.45	6	None	Six-source module
No run no.		5/6	1	0.45	6	None	
No run no.		5/12	2	0.45			
No run no.		5/14	3				
No run no.		5/18	4				
No run no.		5/19	5				
7004-01	4/2/70	4/10/70	5	1.92	10	None	Six source module; center needle was blocked off; used on thrust balance
7004-03	4/13	4/17	5	1.92	10	None	Same as above
7004-05	4/24	5/12	A	1.98	10	1	0.018 in. rim width; TOF probe studies vectoring
7005-01	5/21	6/5	4	1.98	10	1	Bubbling rate studies
No run no.	6/4	6/8	6	1.4	6	None	First use of view probe
7005-04		6/5	5	1.92	10	None	First vertically tested
7006-01	6/10	6/12	7	1.4	6	None	
7006-02	6/10	6/11	6	0.9	10	None	Vertical test
7006-03	6/12	6/17	3	1.39	6	None	
7006-4	6/18	6/29	8 MI	0.9	10	None	Vertical test
7007-01	6/19	7/6	9	1.39	6	None	
7007-02	7/6	7/10	8MI	1.92	24	None	
7007-03	7/8	7/20	7	1.82	10	None	Vertical test
7007-04	7/15	8/17	8MI	1.95	24	None	616-hr life test - bubbling rate studies
7007-05	7/22	8/10	7	0.9	10	None	Vertical - 551-hr life test
7007-06	7/22	7/23	9	1.39	6	None	
No run no.	7/30	7/31	6	0.31	6	None	Pulsed annular emitter
7008-01	8/10	8/14	7-2	2.06	10	1	Poor wetting
7008-02	8/20	8/27	7-2	2.06	10	1	Poor wetting
7009-02	9/8	9/11	7-2	0.85	10	1	Vertical test - poor wetting
7009-03	9/15	9/17	7-2	1.82	10	None	Poor wetting
7009-04	9/21	9/23	7	1.82	10	None	Horizontal performance verification - TOF probes
7009-05	9/25	9/30	7-3	1.82	10	None	Observed bubbling
7010-01	9/30	10/1	7	1.82	10	None	Good performance - observed bubbling
7010-02	10/6	10/15	7-3	1.82	10	None	Vertical scratches inside rim; better wetting - TOF probes

Table 1. Program Experiment Log (Continued)

Run No.	Date Start	Date Finish	Source No.	Vacuum System TOF Distance (meters)	Vacuum System Pump Port Diameter (inches)	Deflector Type	Remarks
7010-03	10/6	10/8	10	1.71	10	None	
7010-05	10/12	11/24	7-2	1.71	10	None	948.4-hr life test; successful rework of source
7010-07	10/16		6B	1.39	6	None	First surface roughened rim - fully roughened
7010-08	10/19	11/9	7	1.82	10	2	417-hr life test; current probes of vectoring
7010-09	10/23	10/29	10B	1.39	6	1	Rim 50% polished
7011-02	11/12	11/13	11B	1.39	6	3	Rework of 10B from last run; smooth rim
7011-03	11/18		12BMI	1.39	6	3	
7011-04	11/23	11/25	7BMI	1.39	6	3	Rework of above 11B; high impedance
7011-05	11/19	11/25	11B	1.82	10	3	
7012-01	12/8	12/11	6BMI	1.39	6	None	Low voltage
No run no.	12/9	12/10	11B	1.82	10	2	
No run no.	1/5/71	1/8/71	7	1.87	24	None	Direct mass flow measurement
7101-01	1/7	1/8	7BM2	1.78	10	3	Life test shakedown
7101-02	1/12	1/14	7BM2	1.78	10	3	As above
7101-03	1/15	1/19	7BM2	1.78	10	3	As above
No run no.	1/21	2/2	11B	1.87	24	None	Direct mass flow measurement
7101-04	1/20	3/5	7BM2	1.78	10	3	1,015-hr life test; vectoring. TOF probes
7102-01	2/3	2/4	7BMI	1.82	10	None	Stability studies with contaminated source
No run no.	3/10	3/11	6BM3	1.39	6	2	First Run, 6BM3
7104-01	4/7	4/9	6BM3	1.87	24	4	Shakedown for life test
7104-02	4/16	5/4	6BM3	1.87	24	4	433-hr life test attempt direct mass flow measurement; vectoring; TOF probes
7105-01	5/11	8/9	6BM3	1.39	6	4	Life test - 2,042 hours; vectoring; TOF probes
7106-01	6/17	6/18	6BM3	1.39	6	4	Deliverable thruster
7107-01		7/9	6BM3	1.78	10	2	20 kv source voltage
7107-03		7/21	6BM3	1.78	10	2	20 kv source voltage

Table 2. Summary - Annular Source Geometries

SOURCE NUMBER	GEOMETRY	RESEARCH OBJECTIVES	RESULTS	REFERENCE MONTHLY REPORT	CONCLUSIONS
A	DRILL OUT CENTER PLUG FOR PROPELLANT FEED, 15° OUTER BEVEL, STRAIGHT INNER WALL	TEST EFFECT OF REMOVING CENTER PLUG	NO TAR FORMATION, SOME GAS GENERATION	1, 3, 4,	PROMISING. TAR GREATLY REDUCED OR ELIMINATED
1	INNER BEVEL, STRAIGHT OUTER WALL	TEST INNER BEVEL CONCEPT, SHALLOW MENISCUS CAVITY	EXCESSIVE BEAM DIVERGENCE, HOLLOW BEAM	3	ANNULUS RADIUS TOO LARGE (0.125 IN.)
2	15° OUTER BEVEL, STRAIGHT INNER WALL 0.090 IN., DEEP MENISCUS CAVITY	TEST SHALLOW MENISCUS	TIGHT BEAM (±20°), UNSTABLE OPERATION, GAS GENERATION	3	MENISCUS CAVITY TOO DEEP
3	SAME AS 1, BUT REDUCED ANNULUS RADIUS	NARROWER BEAM	EXCESSIVE GAS GENERATION, UNSTABLE OPERATION	3	MENISCUS CAVITY TOO DEEP, POOR DESIGN
4	SAME AS 2, BUT 0.010 IN. DEEP MENISCUS CAVITY	TEST SHALLOWER MENISCUS	LOW BEAM SPREAD, STABLE OPERATION, BUT POOR WETTING	3	MENISCUS CAVITY TOO SHALLOW
5	OLD CENTER-PLUG TYPE ANNULUS	PERFORMANCE COMPARISONS	HEAVY TAR FORMATION ON CENTER PLUG	1969 FINAL	INFERIOR DESIGN
6	SAME AS 2, BUT 0.015 IN. DEEP	OPTIMIZE MENISCUS CAVITY DEPTH	STABLE OPERATION, GOOD PERFORMANCE, ±20° BEAM SPREAD	4, 9, 10	MENISCUS CAVITY DEPTH OPTIMIZED
6a	SAME AS 6, WITH SURFACE-ROUGHENED MENISCUS CAVITY	IMPROVED RIM WETTING	IMPROVED, STABLER WETTING, LOWER BEAM SPREAD	14-17	EVENTUALLY CHOSEN AS THE FINAL MODEL
7	SAME AS 6, WITH RIM ROLLED IN AND OUTER BEVEL SHAVED	DECREASE BEAM SPREAD	STABLE, HIGH PERFORMANCE, ± 15° BEAM SPREAD, LONG LIFE TEST, FIRST RIM TAR	4, -10, 12	PROMISING, BUT FABRICATION DIFFICULT, TAR FORMATION QUESTIONED
7b	SAME AS 7, WITH SURFACE-ROUGHENED INTERIOR MENISCUS CAVITY	IMPROVED RIM WETTING	IMPROVED WETTING ACHIEVED	12, 13	DECIDED FABRICATION UNNECESSARILY DIFFICULT
7-1	ATTEMPTED DUPLICATE OF 7, OUTER BEVEL HELD TO 30°	DUPLICATE PERFORMANCE OF 7	UNSTABLE OPERATION, GAS GENERATION, POOR WETTING	7-10	DEFECTIVE MENISCUS CAVITY WAS TOO SHALLOW
7-3	SAME AS 7, BUT LONGITUDINAL GROOVES SCRATCHED ON INNER WALL	IMPROVED WETTING	GOOD WETTING ACHIEVED	8	SURFACE TREATMENT IMPROVES WETTING
8	SIMILAR TO 7, TIPPED BY RIM WAS CUT INSTEAD OF ROLLED, SHARPER BEVEL	IMPROVED PERFORMANCE	SIMILAR TO 7, BUT HIGHER PERFORMANCE, FASTER PERFORMANCE DEGRADATION	4-7	FABRICATION TOO DIFFICULT, TOO MUCH RIM TAR
9	SAME AS 6, BUT SMALLER ANNULUS RADIUS (0.075 IN.)	IMPROVE BEAM FOCUSSING	STABLE OPERATION ACHIEVED, DATA SCANTY	NOT REPORTED	NO IMPROVEMENT NOTICED
10	SAME AS 7, BUT OUTER BEVEL WAS NOT SHAVED, 30° BEVEL	EASIER FABRICATION, STURDIER MECHANICAL PROPERTIES	DEGRADED PERFORMANCE <100DSEC AT 9 UA/SEC	9	PERFORMANCE UNNECESSARILY DEGRADED
10a	SAME AS 10, WITH SURFACE-ROUGHENED INNER MENISCUS CAVITY	IMPROVED RIM WETTING	SIMILAR TO 10	9	SIMILAR TO 10, SURFACE-ROUGHENING IMPROVES WETTING
11b	SAME AS 7B, BUT SLIGHTLY SMALLER ANNULUS DIAMETER	DIFFERENT, EASIER MODE OF FABRICATION	FABRICATION WAS HARDER, PERFORMANCE SAME AS 7B	9, 10, 12	FABRICATION IS IMPRACTICAL
12b	SAME AS 10B, BUT OUTER BEVEL SHAVED SLIGHTLY TO 25° BEVEL	STURDIER AND EASIER TO FABRICATE	PERFORMANCE UNNECESSARILY DEGRADED	10	SURFACE ROUGHENING IMPROVES WETTING, BEVEL ANGLE TOO LARGE

A "B" after the source number refers to the surface roughening technique described in Section 2.1. The designations M1, M2, and M3 denote other source modifications discussed in Section 2.1. Four different types of deflector electrodes are indicated and are also discussed in Section 2.1. A summary of the experimental program approach is presented in Table 2. The experiments are classified according to source design. A brief geometrical description of each design is given, as well as contractual monthly reports which reference the design.

Figure 2 is a schedule of all program tests and shows the time phasing of work on each of the various designs. The intial work done with type 5 and type A stands out, and so does the notable increase in activity around types 6, 7, and 8. These latter types were the best performers.

The annular emitter program was, for practical purposes, a six-phase program. The phases were all interdependent and overlapped in time; however, they started roughly in the sequence given in this section. The following six sections describe these phases in detail.

Section 2.1 presents the 16 different emitter designs and the four different propellant flow impedance designs tested, as well as discussing the vectoring electrodes, thermal design, and module design.

Section 2.2 resents details of performance testing and shows how i. influenced design. Performance capabilities are discussed in terms of thrust, specific impulse, thrust efficiency, performance stability, and beam divergence.

Section 2.3 presents the major results of the electrostatic thrust vectoring investigation.

Section 2.4 is a discussion of the test program undertaken to ascertain the effects, if any, of gravitational asymmetries on performance.

Section 2.5 is a discussion of the seven major life tests conducted during the program.

Section 2.6 is a discussion of the fabrication and testing of a deliverable single source module.

Several aspects of the annular geometry performance were determined during other tasks of the total program and are discussed elsewhere in the report. Section 7.3 describes direct mass flow measurements that were taken during some of the annular source runs. Observations of propellant gas generated by electron bombardment of an annular geometry source are described in Section 6.4. Finally, Section 7.2 is a discussion of the use of time-of-flight probe experiments to obtain angular distributions of thrust, mass flow, current, and local thrust efficiencies in the beam of an annular emitter.

2.1 ANNULAR THRUSTER DESIGN

The design development was continuously correlated with test program results. The first step determined the major effects of emitter geometry on performance. Once a near optimum emitter geometry was found, further testing was directed toward perfecting that geometry and
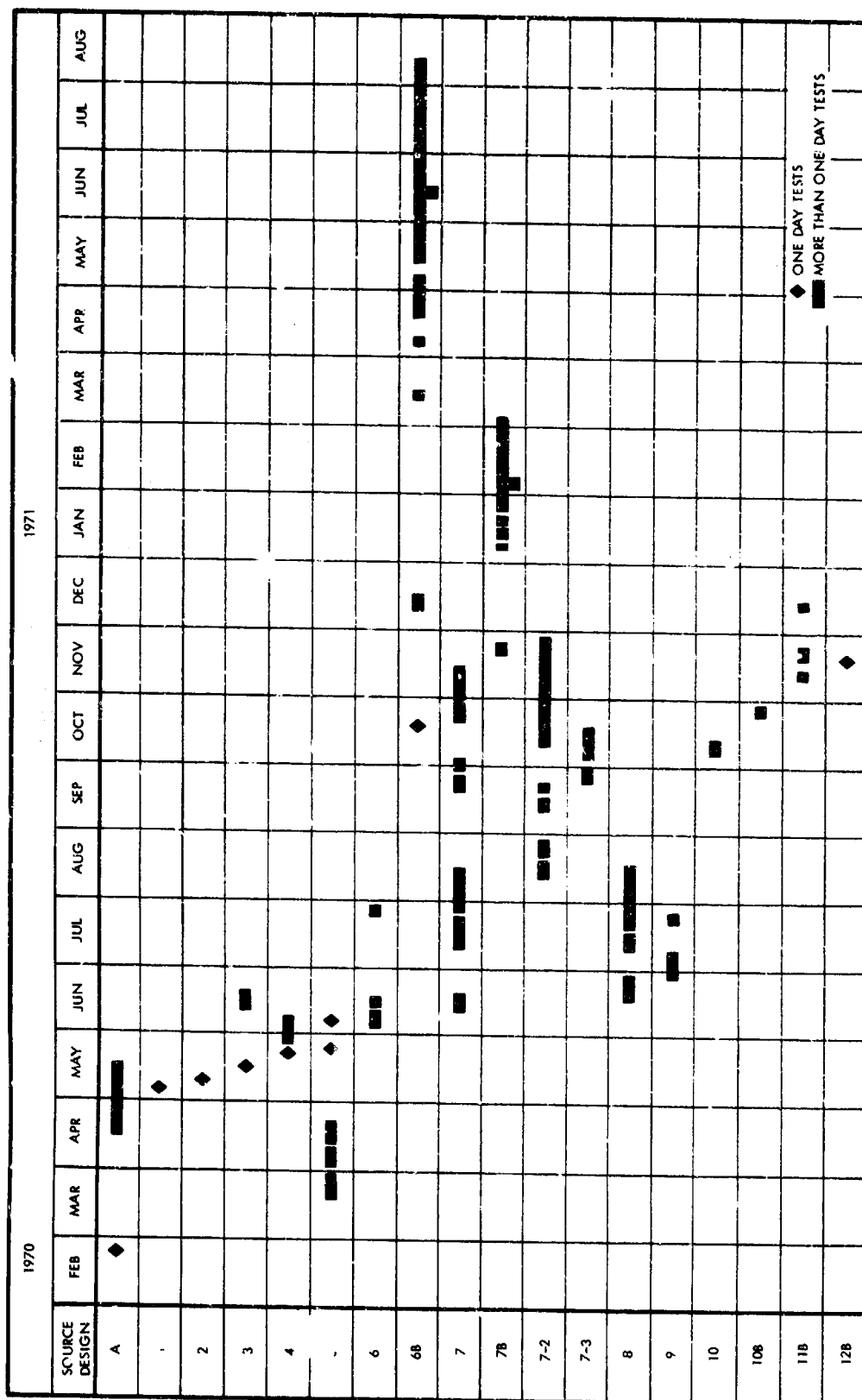
Figure 2. Annular Source Test History

extending operating time. Considerations of cleanliness and simplicity were dominant in determining design changes to an optimum impedance configuration. Finally, thermal design considerations were added to achieve the final source design.

Concurrent with source design, deflector electrode design was continually refined as the result of a strong interaction with performance testing. Reliability, source performance, and vectoring performance were the governing considerations.

2.1.1 Design Procedure

The design process was oriented toward the testing of a wide variety of different concepts to determine the most optimum concept. Differences in concepts were mainly geometrical. The one notable exception was the concept of surface roughening in the meniscus cavity, introduced about halfway through the program.

After sufficient experience, the most worthwhile concept appeared to be represented by the group of source designs numbered 6, 7, and 8, and their type B (surface roughened) counterparts. These were all very similar in geometry. With repeated testing, the small differences in performance and utility of these three could be sorted out. Thus, the final choice was based on a large backlog of fabrication and test experience.

The starting point was a center plug design, in which propellant was fed to the rim through an annular gap. This is designated in Table 2 as source 5. To eliminate a possible site for contaminant build-up, the plug was recessed and the center allowed to fill with propellant. As a next step, the propellant feed path was changed from an annular gap to a small central feed channel. The resulting design is designated as type A in Table 2. To fabricate type A, the center plug was drilled and pushed back to form a shallow well, called the meniscus. This well is counter-sunk and drilled to admit propellant to the center. The well must be deep enough so that the propellant forms a natural meniscus, but shallow enough so that propellant will flow rapidly from the center to the rim before building up a saturation gas concentration.

Several variants of the type A source geometry were tried. A description of these geometries, along with those of the other basic designs, will be found in Section 2.1.2. The designs were labeled 1 to 4. Types 1 and 3 had an inner positive bevel to the meniscus cavity wall, up to the rim. These were found to produce excessive beam divergence and exhibited poor rim wetting characteristics. Types 2 and 4 were more successful and led to the discovery that the depth of the meniscus cavity influenced performance. Deep meniscus wells appeared to be more susceptible to bubble nucleation in the propellant, whereas the meniscus in shallow wells tended to detach, resulting in rim wetting difficulties. When the meniscus cavity depth was optimized, source design 6 resulted.

Along with these studies of gross geometry, a study was made of the effect of rim width on performance. Most of this work was done with source type A. A rim width of 0.001 inch turned out to be optimum. A

sharper rim tended to enhance the ion peak in the beam current distribution and degraded the efficiency. A blunter rim, on the other hand, tended to lower the average charge-to-mass ratio.

During testing of source 6, a new geometry was conceived, primarily designed to decrease beam spread. The design is basically like number 6, except that the rim is tipped inward slightly to produce a negative bevel on the inside of the meniscus well. The argument for decreased beam spread is that there is a given angle formed between the surface of the outer edge of the rim bevel and the surface of the propellant meniscus where it attaches to the rim. The bisector of this angle is close to the direction of maximum field strength. By tipping the rim inward, as indicated, this angle is pointed more toward the axis. Since the beam is expected to be emitted near the direction of maximum field strength, this would tighten the beam. Performance testing of this design indicated favorable results. Some rather interesting observations of the beam pattern of source 7 are discussed in Section 2.2.

Sources 7 and 8 were the two designs to evolve from this concept. The rim of each was fabricated on a lathe, the former by forming, the latter by cutting techniques. Comparison of the results of the testing of sources 7 and 8 was difficult because the test objectives were not consistent. However, after enough experience had been accrued and similar testing had been accomplished with each source, it appeared that the performance differences were not significant. Later, when testing of types 6 and 6B was resumed and surface roughening of the emitter had been introduced, it appeared that the performance advantage of types 7 and 8 over type 6 was not as great as it first seemed. Since fabrication of both new types of emitters imposed difficult problems and resulted in extremely fragile rims, testing was eventually discontinued. The remaining research then concentrated on type 6.

The testing of type 7 sources introduced some important new developments. Two duplicates of the original type 7 source were made and studied. These were labeled 7-2 and 7-3. At first, source 7-2 was subject to poor wetting, the cause of which was difficult to identify. A precise method of measuring the shape of the rim and meniscus cavity was developed; and, with this method, the important defect in source 7-2 was discovered and corrected. After modification, source 7-2 was successfully run in a major life test, run 701005 (Section 2.5).

Figure 3 shows a micrograph of source 7-2, before and after modification. The micrograph was made with a 100X microscope attached to a three-axis comparator. The comparator is accurate to a few ten thousandths of an inch. Measurements on the vertical axis are made by adjusting the microscope for sharpest focus in its narrow depth of field, and measuring the vertical travel of the microscope with a dial indicator comparator. The result is a cross-sectioned profile of the source geometry. Figure 4 shows a micrograph of the original source 7, and Figure 5 shows a later type 7B source for comparison.

The second duplicate of source 7 was called 7-3. This source was modified to promote wetting by covering the inside of the meniscus cavity
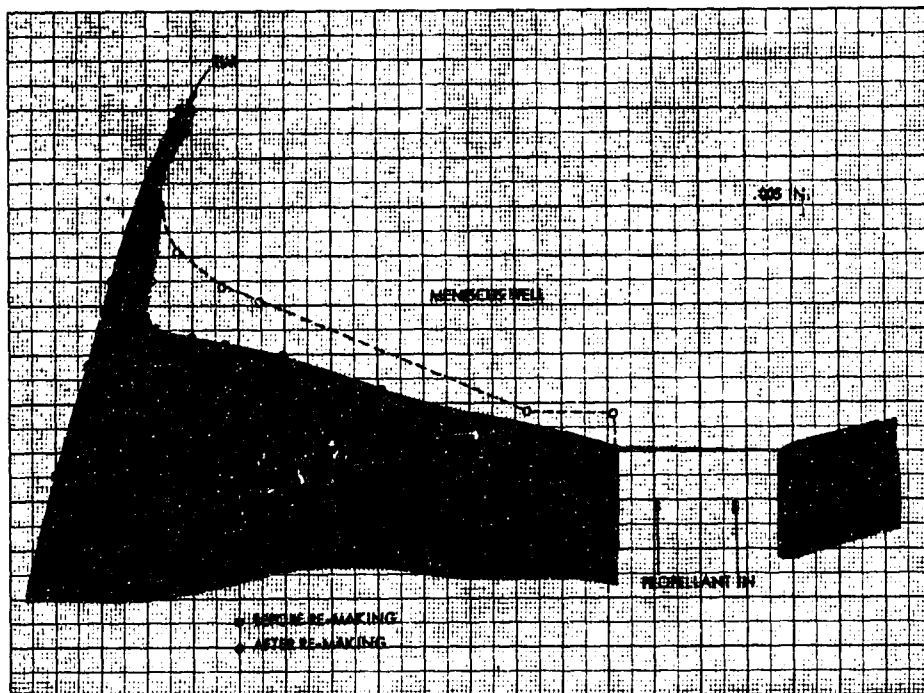
Figure 3.   Micrograph of the Shape of the Rim and Meniscus
            Cavity of the Annular Source 7-2, Before and
            After Modification.   Poin' indicate where surface
            coordinates were read microscopically.
            Approximately two-thirds profile is shown.
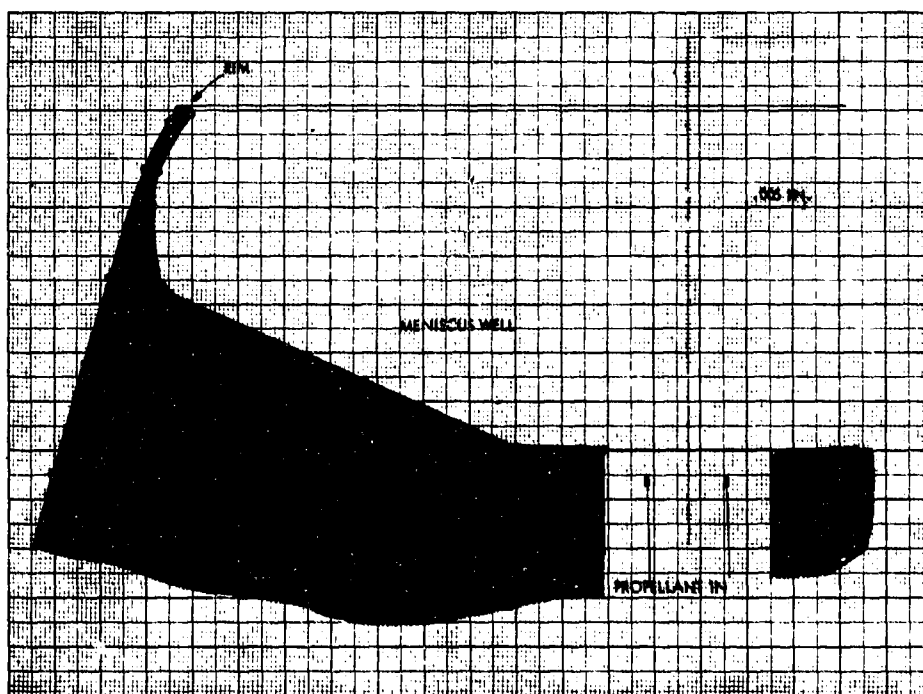
Figure 4.   Micrograph of the Tip of the Original Annular
            Source 7.   Points indicate where surface
            coordinates were read.   Two-thirds profile
            is shown.

13
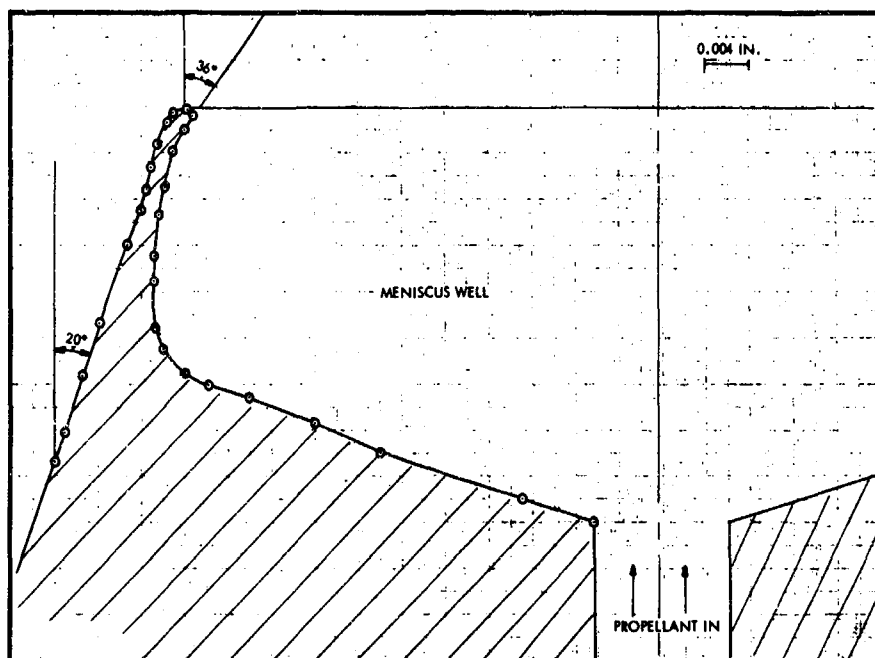
Figure 5. Micrograph of Annular Source Geometry 7B in
Cross Section Showing Rim and Meniscus
Well. Points indicate where surface
coordinates were read microscopically.
Approximately two-thirds profile is shown.

with a series of tiny longitudinal grooves leading up to the rim. In
run 701002, this experiment proved successful and it was concluded that
surface roughening treatment in the meniscus cavity, and on the rim if
desired, would promote and control propellant wetting.

New methods of homogeneous roughening of platinum surfaces were
then developed and tested. A number of new sources with roughened
meniscus cavities and rims were tested. The first source to be so
treated was the original type 6 geometry, which became designated 6B.
This was quickly followed by 7B and a series of new designs, 10B, 11B,
and 12B. All tests demonstrated quicker establishment and better con-
trol of rim wetting by the propellant. Performance aspects of some of
these tests are discussed in Section 2.2. Tests also were conducted
with type 6B to investigate various degrees of rim (as opposed to cavity)
roughening, ranging from completely rough to completely smooth.
Experience indicated that the smooth rimmed devices were superior,
providing more control over the stable location of the jet sites on the
rim.

Further design modifications were made in the form of source types
10, 11, and 12. Their objective was to relieve the fabrication problems
of design 7 while maintaining or enhancing the performance. None of
these attempts was particularly successful: Types 10 and 12 showed too
much loss of local extraction field strength due to rim bluntness; and type
11 was geometrically nearly an exact duplicate of 7, but equally as hard
to fabricate, if not harder.

14

2.1.2 Emitter Design

A total of 18 different emitter geometry designs were investigated during the program. Thirteen of these designs were basic; the five remaining were simple variations or duplicates of some of the basic 13. The basic designs are illustrated in Figure 6. Further descriptive summaries of the emitter designs are given in Table 2. Since source 5 existed before the program began, it formed a starting point for the present program. It is the original center plug type annular emitter and was included in the present sequence for performance comparison.

Source type A is important because it was the first center fed type annular emitter geometry. Modified from an early type 5, it demonstrated the feasibility of the center fed propellant meniscus concept. Testing proceeded from this point with geometry development.

Source types 6, 7, and 8 were the focal point of activity during the middle months of the program. These three similar designs were very close to optimum. Types 7 and 8 appear to be very promising high performance designs; however, the demonstration of their superiority over type 6 was not conclusive. Simplicity and ease of fabrication made type 6 the preferred design.

Toward the middle of the program, a surface roughening technique was developed for platinum. When roughening was applied to the inner rim and meniscus cavity of an emitter, the wetting properties of the rim were greatly improved and provided more uniform propellant feed to the entire rim area. Designs using surface roughening are designated with a letter B after the source number; thus, the final emitter design chosen was type 6B.

Emitter designs 7-2 and 7-3 were simple variations of type 7 involving minor design and geometry changes discussed in Section 2.1.1.

Throughout the program, the source tips were made of platinum/10 percent iridium, which has been found to possess satisfactory machineability as well as resistance to electrochemical erosion. The design is easily fabricated using common lathe techniques.

2.1.3 Impedance Design

After the emitter geometry was fairly well established, attention was focused on the propellant flow impedance. The design of this impedance was modified twice. Figure 7 shows the original design and the two modifications.

Mass flow is partly controlled by the flow impedance through a 0.028-inch OD by 0.004-inch ID platinum-iridium tube. This ID is the same as that of the standard TRW capillary needle and is convenient to work with. Both the original and mod 1 designs used 0.150-inch long impedance tubes. The impedance thus obtained was roughly equivalent to putting seven 1-inch capillary needles in parallel.

15
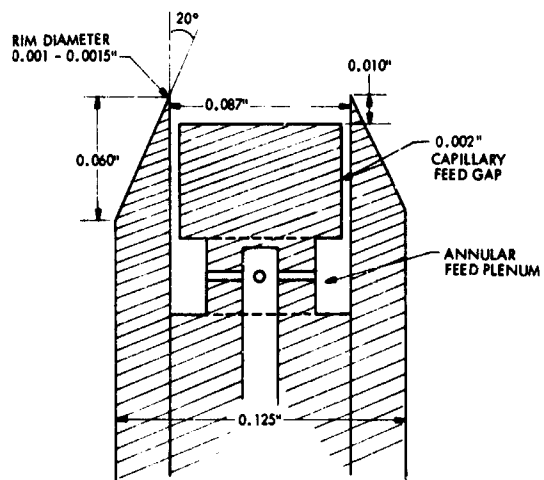
a. Type 5
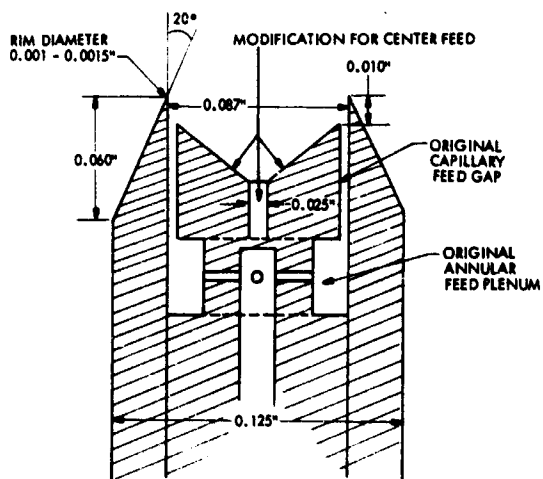
b. Type A
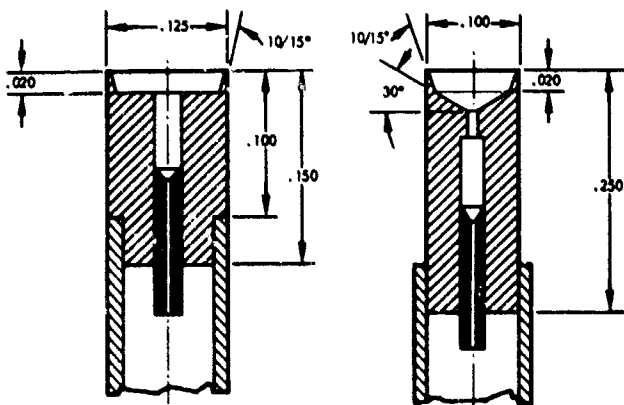
c. Types 1 and 3
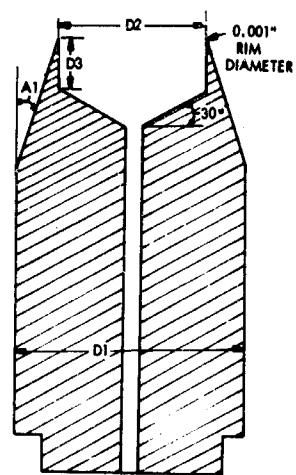
d. Types 2, 4, 6, and 9

DIMENSION	GEOMETRY NO.			
	2	4	6	9
D1 (INCHES)	0.125	0.125	0.125	0.100
D2 "	0.093	0.093	0.093	0.075
D3 "	0.020	0.010	0.015	0.015
A1 (DEG.)	15	15	15	15
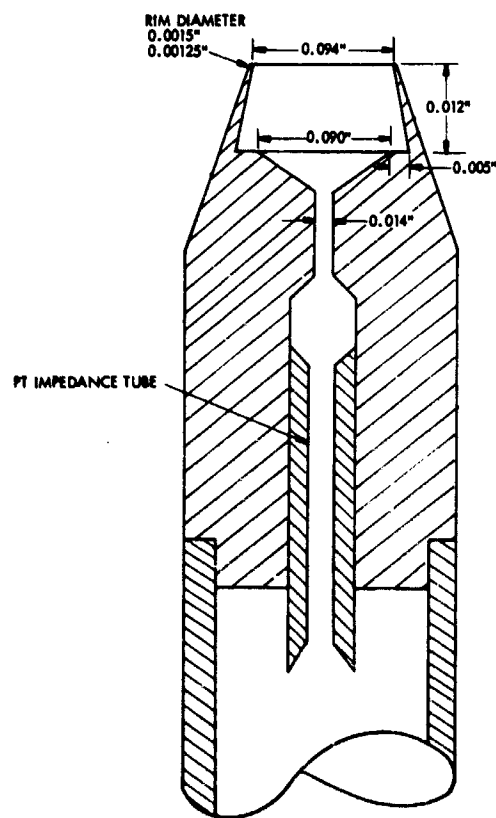
e. Type 8

Figure 6. Annular Emitter Design Geometries

DIMENSION		GEOMETRY NO.		
		7	11	12
D1	(INCH)	0.088	0.088	0.090
D2	"	0.014	0.014	0.015
A1	(DEG)	20	20	25
A2	"	15	15	15
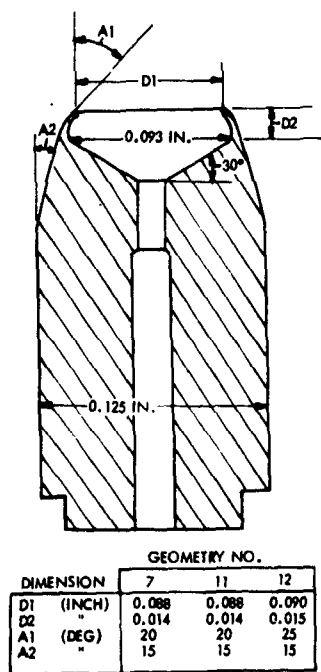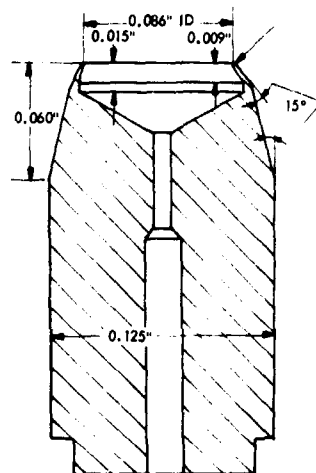
f.　Types 7, 11, and 12　　　　g.　Type 10

Figure 6.　Annular Emitter Design Geometries (Continued)

a.　Original Design

c.　Modification 2　　　　　　b.　Modification 1
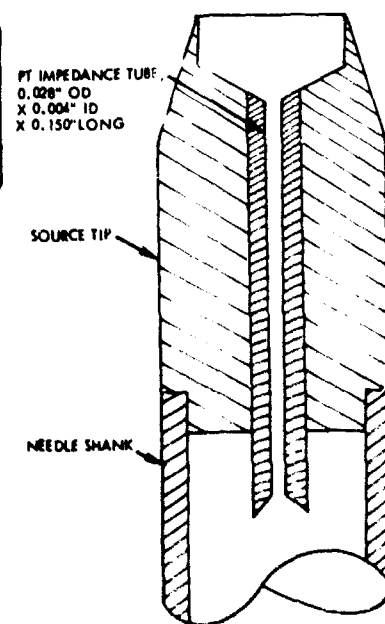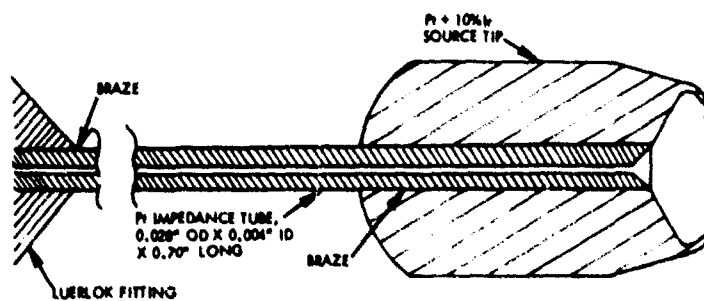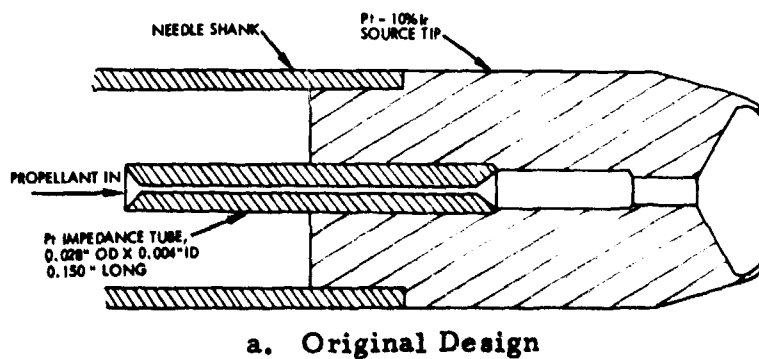
Figure 7.　Three Types of Mass Flow Impedance Designs

17

The first modification eliminated the dead space between the impedance tube and the meniscus cavity. This region was very hard to clean and was believed to be trapping impurities. In the original design, the impedance tube was either brazed in place or fastened with epoxy at the back of the emitter. The mod 1 design was either brazed or press fitted. The entire needle shank, a 1/8-inch OD tube, was filled with propellant during operation.

In the mod 1 design, it was believed that the pocket just upstream of the impedance tube at the base of the source tip might also be a trap area. Again, this area was very difficult to clean. The second modification solved this problem.

The mod 2 design consisted of extending the impedance tube the full length of the source, joining it into a Luerlok or other propellant inlet junction and eliminating the 1/8-inch OD tubing from the propellant path. This design had the advantages of added simplicity and a mass flow impedance more comparable to that of a capillary needle. In practice, the mass flow impedance was nominally 70 percent of a 1-inch needle. The increased impedance also allows more mass flow control capability.

As the impedance tube and shank of the source were modified, it became convenient to refer to them with an M1, M2, etc., after the emitter geometry number designation. Type 6BM3 became the final source design.

2.1.4 Thermal Design

The major thermal design problem considered was that of maintaining the needle temperature as uniform as possible. To increase the thermal conductance to the emitter tip and to add structural strength, a 1/8-inch tube was positioned around the central impedance tube. Since this tube does not contact the propellant, the bonds to the source tip and the base do not have to be leak tight. A hole drilled in the tube allows evacuation of the tube interior. The thermal conductance from the source tip to the baseplate is about 0.004 joule/sec-$^{\circ}$C. About 33 percent of this conductance is in the central, platinum-iridium impedance, which has a relatively high conductivity.

The total heat capacity, or "thermal mass" of a solid body, is defined as $C\rho V$, where C is the specific heat capacity, ρ is the mass density, and V is the total volume. The thermal mass of the 0.20-inch long platinum-iridium source tip is about 0.115 joule/$^{\circ}$C.

The thermal mass/thermal conductance ratio, the thermal response time, has a value of 30 seconds. This time is indicative of how fast the given thermal mass will respond to a surrounding temperature change with heat flow through the given thermal conductance.

Active temperature control is achieved by a thermistor sensor embedded in the thruster base, a surrounding radiant heater, and an electronic temperature controller. The thermistor element and its leads are embedded in a 3/8-inch diameter epoxy plug. The bottom of the plug is threaded to fit an 8-32 screw hole in the filter back. Good thermal

coupling is provided by using high thermal conductivity, high dielectric strength alumina epoxy (Emerson and Cummings Stycast 8250 FT). The radiant heater is a coil of nichrome heater wire placed circumferentially around the thruster module.

The temperature controller's adjustable dead-band is usually set to about $\pm 0.1^{\circ}C$ at a $25^{\circ}C$ control setting. The cycle time is about 2 minutes, or four times the calculated thermal response time.

The maximum steady state temperature difference between the baseplate and source tip due to radiative cooling of the tip can easily be estimated. Assuming a total emissivity of 0.1 and no return radiation from the vacuum system interior, a baseplate held at $25^{\circ}C$ will lose about 3.5 mw through the source thermal conductance. The resulting temperature drop is $1^{\circ}C$.

2.1.5 Vector Electrode Design

Four basic types of vector electrodes were tried during the development program. Type 1 was a set of three longitudinally straight electrodes fabricated from 0.180-inch ID, 0.010-inch thick wall, stainless steel tubing. They were mounted off the extractor plate with 0.5-inch long ceramic insulators. The vector electrodes of this type and all the others were separated from each other and from the source rim by spacings of about 0.030 inch. The electrodes had to stand off voltage differences of up to 13 kv across these gaps. The close spacings were needed to maximize vectoring response.

Type 2 was a set of three electrodes similar to type 1. Instead of being longitudinally straight, however, the electrodes were swaged in at the top, next to the source rim, to form a 0.150-inch inner diameter and to make the electrode-to-rim gap equal to 0.030 inch. Although the intent was to increase vectoring capability and extracting field strength, it had little effect.

Type 3 was the same as type 2, but the mounting was moved from extractor to baseplate to increase the alignment precision, allowing the electrode circle to be centered around the source.

Type 4 was a set of three electrodes, individually cut and tapered for a length of about 0.2 inch, and soldered to individual baseplate-mounted supports. This type was the easiest to align mechanically; also, the least amount of area was exposed to high electric field strength. Type 4 was ultimately chosen for the design of the deliverable thruster module.

The type 4 vector electrode design is discussed in Section 2.1.6. The four types are illustrated in Figure 8, which shows the extractor and baseplate mounted design, the swaged tubing type of design, and the individually cut and tapered type. The straight tubing design is very similar in appearance to the swaged tubing design.
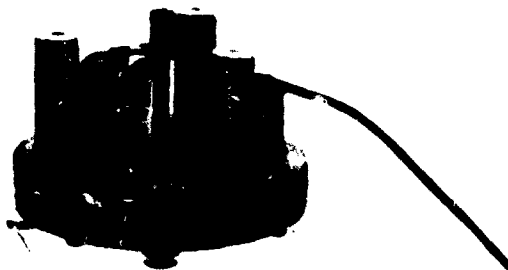
2.1.6 Module Design

Although an 18 source annular emitter module was designed as part of the program effort, the experimental effort was confined to a single source version. One single source version module was fabricated and life tested (run 710501, 2000 hours), and a second module was fabricated, performance tested, and prepared for delivery under contract.

Figure 9 is a plan drawing of the single source module with the filter back and baseplate design adapted directly from previous modules. The cutaway shown for the encapsulated thermistor sensor design is discussed in Section 2.1.4. The high voltage stand-off insulators shown may be either ceramic or Teflon. The slightly improved and integrated vector electrode design shown is adapted from type 4, discussed in Section 2.1.5. Instead of being fabricated from two pieces, the deflector and the support bar may be integrated into a single piece and pressure formed to the desired shape. The result is somewhat smoother and less bulky.

The emitter design for this module is a type 6B which is discussed in Sections 2.1.2 and 2.1.4. In the final design, the impedance tube was a 0.028-inch OD by 0.004-inch ID platinum/10 percent iridium tube. It was press fitted into the source tip at one end, allowed to pass through the baseplate at the other end, and sealed with an epoxy bond. The thermal shank fits over a boss on the baseplate.

Figure 10 is a photograph of a typical source structure. In this picture, the baseplate junction has been replaced with a Luerlok fastener to allow quick removal of the source from the module. Figure 11 is a detailed cutaway drawing of the source. Figure 12 shows several views of the assembled module.

a. Baseplate Mounted, Swaged Tubing

b. Extractor Mounted, Swaged Tubing

c. Individually Cut and Tapered Design

Figure 8. Annular Thruster Vector Electrode Designs
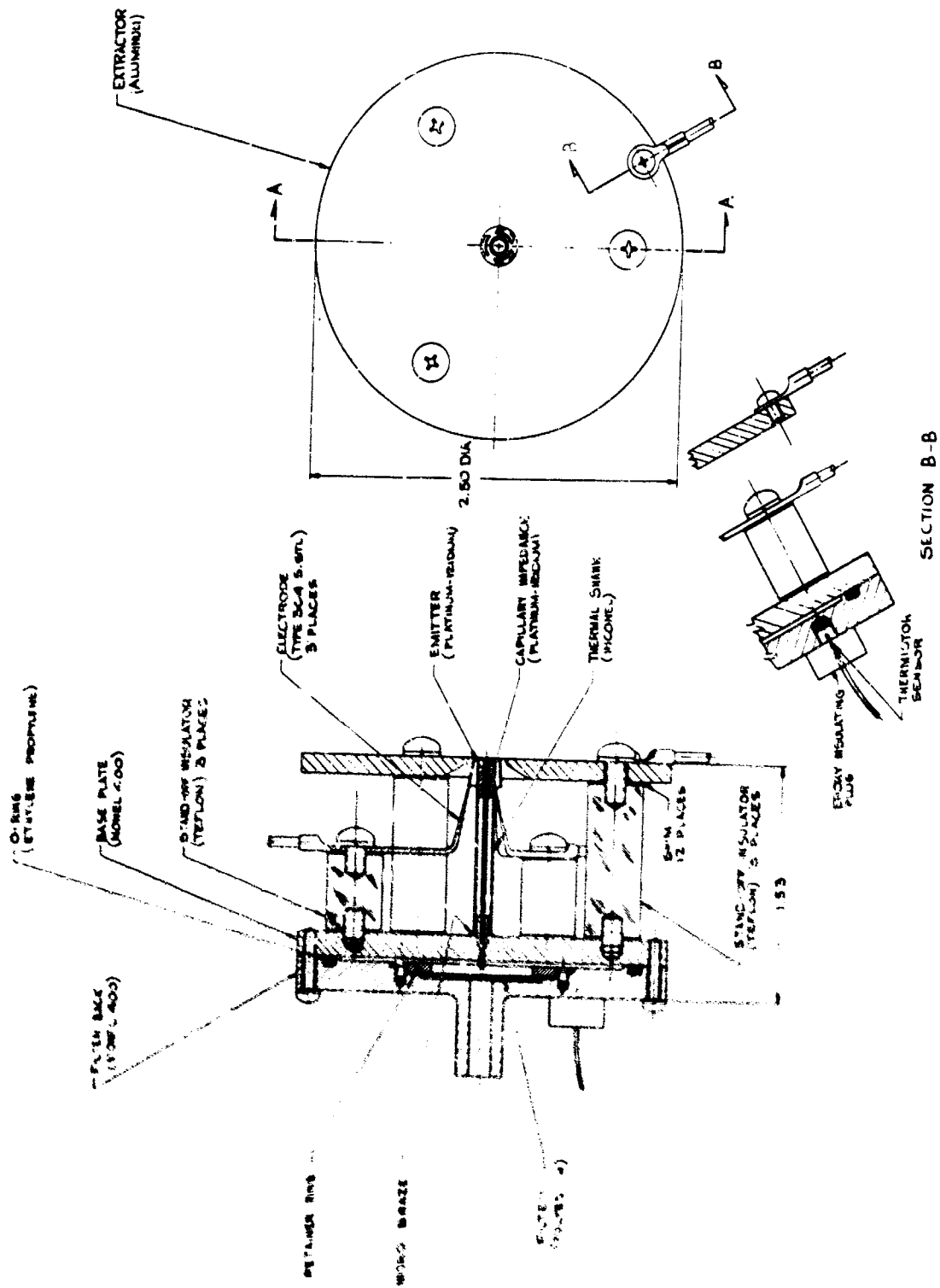
Figure 9. TRV Experimental Annular Source Module Plan Drawing
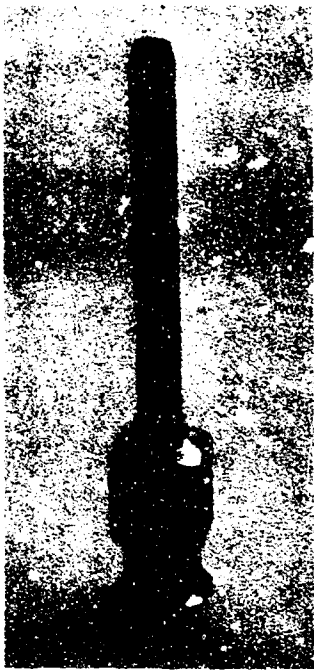
Figure 10. TRW Single Rim Annular Source Removed f. om Module. Emitting rim is around top and the bottom baseplate junction is replaced with a Luerlok fastener for adaptability to different modular designs.

2.2 PERFORMANCE TESTING

Early emitter geometry development testing was conducted in a small vacuum system with a 6-inch diameter diffusion pump and a 1.4 meter time-of-flight distance. Most of this testing was performed with an early module design and without vector electrodes. At the end of this period, geometry configuration 6 seemed particularly promising. It was stable and showed a low beam spread. Early time-of-flight results showed high thrust and low specific impulse, but they were later proven erroneous.

To measure the beam spread, a device called a "view-probe" was installed to allow direct visual observation of the beam profile. The view probe is a flat copper screen disc, about 70 percent open, mounted to move in or out of the beam in a plane perpendicular to the beam direction. The screen is grounded. When out of the beam, it does not affect the beam or source performance. When in the beam, the incident particles produce a luminescent pattern that gives a sharp visual picture of beam current density over the exhaust plane. Several index marks, starting at the center and spaced at distances of 1 inch along the probe radius, allow accurate visual determination of the beam width.
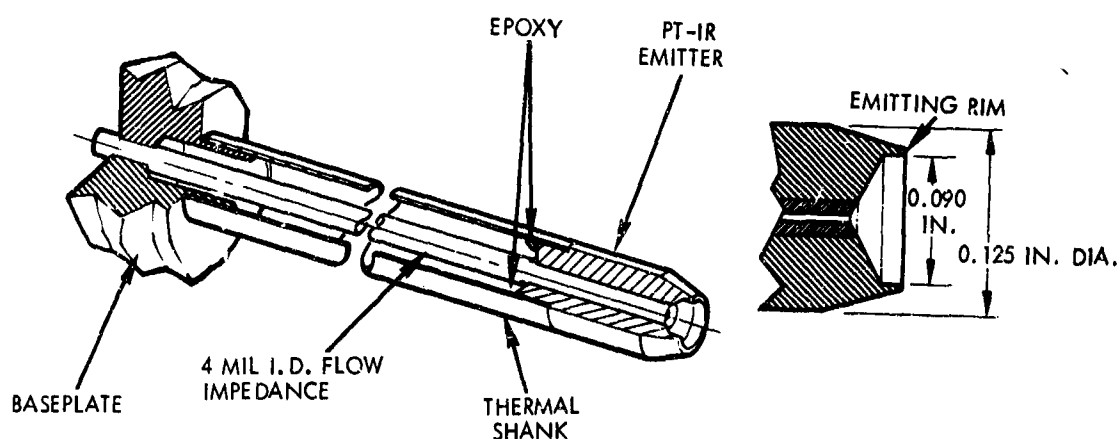
Figure 11. Schematic Cutaway Drawing of TRW Single Rim Annular Source 6BM3

22

a. Top View - Extractor Aperture and Deflector Electrode Alignment
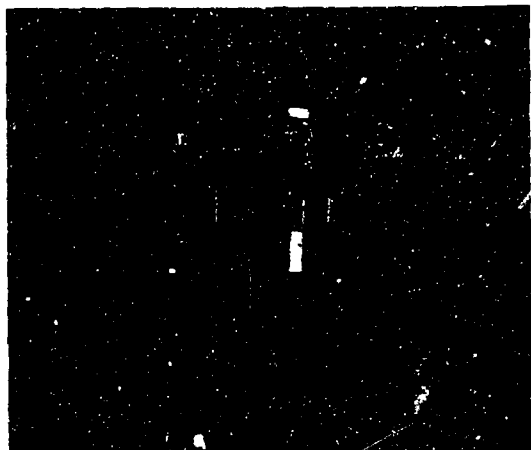
b. Side View - Electrode Understructure

c. Top View - Entire Assembly

Figure 12. TRW Single Rim Annular Source Module with Three Deflector Electrodes

The view probe is inserted in the beam about 6 inches in front of the needle. The time it may be left in the beam is limited to about 30 seconds because of excessive copper sputtering and back-scattering.

View probe measurements with configuration 6 indicated the entire beam was contained within an 18-degree half-angle cone. Nominal operation was at 14-kv needle voltage and 90-μamp needle current. Feed pressure was approximately 4 inches.

The view probe was used several times in later runs. Although it was eventually replaced by the use of more quantitative probe data, it proved to be a valuable visual tool.

Concurrent with the small scale unvectored testing, a program was undertaken to study the performance of a vectored annulus. These tests were performed in a large 4 by 8 foot vacuum station with a 10-inch diffusion pump. The facility was provided with horizontal and vertical probes to measure the thrust vectoring capability (Section 2.3). The first full scale time-of-flight (TOF) performance studies were conducted during this phase.

The following sections discuss individual tests which resulted in significant operational data or performance improvements for a given source design.

2.2.1 Source Design A: Run 700405

This run actually consisted of two separate tests for two slightly different configurations. In addition, this was the first time that time-of-flight probe vectoring and beam profile mass distribution data had been obtained for this type of source. Table 3 lists the nominal operating parameters.

23

Table 3. Nominal Time-of-Flight Data: Run 700405,
for Performance Map of Figure 13

	Source	Extractor	Deflectors	Collector	Screen	Suppressor
Voltage	14 kv	-2 kv	5 kv	0	45 v	-20 v
Current	85 μa	2 μa	0	25 μa	-	-

Feed Pressure = 4 in. Hg   Tank pressure = 6×10^{-6} torr

Time-of-Flight Distance = 1.95 m

Thrust	Mass Flow	Efficiency	I_{sp}	Average g/m
25 μlb	7.9 μgm/sec	72%	1490 sec	10,650 c/kg

Thrust and flow rates are based on source current and are uncorrected for beam spread or energy loss. The propellant was a NaI-glycerol solution of approximately 4700 ohm-cm resistivity.

Figure 13 shows the effect of varying feed pressure on thrust and I_{sp}. Thrusts of the order of 25 μlb could be achieved at a specific impulse near 1500 seconds. In general, efficiency decreases with decreasing mass flow since this usually results in an increase in the ion fraction contained within the beam.
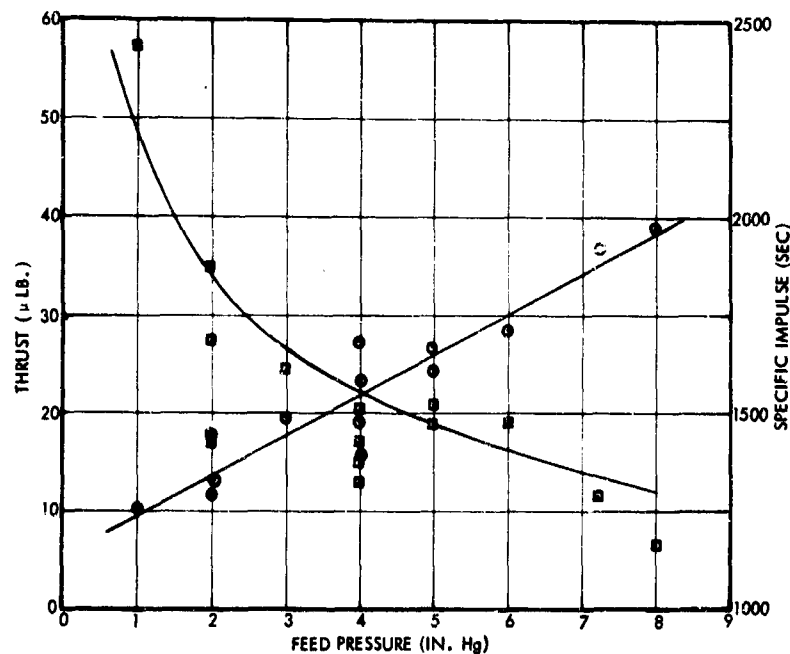
Figure 13. Run 700405 - Thrust and I_{sp} as a
Function of Feed Pressure,
Uncorrected Time of Flight Data

The source was removed from the test station, cleaned and reworked. The centerpiece height was reset to give a meniscus cavity depth of 0.020 inch instead of 0.015 inch. In addition, the rim was dulled to a width of 0.002 inch rather than 0.001 inch. This was later determined to be too dull for good performance. Table 4 lists nominal operating parameters during this part of the run.

Figure 14 shows the effect of varying feed pressure on thrust and I_{sp}. Specific impulse data could be fitted by a single curve. The thrust data require upper and lower limit designations. The two points on the upper limit curve were taken at the same time but at a different time than the points on the lower limits, three of which were also taken all at once. The remaining points, at 4 inch Hg feed pressure, were taken during a probing sequence.

2.2.2 Source Design 7

The four runs that figured most significantly in the evaluation of source configuration 7 are described below.

Run 700601 was the first run. The source rim was carefully machined to the order of 0.001-inch width. It was then installed, without deflectors, in the small view probe vacuum station.

The most significant aspect of the run was the visually determined beam profile. View probe measurements indicated that the entire visible beam was contained in a cone of 10-degree half angle. Also, a diamond-shaped luminescent glow was clearly visible just beyond the emitter tip, probably due to particle crossover trajectories. This phenomenon had never been noticed before and an attempt was made to capture the effect on film. It was only partly successful. The results are shown in Figure 15. Part a shows the entire beam. It was taken on speed 3000 film at F5.8, 3-minute exposure. In part b, the exposure time was

Table 4. Nominal Time-of-Flight Data for the Main Collector, Including TOF Parameters for the Performance Map of Figure 14

Source	Extractor	Deflectors	Collector	Screen	Suppressor
Voltage 14 kv	-2 kv	5 kv	0	50 v	-50 v
Current 50 μa	1 μa	0	13 μa	-	-

Feed Pressure = 4 in. Hg   Tank Pressure = 8×10^{-6} torr

Time-of-flight Distance - 1.95 m

Thrust	Mass Flow	Efficiency	I_{sp}	Average q/m
20 μlb	7.54 μgm/sec	75%	1180 sec	6.36 c/gm

25
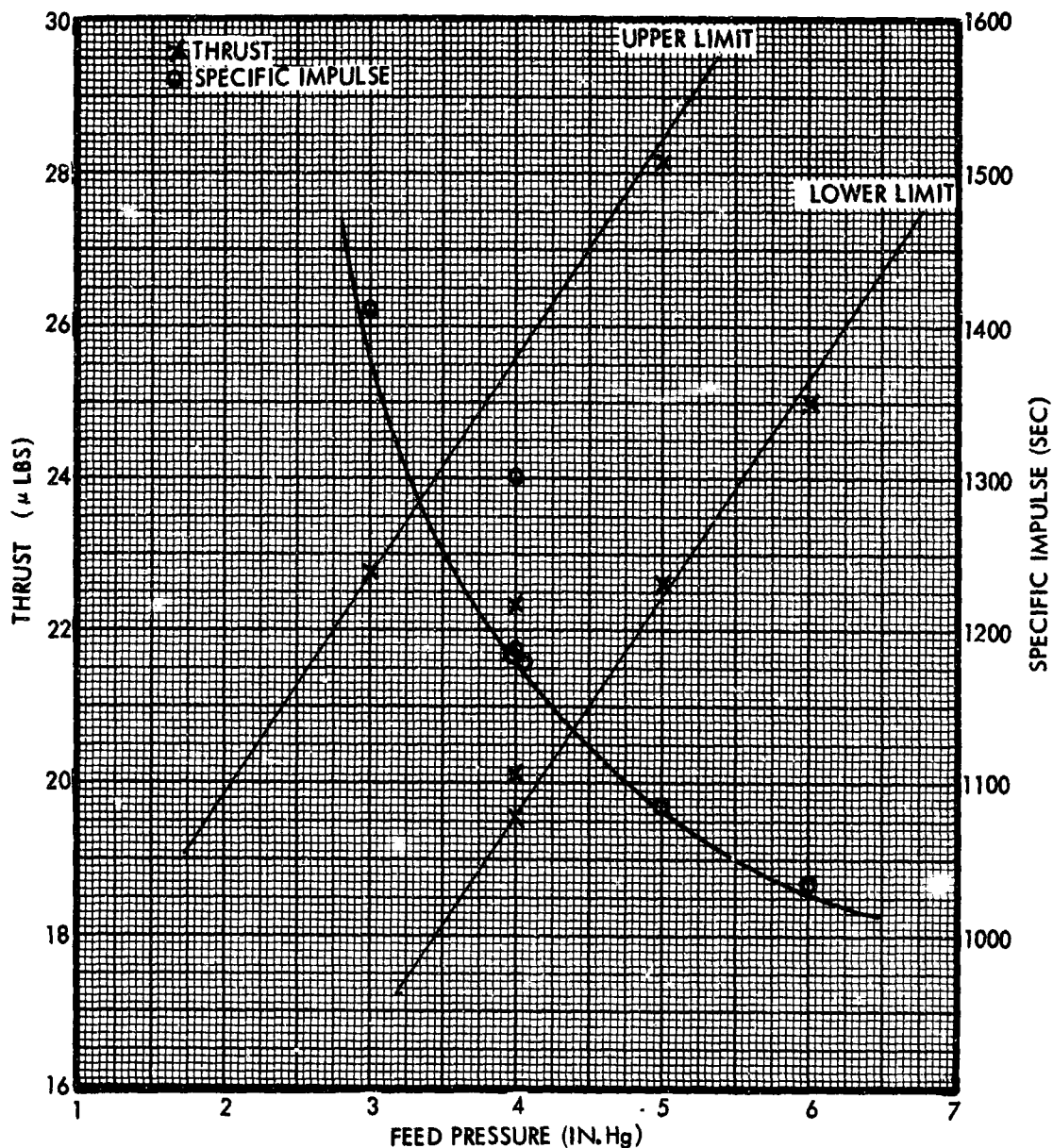
Figure 14. Run 700405: Thrust and I_{sp} as a Function of Feed
Pressure, After the Rim was Blunted
(Uncorrected Time-of-Flight Data)

reduced to about 30 seconds, attempting to catch only the crossover
diamond at the needle tip.

Run 700703 tested source 7 without deflectors and oriented
vertically with respect to gravity. This test ran 267 hours; it is also
discussed in Section 2.4.

The operating voltage was nominally 14.1 kv for the entire run.
This voltage allowed operation near 25-μlb thrust and 1500-second specific
impulse. Performance was mapped at 75 hours into the test and is shown

a. Gross Beam Outline,
3-Minute Exposure

b. Diamond Formed by Crossover
Trajectories, 30-Second
Exposure

Figure 15. Beam from Source
Configuration 7 at
14 kv and 106 μamp

in Figure 16. Other nominal time-of-flight parameters for this run are presented in Section 2.4.

Run 700904, after further vertical testing, was then successfully run horizontally for 45 hours without deflector electrodes. A thrust of 27 μlb at a specific impulse of 1560 seconds was obtained shortly after the test started and was maintained throughout the test, except during short periods when performance was being mapped.

The vacuum was nominally 4×10^{-6} torr and the source voltage was 14 kv. Thrust efficiency was 70 percent for the rated thrust and specific impulse, but was found to vary with specific impulse being 60 percent at 1740 seconds and 80 percent at 1100 seconds. Figure 17 shows the feed pressure and beam current as a function of time-of-flight mass flow. Figure 18 shows the performance parameters, thrust and specific impulse. The successful completion of this test proved the performance of source 7 operating horizontally, without deflector electrodes.

Run 701008 was a 417-hour horizontal life test of source 7, using type 2 deflector electrodes. The specific impulse was generally above 1200 seconds, thrust above 20 μlb, and thrust efficiency at or above 60 percent uncorrected.

Figure 19 shows the performance at start-up. The source voltage varied slightly around 16 kv. A thrust of 25 μlb was obtained at 1600 seconds specific impulse. Other nominal operating parameters are shown in Table 5.

Figure 20 shows a performance map after 350 hours. The data indicates a thrust of 25 μlb could be obtained at a specific impulse of 1300 seconds. The performance degradation relative to start-up time was probably due to solid contaminant deposition on the rim. Other aspects of the life test are discussed in Section 2.5.

Figure 16. Thrust and Specific Impulse versus Feed Pressure for Run 700703 - Source Configuration 7 in Vertical Testing (From Uncorrected TOF Data Taken Between 75 and 165 Hours)

28
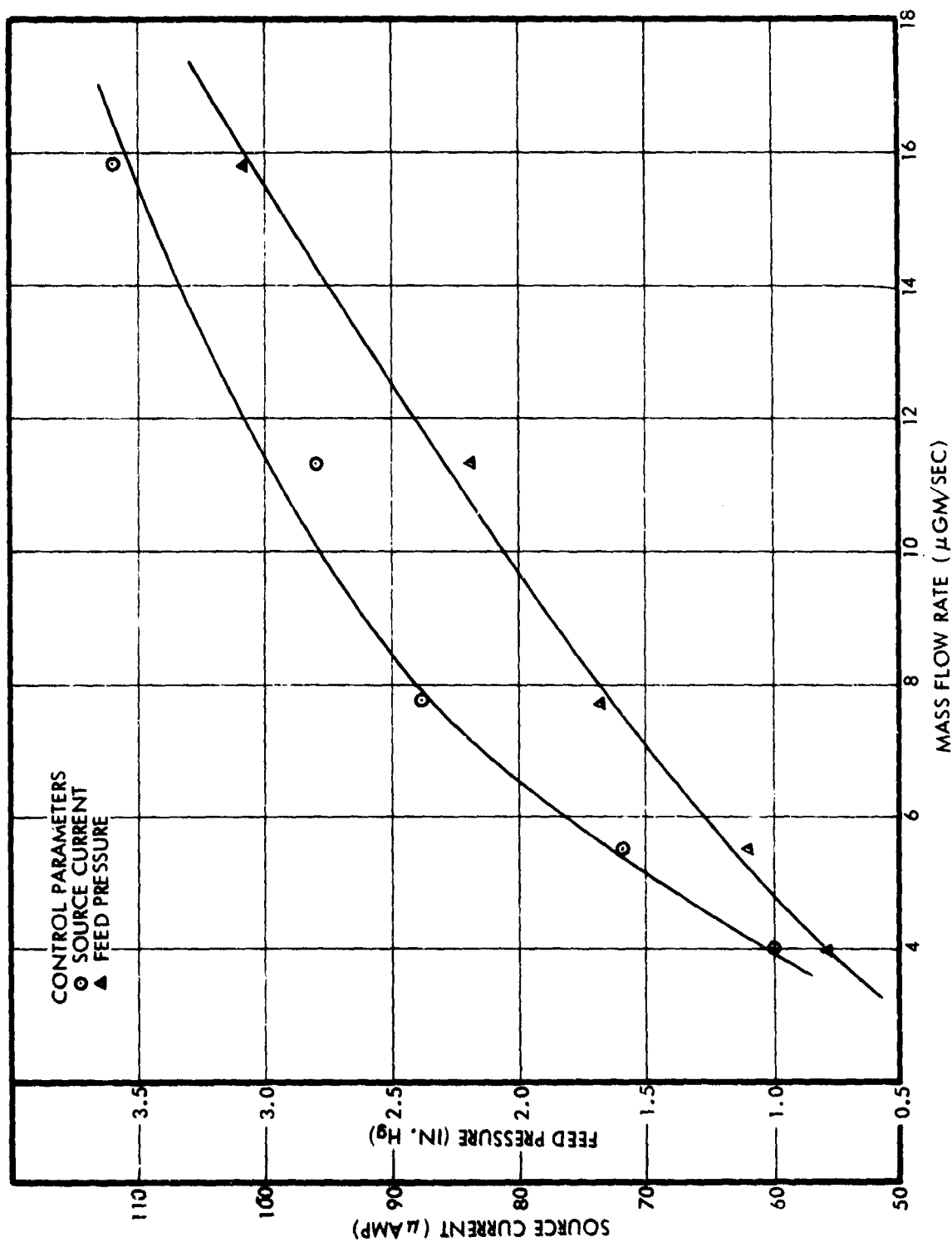
Figure 17. Feed Pressure and Source Current as a Function of Time-of-Flight Mass Flow Rate; Annular Source 7, Run 700907

29
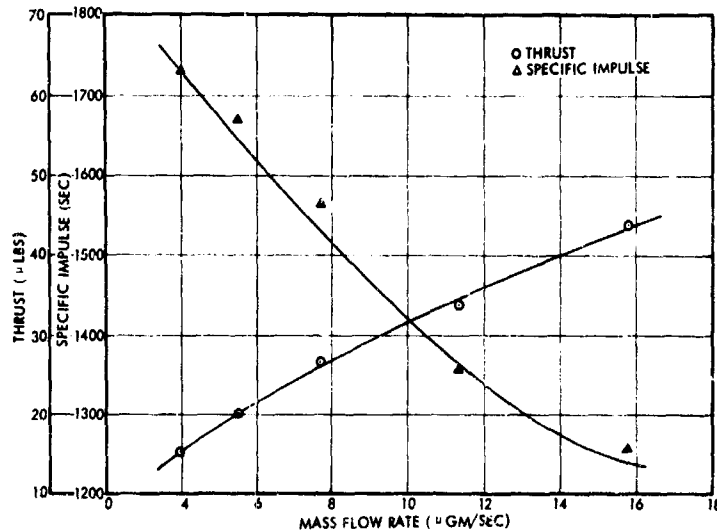
Figure 18. Time-of-Flight Thrust and Specific
Impulse as a Function of Mass Flow
Rate, Annular Source 7,
Run 700907
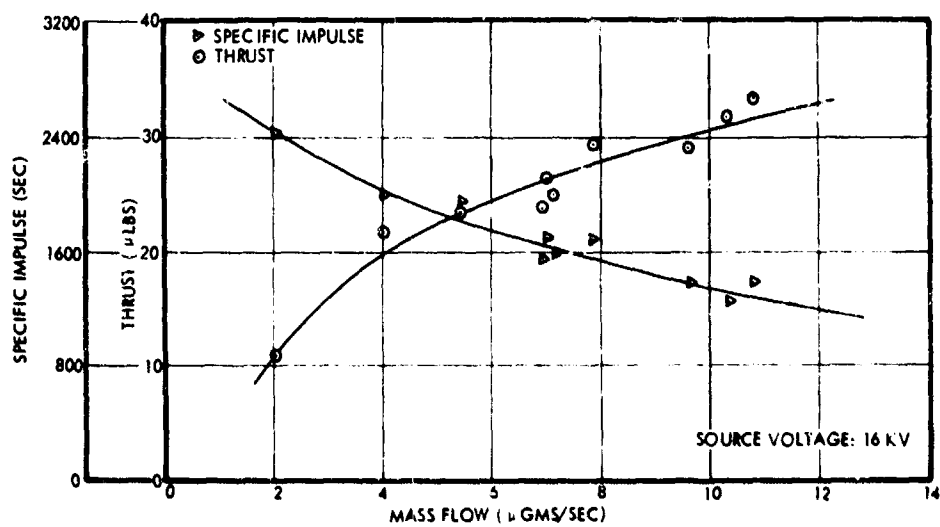
Figure 19. Thruster Performance for Annular Geometry 7
Shortly After Start-up, Run 701008 with
Deflectors in NRC-2

Table 5. Nominal Operation of Source 7
During Run 701008

Source: Voltage, 16 kv; current, 90 μamp
Extractor: Voltage, -12 kv; current, 1-6 μamp
Deflectors: Voltage, 12.5 kv; current, 0-5 μamp
Feed Pressure: 1.5 in. Hg
Tank Pressure: 10^{-5} torr
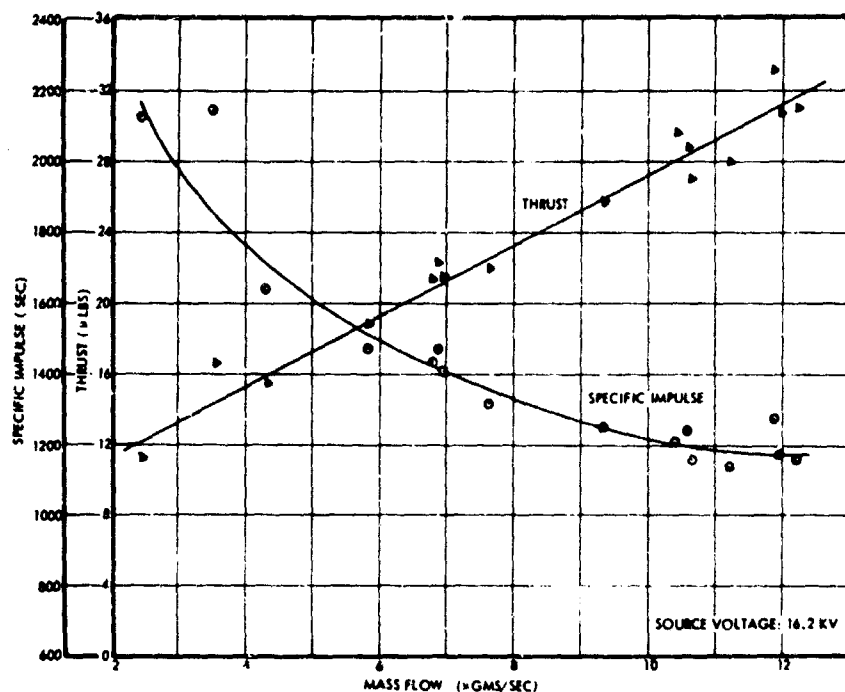
Figure 20. Thruster Performance for Annular
Geometry 7 after 350 Hours,
Run 701006, with Deflectors
in NRC-2

2.2.3 Source 7-2: Run 701005

Source 7-2 was essentially an attempt to reproduce source 7. It
was used for a 948-hour endurance test without deflector electrodes. Its
performance was mapped at the beginning of the test. The data shown in
Figure 21 was obtained under the test conditions shown in Table 6. This
table also shows the performance after 950 hours. The test is further
discussed, as a life test, in Section 2.5.

2.2.4 Source Design 8: Run 700702

Source 8 had undergone two prior tests (see Section 2.4) in which
dramatically high performance was achieved in the vertical orientation.
However, there seemed to be excessive degradation of performance with
time.

To continue the sequence of testing on source 8, it was refinished,
cleaned, and installed horizontally, without deflector electrodes, in the
4 x 8 foot tank with the 24-inch Edwards pump.

Prior to the run, the rim of the source was inspected micro-
scopically. It was found to be a uniform one mil in width and was one of
the finest rim finishing jobs we have obtained. The impedance measured
was equivalent to approximately 5.5 standard 0.014 inch OD x 0.004 inch
ID x 1 inch long needles placed in parallel.

31
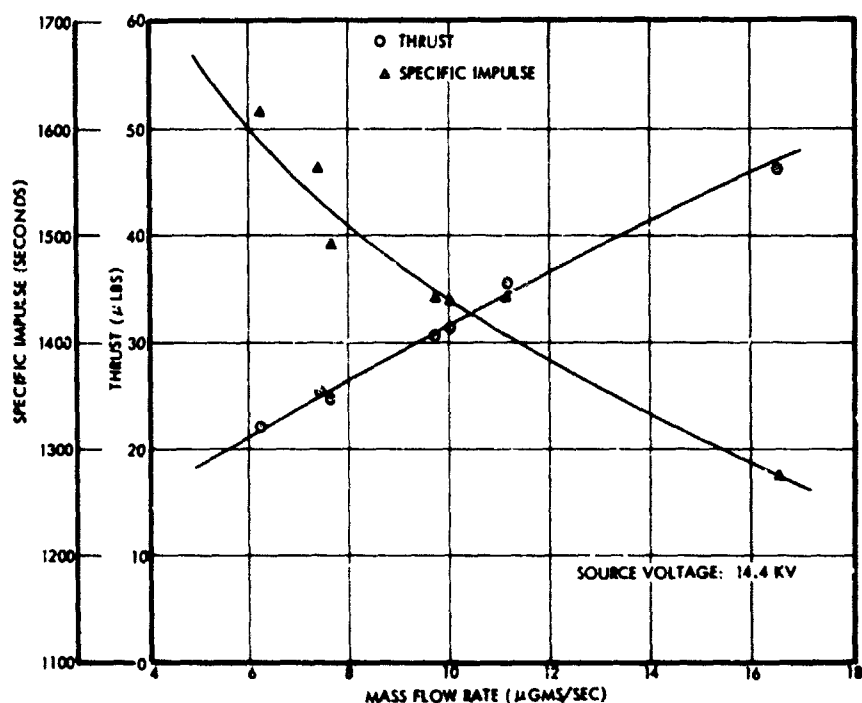
Figure 21. Time-of-Flight Thrust and Specific Impulse
as a Function of Mass Flow for Annular
Source 7-2, Run 701005, First 60 Hours

Table 6. Nominal Operation of Source 7-2 During Run 701005

		50 Hours	950 Hours
Instrumentation			
Source:	Voltage (kv)	14.2	15.2
	Current (μamp)	100	50
Extractor:	Voltage (kv)	-2	-2
	Current (μamp)	0.1	0.5
Feed Pressure (in.-Hg)		1.5	1.3
Tank Pressure (torr)		4.5×10^{-6}	$4 \times 10^{-}$
<u>Time of Flight Performance</u> <u>(Uncorrected)</u>			
Thrust (μlb)		31	22.5
Specific Impulse (sec)		1440	1067
Mass Flow (μgm/sec)		10	9.6
Thrust Efficiency (%)		68	67.6
Average q/m (coul/kg)		,0,000	5,300

32

Observations of the performance showed a change from vertical operation; typically, the current was lower, about 100 μamp at 14 kv. The change was caused by the source rim, which was never wet fully during this run. The occasional non-wetting character of the source rim has since been explained in terms of causes other than gravity (Section 2.1.1). The difference in performance was not significantly a function of horizontal versus vertical testing.

The thrust and specific impulse are plotted as functions of mass flow rate in Figure 22. This uncorrected time-of-flight data was taken
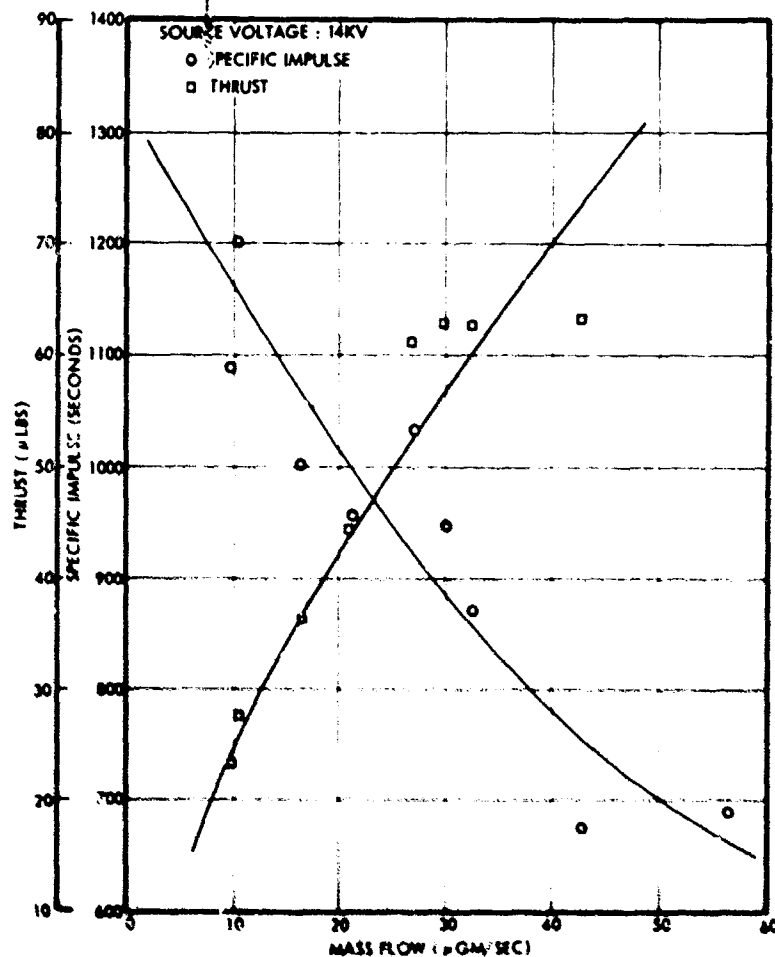
Figure 22. Performance of Source 8 in Horizontal Testing with Imperfect Rim Wetting (from Uncorrected TOF Measurement Data)

with a grounded collector, a screen grid voltage of +100 volts, and a suppressor voltage of -200 volts. The thrusts obtained were of the order of 25 μlb. The thrust and I_{sp} were generally lower than had been obtained vertically, although the characteristic thrust and I_{sp} curve shapes remained essentially unchanged.

The source tip was observed microscopically during the run. Although the entire rim could be wet by leaving the high voltage off for short periods of time, reapplication of the voltage would cause the meniscus to recede from the upper rim, leaving only the lower portion wet and probably accounting for the low I_{sp}.

The source failed after about 54 hours of operation because of a pinhole leak in the epoxy bond between the source tip and the shank. A later test, run 700704, lasted 616 hours and is discussed in Section 2.5 as a life test. In this run, the rim achieved full wetting, and normal performance was attained. Performance comparable to that seen in vertical testing, about equivalent to or slightly higher than that of design 7, was recorded.

2.2.5 Source Design 6B

The type 6 emitter with a surface roughened meniscus cavity interior was eventually chosen for the final module design. A module with a 6BM2 type source completed a 2000-hour life test. Another was fabricated and performance tested for delivery under contract. The results of this performance test, run 710601, are given in Section 2.6.

The first performance data for the type 6B source were taken during run 701007. At this time, as described in Section 2.1, the surface roughening technique was being evaluated by comparing the performances obtained with various surface finishes. During this run, the entire rim was fully roughened. Deflector electrodes were not used.

Figures 23 and 24 show the source performance, with feed pressure (mass flow) and source voltage, respectively, as independent variables. In Figure 23, thrust and specific impulse are given as functions of mass flow at a source voltage of 13.3 kv, with source current varying from 65 to 135 μamp. Figure 24 shows the effect of varying source voltage at constant feed pressure. The mass flow is essentially independent of voltage. The scatter is due to lack of control of wetting on the highly roughened rim.

These data show that a thrust of 25 μlb can be achieved with this source at a specific impulse of more than 1500 seconds and a source voltage of 14 kv. The source efficiency, however, was between 60 and 65 percent due to a high ion peak. Beam spread was also high — about 20 to 25 degrees. Both these effects are caused by emitting sites too far out on the rim, a result as having also roughened the rim exterior.

The source was then tested briefly with a partially roughened rim (run 701201). The source was mounted in a module without deflectors and was run for four days in the 6-inch pumping station with the 1.4 meter time-of-flight distance. Vacuum pressure was 1-2 x 10^{-5} torr. An

34
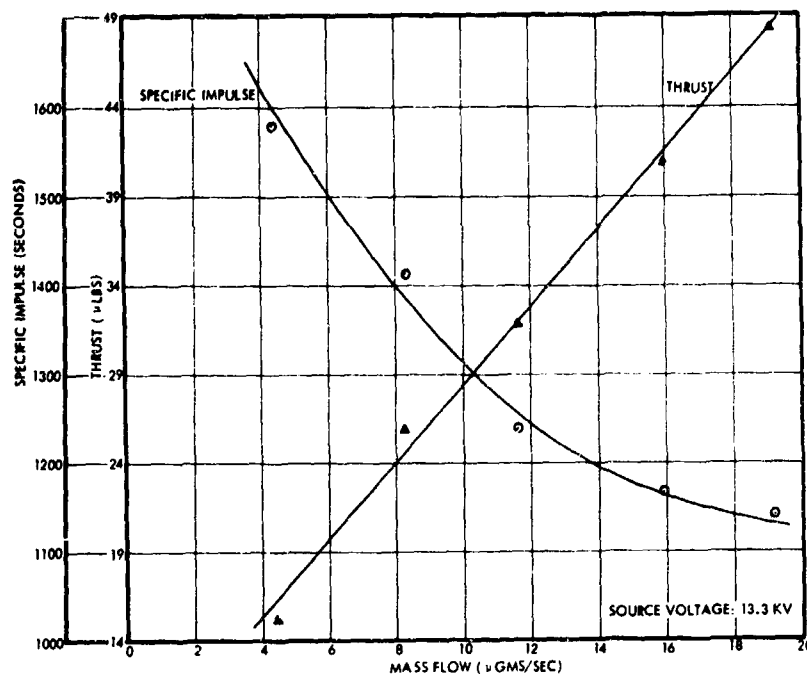
Figure 23. Performance of Annular Source 6B with
Surface Roughened Interior, Independent
Variable, Mass Flow Rate

extractor voltage of -1.7 kv was applied, and the extractor drain varied
from 0.5 to 1.5 μamp.

The source was started at a voltage of 8 kv and a feed pressure of
3 inch Hg. The source had low flow impedance, and nominal performance
was achieved, after start-up, at about 1.5 inch Hg feed pressure. At
14 kv, the source produced a specific impulse of 1515 seconds, a thrust
of 30 μlb, a mass flow of 8.89 μgm/sec, and a thrust efficiency of
61 percent.

When th type 6B source was run with a completely smooth rim
(but still a roughened interior), the performance and wetting qualities of
the rim were most satisfactory. The interior of the meniscus cavity was
wet up the inner edge of the rim and no further. The jet site locations
seemed to give most optimum performance. At one time, so much of
the rim was left smooth that the emission sites anchored well down inside
the meniscus cavity, at the edge of the roughening, where the extracting
field was too low to achieve the desired average charge-to-mass ratio.
A great deal of control was thus demonstrated over the wettability of the
source rim, and these initial runs showed that the surface roughening
technique could have a beneficial effect on source performance and
controllability.

2.2.6 Source Design 7B: Run 701104

Source type 7B was fabricated with a surface roughened meniscus
cavity. The rim was also rou hened to its outside edge. The source was
supplied with a 0.450 inch long impedance tube, and had an impedance of

35
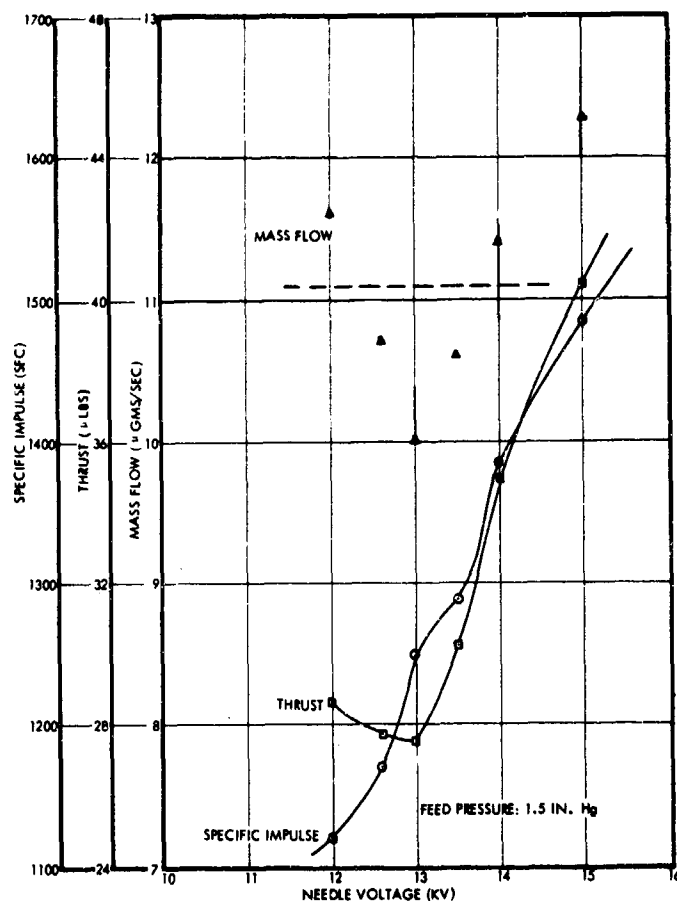
Figure 24. Performance of Annular Source 6B,
with Surface Roughened Interior,
Independent Variable, Source
Voltage

about a half a standard needle length. The rim was 1 to 1.3 mils wide.
A micrograph of the source rim and meniscus cavity, in cross section,
is shown in Section 2.1.

The source was mounted with a set of deflector electrodes, spaced
from 0.028 to 0.031 inch out from the source rim and about 0.003 inch
above it. It was run in the 6-inch pumping station with a 1.4 meter time-
of-flight distance. The thrust efficiency ranged from 63 percent at 16.5 kv
to 70 percent at 14 kv. Interpolation of the time-of-flight data indicates
that, at 15 kv, 67 percent thrust efficiency, 1500 seconds specific
impulse, 17 μlb thrust, 5.25 μgm/sec mass flow, and 56 μamp source
current can be attained. A specific impulse of 1400 seconds can be
attained at 25 μlb thrust, 8.1 μgm/sec mass flow, and 75 μamp source
current.

This was the first type 7B to be run. The brief performance study
indicated a capability approximately equivalent to, and certainly no better
than, that of 6B. This was the first clue that the surface roughening
techniques used had improved the type 6 design to the point that it was as

36

good as the type 7 design. The expensive and time consuming fabrication
processes used on the type 7 design could thus be eliminated.

2.2.7 Source Design 11B: Run 701102

A type 11B source was fabricated with a 100 percent polished rim,
while the interior remained surface roughened up to the rim. This source
was run with deflectors, and some performance mapping was done. The
deflector-to-rim spacing was noted to be 0.30 inch. The test was again
conducted in a small 6-inch vacuum station. The source was self-wetting
at start-up.

Some performance curves are shown for this run in Figure 25. A
thrust level of 20 µlb was obtained at 14 kv source voltage and 7.2 kv
deflector voltage, considerably lower than obtained earlier for the same
source with a roughened rim. A view probe inspection showed the same
beam profile at 8 kv deflector voltage. It was also noted that, as deflector
voltage was lowered, the beam spread increased to about 20 degrees at
6 kv. The performance curves show the effect of varying deflector
voltage when other parameters are held constant.

2.2.8 Source Design 12B: Run 701103

The type 12B source, which had a blunt rim, was performance
tested once in the small 6-inch vacuum station. The source was mounted
with deflectors, which were spaced 0.040 inch from the source rim.
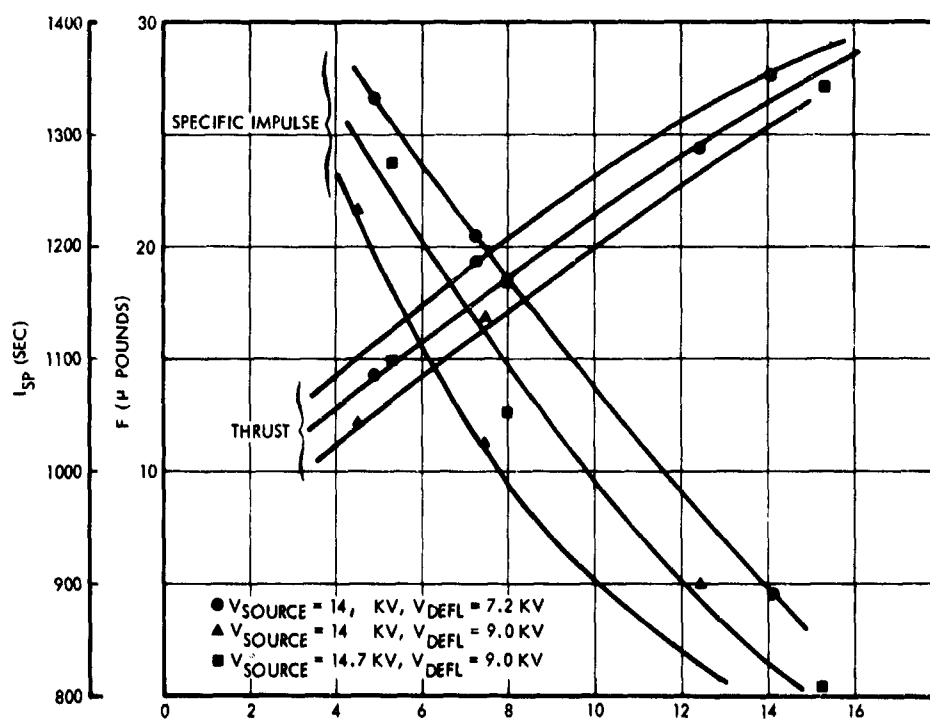
Figure 25.   Performance of Annular Source 11B,
Run 701102

37

The source started nicely and wet the entire rim at 10 kv source
voltage and 5-inch Hg feed pressure, a typical operating pressure. The
bluntness of the rim caused a low specific impulse. At 14 kv source volt-
age, less than 1000 seconds specific impulse was attainable. View probe
observations showed a uniform beam of approximately 15-degree half angle.

A series of data points were taken at constant feed pressure;
Figure 26 shows the variation of mass flow with voltage at this feed
pressure. Comparison with Figure 24, and with similar data from Run
701104 indicates that mass flow is relatively independent of voltage for
constant feed pressure, although a good deal of scatter is experienced,
possibly from temperature variations, or local wetting fluctuations.

2.2.9 Summary of Performance Testing Results

As the annular geometry passed through its several development
phases, performance improved and became better defined. Performance
characteristics were widely investigated for three source types; 6B, 7,
and 7B. For the final design, a type 6BM3, a wide range of operating
parameters was investigated. Performance was demonstrated ranging
from 13 μlb and 1400 seconds at 65-percent efficiency and 13-kv source
voltage to 30 μlb and 1800 seconds at 68-percent efficiency and 16-kv
source voltage. Thrust efficiencies ranged from 65 to 75 percent and
showed a tendency to increase with increasing mass flow rate. The spe-
cific impulse proved to be a decreasing function of mass flow rate.

The maximum thrust demonstrated was 71 μlb at 545 seconds I_{sp}
and 79-percent efficiency. Maximum specific impulse demonstrated was
2000 seconds at 20 μlb thrust, 15-kv source voltage, and 70-percent
efficiency.
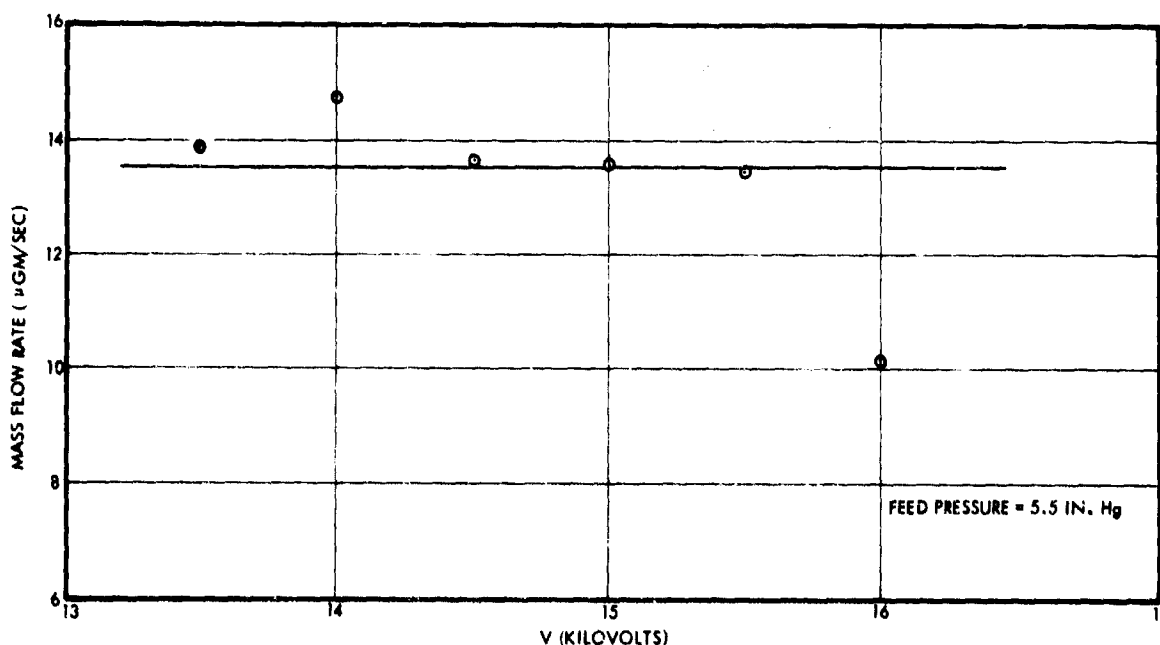
Figure 26. Mass Flow Rate as a Function of Source Voltage for
Constant Feed Pressure, Source 12B, Run 701103

38

2.3 THRUST VECTORING

Electrostatic thrust vectoring is achieved with three high voltage vector electrodes, which, when operated at the appropriate bias voltages, deflect the beam in any desired direction relative to the nominal thrust axis.

Figure 27 is a schematic showing the placement of the vector electrodes around the source, and their numbering convention. The electrodes are normally left at half the source voltage when the beam is not vectored. In order to vector horizontally in the diagram, a voltage differential is applied between deflectors 1 and 2, keeping their average voltage at half the source voltage. In order to vector vertically, a voltage differential is applied between deflector 3 and the other two electrodes, which are kept at equal voltages. Again, the average of the three voltages is kept at half the source voltage.
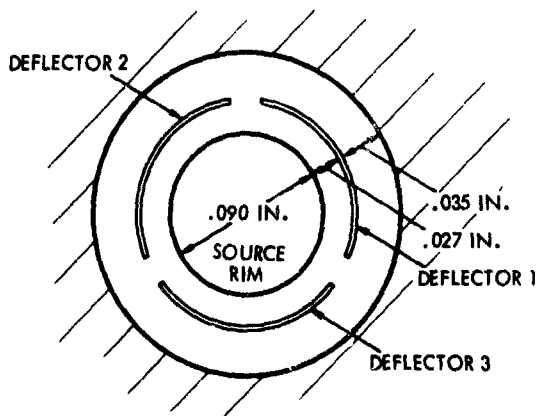
Figure 27. Schematic for Placement of Deflector Electrodes. Cross hatched region is extractor area.

With this scheme, the horizontal vectoring field is antisymmetric. The vertical vectoring field, however, is completely asymmetric. Later in the program, starting with run 701105, the vector electrode structure was rotated 90 degrees clockwise from the configuration shown in Figure 27 so that any observed asymmetries in vertical vectoring could be attributed to gravitational effects, and not to the configurational asymmetry.

Typical vectoring capability found with this scheme was 0.25 to 0.75 degree deflection angle per kilovolt deflecting voltage differential. The greatest vectoring angle seen was about 7 degrees. Four degrees was more typical.

Vectored beam profiles were mapped using the time-of-flight current probes described in Section 7.2. In general, only current density was mapped. Thrust density was then inferred from these data. The rationale for this approach was the proportionality between current density and thrust density, demonstrated during run 701105.

The source and vector electrode high voltages were obtained from a single power supply. A control circuit was designed to allow each vector electrode voltage to be set independently without influencing the other voltages. This circuit is described below. In addition, the results of eight important vectoring runs are presented.

39

2.3.1 Deflector Electrode Voltage Controller

The controller circuit diagram is shown in Figure 28 and Table 7 lists the components. All circuit components were packaged on a single chassis. Current and voltage meters were mounted on a Plexiglas base. An extractor meter and monitoring circuits for both source and extractor voltage were also integrated on the same chassis.

The controller allows the needle and deflector voltages to be individually supplied from a single high-voltage supply. A given deflector voltage is obtained by applying the source voltage, nominally 15 kv, across a resistor (e.g., R6) in series with a high voltage triode whose plate is connected to the deflector. The triode grid, and hence deflector voltage, is controlled by a potentiometer (e.g., R15). A small transformer-diode circuit provides tube filament power and a dc negative grid bias.

The tube provides voltage regulation for the deflectors, since the grid supply acts to keep the voltage drop through the tube constant. The differential between needle voltage and deflector is read with meter E.
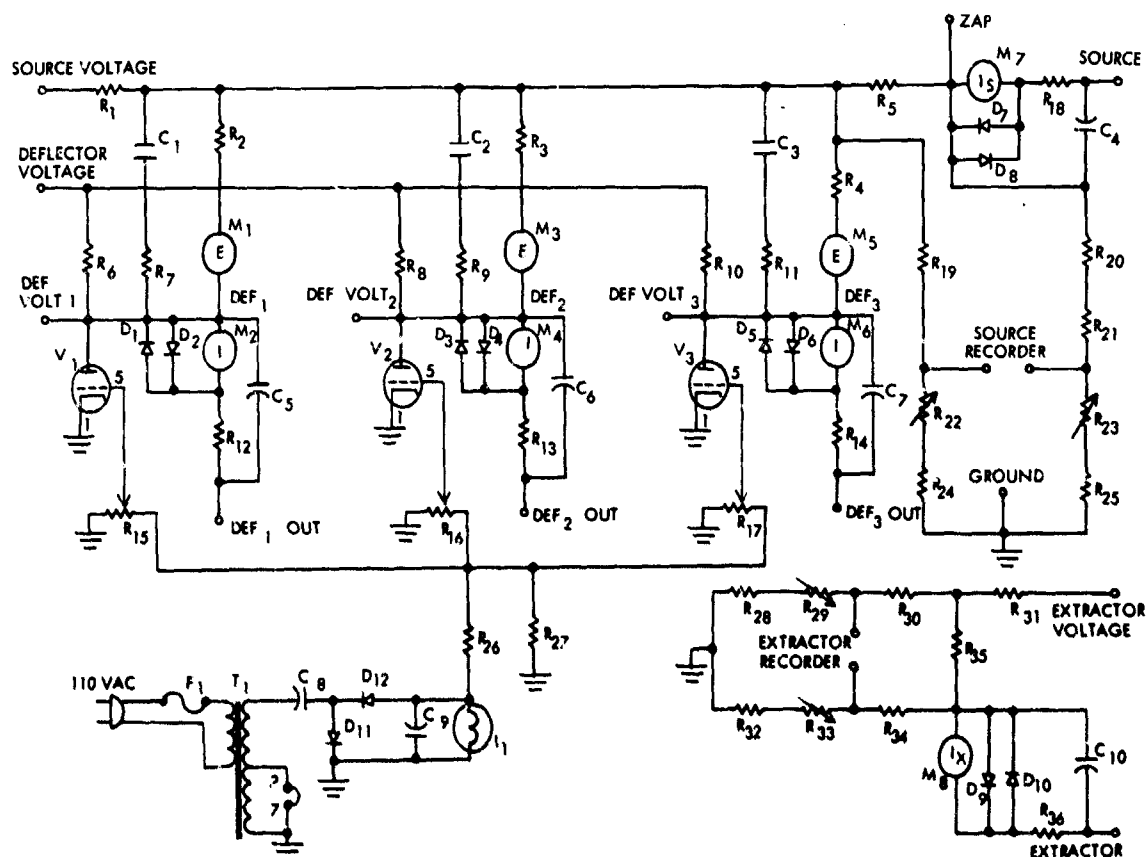
Figure 28. Annular Source Deflector Electrode Voltage Control and Monitor Unit

40

Table 7. Annular Source Deflector Electrode Voltage Control and
Monitor Unit Component List

Resistors	Capacitors
R_1 - 3 x 3.9MΩ-2W-5%	C_1, C_2, C_3 - 0.005 mfd - 10 kv
R_2, R_3, R_4, R_{19}, R_{20} - 1000MΩ	C_4 thru C_{10} - 100 mfd - 50V-electrolytic
R_5 - 5 x 1MΩ- 2W-5%	
R_6, R_8, R_{10}, R_{30}, R_{34}, - 100MΩ	Meters
R_7, R_9, R_{11}, - 5 x 3MΩ- 2W-5%	M_1 thru M_6 -0-25-0 a dc
R_{12}, R_{13}, R_{14}, R_{18}, R_{36}, - 10KΩ-1/2W-5%	M_7 - 0-200 a dc
R_{21}, R_{35}, - 1MΩ- 2W-5%	M_8 - 0-20 a dc
R_{24}, R_{25} - 6.8KΩ- 2W-5%	
R_{26} - 300KΩ- 2W-5%	Miscellaneous
R_{27}, R_{31}, - 100KΩ- 2W-5%	D_1 thru D_{12} - 1N647
R_{28}, R_{32}, - 68KΩ- 2W-5%	F_1 - .5A-S. B.
R_{15}, R_{16}, R_{17}, 1MΩ-2W-potentiometer	I_1 - 28 v lamp
R_{22}, R_{23}, - 2.5KΩ- 2W-presets	V_1, V_2, V_3 - 6BK4
R_{29}, R_{33} - 10KΩ- 2W-presets	T_1 - 110 to 12.6 v secondary

41

The resistance R1 provides protection to the needle and thyratron time-of-flight circuit in case of high voltage breakdown. The series elements C1 and R2 are for the purpose of pulling the deflector voltage down during time-of-flight initiation.

2.3.2 Run 700405: Source A, Type 1 Deflectors

This was the first complete set of time-of-flight data taken for a vectored beam. Data were initially taken under the operating conditions given in Table 8. Horizontal and vertical scans were made with the beam unvectored, and with the beam vectored horizontally. Probe measurements were made uniformly across the tank, at intervals of about 5 degrees in relation to the thruster. The entire series was completed in 2 hours.

Figures 29 and 30 show the horizontal and vertical thrust profiles. Each figure shows a curve for the unvectored state, and for the vectored left condition. On these figures, the centroids of each thrust profile are indicated as well as the 1 sigma limits, inside which 68 percent of the thrust density lies. The horizontal profile indicates a thrust density centroid shift of about 8 degrees.

The average deflector voltage was raised for the vectored condition, causing a drop in total needle current. Considering the voltage differential between electrodes one and two as supplying the deflecting field, the horizontal vectoring capability is about 0.9 degree/kilovolt.

Table 8. Time-of-Flight Probe Data for Horizontal Vectoring

	Source	Extractor	Probe Screen	Probe Suppressor	Deflectors		
					1	2	3
Unvectored Voltage	14 kv	-2 kv	+45 v	-45 v	5 kv	5 kv	5 kv
Vectored Voltage	14 kv	-2 kv	+45 v	-45 v	4.2 kv	13 kv	8.8 kv
Unvectored Current	84 μa	1.5 μa	--	--	0	0	0
Vectored Current	50 μa	1.5 μa	--	--	0	0	0

Feed Pressure = 4 in. Hg   Tank Pressure = 8×10^{-6} torr

Probe Time-of-Flight Distance, 0.965 m at center

Total Thrust*	Total Mass Flow*	Total Efficiency*	Total I_{sp}*	Average q/m*
25.9 μlb	7.9 μgm/sec	71.5%	1490 sec	10.65 c/gm

*Measured from big time-of-flight collector while unvectored.

42
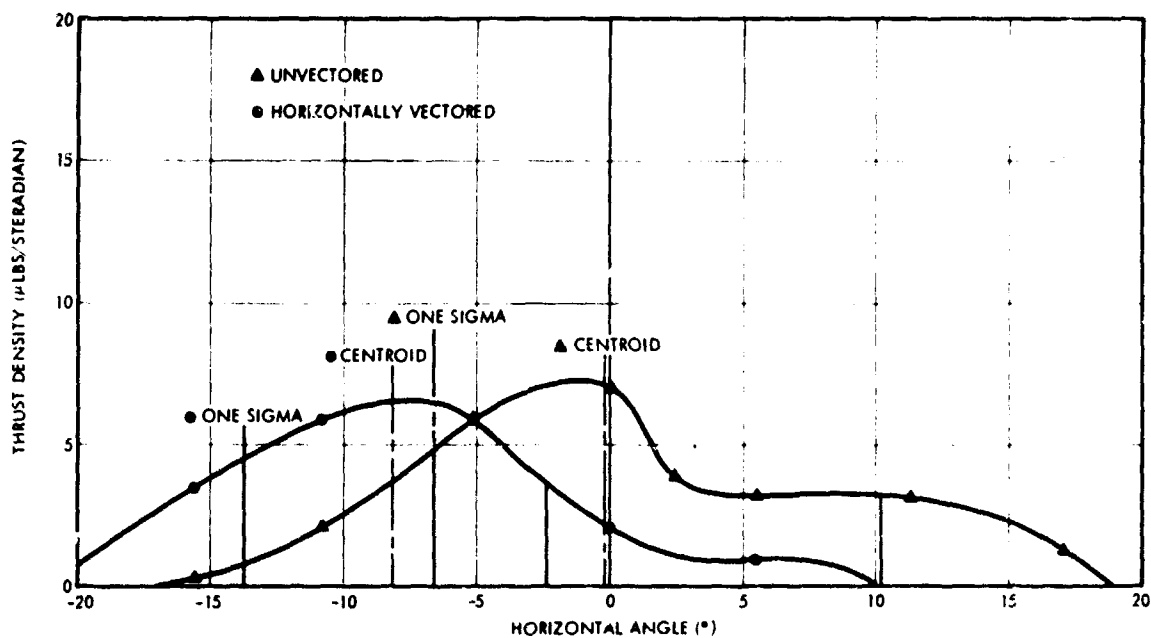
Figure 29. Run 700405: Horizontal TOF Probe Thrust Density
Measurements, Uncorrected for Energy Loss. Sixty-
eight percent of thrust density in the probe plane is
contained between the 1 sigma limits.
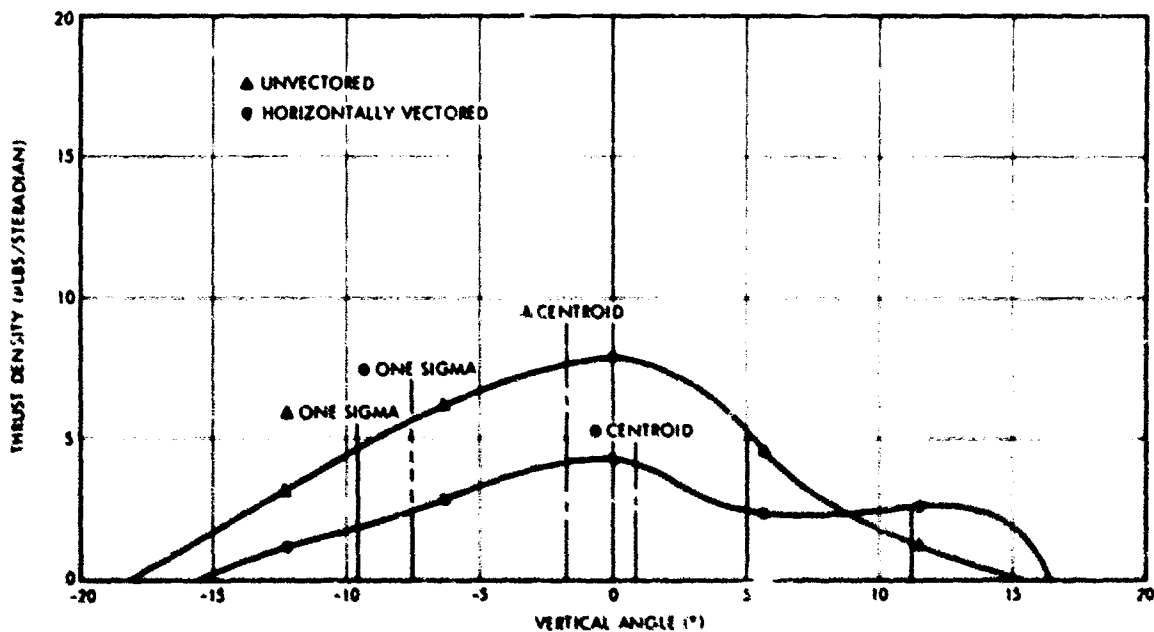
Figure 30. Run 700405: Vertical TOF Probe Thrust Density
Measurements, Uncorrected for Energy Loss.
Sixty-eight percent of thrust density in the probe
plane lies between the 1 sigma limits.

43

Figures 31 and 32 show the specific impulse profiles, taken from probe data, along the horizontal and vertical axes for the vectored and unvectored conditions. The discrepancies in readings along the thrust axis (where the vertical and horizontal probe traverses cross) are mostly caused by time-of-flight probe scaling errors, and partly by fluctuations in operating conditions during the time period covered by the experiment.

From the limited probe data available, qualitative contour maps of the thrust density profile can be constructed. These are shown in Figure 33 for the unvectored state, and in Figure 34 for the vectored state.

Probe data were then taken at the operating conditions given in Table 9. The set consisted of horizontal and vertical scans with the beam unvectored and then with the beam vectored vertically upwards.

The drop in vectored current density is again caused by the average vector electrode potential, in the vectored condition. This leads to a loss in thrust and I_{sp}. Assuming the mass flow rate and beam efficiency remain unchanged, thrust should go approximately as current to the 3/2 power. From the data in Table 9, one can calculate a reduction in total thrust of 56 percent.

Figures 35 and 36 show the horizontal and vertical thrust profiles. Each figure shows a curve for the unvectored state, and for the vectored-up condition. The centroids and 1 sigma boundaries of each thrust density profile are given. A thrust density centroid shift of 3 degrees was obtained, considerably less than the 8 degrees obtained with horizontal vectoring. There was little indication of beam asymmetry due to gravitational effects. The voltage differential on the electrodes was 8.6 kv, between the top (1 and 2) and the bottom (3).

Figures 37 and 38 show the specific impulse profiles along the horizontal and vertical axes for the vectored and unvectored conditions. Again, gravitational effects are minimal.

Figures 39 and 40 are qualitative contour maps of the unvectored and vectored thrust densities, similar to those for horizontal vectoring. Since no probe data were taken off the two axes, the behavior in the interior of the quadrants is based on the assumption of relatively smooth beam profiles.

2.3.3 Source 7-2, Type 2 Deflectors

The first vectoring studies with type 2 vector electrodes were made during runs 700801 and 700802. During run 700802 it was possible to attain 1500 seconds of specific impulse at 20 μlb thrust and 70 percent efficiency. A series of time-of-flight probe measurements was made, both unvectored and vectored upward. The probe showed a tight beam with a 10-degree half angle. A 3-1/2-degree vectoring angle was obtained with 10 kv difference on the deflectors.

44
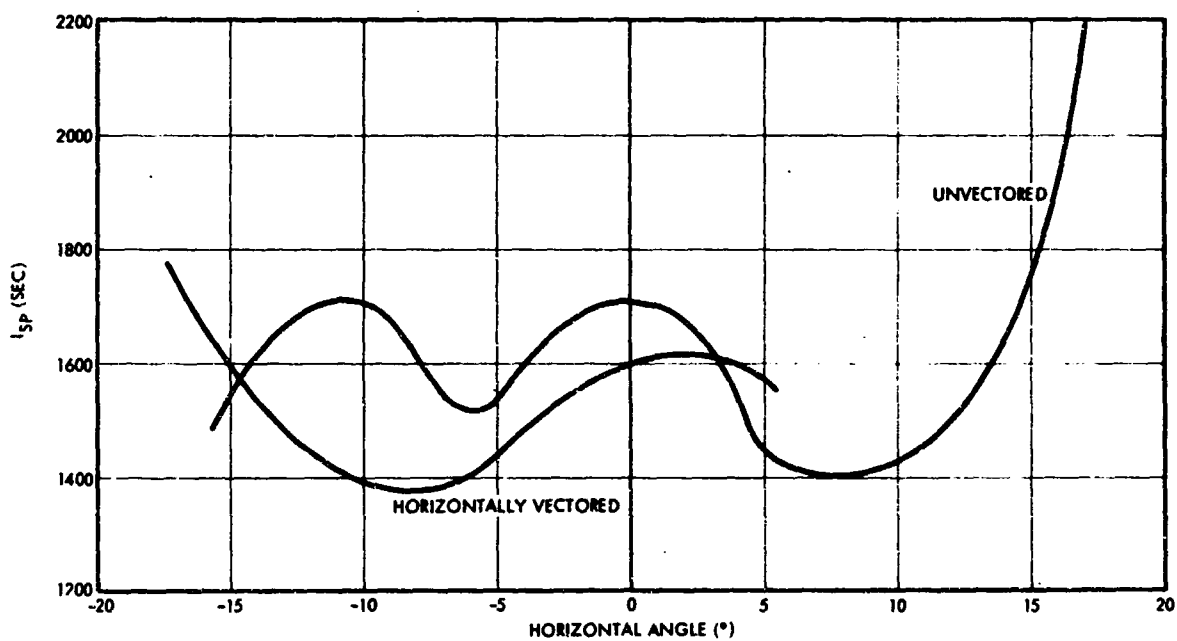
Figure 31. Horizontal TOF Probe Measurements of I_{sp}. Data points are at the same angles as in Figure 29.
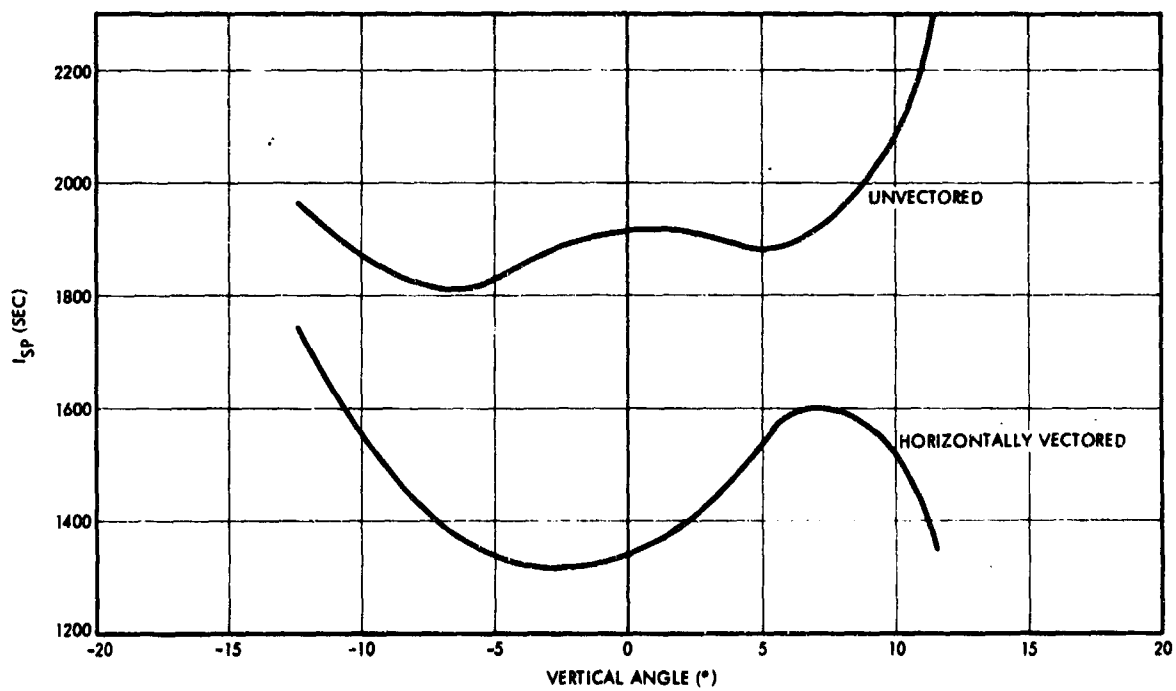
Figure 32. Vertical TOF Probe Measurements of I_{sp}. Data points are at the same angles as in Figure 30.

45
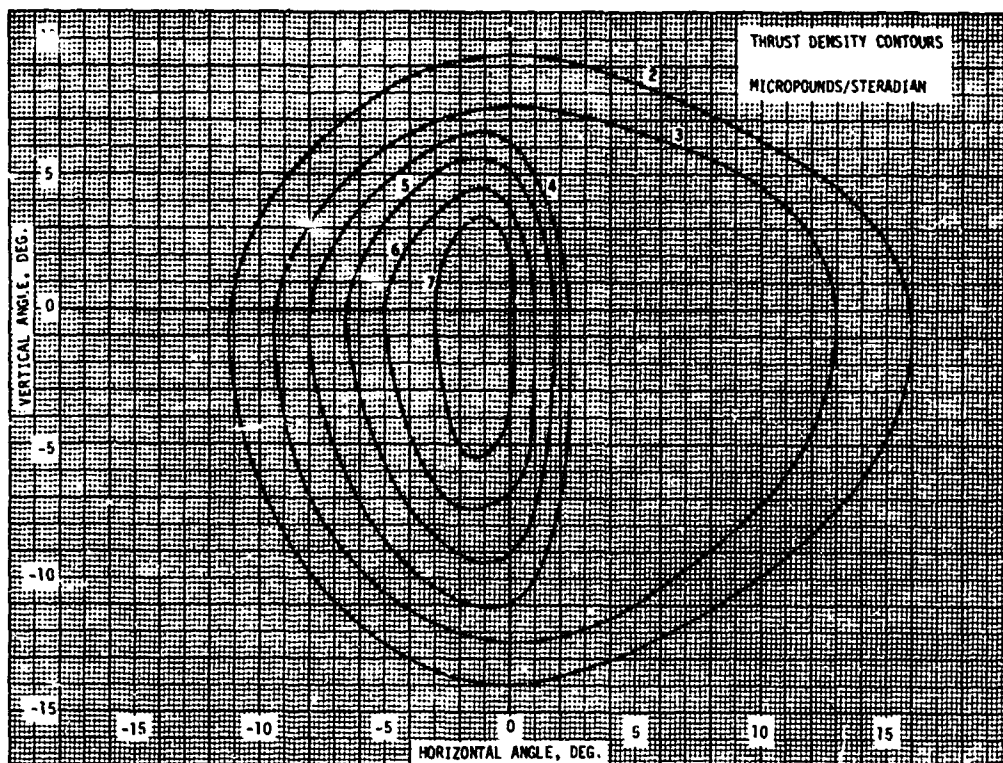
Figure 33. A Qualitative Map of Thrust Density Contours for the Unvectored Beam of Run 700405
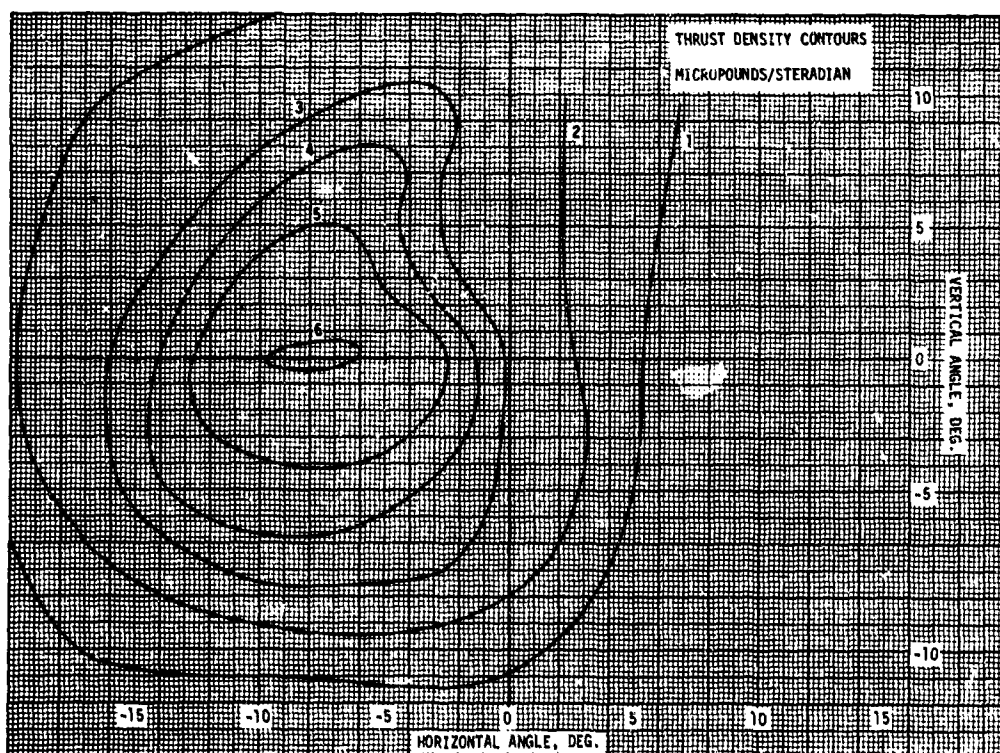
Figure 34. A Qualitative Map of Thrust Density Contours for the Horizontally Vectored Beam of Run 700405

46

Table 9. Time-of-Flight Probe Data for
Vertical Vectoring

	Source	Extractor	Probe Screen	Probe Suppressor	Deflectors (kv)		
					1	2	3
Unvectored Voltage	14 kv	-2 kv	+45 v	-45 v	5	5	5
Vectored Voltage	14 kv	-2 kv	+45 v	-45 v	4.5	4.5	13.1
Unvectored Current	60 μa	1 μa			0	0	0
Vectored Current	35 μa	0.5 μa			0	0	0

Feed Pressure = 4 in. Hg   Tank Pressure = 10^{-5} torr

Probe Time-of-Flight Distance - 0.965 m at center

Total Thrust*	Total Mass Flow*	Total Efficiency*	Total I_{sp}*	Average q/m*
22.2 μlb	7.7 μgm/sec	73%	1302 sec	8 c/gm

*Uncorrected time-of-flight data from main collector, while beam
was unvectored.

2.3.4 Run 701008: Source 7, Type 2 Deflectors

This run was a 400-hour endurance test of source 7. Since it was
a life test it is also discussed in Section 2.5.

The beam was vectored three times during the run. Vectoring
was accomplished with a voltage of 6.3 kv on two electrodes, and 13.7
on the third. Drain currents on two electrodes remained zero; the third
(6.3 kv) had a slight drain current which was always less than
5 microamps.

Vectored and unvectored current density profiles are plotted in
Figures 41 and 42. In this case the deflection was upward and to the
left in a direction about 30 degrees from perpendicular. The thrust
density is proportional to the current density across the beam to within
10 percent. The net vectoring angle was 3 degrees resulting in a vectoring
ing capability for this mode of about 0.4 deg/kilovolt, similar to earlier
results.
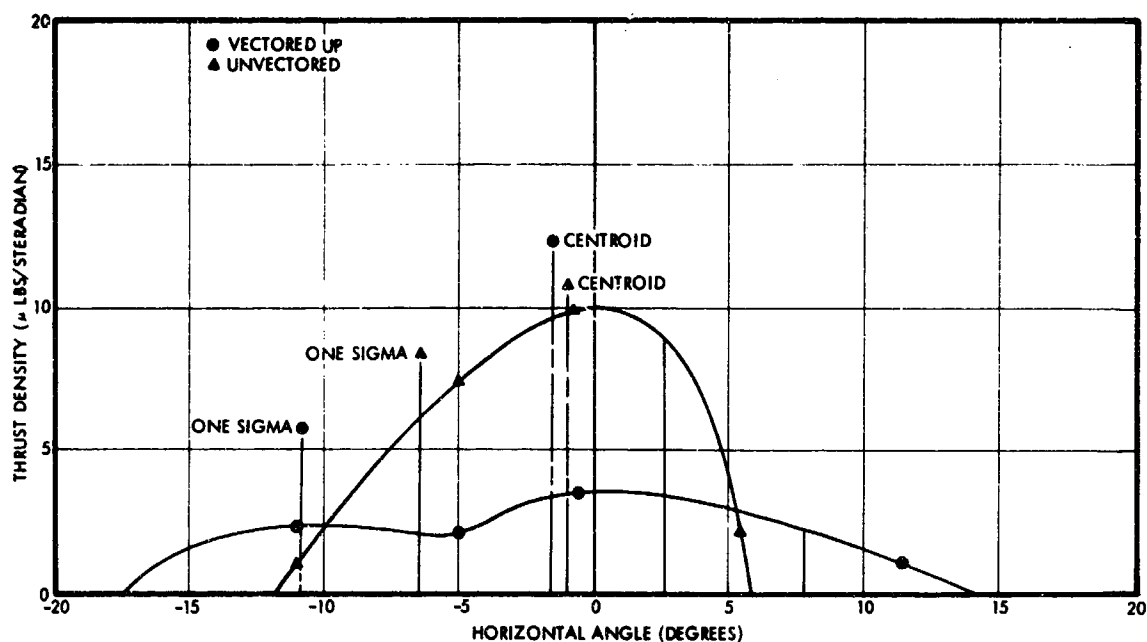
Figure 35.   Horizontal TOF Probe Thrust Density Measurements,
Uncorrected for Energy Loss. Sixty-eight percent of
thrust density in the probe plane is contained between
the 1 sigma limits.
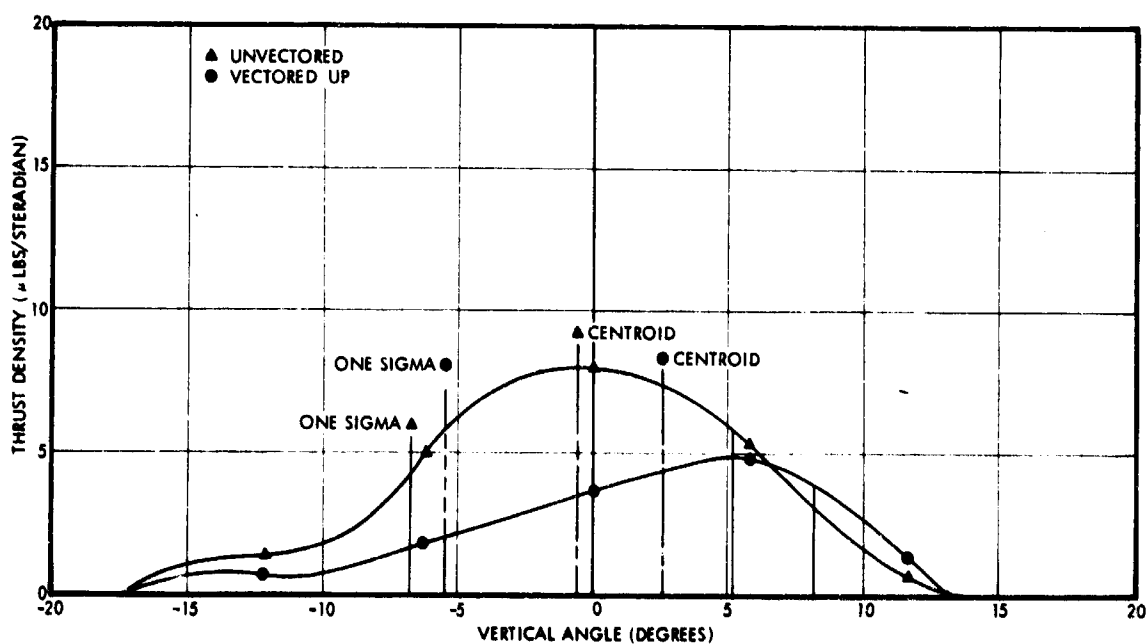
Figure 36.   Vertical TOF Probe Thrust Density Measurements,
Uncorrected for Energy Loss. Sixty-eight percent
of thrust density in the probe plane is contained
between the 1 sigma limits.

48
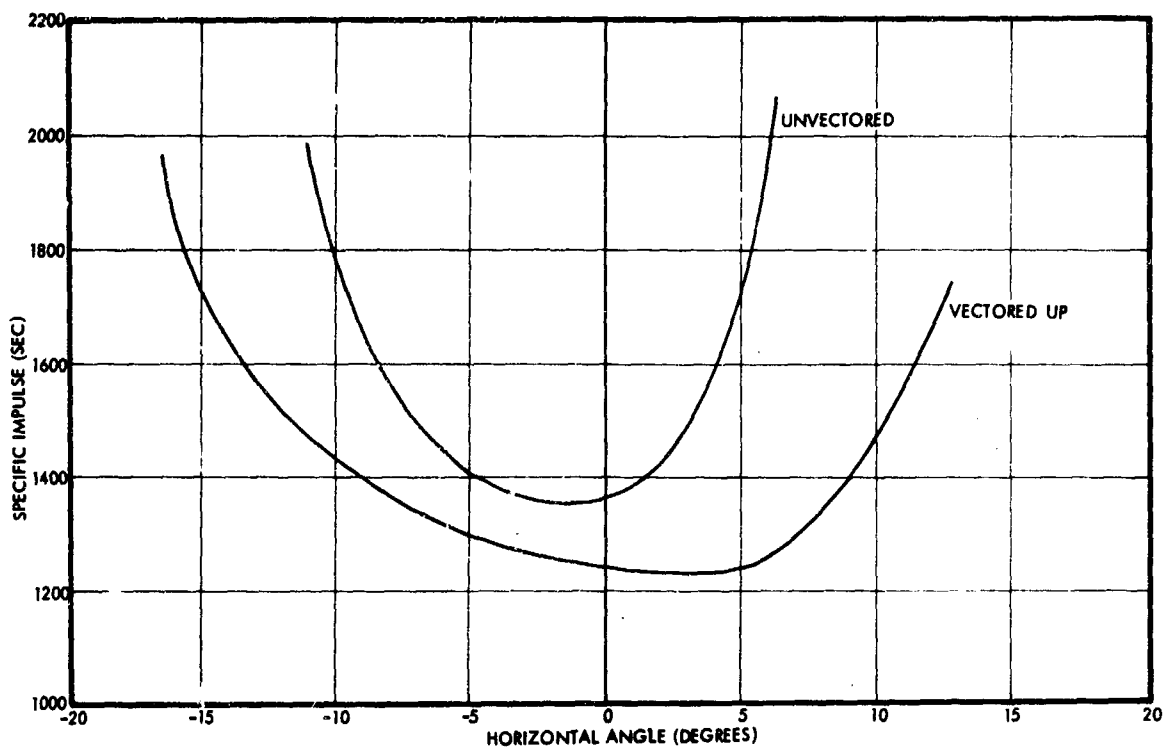
Figure 37. Horizontal TOF Probe Measurements of I_{sp}. Data were taken at the same points as in Figure 35.
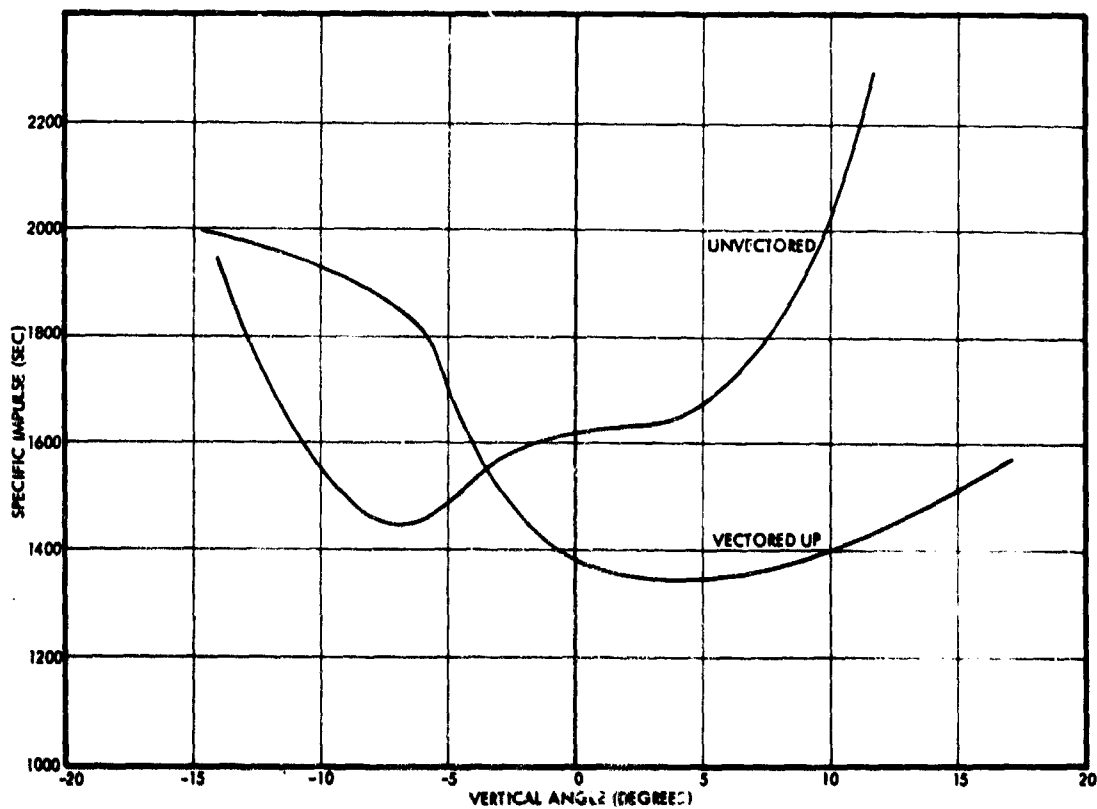
Figure 38. Vertical TOF Probe Measurements of I_{sp}. Data points taken at the same angles as in Figure 36.

49
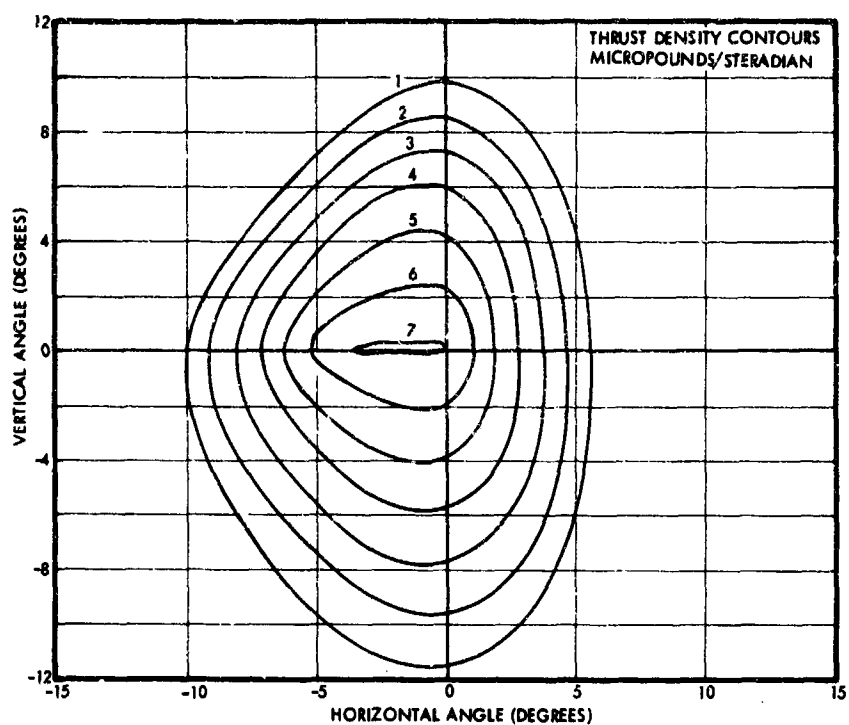
Figure 39.   A Qualitative Map of Thrust Density Contours for
Unvectored Beam (taken just before vectoring
experiment)
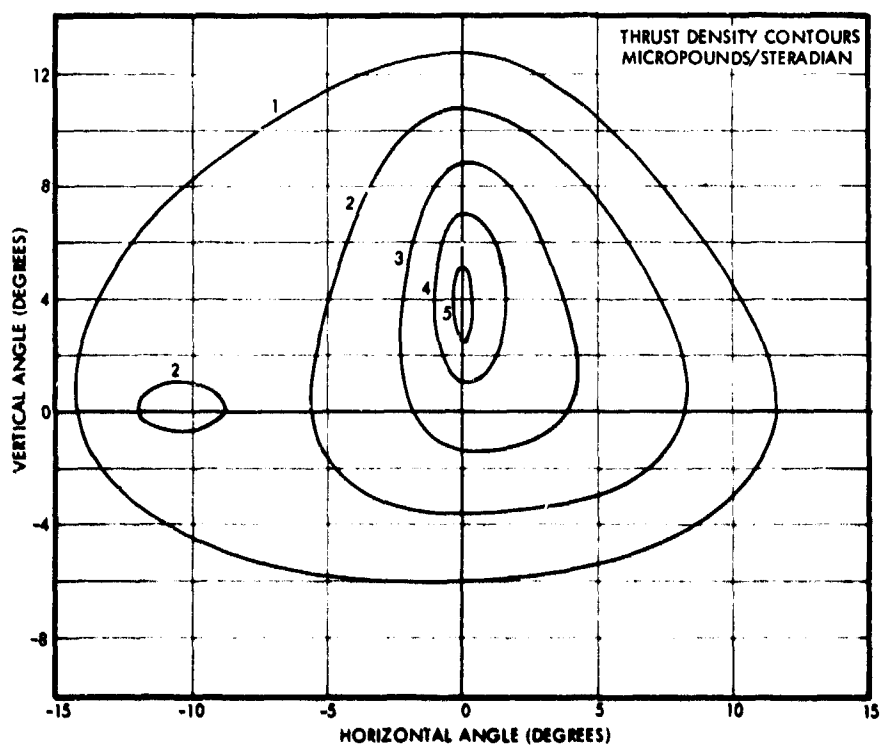
Figure 40.   A Qualitative Map of Thrust Density Contours for
Vertically Vectored Beam

50
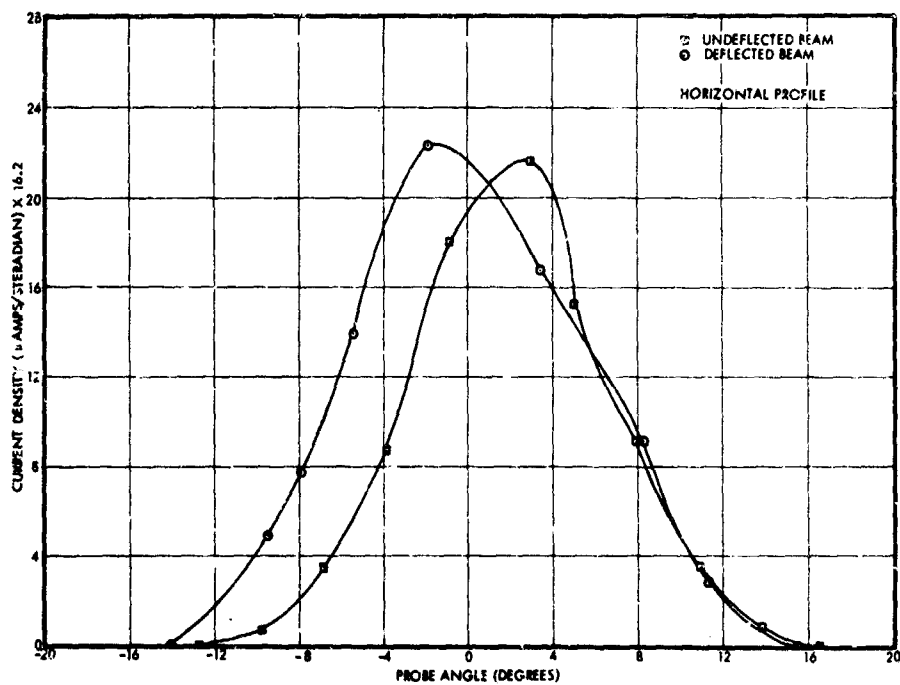
Figure 41. Deflected and Undeflected Current Density Profiles
for Horizontal Probe Scan. Annular source 7,
Run 701008.
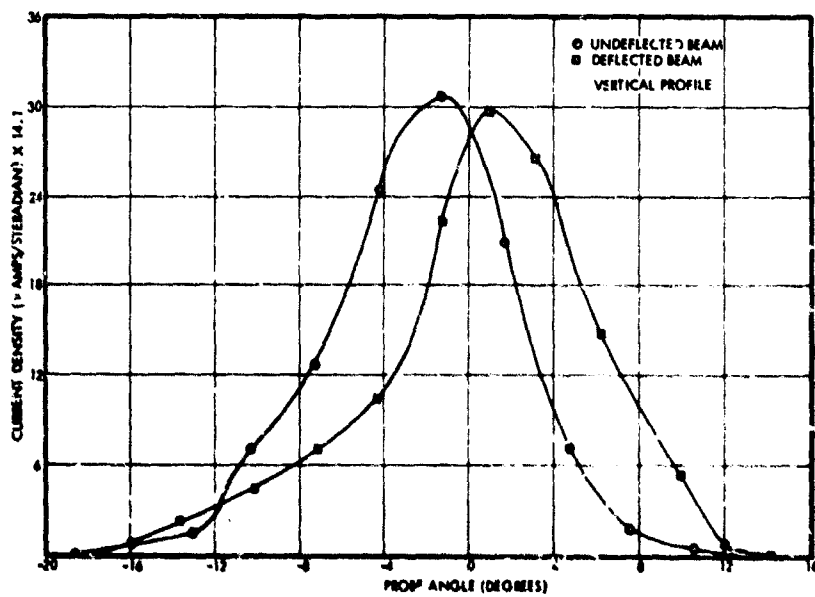
Figure 42. Deflected and Undeflected Current Density Profiles
for Vertical Probe Scan. Annular source 7,
Run 701008.

51

Probe data from Run 701002 (Section 7.2) were analyzed to verify the collector transmission factor for each of the probes. It was found that the current striking the frontal area of the vertical probe, only 8.67 percent reaches the collector. The corresponding factor for the horizontal probe is 6.41 percent. The ordinate scaling factors in Figures 41 and 42 apply to these corrections.

2.3.5 Run 701105: Source 11B, Type 3 Deflectors

The deflectors were mounted so that the vectoring configuration symmetry axis was horizontal. Previous measurements have shown that ±7 degrees vectoring can be achieved normal to this axis of symmetry when it is vertical. However, vertical vectoring along this axis had been limited to about 4 degrees.

In the run 701105 experiment, the source was run at a voltage of 15 kv, with specific impulse of 1100 seconds, thrust of 30 μlb, mass flow of 12.5 μgm/sec, and thrust efficiency of about 60 percent. The beam was vectored right and left. The probe results are shown in Figure 43. Time-of-flight photographs were taken with the probes. The photos were analyzed, and thrust density from the analysis is plotted against current density in Figure 44. The linearity assumption, within a 10 percent scatter, appears good. Since about 10 points were used to obtain each current density profile, the center of thrust should be accurate to about 5 percent. The angles measured indicate roughly a ±6-degree vectoring capability in this mode. In each case, the voltage differential was about 13 kv: in the case of left vectoring, D1 and D2 was held at 2 kv and D3 at 15 kv, and in the case of right vectoring, D1 and D2 were held at 15 kv and D3 at 2 kv. We thus obtained about 0.5 deg/kv vectoring.

2.3.6 Run 710104: Source 7BM2, Type 3 Deflectors

This was a 1000-hour life test with vectoring electrodes. (It is also discussed in Section 2.5.) The beam was vectored in four directions, once at 196 hours and again at 317 hours. Each time, the source was in the vectored state for about 1 hour. Voltage differentials of 10 to 11 kv were used to accomplish vectoring. The vectoring response was virtually undetectable.

The source was vectored the third time at 650 hours. The probe data taken during this series indicated a beam spread of about ±18 degrees, a few degrees more than at the beginning of the run. In the leftward direction, we can optimistically say that vectoring was 7 degrees; however, the direction of the unvectored beam was uncertain. It appeared to lie about 4 degrees to the right.

During this series, a voltage breakdown occurred between one of the vector electrodes and the emitter. The meniscus, which had been completely quiet up to this point, began to bubble slowly, even in the unvectored state. The source voltage was lowered to 14 kv, and the temperature control set point was lowered to 24.2°C in an attempt to stop the gas generation. This was partially successful and the voltage was eventually restored to 15 kv. The temperature was not reset; however, the feed pressure was raised gradually.

52
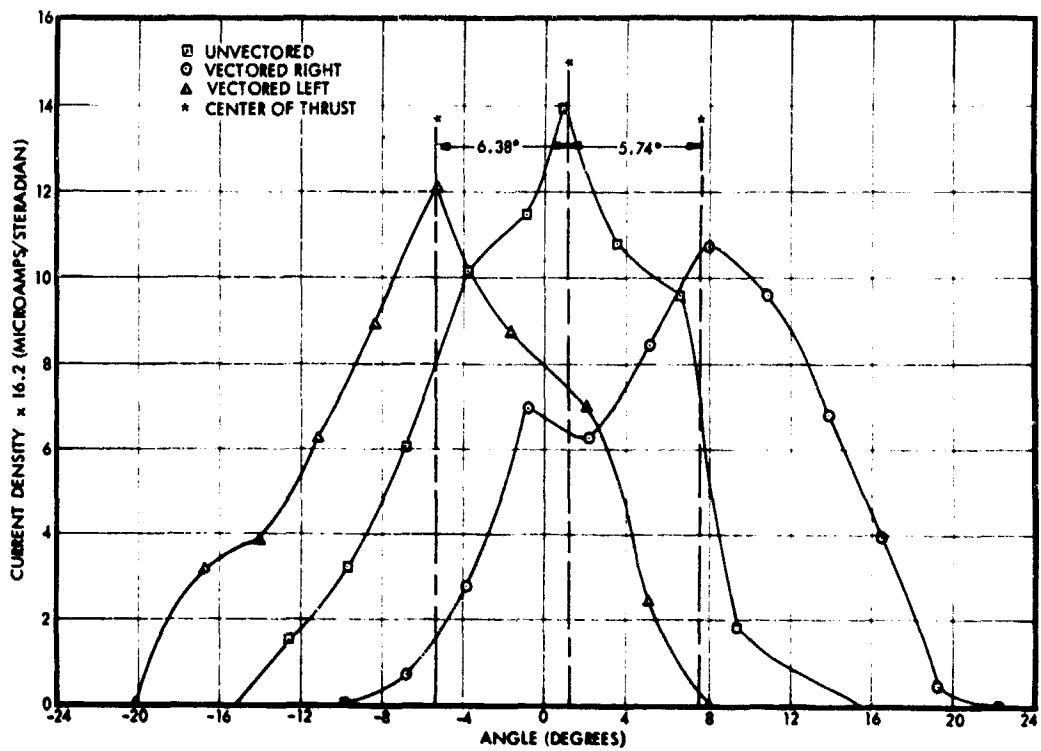
Figure 43. Run 701105 Probe Results for Horizontal Vectoring
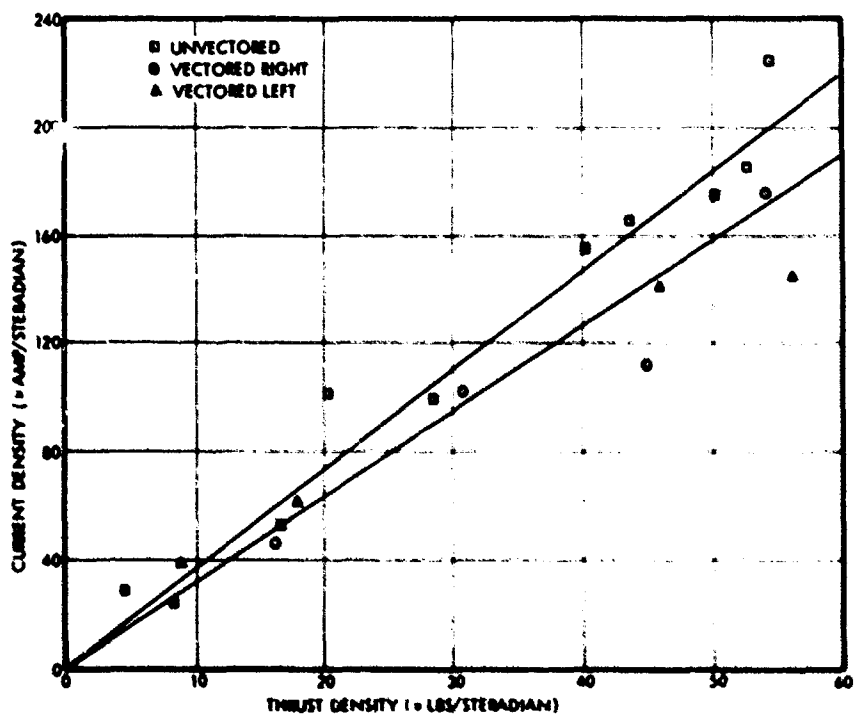
Figure 44. Run 701105 Localized Current Versus Thrust
for Various Probe Locations

53

At 1030 hours the thruster was vectored for the fourth and final time. The beam was deflected vertically up, and then horizontally to the right. Performance and stability during the vectoring period were generally satisfactory, although at one point a drain current to one of the deflectors developed. This was quenched by temporarily raising the voltage on this deflector (thus lowering the differential between it, its neighbor and the source). The voltage was then reset and vectoring continued.

At this time all of the beam current in the unvectored state was still contained in a cone of half angle 17 to 20 degrees. However, the vectoring response was still poor.

2.3.7 Run 710402: Source 6BM3, Type 4 Deflectors

This run, which lasted 433 hours and is also discussed in Section 2.5, was the first long duration test with the final module design.

The source was vectored three times. It was vectored vertically up at 120 hours and then horizontally, in one direction at 165 hours. At 425 hours a complete vectoring sequence was undertaken. The source was vectored up, down, and in both directions horizontally. Voltages and currents for the vectoring operations are shown in Table 10.

A vertically vectoring capability ±2 degrees and horizontally ±3 degrees was demonstrated. Figures 45 and 46 present the probe data in a way that most clearly illustrates the vectoring. These current density versus angle traces are corrected for probe angle and time-of-flight distance.

2.3.8 Run 710501: Source 6BM3, Type 4 Deflectors

This run was the final 2000 hour life test run with the final module design. Other aspects of the test are discussed in Section 2.5. The source was vectored twice during the test; after 26 hours and after 1032 hours. The source was vectored up, down, left and right. Voltages and currents for the first vectoring experiment are shown in Table 11.

The extractor drain was steady and small, about 0.2 microamp throughout the entire vectoring sequence. The deflector drains were nominally zero (<0.5 microamperes). No gas generation or meniscus surface instabilities were observed.

Table 10. High Voltages for Run 710402 Vectoring Operations

Vectored Condition	Source		Deflectors					
	V kv	I µa	V1	I1	V2	I2	V3	I3
Vectored up	14.85	96	5.5	-2	13.3	0	9.2	0
Vectored down	14.5	120	13.4	0	5.0	-3	9.1	1
Vectored right	15	35	9	6	9.1	0	2.5	0
Vectored left	14.7	100	3.5	-1	3.5	0	13	0
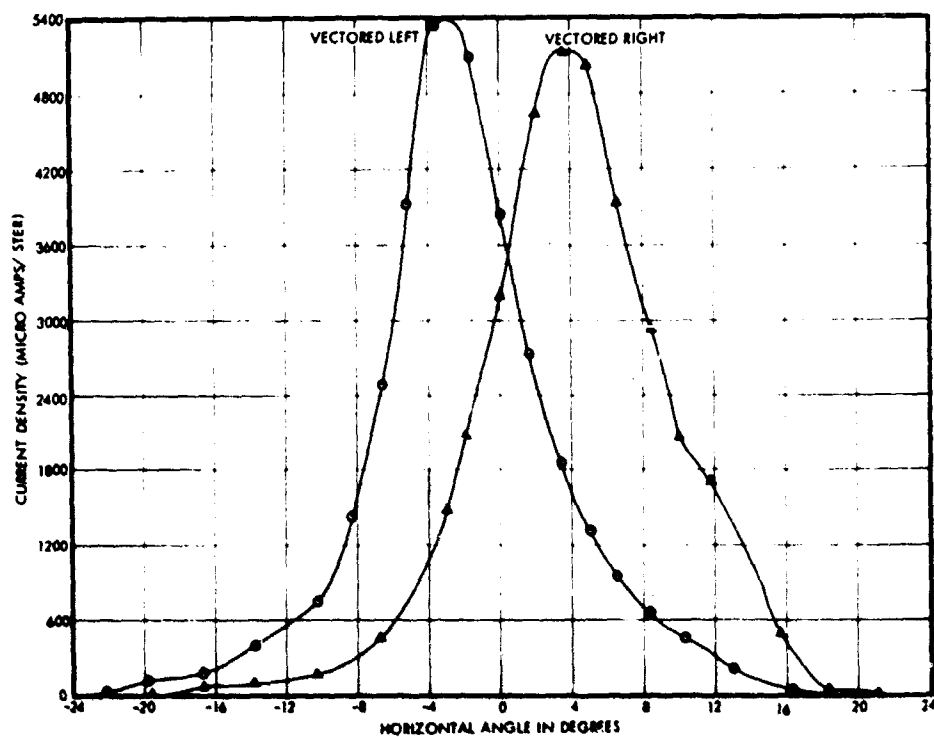
Figure 45. Run 710404, Horizontal Vectoring Data
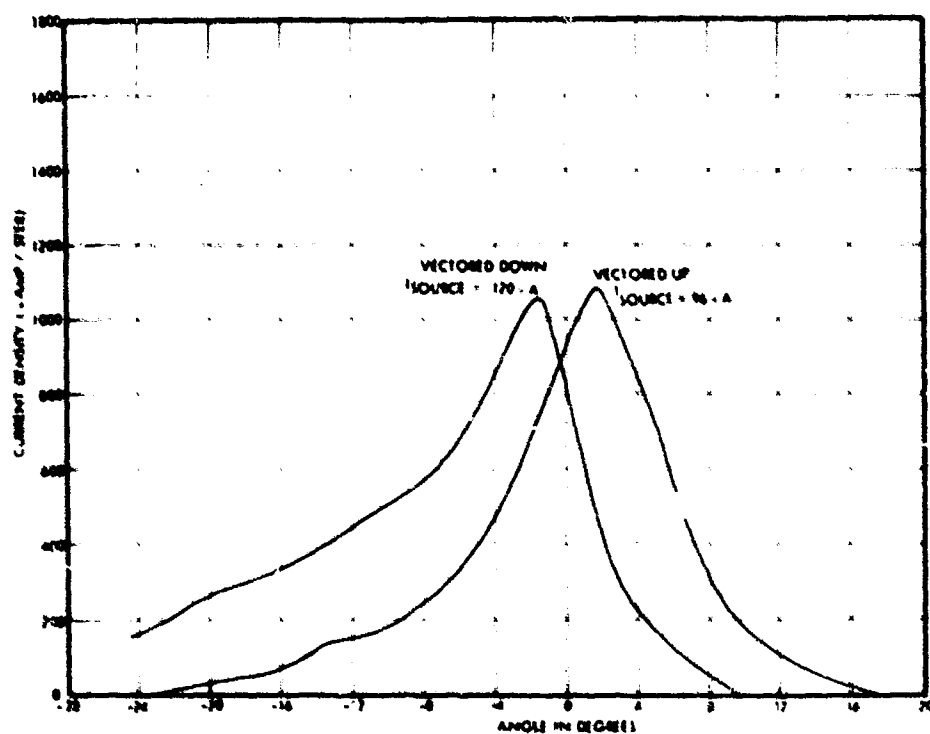
Figure 46. Run 710402, Vertical Vectoring Data

55

Table 11. Vectoring Voltages and Currents - Run 710501

Vectored Condition	Source				Deflectors			
	V (kv)	I (μa)	V1	I1	V2	I2	V3	I3
Unvectored	13.9	86	7.17	0	7.19	0	7.19	0
Vectored Up	13.8	96	2.2	0	12.6	0	7.55	0
Vectored Down	14.1	80	12.7	-0.5	2.5	0	7.55	0
Vectored Right	14.0	80	10.25	0	10.2	0	0.5	0
Vectored Left	13.9	89	5.34	0	5.38	0	12.82	0

Figures 47 and 48 present the horizontal and vertical vectoring probe data. On the average, vertical vectoring of ±4 degrees and horizontal vectoring of ±2 degrees was achieved. Based on the voltage differential between deflectors 1 and 2, this results in a deflection angle of 0.4 degree per kilovolt vertically. Horizontally, based on the differential voltage between deflectors 3 and 1 or 2, the average is 0.35 degree per kilovolt.

Figures 49 through 51 present the TOF probe current density profiles, both horizontal and vertical, for the conditions of unvectored, vectored up, and vectored horizontally, respectively. Current density versus angle values are corrected for probe angle and time-of-flight distance. There was an internal inconsistency between the horizontal and vertical probes which is believed to be caused by a bad electrical connection in one probe.
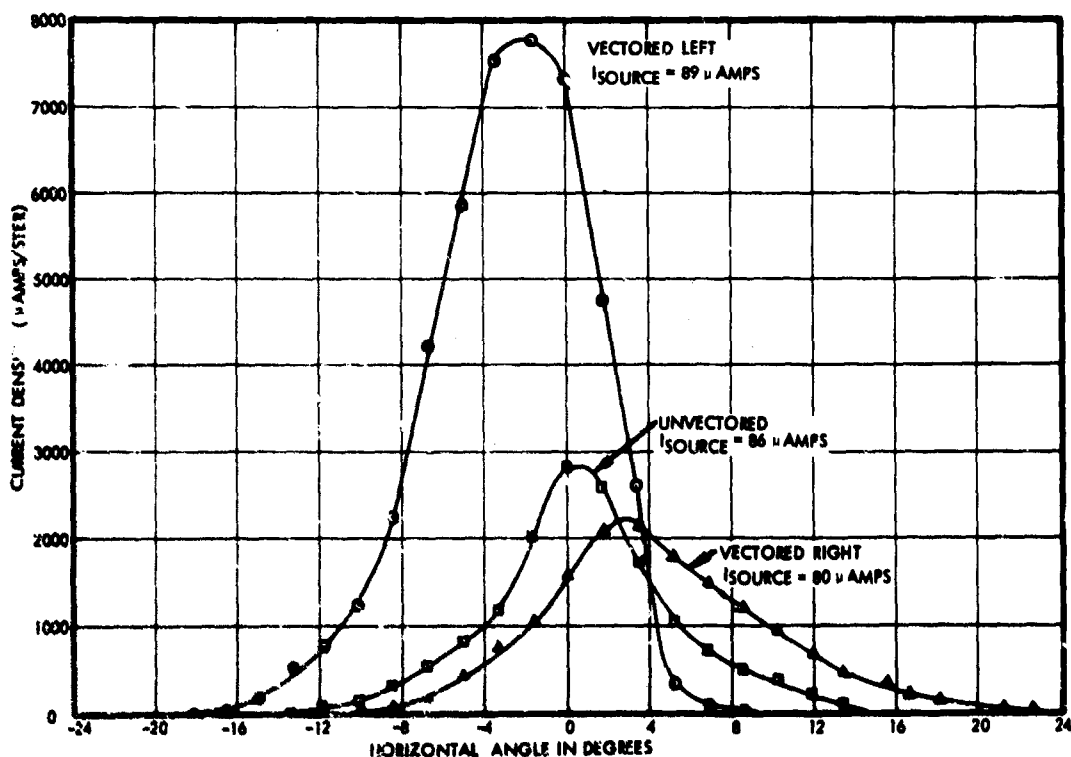
Figure 47. Run 710501, Horizontal Vectoring Data at 26 Hours
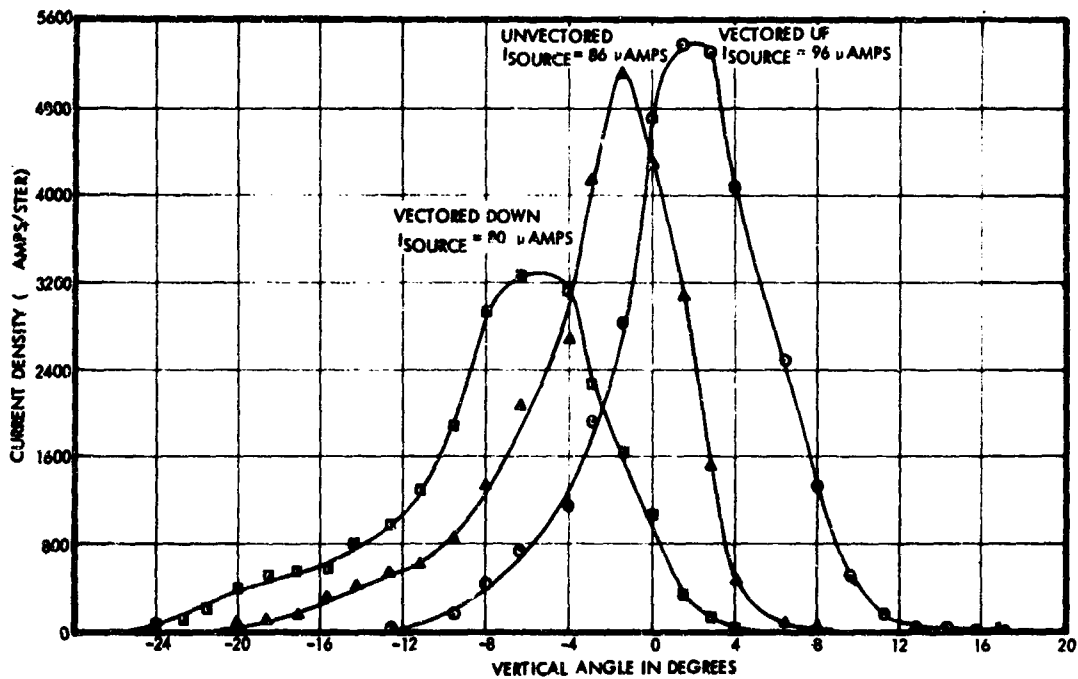
Figure 48.   Run 710501, Vertical Vectoring Data at 26 Hours
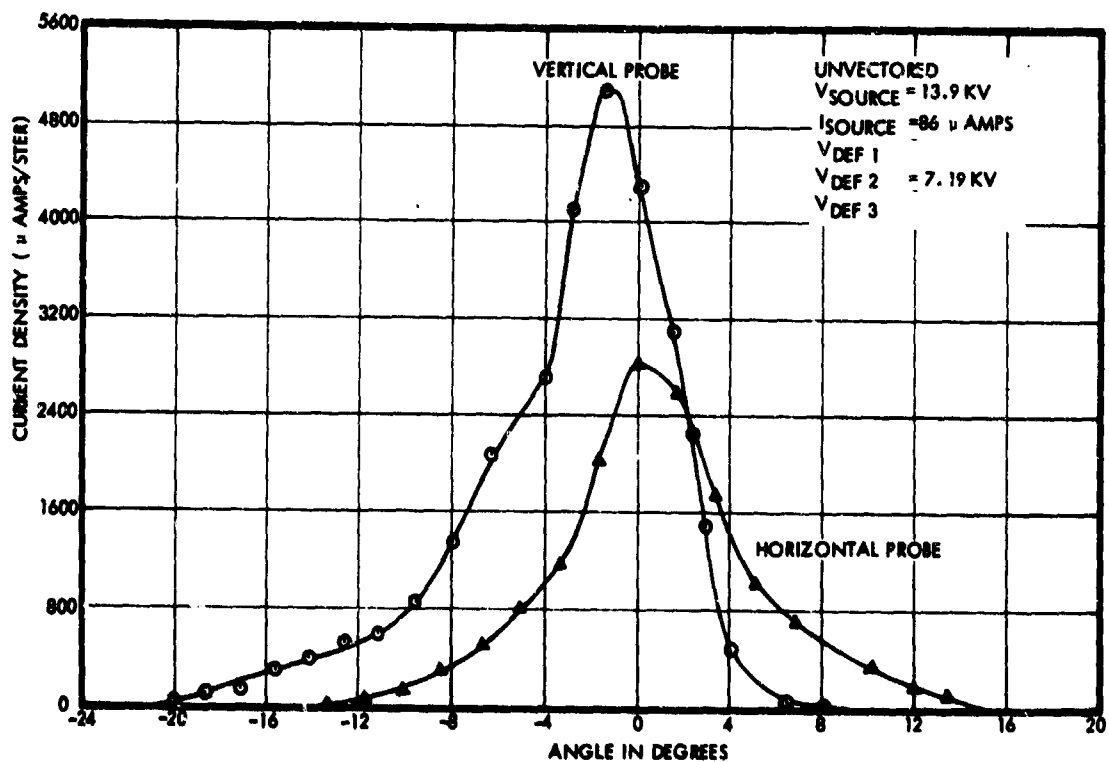
Figure 49.   Run 710501, Vertical and Horizontal Current Densities
for Unvectored Beam After 26 Hours
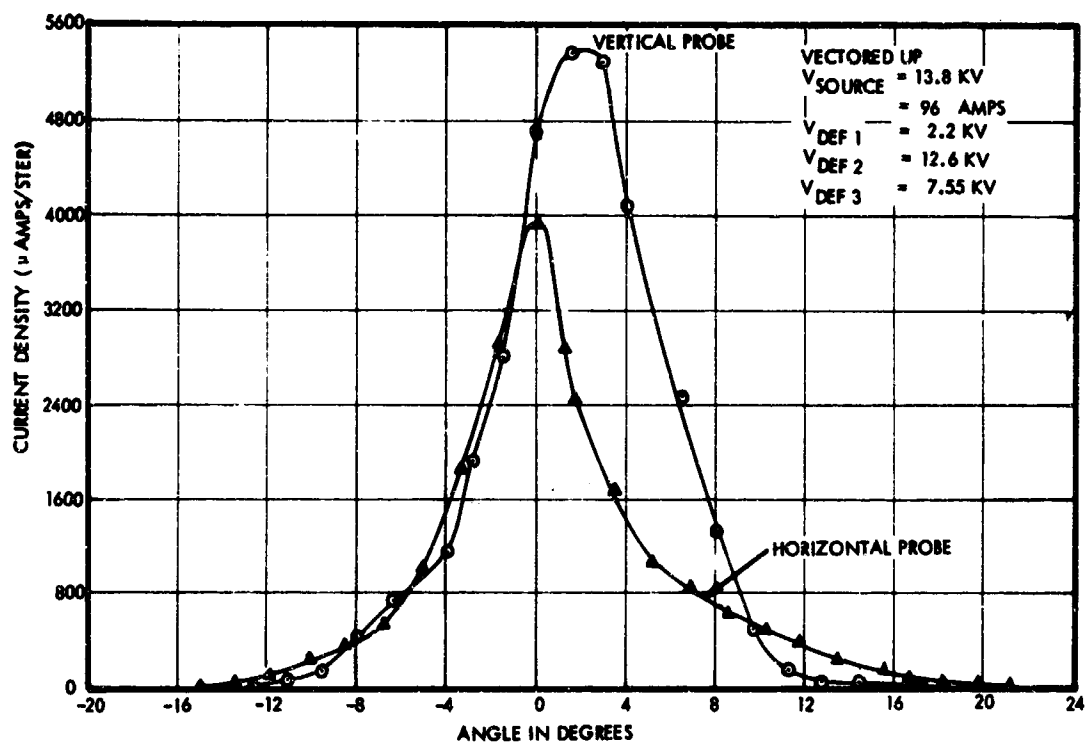
Figure 50. Run 710501, Vertical and Horizontal Current Densities
for Upward Deflection After 26 Hours
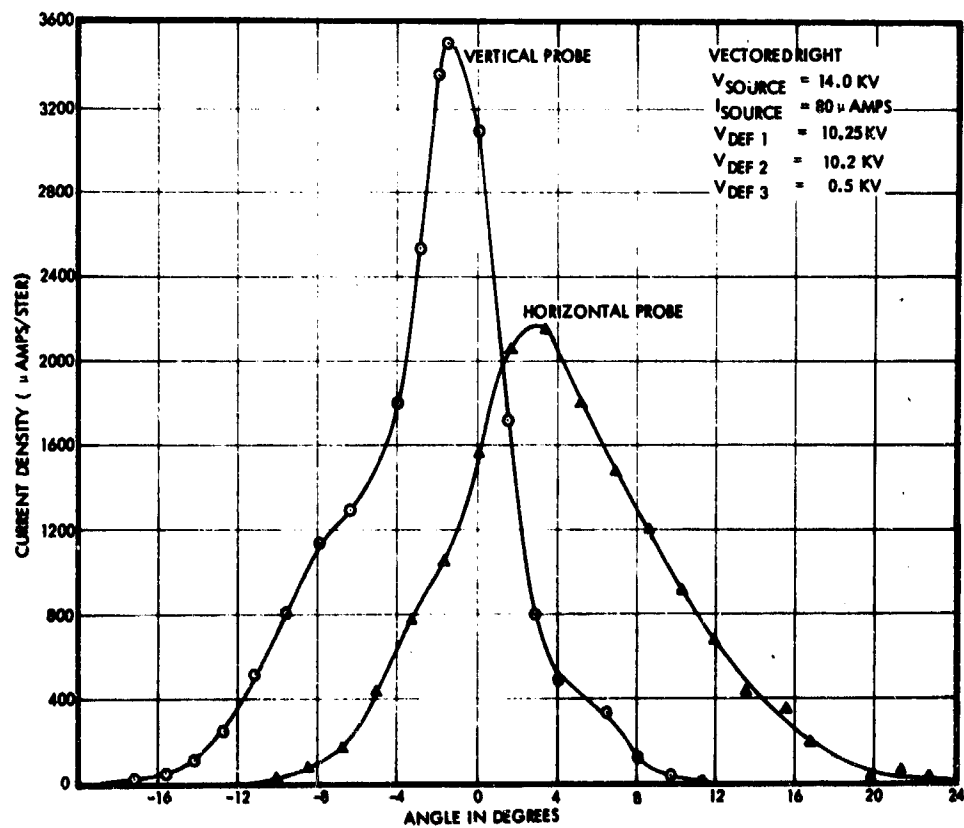
Figure 51. Run 710501, Vertical and Horizontal Current Densities
for Deflection to the Right at 26 Hours

58

The second vectoring sequence was done after the 1000-hour goal had been passed. The source beam was again vectored in four directions. About halfway through the vectoring sequence, which covered a total of 4 hours, a fairly large current drain developed to one of the deflectors (about 20 μamp) and the vectoring was temporarily interrupted to reestablish stable operation before continuing. The probe results are presented in Figures 52 and 53.
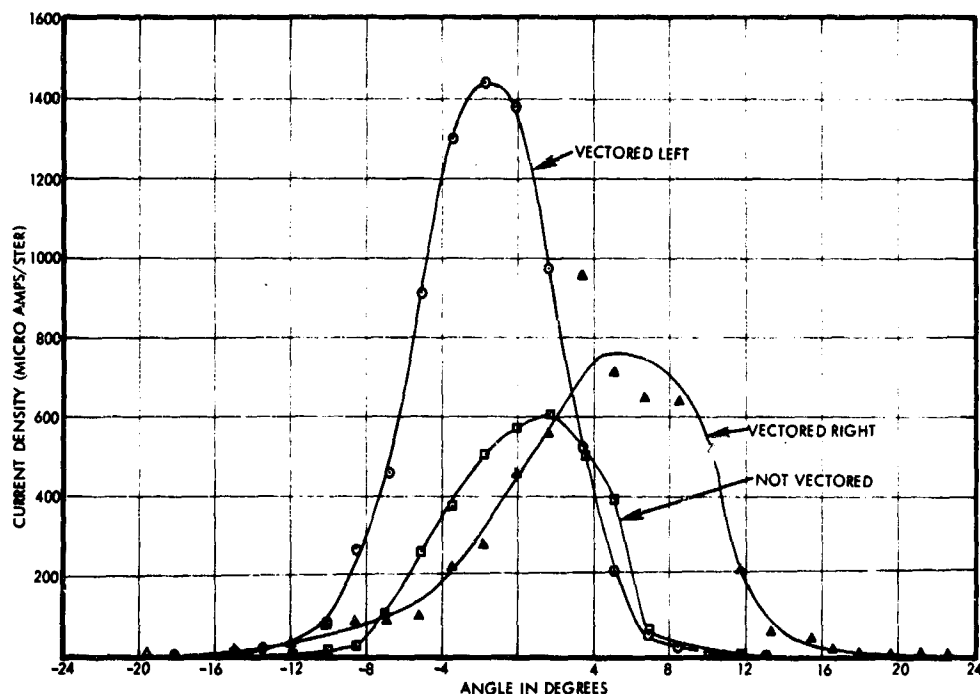
Figure 52. Run 710501, Horizontal Vectoring Data After 1000 Hours
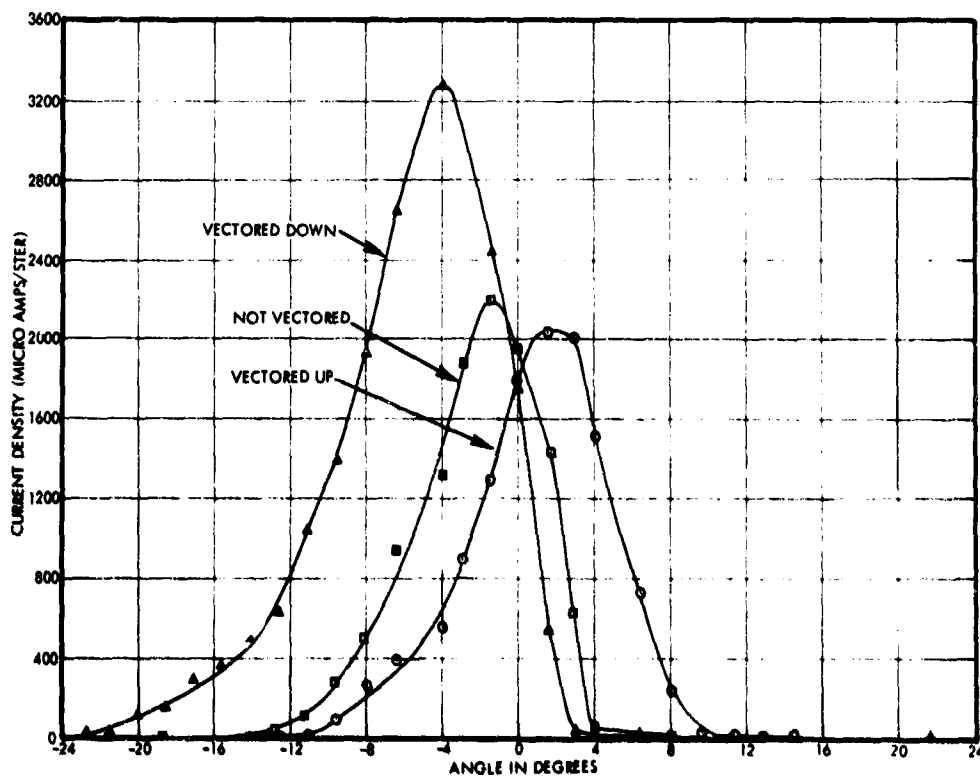
Figure 53. Run 710501, Vertical Vectoring Data After 1000 Hours

59

2.4 VERTICAL TESTING

An experimental station was set up to test the effect of firing an annular source vertically downward. This was done in a 4 by 8 foot horizontal vacuum chamber with a 10-inch diffusion pump and without benefit of a cryo wall. The interior was modified so that the source, extractor, and propellant feed assembly fit through an 8-inch-diameter port in the top of the tank near the front door. The source fired onto a 2-foot diameter collector placed on the floor of the chamber. The time-of-flight distance was 0.9 meter. Existing feedthroughs in the chamber front door were used for the high voltage leads.

The feed system for the experiment was designed so that a negative head could be maintained on the source if desired. After the propellant was outgassed, it was forced through a feed tube into a propellant reservoir inside the tank (see Figure 54). When the reservoir was full, the feed tube was withdrawn from the propellant. Feed pressure was then applied through the tube, thus forcing the propellant over another positive gravity head into the needle plenum. The propellant volume initially transferred was selected to ensure that the final propellant reservoir level was at the same height as the needle. The feed pressure was then exactly equal to the applied pressure.

A total of six significant test runs were made. Three of these were with type 7 sources; types 6 and 8 were each tested once. The initial test was made with a type 5 source. All but one of these tests were made without deflector electrodes. The objective of this testing was to determine gravitational effects on annular source operation and performance. The results lead to a tentative conclusion. On the basis of these tests and other supporting data, we have not been able to find any significant effect of gravity on annular source performance.

Several other results were also obtained in the vertical test program: a high thrust-low specific impulse mode of operation was demonstrated; a 551-hour endurance test was accomplished in the vertical mode; and finally, some important effects of operating the source in the relatively degraded vacuum (10^{-5} torr range) accompanying the absence of a cold wall could be studied.

In the following paragraphs, results from each of the six tests are summarized. Then, in an overall summary, some of the relevant comparisons are discussed, showing how the above conclusions were obtained.

2.4.1 Run 700504: Source 5

This initial run more or less acted as a "shake-down" for the system. For this reason, the source remained in the tank and was operated for 9 days, although much of this time was at idle operation with fairly low mass flow. The source voltage was held constantly at 14 kv or above.
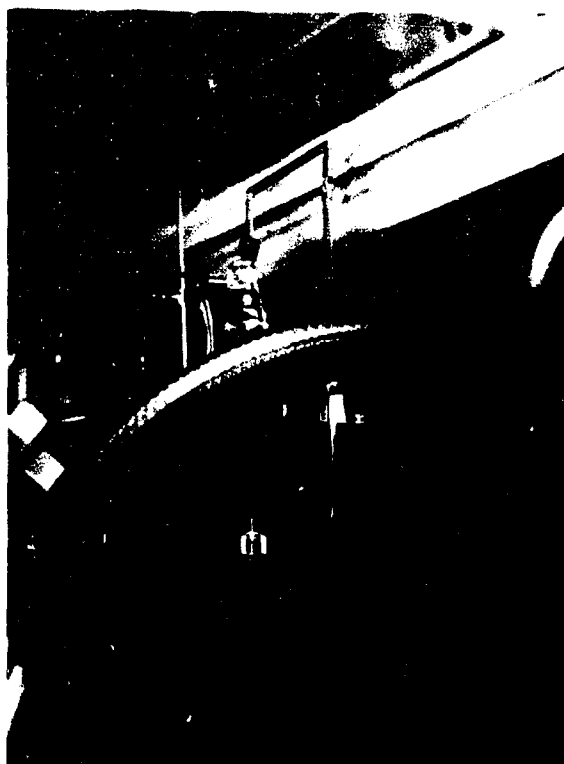
a. Without screen. Module to left, propellant reservoir at lower right inside tank. Propellant storage flask and pressurization above tank.

b. Showing screen installed, and portion of collector at the bottom.

Figure 54.
Vertical Firing Facility

The type 5 source was also tested to determine if vertical operation would help keep propellant from the center plug. It failed to do so. The source rim was a little more than 0.002 inch wide, and as a result, the source was run at low specific impulse. In fact, the run was a good demonstration of high thrust-low specific impulse operation when run at high mass flow. Table 12 shows some typical results.

A maximum specific impulse of the order of 1200 seconds was obtained at a source voltage of 20 kv, a source current of 70 microamps and a lower mass flow rate than shown above.

2.4.2 Run 700602: Source 6

This run lasted about two days, and was characterized by low mass flow-high specific impulse operation. The source flow impedance was anomalously high, and no data could be obtained at high mass flow rates. It was later determined that the propellant feed system, part of the laboratory experimental apparatus, was not properly filtered, and the thruster impedance tube had clogged.

Table 13 shows a sample of time-of-flight results obtained from this run. The data shown are for different mass flows taken at 14 and 15 kv source voltages. The data afford some comparison with type 6 needles run horizontally at low mass flow and high specific impulse. Such comparison shows virtually no difference. The data presented are uncorrected for beam spread or energy loss effects.

Table 12. Uncorrected Time-of-Flight Data for Vertical
Test Station - Run 700504

Feed Pressure (in. Hg)	Beam Current (μa)	Thrust (μlb)	I_{sp} (sec)	Thrust Efficiency (%)	Mass Flow ($\mu gm/sec$)	$\overline{q/m}$ (coul/kg)
7.5	50	51.1	468	72.8	49	1010
10	64	54.6	700	78	47	1360
12.5	71	63.3	575	80	50	1420
15	77	71.4	545	78.8	59.5	1300

Source Voltage, 14 kv; Time-of-Flight Distance, 0.9 m; Screen Voltage, +50 v; Suppressor Voltage, -130 v; Grounded Collector.

Thrust and Mass Flow based on beam current

Table 13.   Time-of-Flight Results from Vertical Test
Number 700602, Source Configuration 6

Source Voltage (kv)	Source Current (μamp)	Thrust (μlb)	Mass Flow (μgm/sec)	Thrust Efficiency (%)	Specific Impulse (sec)
14	90	22	5.48	68	1807
15	145	23	5.6	66	1862
14	110	14	1.8	69.2	3503
15	125	14.4	1.64	66.8	3984
14	150	24	3.9	70.2	2807
15	170	26	3.95	66.4	2987
14	175	32.9	6.26	69.9	2386
15	200	35.	6	67.6	2654

A window in the test chamber was situated so that collector and beam luminescence could be observed with the lights extinguished. Careful inspection of the beam luminescence showed that the beam was rather tight and uniformly dense, with peak intensity near the center. Beam spread was less than 20 degrees.

2.4.3 Run 700604: Source 8

This run was the first test of the new source design 8. The run consisted of two separate tests. Each of these achieved very high performance during the first 20 to 80 hours, after which the thrust and specific impulse deteriorated. Later horizontal testing of source 8 was not consistent with these results, nor were the results of vertical tests performed on other sources. Later experience showed that this degradation, which was probably the result of excessive build-up of solid contamination on the source, was caused by the combined effects of the degraded vacuum in the test chamber and the short time-of-flight distance which intensified back-scattering from the collector.

In each test, the source required a "pre-wetting" procedure, with the high voltage turned off for 1.5 minutes and full flow rate to the source. This pre-wet was necessary to wet the inside of the meniscus cavity. After start-up, the source appeared to operate optimally at 13 kv. The initial source current was about 150 microamps in each case.

During the first test, the beam illumination pattern was observed on the collector. All visible beam lay within a uniform circle of about 18 inches in diameter, corresponding to a cone half-angle of 15 degrees.

Figure 55 shows a graphical time history of the first test. From 25 to 70 hours, no adjustments were made to control parameters, and all changes in operating level were spontaneous. The mass flow remained constant, and there was no evidence of clogging of the propellant flow passage. At 72 hours, higher voltage operation was investigated. Degraded vacuum and high current caused overheating and instability (there was no temperature control), and the test was terminated.

The second test began as the first, but performance degradation was more gradual, and occurred only after some 80 hours of operation. The test ran longer, nearly 120 hours, and was terminated because of a clogged propellant feed impedance caused by dirty propellant and the absence of a propellant filter. Figure 56 shows the time history of this test.

2.4.4 Run 700703: Source 7

This test was a minor endurance test of source 7, and ran for 267 hours before it was terminated automatically by a vacuum system failure. The source was again started with a pre-wet action, similar to that described above. The run began with a low source current, a high mass flow and a low specific impulse. After about 75 hours, the mass flow was lowered and a specific impulse in excess of 1500 seconds was obtained. This performance was maintained until 190 hours, the course of the test to this time is shown in Figure 57. After this time, the performance did not change appreciably. The entire run was made with a source voltage between 14 and 14.2 kv.

Early in the run, a visual examination of the collector illumination indicated a beam cone with a half-angle of 10 degrees.

2.4.5 Run 700705: Source 7

This run lasted for 551 hours, and is described as an endurance test in Section 2.5. In that section, the performance time history of the run is also presented. Between approximately 90 and 390 hours, thrust was greater than 25 μlb and specific impulse was about 1500 seconds. Thrust efficiency was maintained between 70 and 75 percent for the entire run.

Long-term performance and source operation for this run were equivalent to that of source 7 when it was tested horizontally under equivalent vacuum conditions (e.g., run 701008). Some long-term performance degradation occurred because of the poor vacuum, which was of the order of 5×10^{-5} torr.

2.4.6 Run 700902: Source 7-2

This was the last test performed in the vertical test facility. The test did much to help resolve the meniscus cavity design problem discussed in Section 2.1.1. It was run before the meniscus cavity had been redesigned and, as a result, the source was still exhibiting non-wetting characteristics. The test lasted about 24 hours. It was run with deflector electrodes, but no vectoring voltage differentials were applied. For a short period of time in which normal operation could be achieved with a wet rim and a low mass flow rate, a specific impulse of 1830 seconds and a thrust of 16.4 μlb were obtained.
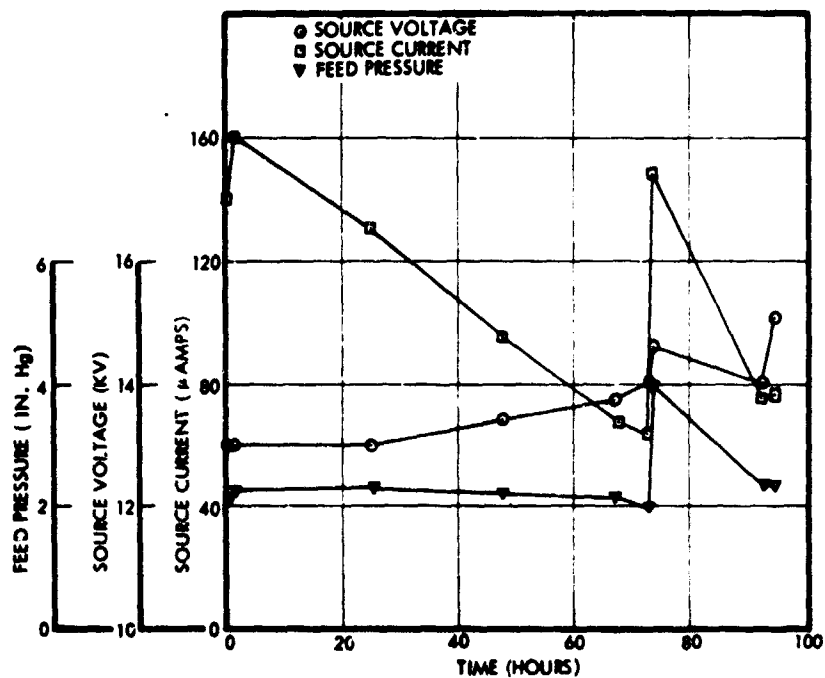
Figure 55a. Operating Parameters Versus Time—Run
700604, First 100 Hours. Source design
8 in vertical testing.
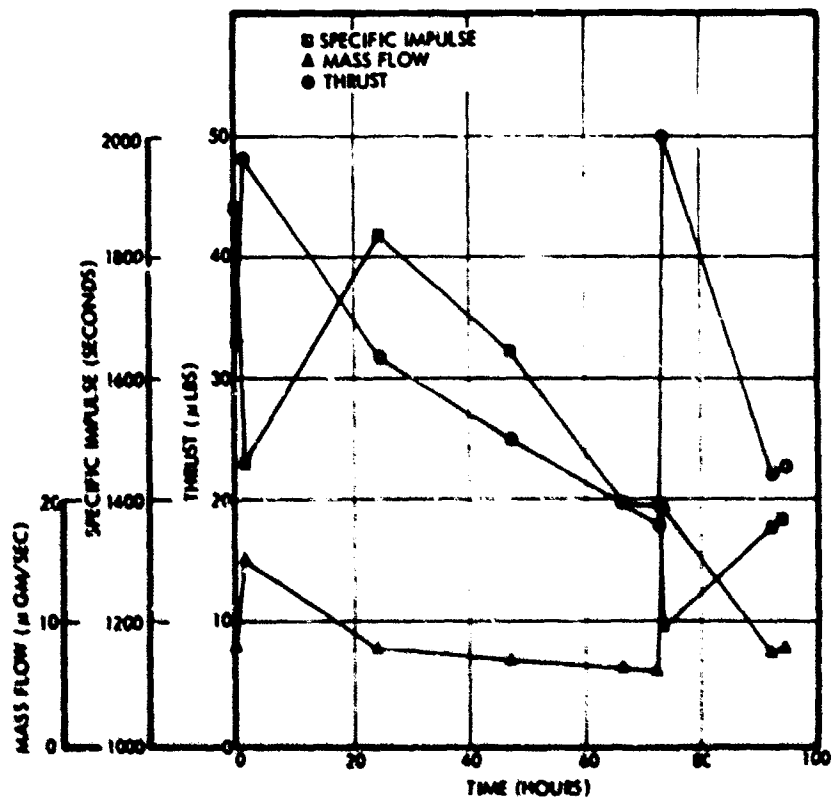
Figure 55b. Time-of-Flight Performance Parameters
Versus Time — Uncorrected TOF Data
for Run 700604, First 100 Hours. Source
design 8 in vertical testing.

65
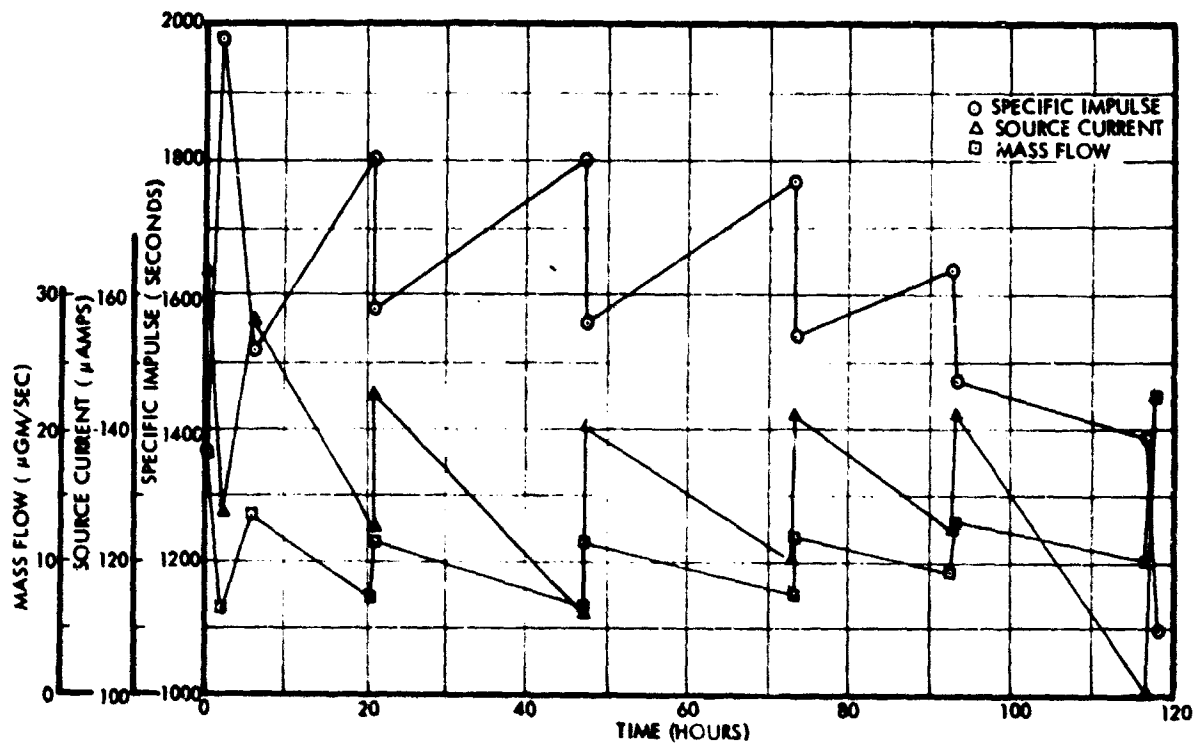
Figure 56a. Source Current, Specific Impulse and Mass Flow Versus Time — Run 700604, Second 120 Hours. Source design 8 in vertical testing.
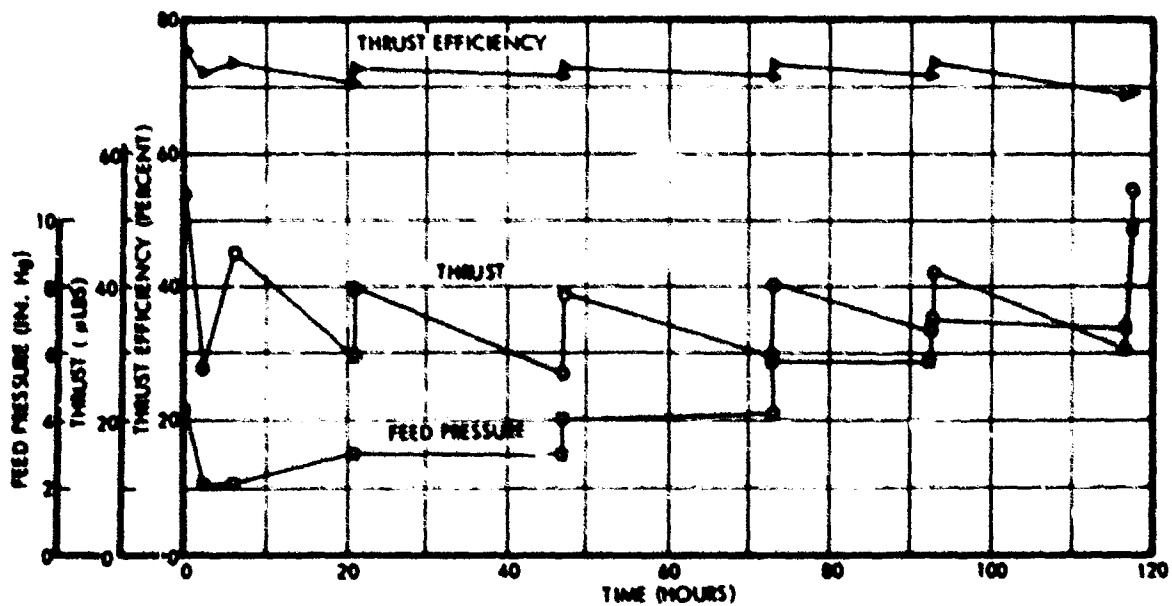
Figure 56b. Thrust Efficiency, Thrust and Feed Pressure Versus Time — Run 700604, Second 120 Hours. Source design 8 in vertical testing.

66
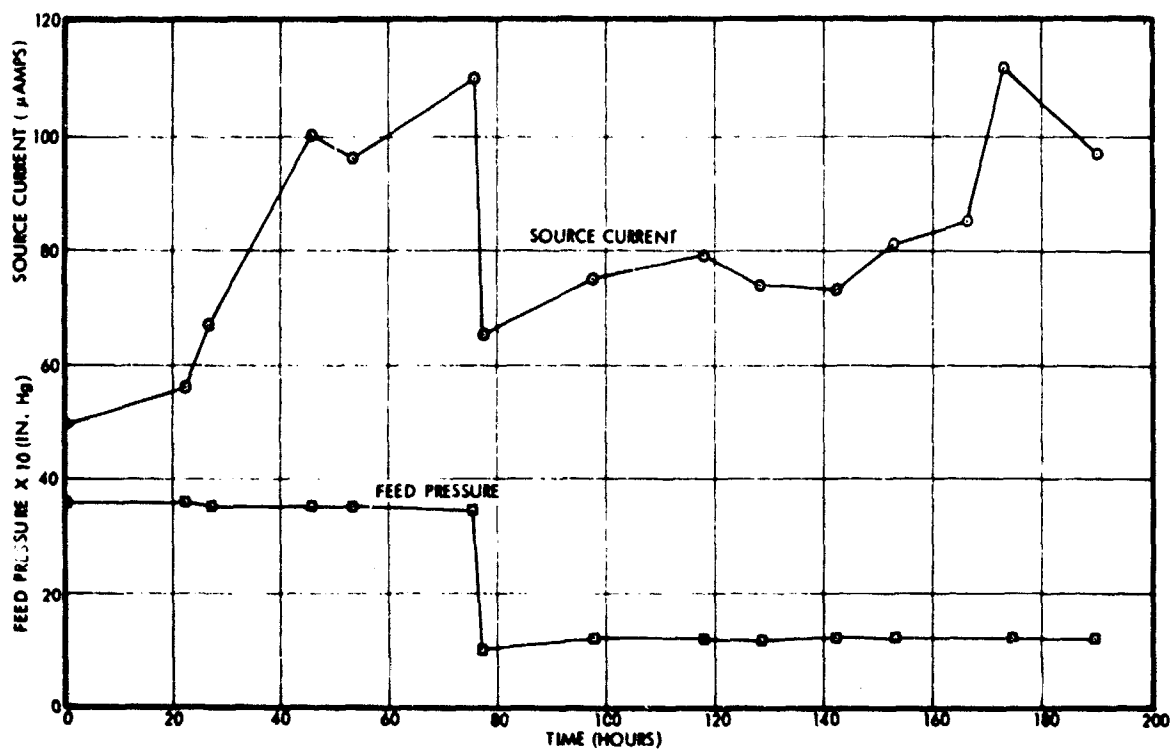
Figure 57a. Feed Pressure and Source Current Versus Time — Run
700703, Source Configuration 7
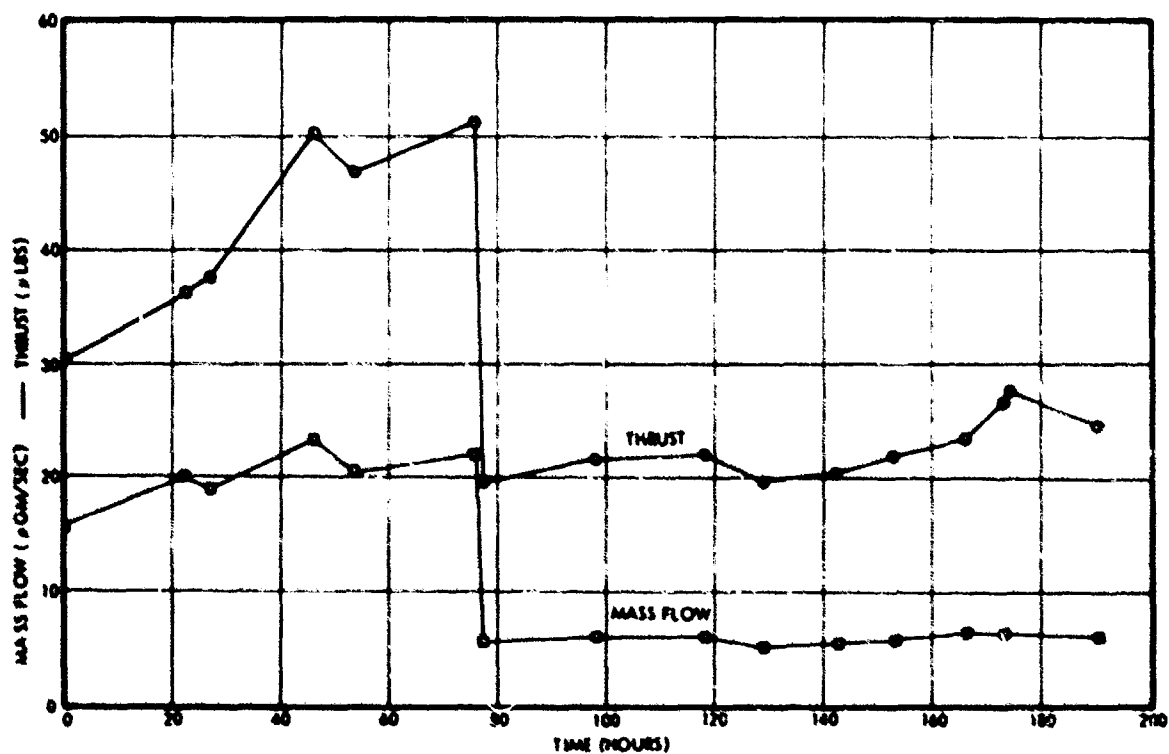
Figure 57b. Thrust and Mass Flow Versus Time — Run 700703, Source
Configuration 7 (From Urcorrected TOF Data)

67

Figure 57c. Specific Impulse and Thrust Efficiency Versus Time — Run 700703, Source Configuration 7 (From Uncorrected TOF Data)

2.4.7 Summary of Vertical Testing

The most useful conclusions to be drawn from the vertical testing described above are the performance comparisons, both between horizontal and vertical testing and between two or more different types of sources. Such conclusions must certainly be tentative, for two reasons. First, only a limited amount of testing was done, and this was accomplished early in the program when factors important to source design and operation were still being discovered and defined. Second, the differences between horizontal and vertical source operation are difficult to disentangle from secondary differences in vacuum test stations, including, for example, the quality of the vacuum, the time-of-flight collector distance, and the type of diffusion pump cold trap.

For the three sources, 6, 7 and 8, both horizontal and vertical testing were accomplished, thus, a matrix such as that shown in Table 14 was investigated. A detailed comparison of these runs reveals little significant difference between horizontal and vertical testing.

68

Table 14. Summary of Runs Giving Comparative Data on Horizontal and Vertical Testing of Three Sources

	No. 6	No. 7	No. 8
Horizontal	Run 710601, 701007	Run 701008, 700904	Run 700702, 700704
Vertical	Run 700602	Run 700703, 700705, 700902	Run 700604

Table 15 details several of the important differences among the test stations used to perform the testing referred to in Table 14. The same vertical test facility was used, of course, to test all three sources. Horizontal testing, in the runs referred to in the table, was accomplished in three different systems for the three sources.

In Table 14, the columns corresponding to sources 7 and 8 provide the most valid comparison of horizontal and vertical test results. We have set down such comparisons in Table 16 for source 7, and Table 17 for source 8. In each case, the most interesting runs were chosen for comparison.

In the comparison made for source 7, the elapsed run times were comparable. The horizontal test was run with vector electrodes. The voltage settings for this test were taken to most closely duplicate source performance without electrodes (optimum performance). Nominal ambient pressures were different by a factor of about two, and the performance was comparable in the two tests.

In comparing source 8, account must be taken of the difference in elapsed time. The most important system difference was in the ambient pressure, a factor of 10 between the two. Accounting for these differences, no significant overall difference in performance between the two tests can be identified.

2.5 LIFE TESTING

Seven endurance tests of more than 400 hours duration were run during this program. Four of these were in the 400 to 600-hour duration range, two were nominally of 1000 hours duration, and one was of 2000 hours duration. The life test runs are indicated in the run log, Table 1, and are also summarized in Table 18.

Sources tested were of types 6, 7 and 8. Early, short-term tests were oriented toward resolving performance differences, if any, between the various source designs. Also, one test (run 700705) was conducted with the source firing vertically as part of a comparison of horizontal testing versus vertical testing. The results showed that in general such effects were very minor. Long-term performance differences among the three sources were also determined to be relatively minor.

69

Table 15. Comparison of Colloid Research Vacuum Test Facilities

Vertical Test Facility	Horizontal Testing - Source 8
10 in. NRC Diffusion Pump, LN2 trapped	24 in. Edwards Diffusion Pump, trapped with cold water baffle
No cold wall	Rear cold wall - LN2
Typical vacuum during tests, 2×10^{-5} torr	Typical vacuum during test, 8×10^{-7} torr
0.9 meter time-of-flight	2 meter time-of-flight
No telescopic observation	Telescopic observation from 5 feet, direct lighting
Beam pattern visible on collector	Beam pattern visible on 6 in. view probe
Horizontal Testing Source 7	Horizontal Testing Source 6
10 in. NRC Diffusion Pump trapped with Freon refrigerant	6 in. CHA Diffusion pump, LN2 trapped
Rear cold wall - LN2	No cold wall
Typical Vacuum during test, 5×10^{-6} torr	Typical vacuum during test, 5×10^{-5} torr
2 meter time-of-flight	1.4 meter time-of-flight
Telescopic observation from 5 feet, side lighting	Telescopic observation from 5 feet, direct lighting
Beam visible only from ambient molecular excitation	Beam pattern visible on 6 in. view probe

70

Table 16. Comparison of Horizontal and Vertical Testing of Source 7

Facility: Horizontal - NRC; Run: 701008	Facility: Vertical; Run: 700705
Total Elapsed Time: 417 hr	Total Elapsed Time: 551 hr
Type 2 Deflector Electrodes	No Deflector Electrodes
Operating Voltage: 16 kv	Operating Voltage: 14.1 kv
Operating Current: 95 μamp	Operating Current: 110 μamp
Nominal Ambient Pressure: 4×10^{-6} torr	Nominal Ambient Pressure: 10^{-5} torr
Demonstrated 300 non-continuous hours above 1500 sec I_{sp} and 25 μlb thrust	Demonstrated 300 continuous hours above 1500 sec I_{sp} and 25 μlb thrust
Telescopic observation showed uniform wetting with no detectable asymmetry	No telescopic observation available during the run
Time-of-flight probe studies showed a uniform beam, directed downward about one degree	Collector pattern observation showed a generally uniform beam with no appreciable asymmetries

Later in the program, an important milestone was achieved by the demonstration of the ability of a colloid source to run for 2000 hours with a neutralizer, and exceeding 1000 seconds specific impulse. The ability of the thruster to be stopped and restarted without breaking vacuum was also demonstrated.

A brief summary of the important aspects of each life test is presented in the following sections.

2.5.1 Run 700704: Source 8, 616 Hours

Configuration 8 was installed in the 4 by 8-foot test station with the 24-inch Edwards diffusion pump. No deflector electrodes were used. The system had a heater for the thruster module, but no closed loop temperature control. A liquid nitrogen cold wall was used. Although more than 600 hours of testing were achieved, the main objective of the test was not endurance, but the performance of gas generation measurements (Section 6.4), performance measurements, and other auxiliary experiments. Also this allowed a comparison between source type 7 under horizontal test conditions, and source 8 (same source) under vertical test conditions.

71

Table 17. Comparison of Horizontal and Vertical Testing
with Source Configuration 8

Facility: Horizontal - Edwards; Run: 700704	Facility: Vertical; Run: 700604
Total Elapsed Time: 615 hr	Total Elapsed Time: 120 hr
Operating Voltage: 13 kv	Operating Voltage: 13 kv
Operating Current: 100 μamp	Operating Current: 130 μamp
Nominal ambient pressure, 10^{-6} torr	Nominal ambient pressure, 10^{-5} torr
Demonstrated 230 hr of non-continuous operation above 1500 sec I_{sp} and 25 μlb thrust	Demonstrated 100 continuous hr above 1500 sec I_{sp} and 25 μlb thrust
Microscopic observation showed uniform wetting with no detectable asymmetry	No microscopic observation available during the run
Viewprobe observation showed a generally uniform, dense beam with asymmetries unrelated to gravity when they occurred	Collector pattern observation showed a generally uniform dense beam with asymmetries related to nonuniform rim wetting

Table 18. Summary of Annular Emitter Life Tests

Run Number	Source Number	Duration (hours)
700704	8	516
700705	7	551
701005	7-2	948
701008	7	417
710104	7B	1015
710402	6B	433
710501	6B	2042

All performance was at 65 to 68 percent time-of-flight thrust efficiency. About 250 hours of the run (not all continuous) were conducted with thrust and specific impulse above the rated 25 μlb and 1500-second level. Performance was comparable to that of source 7.

Two accidental shut-downs occurred. These incidents demonstrated that the source was restartable after at least several hours off time.

2.5.2 Run 700705: Source 7, 551 Hours

This run demonstrated long-term performance when firing vertically. No deflector electrodes were used. The performance history is shown in Figures 58 through 62. For approximately 300 hours, greater than 25 μlb thrust and 1500 seconds specific impulse were maintained. Thrust efficiency varied between 70 and 75 percent for the entire run.

2.5.3 Run 701005: Source 7-2, 948 Hours

This test of an early type module without deflectors was made in a 4 by 8-foot test facility. A LN_2 cold wall was used, and a radiation heater was installed near the propellant filter. A thermocouple installed on the ground screen near the module read from $25°$ to $28°C$ while the module was running. Nominal ambient pressure was 10^{-6} torr.

This run was important from several standpoints. It was the only 1000-hour run performed without deflectors. An important design factor was made clear when source performance was improved by a simple geometry change in the depth of the meniscus cavity (Section 2.1). Performance data were obtained, and a performance comparison was made after long-term operation (Section 2.2). Finally, a first look was obtained at long-term performance characteristics.

Performance characteristics at the beginning and end of the run are summarized in Section 2.2.

The performance time history is shown in Figures 63 through 65. The source voltage was about 14.5 kv when the run began. By the end of the run, it had been raised about 1 kv to keep the specific impulse up in order to compensate for an observed decrease in q/m (cf. page 78).

Figure 63 shows the time history of the control parameters, voltage and feed pressure, and the source current. Good feed pressure regulation was maintained throughout the run with a pressure regulated dry nitrogen bleed-pump system. The earlier hours seem to be characterized by a high, variable needle current. After 20 or 30 hours the needle was thoroughly wet, and by 150 hours performance reached its peak. After that it began to fall off and stabilize gradually. Figure 64 shows the uncorrected time-of-flight thrust efficiency, and the average charge-to-mass ratio. Thrust efficiency remained fairly constant. Figure 65 shows the uncorrected time-of-flight specific impulse, thrust and mass flow rate.

73
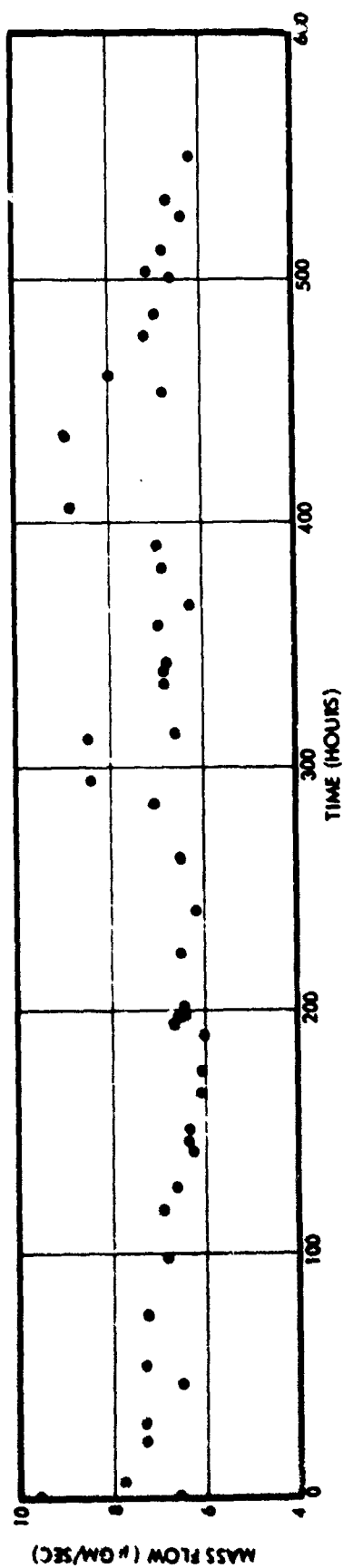
Figure 58. Annular Source 7 in Vertical Test – Run 700705; Time History of Mass Flow
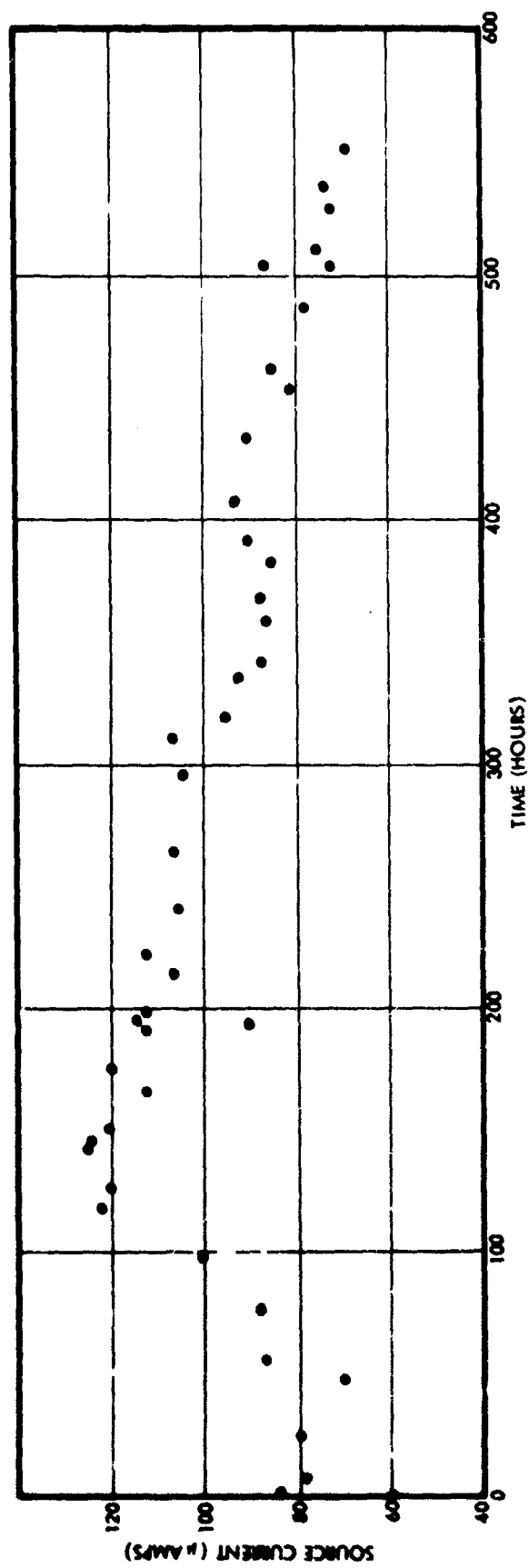
Figure 59. Annular Source 7 in Vertical Test – Run 700705; Time History of Source Current

74
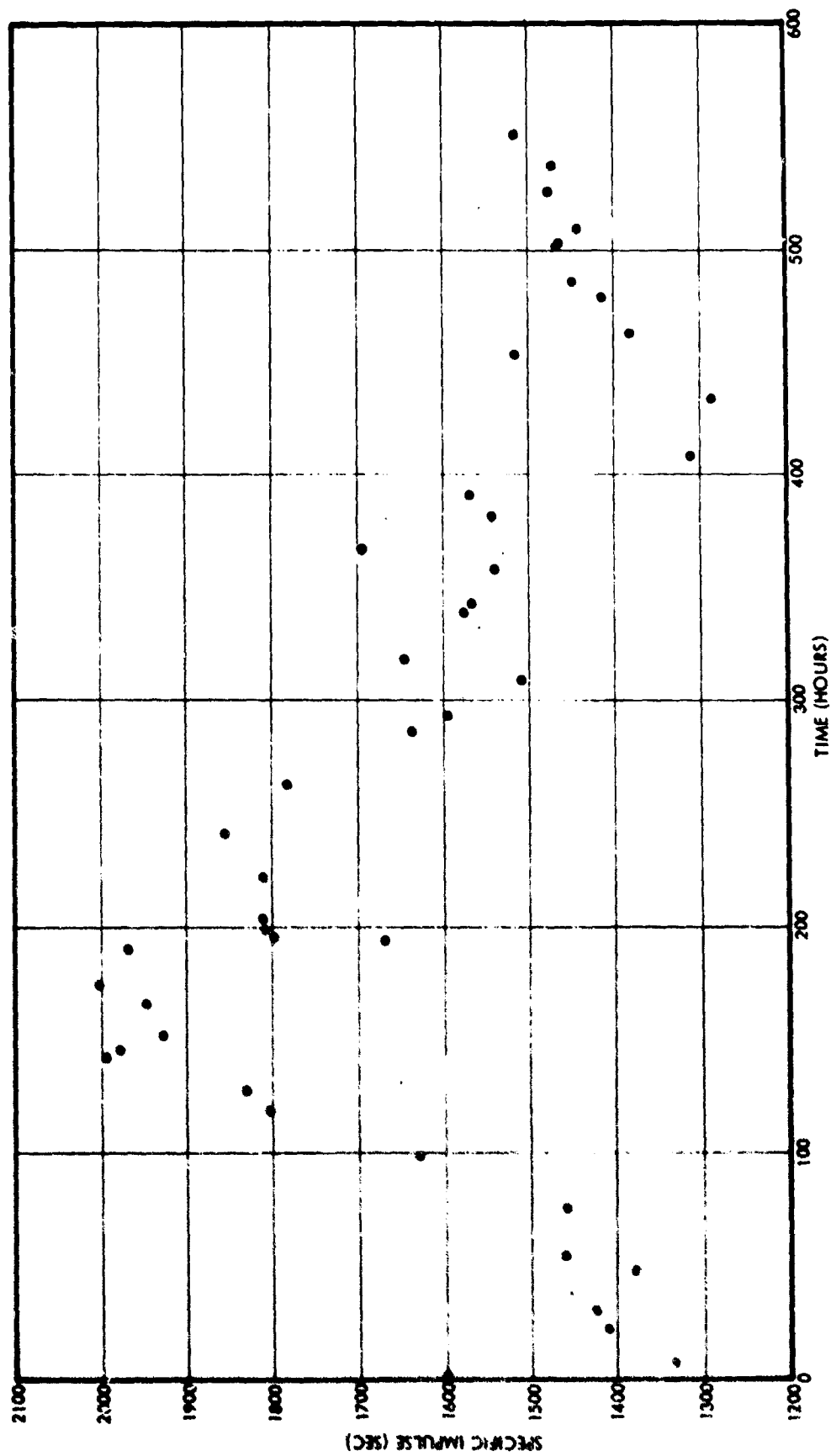
Figure 60. Annular Source 7 in Vertical Test - Run 700705; Time History of Specific Impulse

75
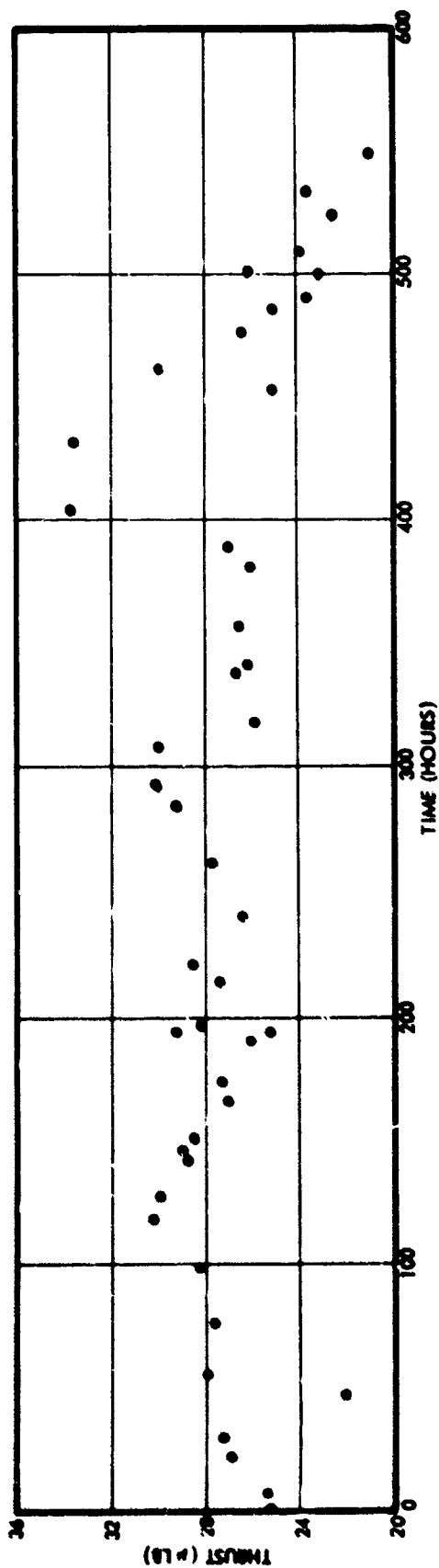
Figure 61. Annular Source 7 in Vertical Test - Run 700705; Time History of Thrust
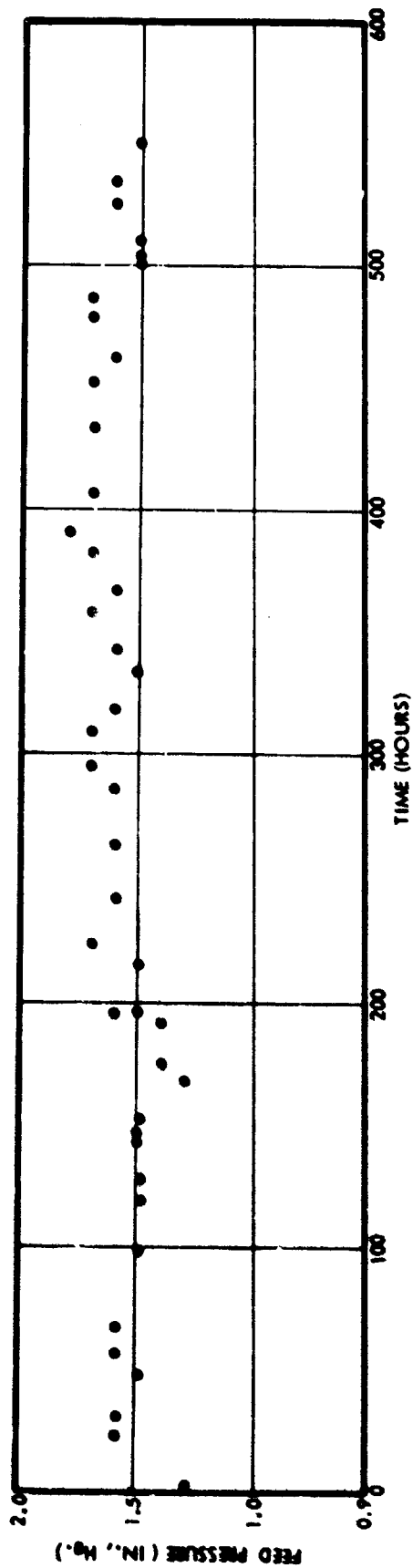
Figure 62. Annular Source 7 in Vertical Test - Run 700705; Time History of Feed Pressure

76
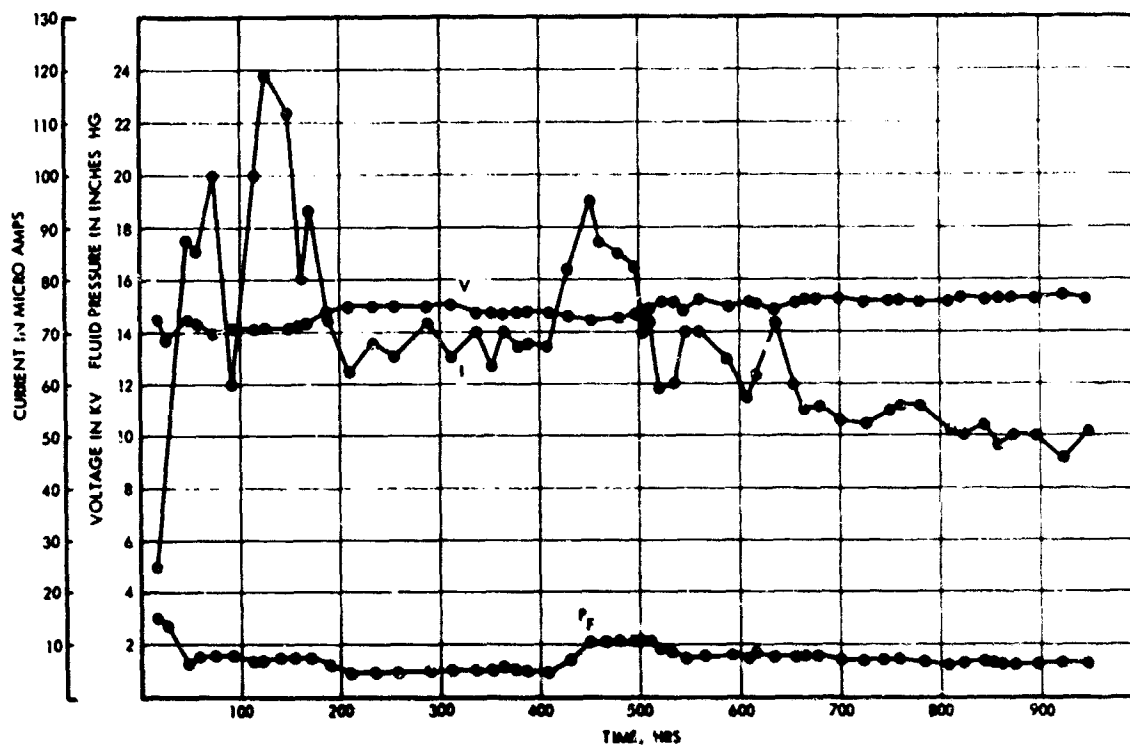
Figure 63. Control and Operating Parameters for Annular
Source 7-2, Run 701005
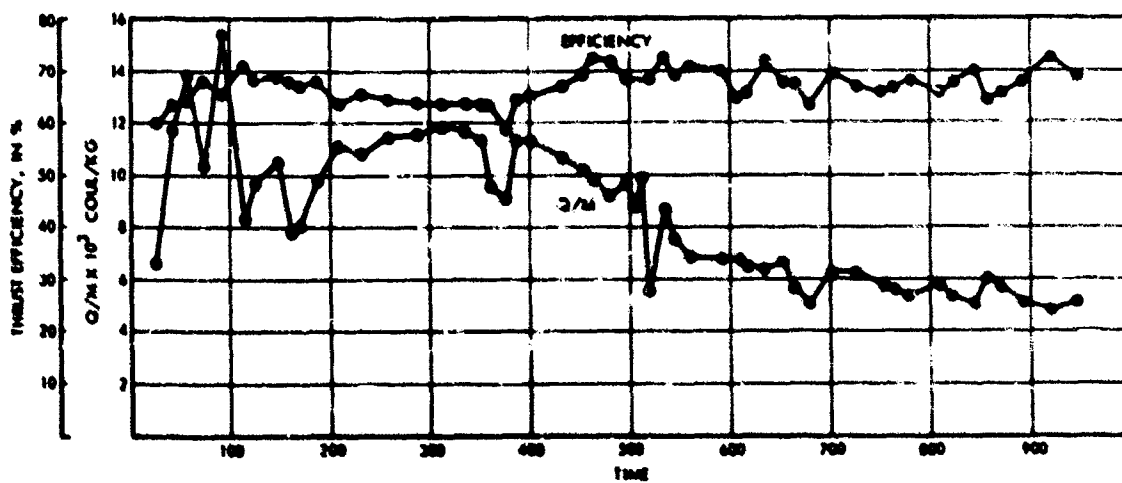
Figure 64. Thrust Efficiency and Average Q/M for Annular Source
7-2, Run 701005; Uncorrected Time-of-Flight Data
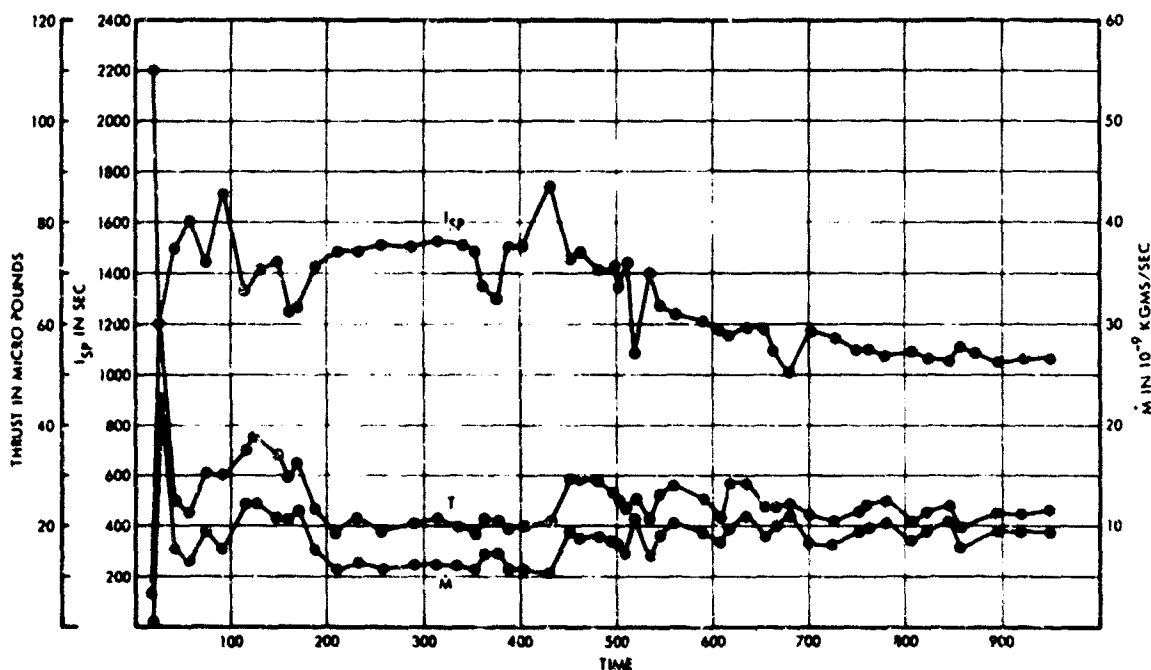
Figure 65. Thrust, Mass Flow Rate and Specific Impulse for Annular Source 7-2, Run 701005; Uncorrected Time-of-Flight Data

A small spot on the source rim had been damaged (bent) before the run began. No immediate effects on performance were noticeable. After 500 hours, a degradation in average q/m was seen. Post-run examination showed that a microscopic layer of solid tar had coated the rim around the area of the imperfection. Low q/m emission from this part of the source rim would have caused the performance drop. About half of the remaining rim also had patches of solid contaminants of a microscopic size, less than 0.001 inch in diameter.

2.5.4 Run 701008: Source 7, 417 Hours

Annular source 7, with type 2 deflector electrodes, was endurance tested in a 10-inch pumping facility. The specific impulse was generally about 1200 seconds, thrust above 20 micropounds, and thrust efficiency at or above 60 percent, uncorrected. Exceptions were during short periods when the performance was being mapped, or the feed pressure regulation malfunctioned.

Performance mapping at the beginning and end of the run is discussed in Section 2.2. The thrust vectoring data are discussed in Section 2.3. The test also yielded performance comparisons between sources 7 and 8 in horizontal testing, and between horizontal and vertical testing with source 7. Neither comparison showed any significant difference.

The test was run in a relatively poor vacuum environment (5 - 10 x 10^{-6} torr), since there was no cold wall. Some of the usual problems attendant to low vacuums were experienced here. One of

78

the deflectors experienced intermittant breakdown problems, ranging from field emission to direct impingement. The extractor current would increase in response to an increasing deflector current. The deflector currents were zero for most of the time, however, and the extractor current was low; of the order of a microamp.

The poor vacuum also resulted in a microscopic layer of solid contamination forming on the rim. It density was greater than in the previous 948-hour run, which may be attributed to the difference in vacuum environments.

Figure 66 shows a time history of the control parameters of the run. Figures 67 and 68 show the performance history, which had considerable scatter due in great part to a faulty feed pressure regulator which tended to allow the feed pressure to drift downwards.

2.5.5 Run 710104: Source 7BM2, 1015 Hours

This was the only test run with the successful but hard to make 7BM2 source design (see Section 2.1). A set of type 3 deflector electrodes was used. The module was fully temperature controlled, with a radiant heater and a thermistor, as described in Section 2.1. A LN2 cooled cryowall was provided to help reduce the vacuum.

The test was run in a 4 by 8 foot tank with a 1.8 meter time-of-flight distance, and a 10-inch diffusion pump port. Horizontal and vertical time-of-flight probes were used to obtain beam profiles (Section 7.2) and also to study the vectored beam profile (Section 2.3).
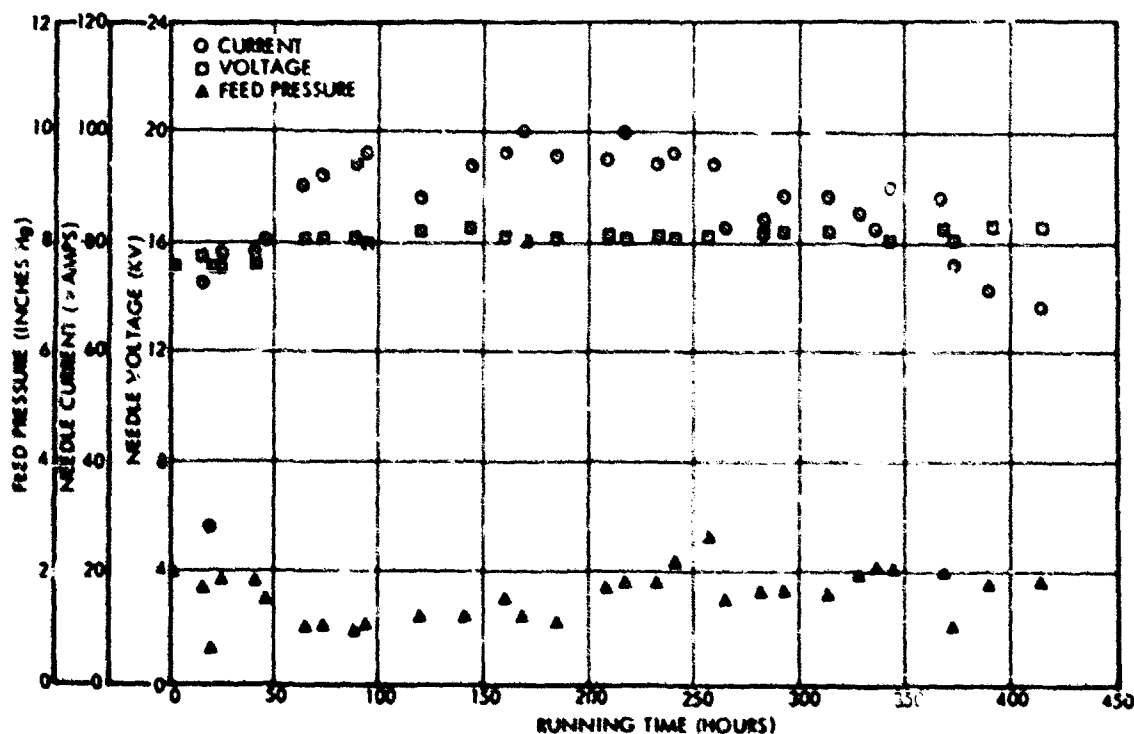
Figure 66. History of Control Parameters: Run 701008, Annular Source 7 with Deflectors, in NRC-2 for 400 Hour

79
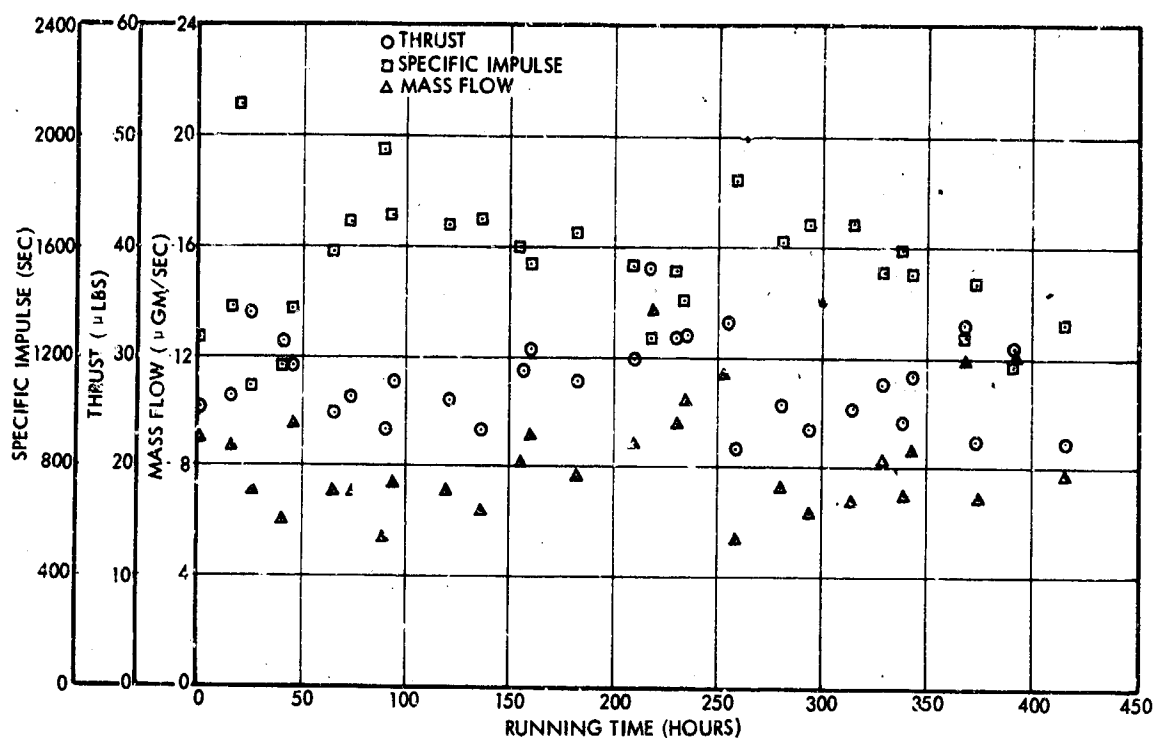
Figure 67. History of Performance Parameters: Run 701008, Annular Source 7 with Deflectors, in NRC-2 for 400 Hours
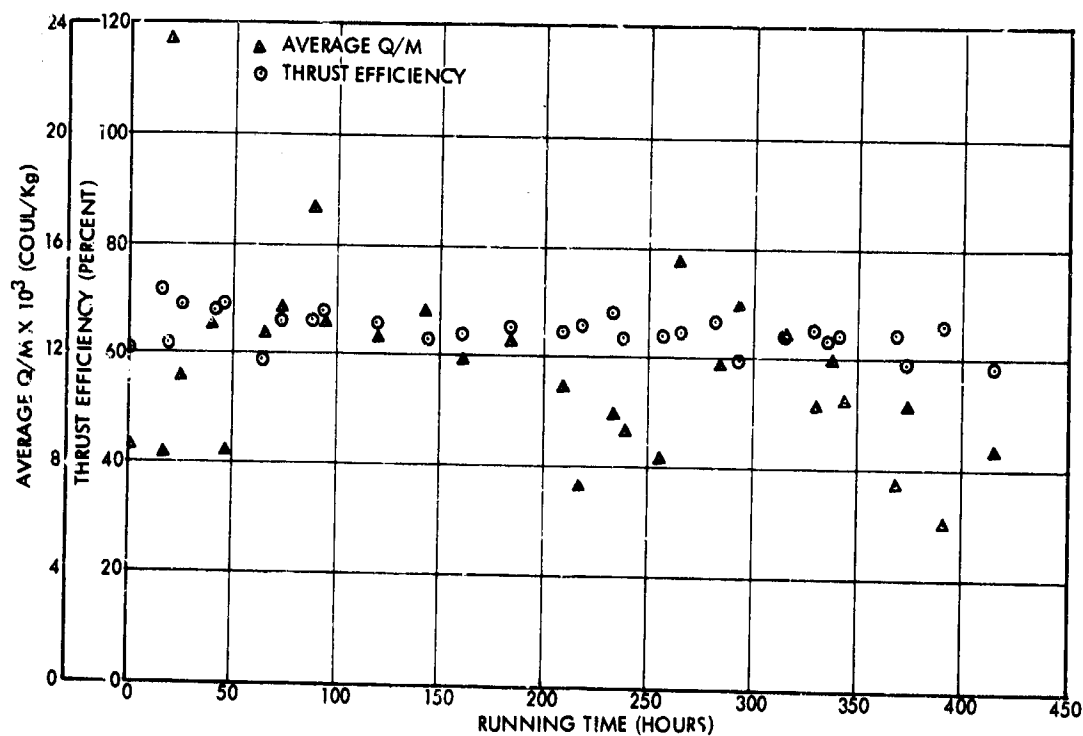
Figure 68. Average Charge to Mass Ratio and Thrust Efficiency: Run 701008, Annular Source 7 with Deflectors, in NRC-2 for 400 Hours

80

Figure 69 through 72 show a time history of the test, which was originally intended as a 400-hour milestone test, and therefore was run without a neutralizer. Since the operation was so smooth, it was decided to continue the test for a goal of 1000 hours. The erratic extractor current was caused by an adjacent grounded screen which had been positioned too close to the thruster. It had no other effect on performance. The increase in feed pressure through the run indicates a slight clogging of the feed line, probably at the filter. (The module itself was an intermediate design, and had no filter. The impedance of the source remained unchanged through the run.)

The extractor voltage was held constant at -2 kv. The deflector voltages were held at 8 kv during unvectored operation. The deflector drain currents were less than 0.1 μamp (limit of resolution of meters) during all unvectored running, and less than 1 μamp while vectoring. The source temperature, measured on the module baseplate, varied only 0.1 degree from 25.2°C. The tank pressure was held steadily between 3.5 and 4.5 x 10^{-6} torr.

All time-of-flight results on this run were obtained with the automatic system described in Section 7.1. The time-of-flight collector was a 3-foot honeycomb collector with a suppressor and a screen grid. The screen and suppressor were set at 60 and -120 volts, respectively.

A visual observation made of the beam glow at 357 hours indicated that the beam was dense and uniform with an apparent spread of ±10 to 15 degrees; an observation later verified by probing. Most, but not all, of the beam was striking the collector. During this period, the beam was also observed as it was vectored upward and downward (across the plane of symmetry of the vector electrodes) with the maximum available voltage differential.

The control philosophy used for the run was to keep the thrust and specific impulse above an acceptable level. Thus, the feed pressure and mass flow were increased during the latter part of the run, to keep the thrust above 20 μlb. There was a temporary increase in extractor current; however, it soon fell back to normal.

The total clock time recorded was 1036.9 hours. The first 20 hours were devoted to preliminary breaking in and time-of-flight analyses to establish the desired steady-state performance levels. For the remainder of the test, the specific impulse was always above 1230 seconds, and the thrust was always above 20 μlb except for one point where it dipped to 19.5 μlb.

The source was vectored for the third time during the run at 650 hours. The beam was vectored in three directions: up, down, and to one side. Probe measurements were taken for all three vectored states, as well as the unvectored one. During this series, one of the vectoring electrodes experienced a serious breakdown. The voltage on this electrode was raised, and it recovered sufficiently to finish the probe scan, but the vectoring experiment was then terminated. The breakdown changed the physical characteristics of the source in some way so that the meniscus began to bubble at that time. It continued to
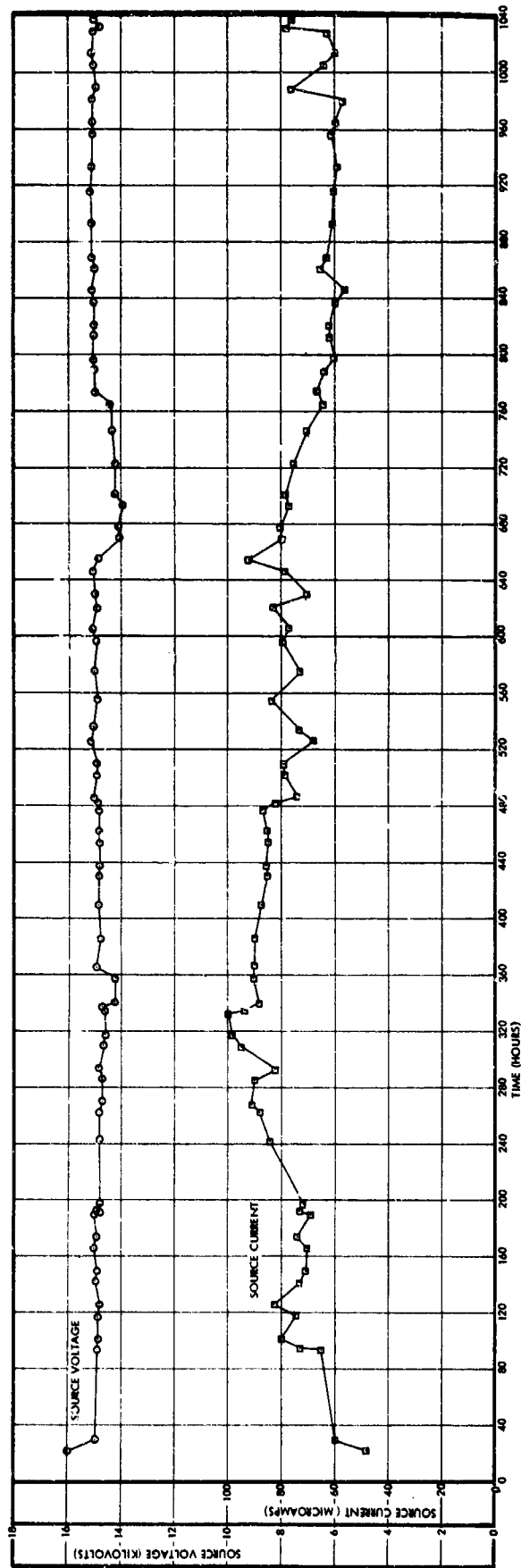
Figure 69. Run 710104: Source Voltage and Current Versus Time for Life Test of Source 7BM2
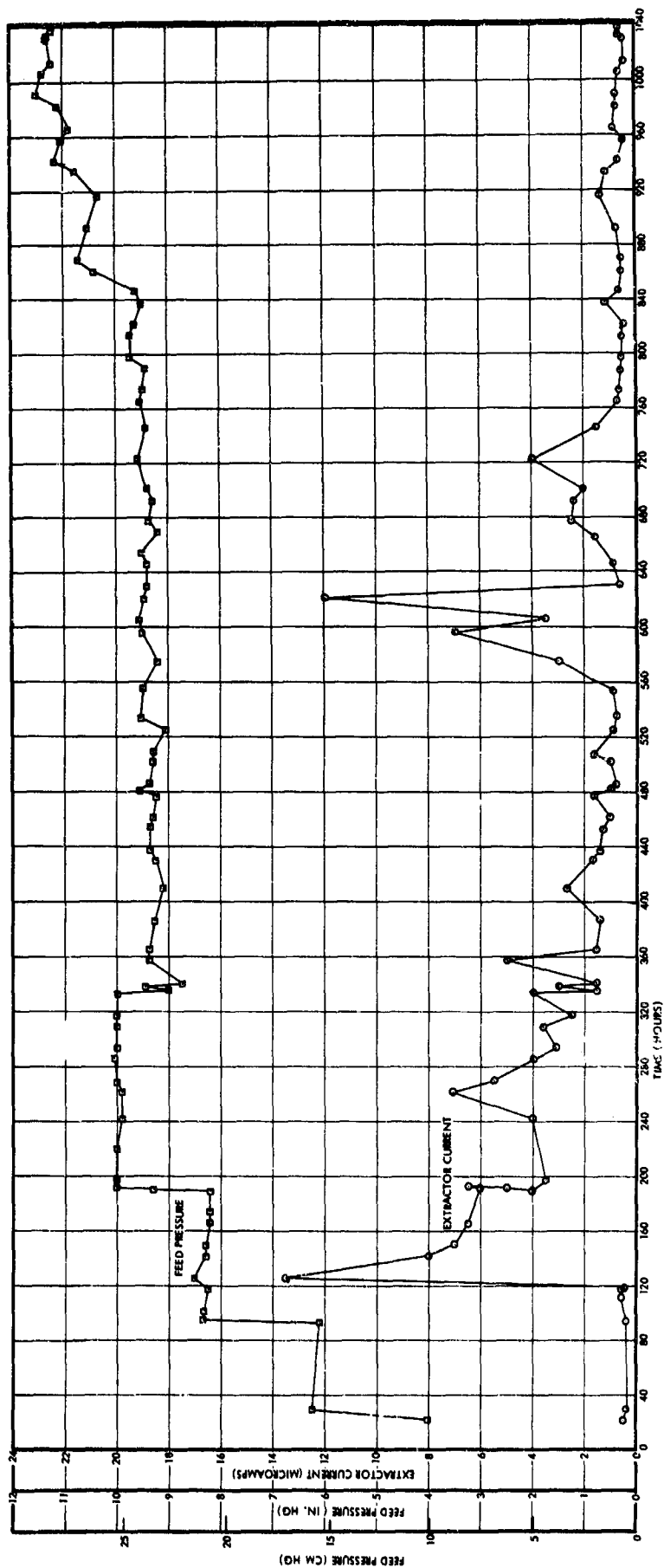
Figure 70. Run 710104: Feed Pressure and Extractor Drain Current Versus Time For Life Test of Source 7BM2. Curves connecting data points represent trend only. Discontinuities in feed pressure are clearly shown.

83
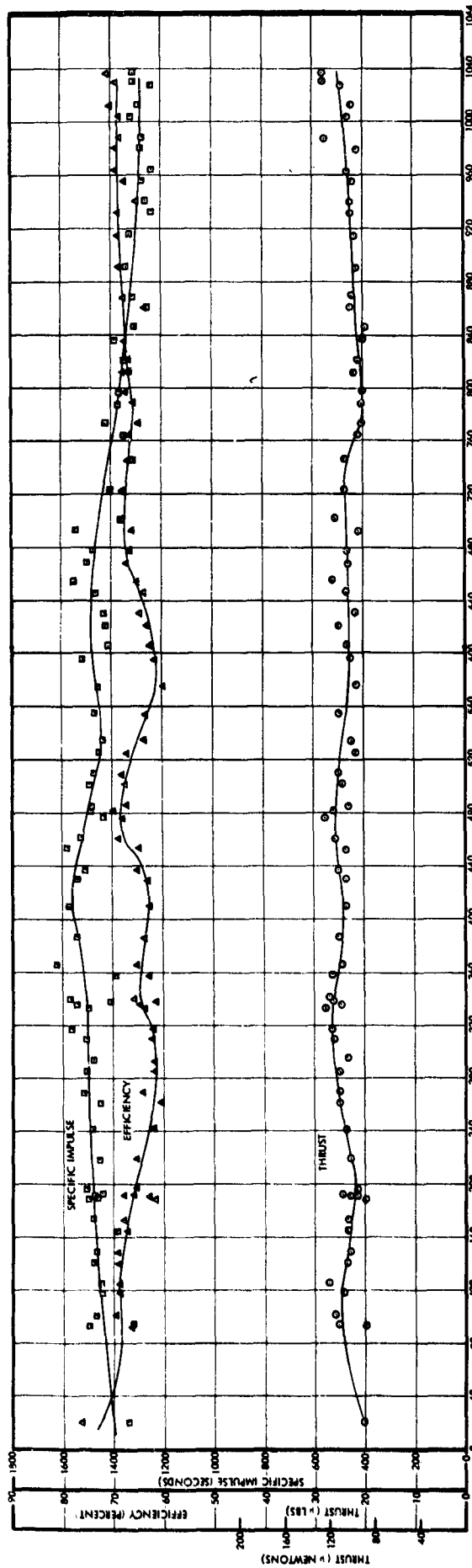
Figure 71. Run 710104: Time-of-Flight (Uncorrected) Specific Impulse, Thrust Efficiency and Thrust Versus Time for Life Test of Source 7BM2. Curves represent trend only. Discontinuities are not shown.

84
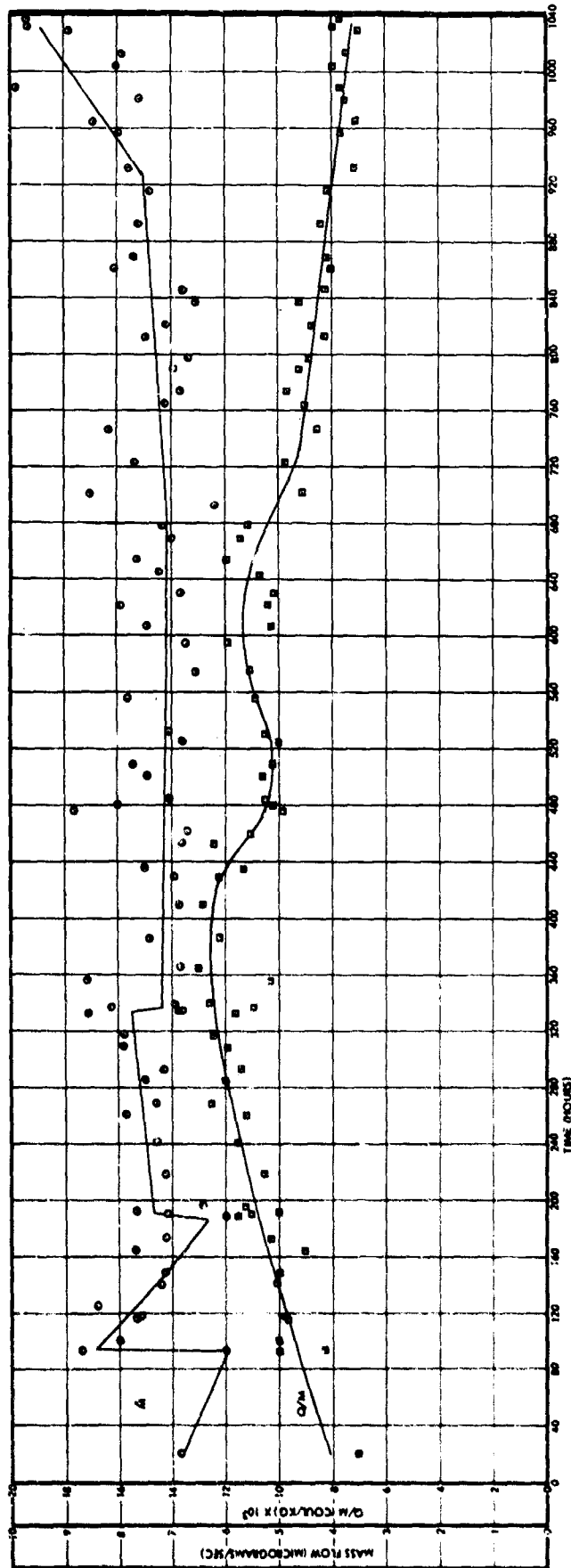
Figure 72. Run 710104: Time-of-Flight (Uncorrected) Mass Flow Rate and Average Charge to Mass Ratio Versus Time for Life Test of Source 7BM2. The discontinuties in mass flow rate, due to feed pressure changes, are indicated.

85

bubble throughout the remainder of the test at a rate of about 10 bubbles per minute. Shortly after this, at about 680 hours, there was a gradual degradation in average q/m. There is a good possibility that these two events are interrelated.

At 940 hours, visual observations were again made of the beam glow. The appearance of the beam and the beam spread had not changed appreciably since the previous observation at 360 hours. The beam was uniform, and the visual half angle was 10 to 15 degrees. Current glow illuminated most of the far shroud, but none of the front half of the tank. The visible portion of the collector illumination was uniform.

Figure 73 is a face-on photograph of the module, still mounted, immediately after the test. The light area on the extractor, around the extractor hole, was covered with a thin film residue of exhaust products. The darker area outside is actually polished metal which had been kept clean by bombardment by secondary positive particles returning from the vacuum chamber. The second lighter ring, on the outside, is similar to the first. The first inner light area is evidence that no significant positive secondary bombardment occurred in the immediate vicinity of the extractor aperture.

The source rim was physically unaltered except for the presence of 1/2 to 1/4 mil sediment patches over about one third of the rim. One 0.004-inch speck formed at the time of the vectoring accident at 650 hours
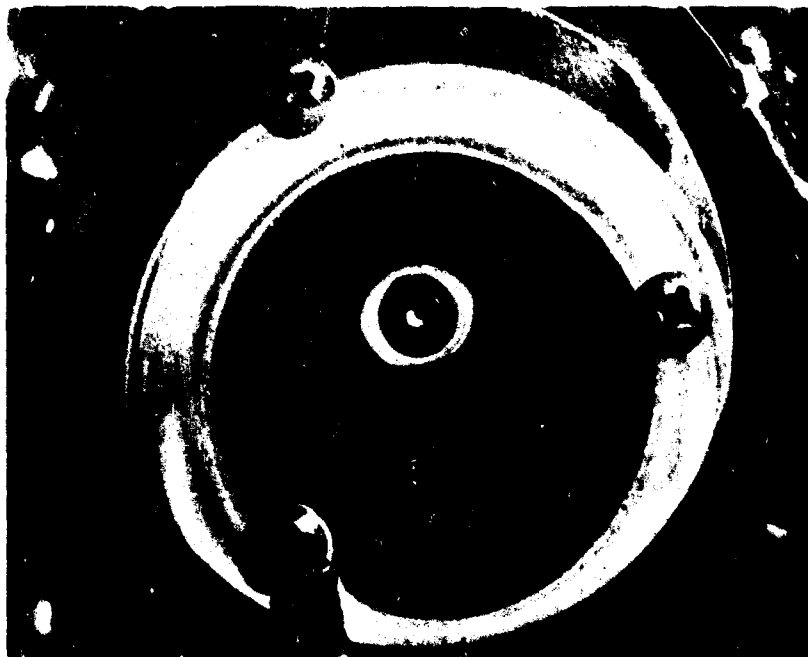
Figure 73. Run 710104: Front View of Module, as Mounted, Immediately After Tank Was Opened. The source and vector electrodes can be seen within the extractor aperture.

was probably the only performance-degrading formation present. In general, it has been observed that such build-ups are caused by external accidents rather than fundamental thruster operational properties.

2.5.6 Run 710402: Source 6BM3, 433 Hours

This was the first major test in which the source was incorporated into the final module design. Design details are given in Section 2.1. The module was fully temperature controlled. The test was conducted in the 4 by 8 foot facility with the 24-inch diffusion pump port. A LN_2 cryowall was added to improve the vacuum, and the nominal operating vacuum was $9-10 \times 10^{-7}$ torr.

A series of thrust vectored beam profiles was also obtained, and is discussed in Section 2.3 Time-of-flight beam profiles were made as discussed in Section 7.2. Neutralization of the beam is discussed in Section 5.

This run was intended to be a 1000-hour life test during which direct mass flow measurements would be made in addition to neutralization, thrust vectoring and beam profile measurements. The run ended after 432.8 hours immediately after a series of vectoring experiments was completed. A deflector drain current developed during the vectoring experiments, and while this was probably a contributory factor, the main cause of the failure is believed to be gas in the propellant caused by problems associated with the direct mass flow measurements (see discussion in Sections 6.4 and 7.3). Surface instabilities had been observed throughout the experiment and the final failure was caused by a sudden surge in needle current and a simultaneous breakdown to one of the vector electrodes. Even after the feed pressure was removed, there was still a temporary persistance of propellant flow from the source. The most probable cause of this unusual behavior was the nucleation of bubbles within the feed line.

Similar problems had been observed on a previous run, after which several leaks in the feed line were located and repaired. This time a post-run check of the feed line ahead showed no leaks. Subsequently, it was realized that the experimental set-up was responsible for continuous electrolytic gas generation within the propellant.

Performance was characterized by a nominal thrust of 21 μlb, a thrust efficiency of 65 percent, an average charge-to-mass ratio of 10,000 to 14,000 coul/kg and a specific impulse which varied between 1300 and 1800 seconds. These data are all based on uncorrected time-of-flight obtained with ±150 volts screen and suppressor biases and a time-of-flight distance of 1.87 meters. The time-of-flight honeycomb collector was 4 feet in diameter.

Figures 74 and 75 show the time history of the source voltage, current, and feed pressure. The source voltage was held at 15 kv throughout the first part of the run, and increased slowly to 15.4 kv during the last part of the run.
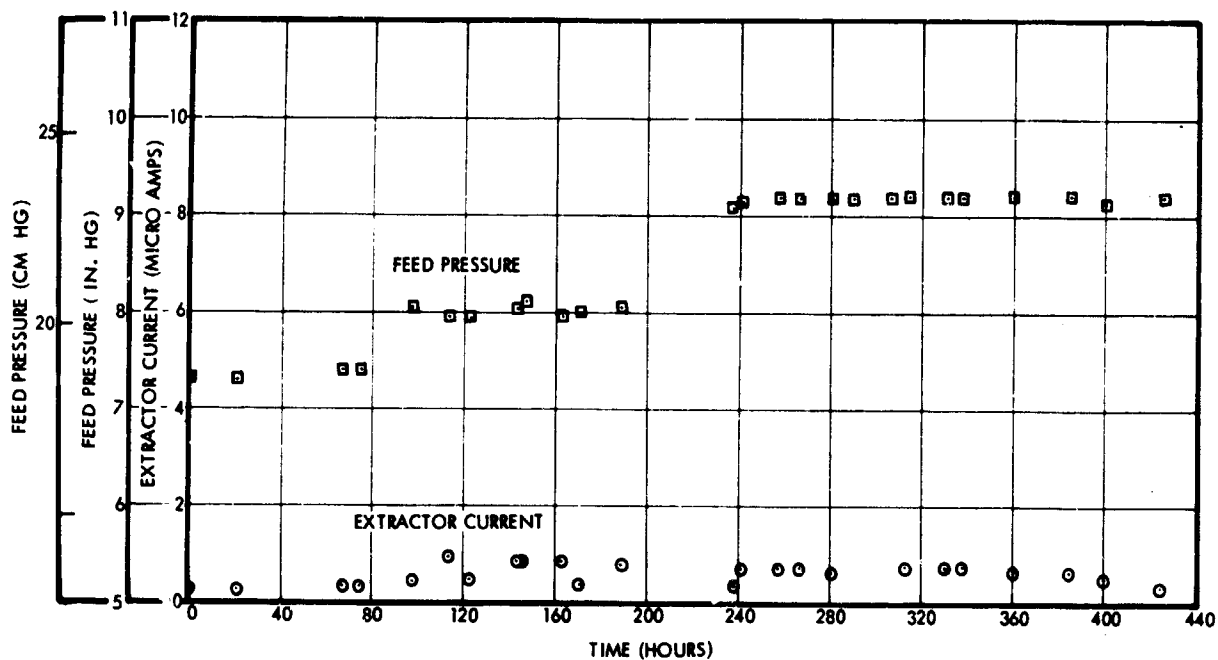
Figure 74. Run 710402: Feed Pressure and Extractor Current as Functions of Time
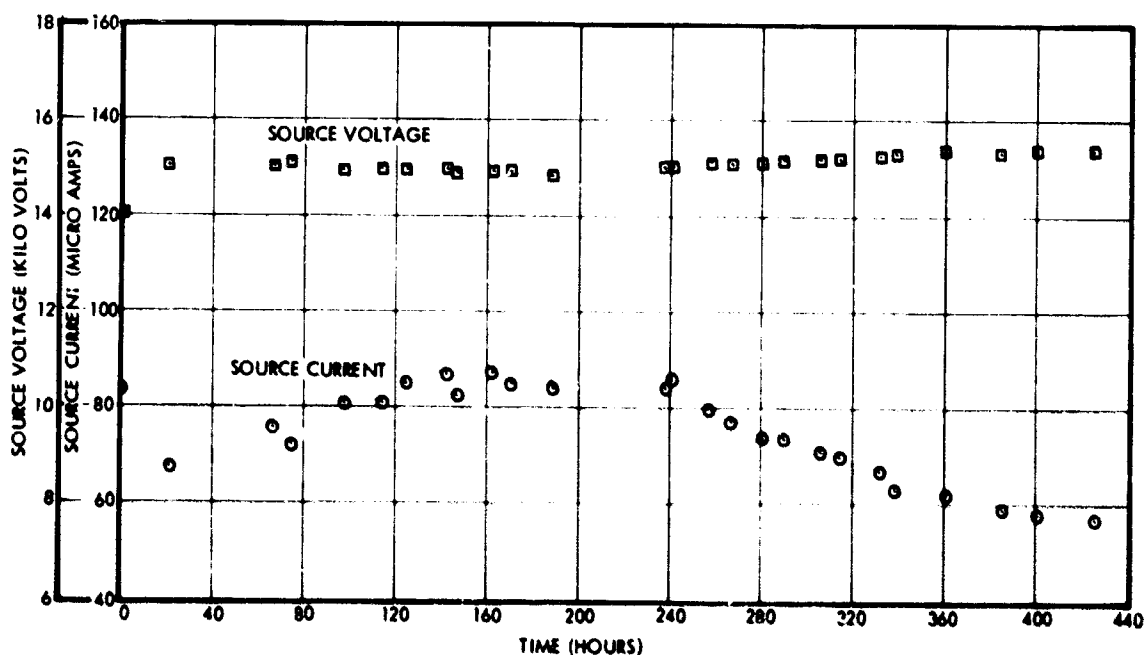
Figure 75. Run 710402: Voltage and Current as Functions of Time

88

Figures 76 and 77 show the performance time history in terms of thrust, specific impulse, thrust efficiency and average charge to mass ratio. Average charge-to-mass ratio was about 14,000 coul/kilogram for the first 240 hours, later dropping to 10,000 coul/kilogram. There was a coincident increase in gas generation during the latter part of the run which was probably related to this decrease. A small amount of gas generation was also observed during the first part of the run.

The extractor current, also shown in Figure 74, was less than 1 μamp until 425 hours when vector electrode drains developed. Vector electrode currents were zero except when the source was being vectored. At these times, drains were less than 5 microamps, until 425 hours.

At 425 hours, the source was vectored, and the first vector electrode developed a 15-microamp drain which grew worse until the test terminated. Coincident with the development of this drain, the outgassing of the propellant meniscus increased drastically.

2.5.7 Run No. 710501: Source 6BM3, 2038 Hours

This was the final life test of the program. As with the previous life test, it was conducted with the final source design, 6BM3, and the final module design. The module was fully temperature controlled. Two neutralizers were provided, one was an electron gun type whose activated cathode was poisoned early in the test; the other was a bare tungsten filament, that operated successfully during the entire test. The neutralization results are discussed more fully in Section 5.

The test was conducted in the 4 by 8 foot vacuum facility with the 24-inch diffusion pump port. A liquid nitrogen cryowall was run, and the nominal operating vacuum was 7×10^{-7} torr. Time-of-flight results were obtained with the automated data acquisition system. A 4-foot-diameter honeycomb time-of-flight collector was used, with a screen and suppressor grid. The collector, together with front and rear walls and front baffle, formed an enclosure which collected the entire beam whether neutralized or not. This enclosure could be electrically floated during neutralization. Currents to each of the collecting surfaces were monitored.

Feed pressure regulation was accomplished with a Cartesian Driver regulator system. The pressurizing gas was from a pressure-regulated dry nitrogen source. Regulation was maintained with a gas flow pressure drop through a small regulated orifice. Regulation was very steady, requiring no adjustment over periods of up to 2 weeks.

Time of-flight probes were included in the experimental set-up, and time-of-flight beam profiles were made, as discussed in Section 7.2. Thrust vectoring was accomplished, and is discussed in Section 2.3.

89
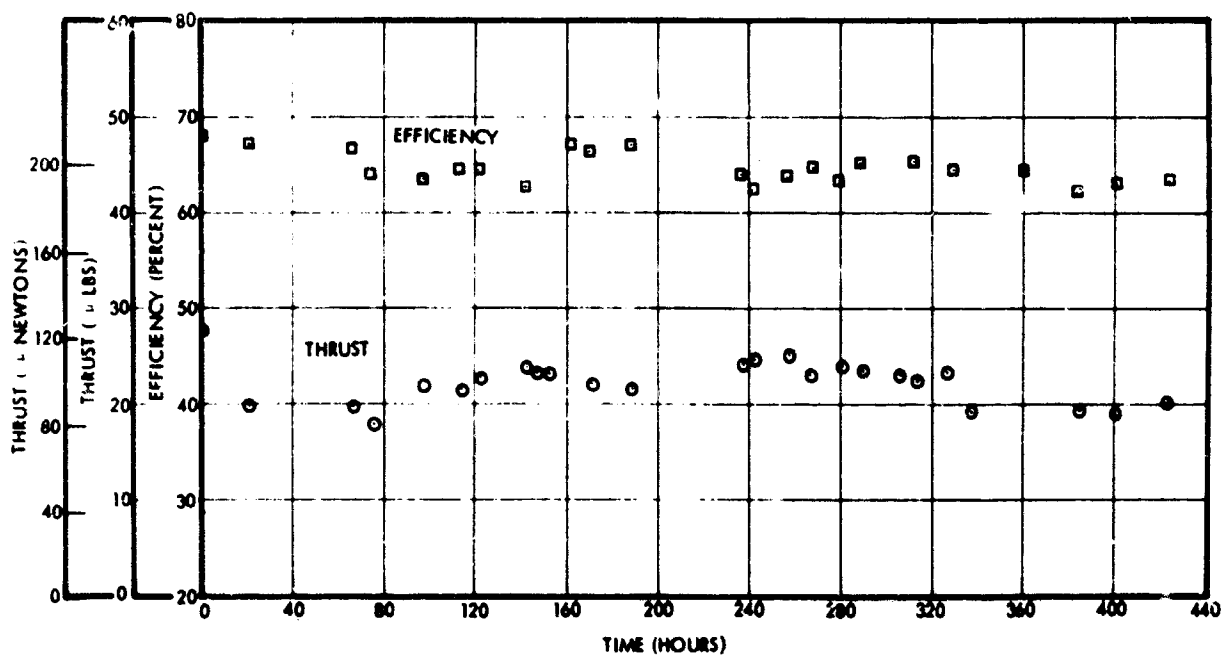
Figure 76. Run 710402: Thrust and Efficiency as Functions of Time
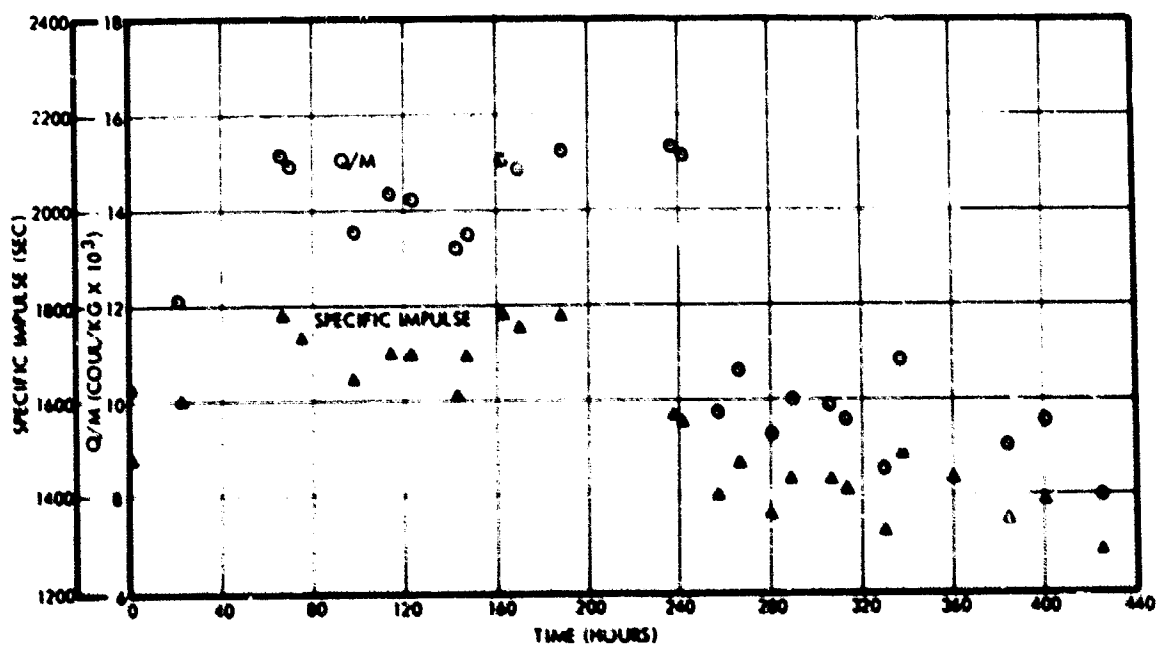
Figure 77. Run 710402: Specific Impulse and Charge-to-Mass Ratio
as Functions of Time

90

The original test goal was 1000 hours. Since operation was still very stable, the goal was later extended to 2000 hours in order to better observe long-term effects. Performance during the first 1000 hours was 20 to 30 μlb at 1600 to 1250 seconds with a thrust efficiency of 65 - 70 percent. Operating voltage was about 14.5 kv on the average, for the major portion of the run. Figures 78 through 81 show a complete time history of the performance of the test.

At 880 hours into the test, the first recorded observation of discoloration in the vicinity of the emitter rim was made. Under maximum magnification of telescopic observation, the rim appeared to be uniformly, very slightly discolored.

Extractor drain current was negligible and deflector electrode drain currents were zero throughout the test except for a few isolated incidents of short duration. The first such incident occurred at 1032 hours during the second vectoring sequence. A deflector current drain developed and gas generation appeared in the propellant meniscus for the first time since the inception of testing. Both problems were cleared up before vectoring was completed.

Except for this incident, the meniscus was completely stable for the entire test up to 1130 hours. At this time, during unattended night operation, a 0.01-inch-diameter reddish brown patch formed inside of the lower rim. About 10 small bubbles per minute were nucleating at this site. These were eliminated by lowering the source voltage to 13.1 kv and the mass flow to 4 μgm/sec. This reduced the thrust to 15 μlb at 65 percent efficiency. Later, around 1400 hours, the mass flow was increased and some of the performance was regained. Eventually, the source voltage was raised back to its original value.

At 1724 hours, a laboratory circuit breaker tripped and shut the test off for 20 minutes. The automatic pump-back for the feed pressurization system was disabled, and the source was flooded. Enough propellant escaped to the outside of the rim to jump across to one of the deflectors when the experiment was restarted. Consequently a high drain current developed between the source and the deflector. Operation became dangerously unstable, and the decision was made to shut down.

The voltages were turned off, and the feed pressure was pumped back to negative head. The propellant did not withdraw from the module, which indicates that no gas bubbles were present inside the module - at least, not in a position where they could expand. Telescopic observation of the meniscus showed that it was stable also. It was decided to wait and see if the propellant contaminant on the deflector would dry up.

The test was left shut off for a period of 115 hours or approximately 5 days. This shut-down time is indicated in Figures 78 through 81. The test was then restarted, and performance reestablished. Before start-up, the propellant in the meniscus was cloudy. After the start, the propellant cleared up very quickly. The red-brown patch of contaminant could still be seen inside the meniscus cavity. The deflector drain redeveloped; however, this emission was occurring from some crystalline residue left on the deflector. After about 12 hours, this residue was burned off, and the current drain disappeared.

91

A

TIME (HOURS)

F

TIME (HOURS)
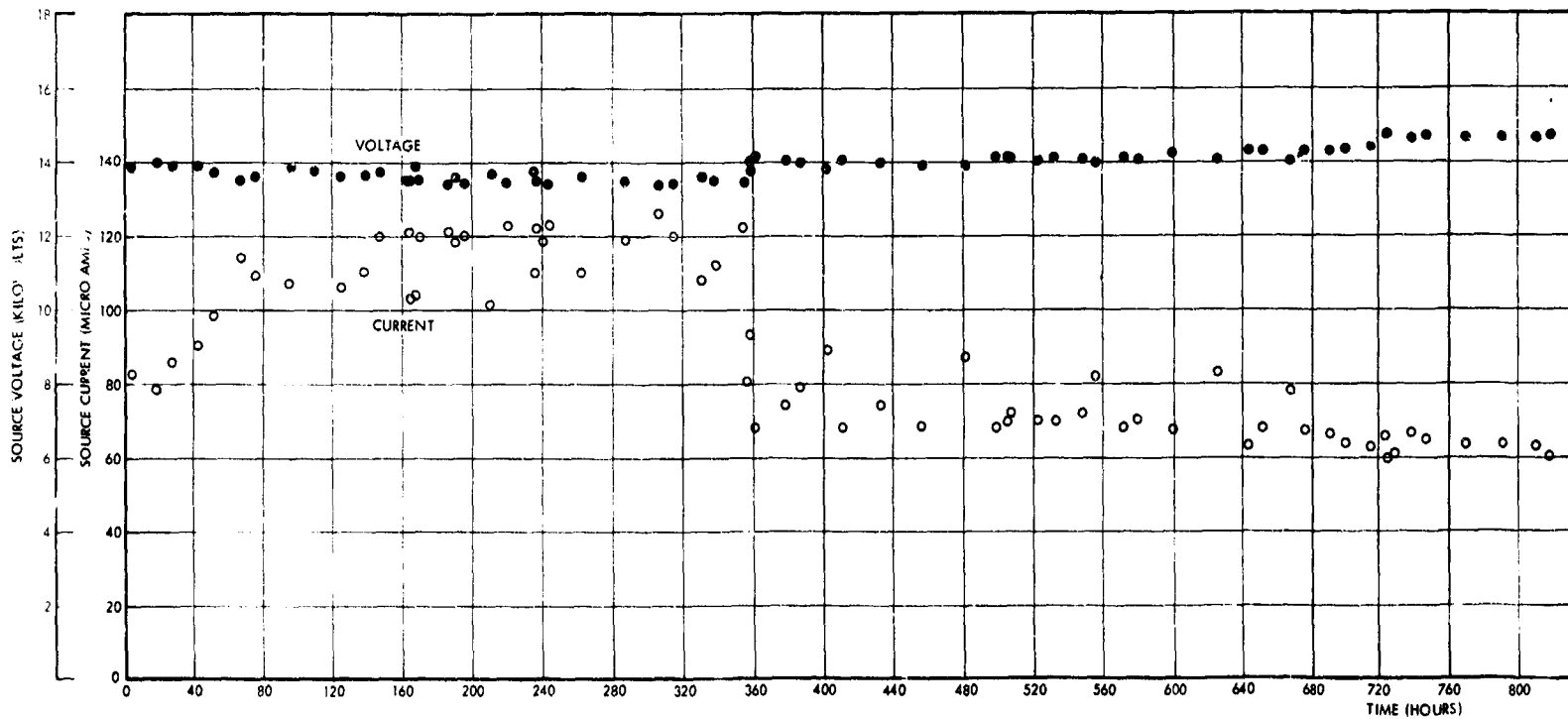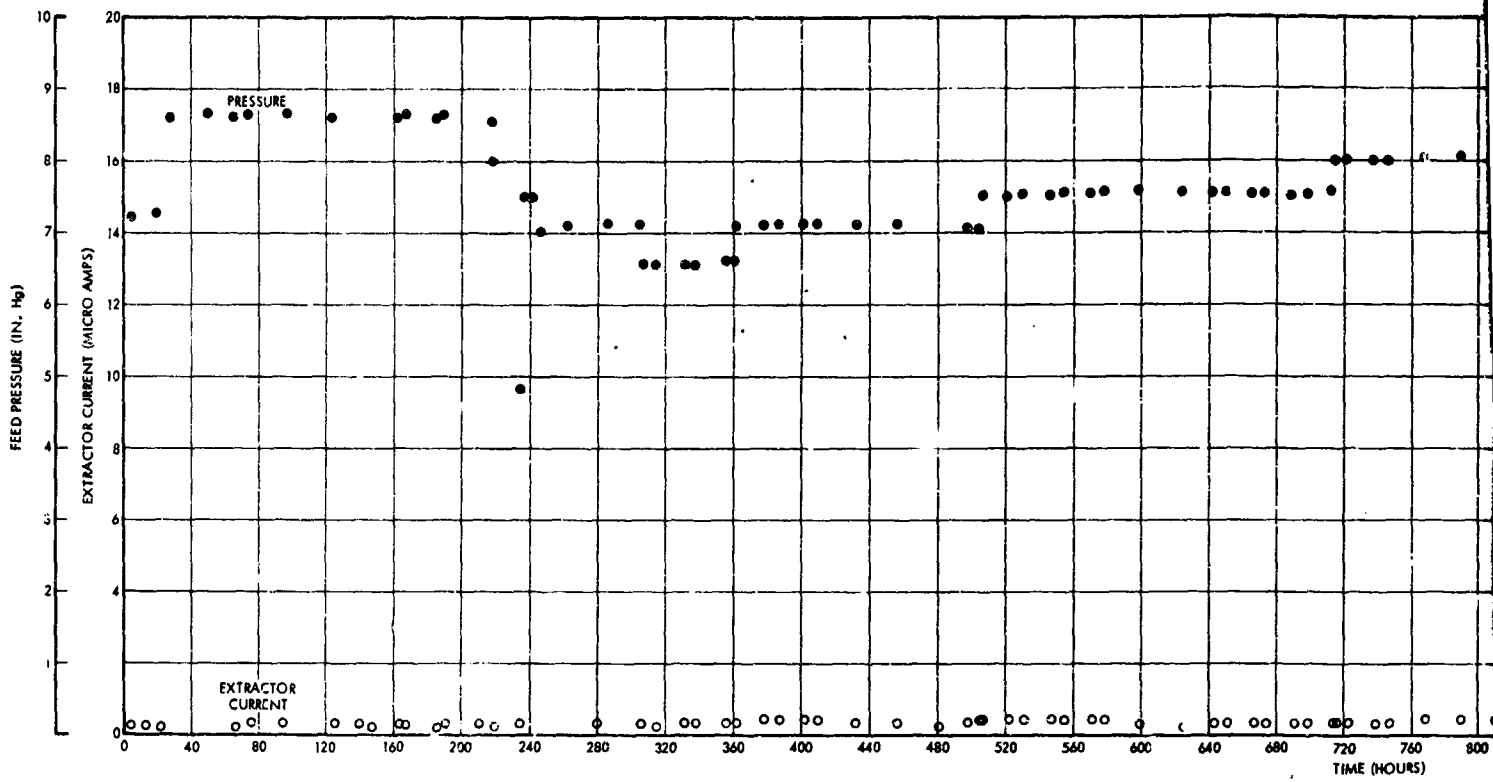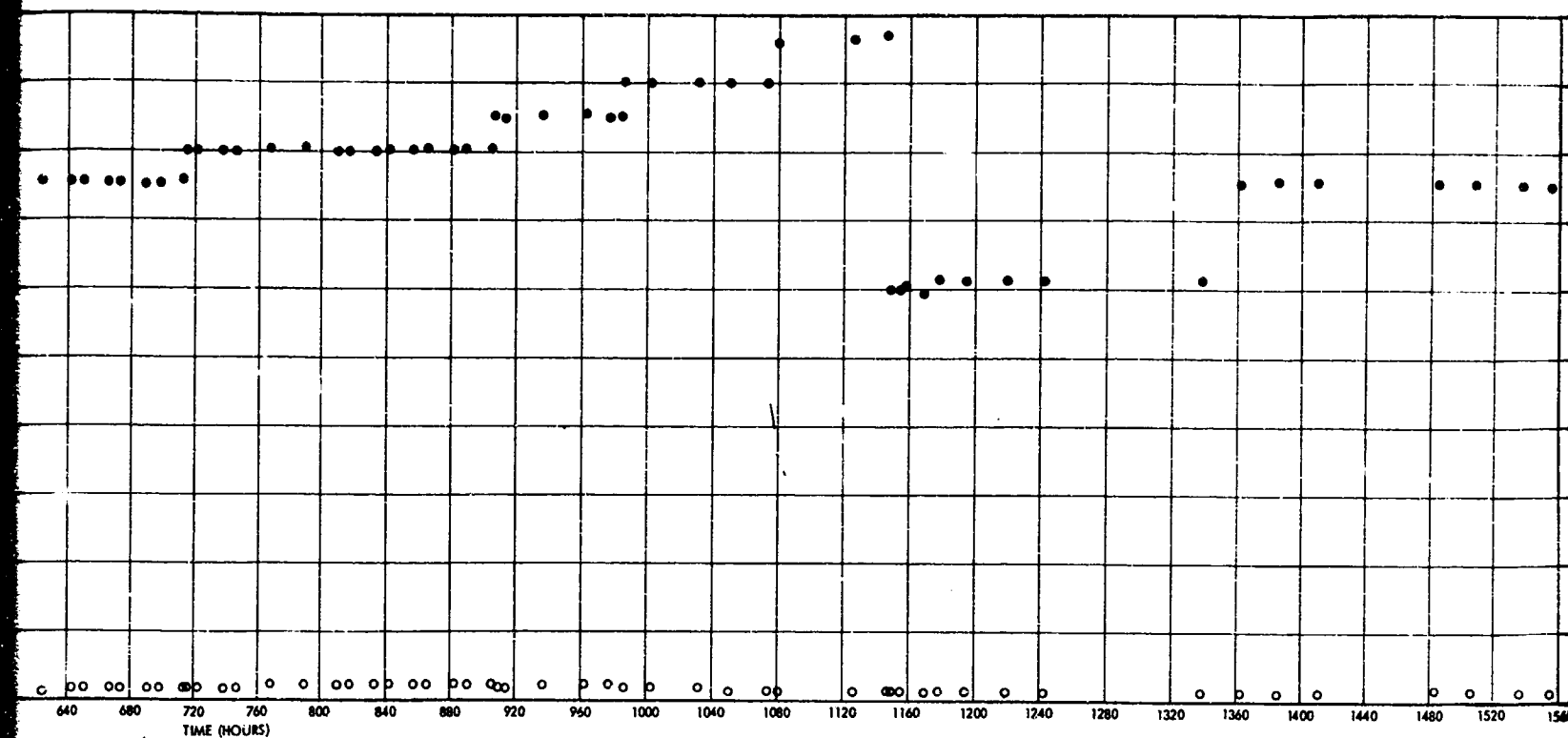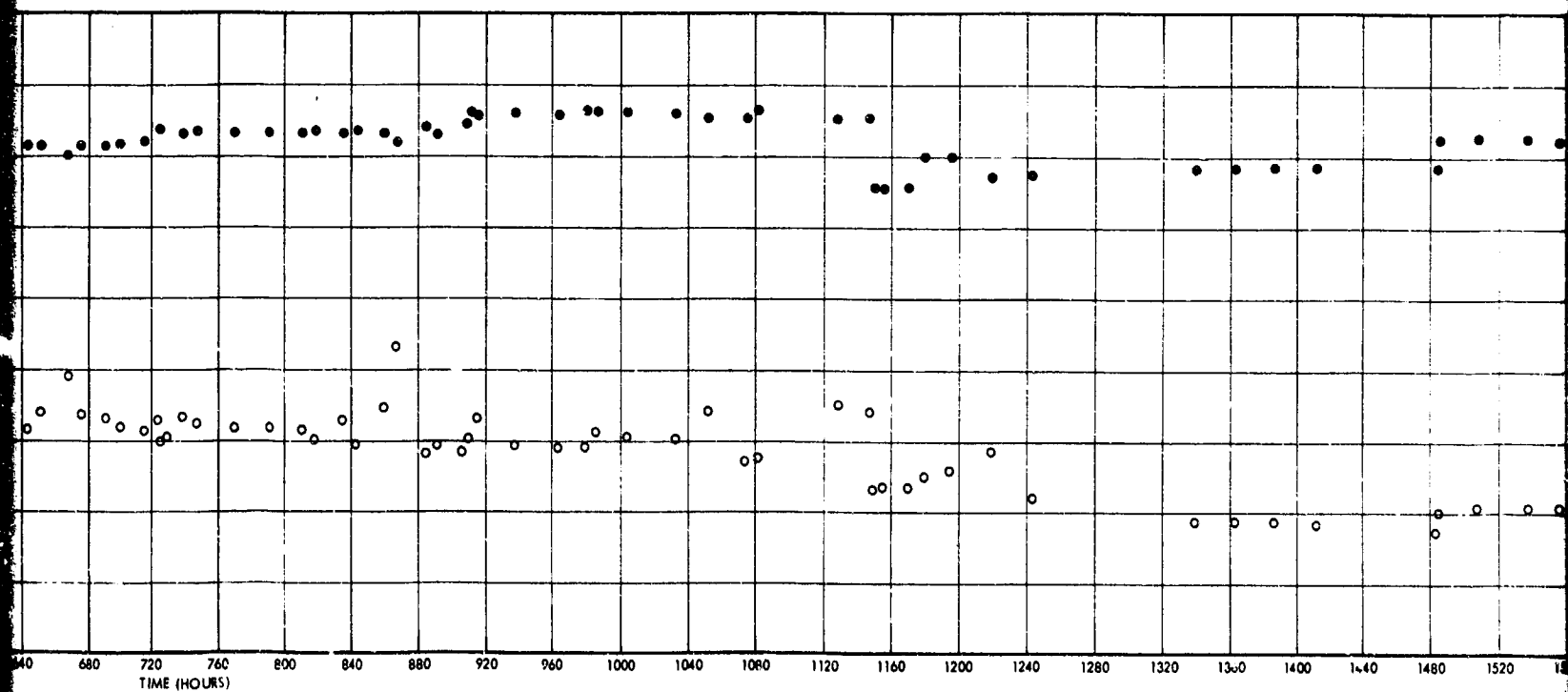
Fi

B
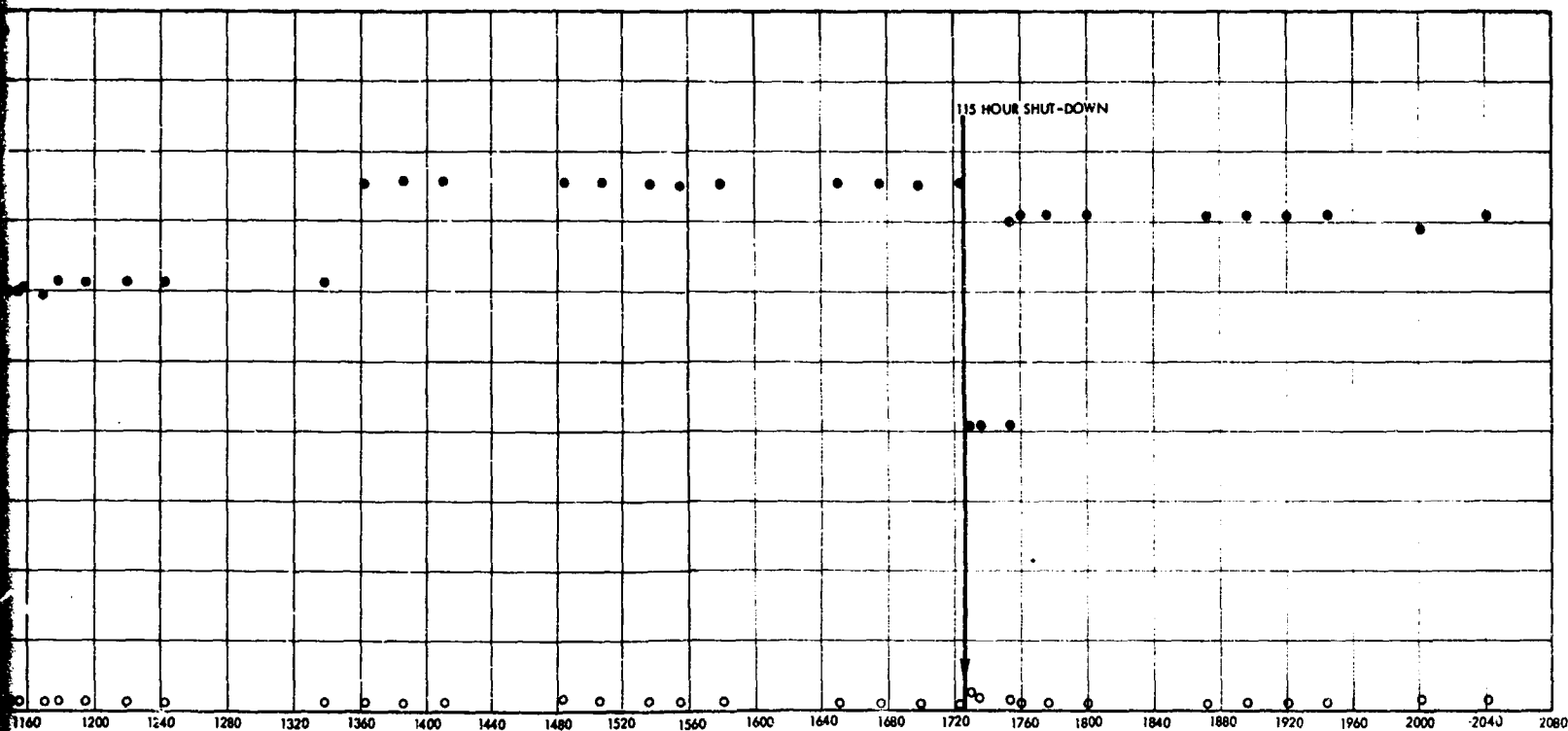
Figure 78. Run 710501: 1000 Hour Life Test - Source
Voltage and Source Current Versus Time
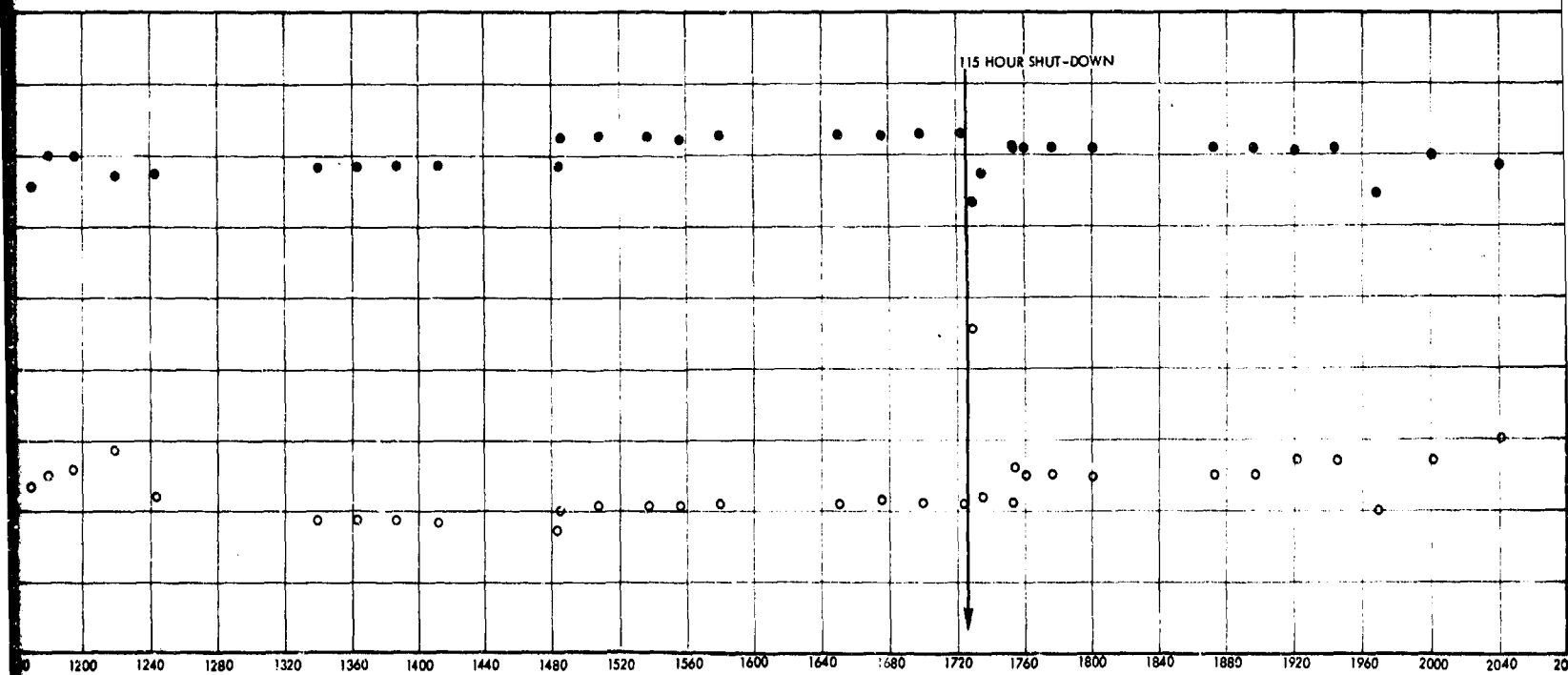
Figure 79. Run 710501, 1000 Hour Life Test - Feed
Pressure and Extractor Current Versus Time

93

A

TIME (HOURS)

B.

15 HOUR SHUT-DOWN
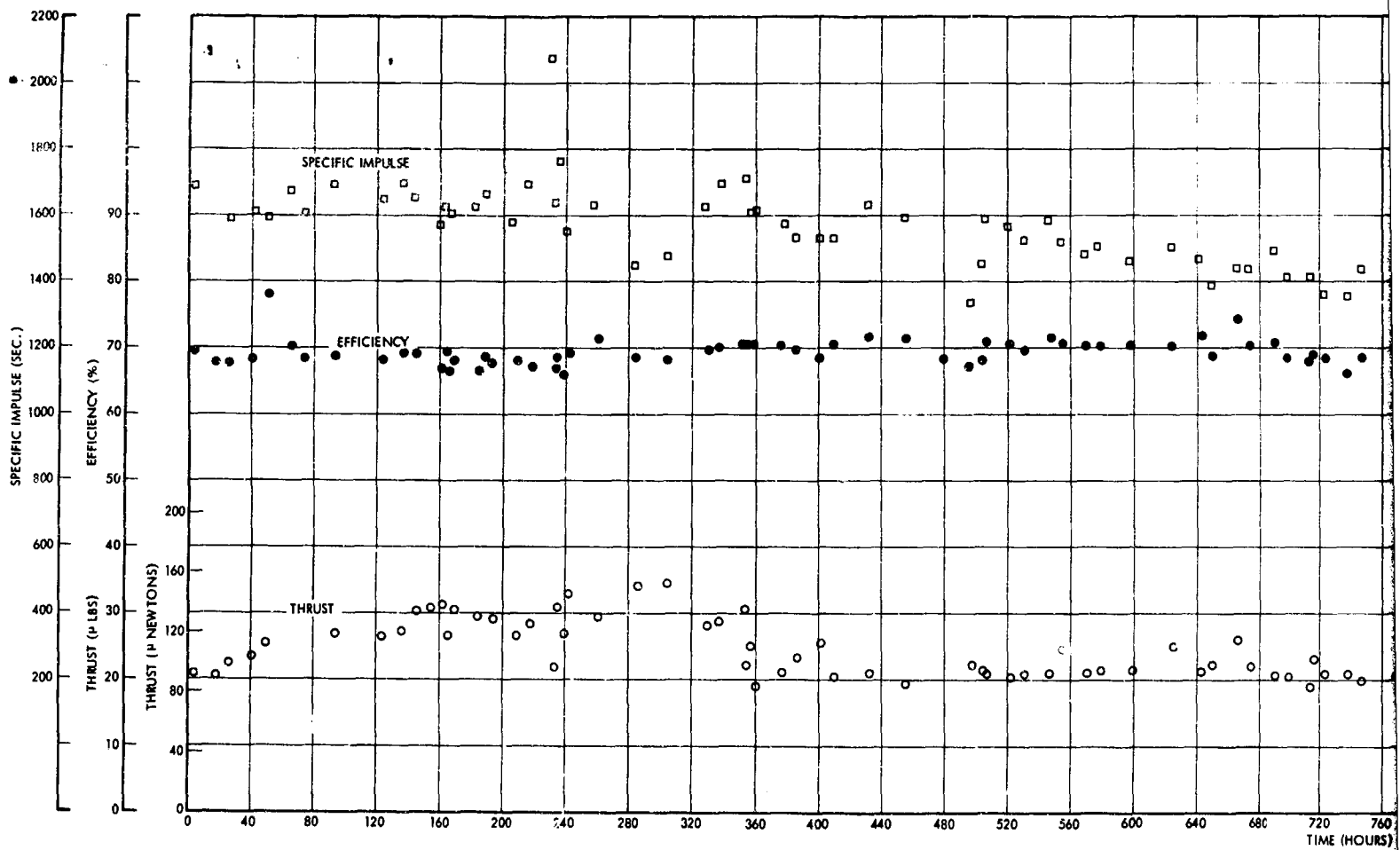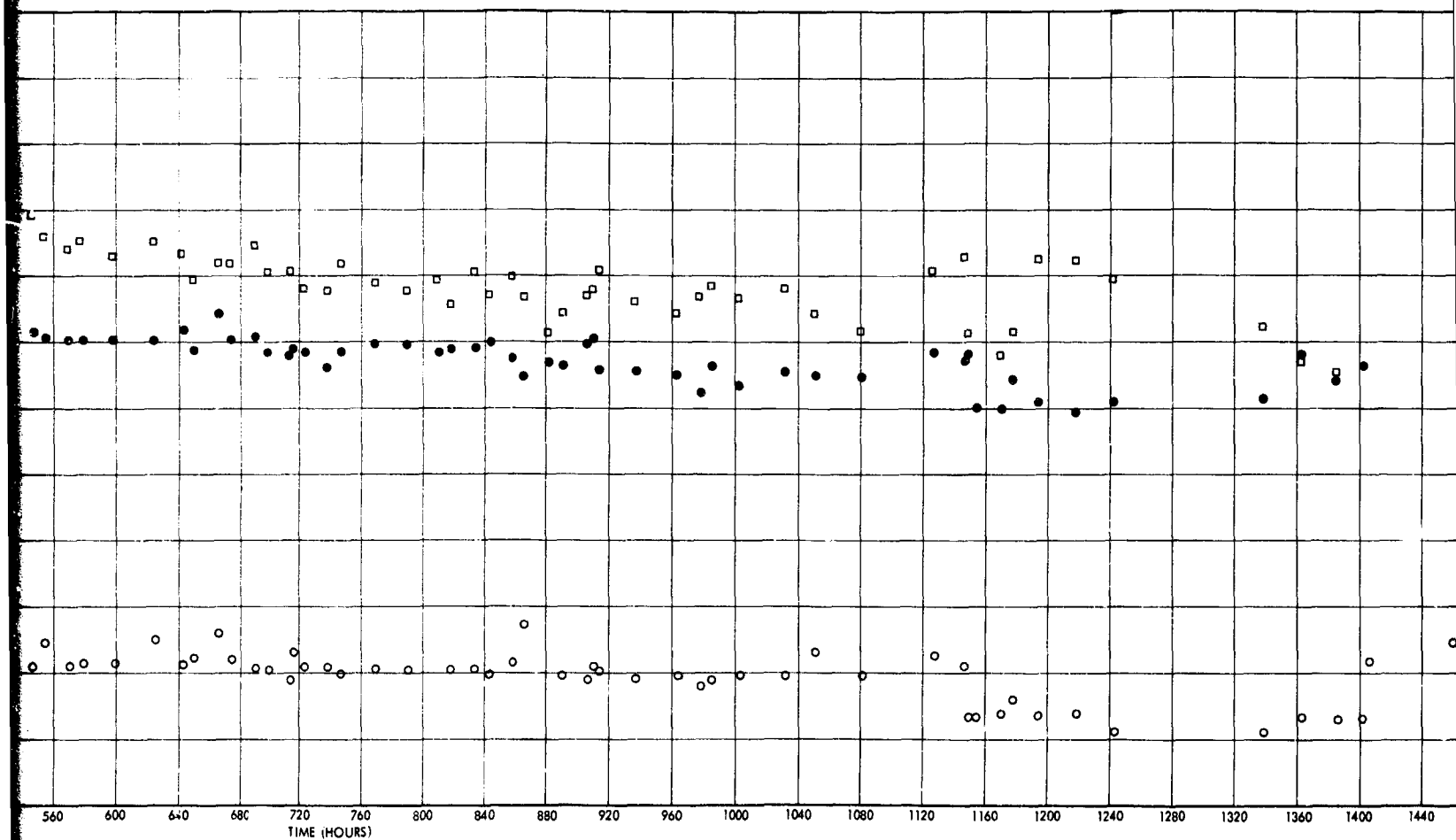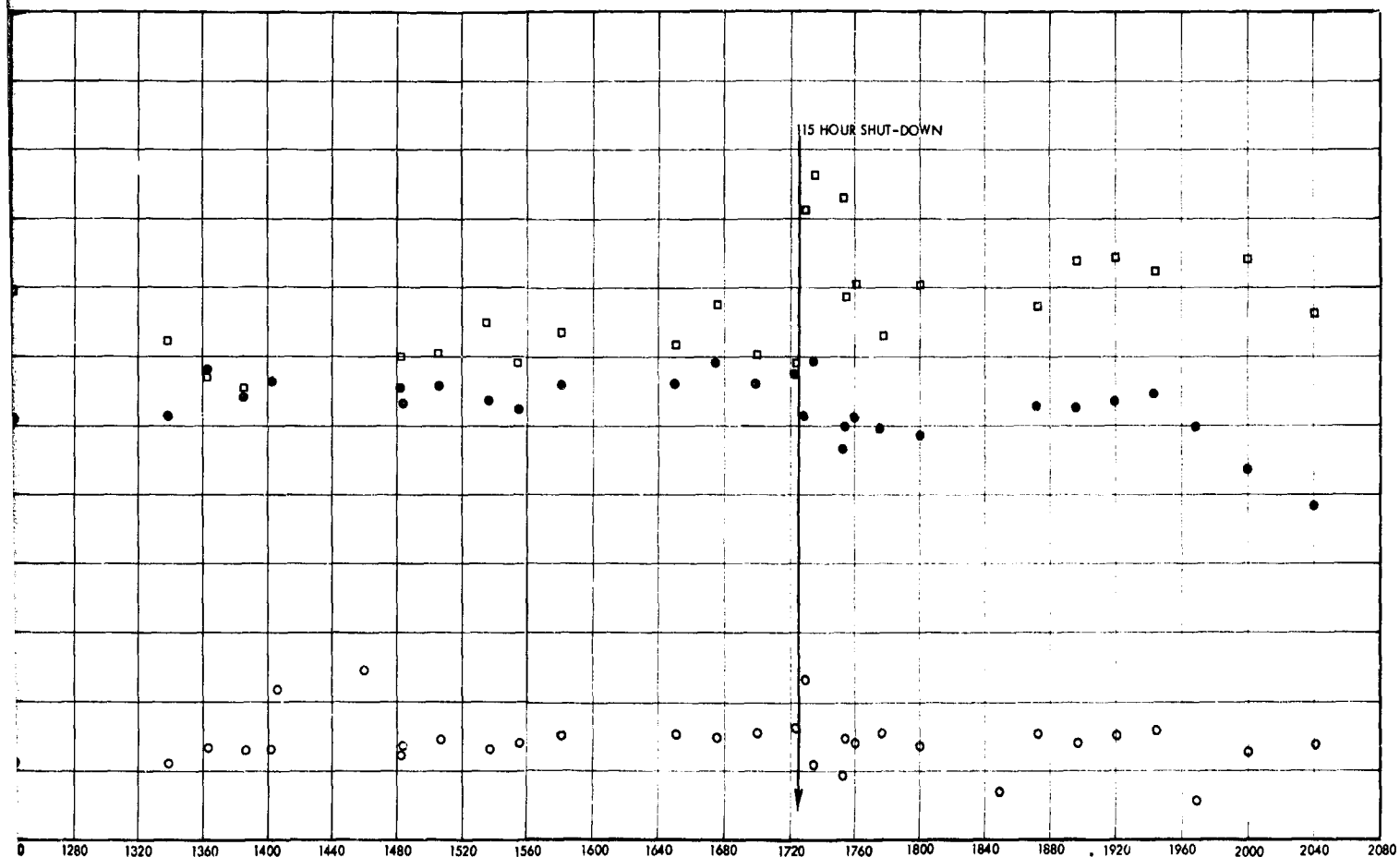
Figure 80. Run 710501: 1000 Hour
Life Test. Specific Impulse,
Efficiency and Thrust Versus
Time

A

TIME (HOURS)

B2
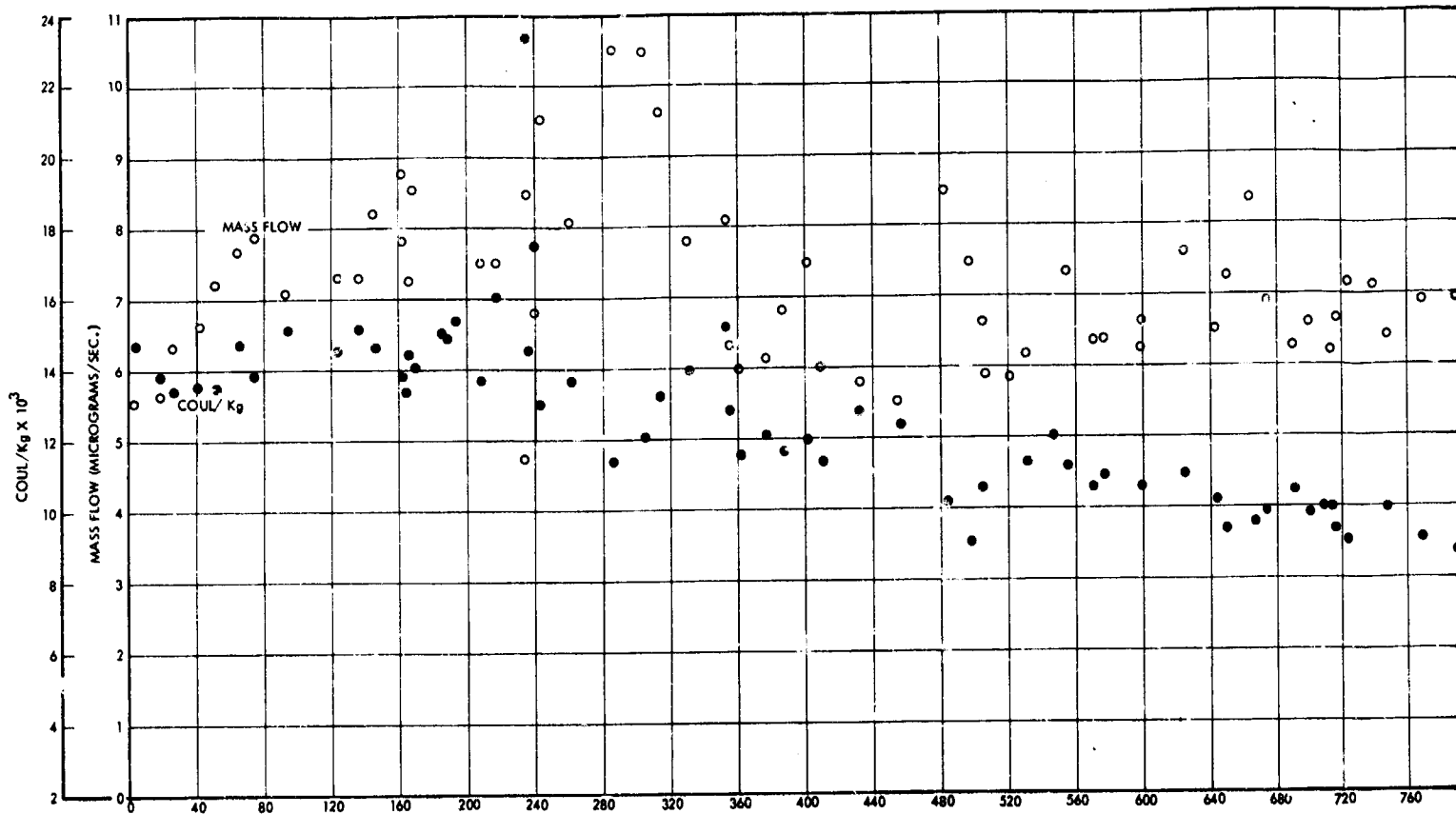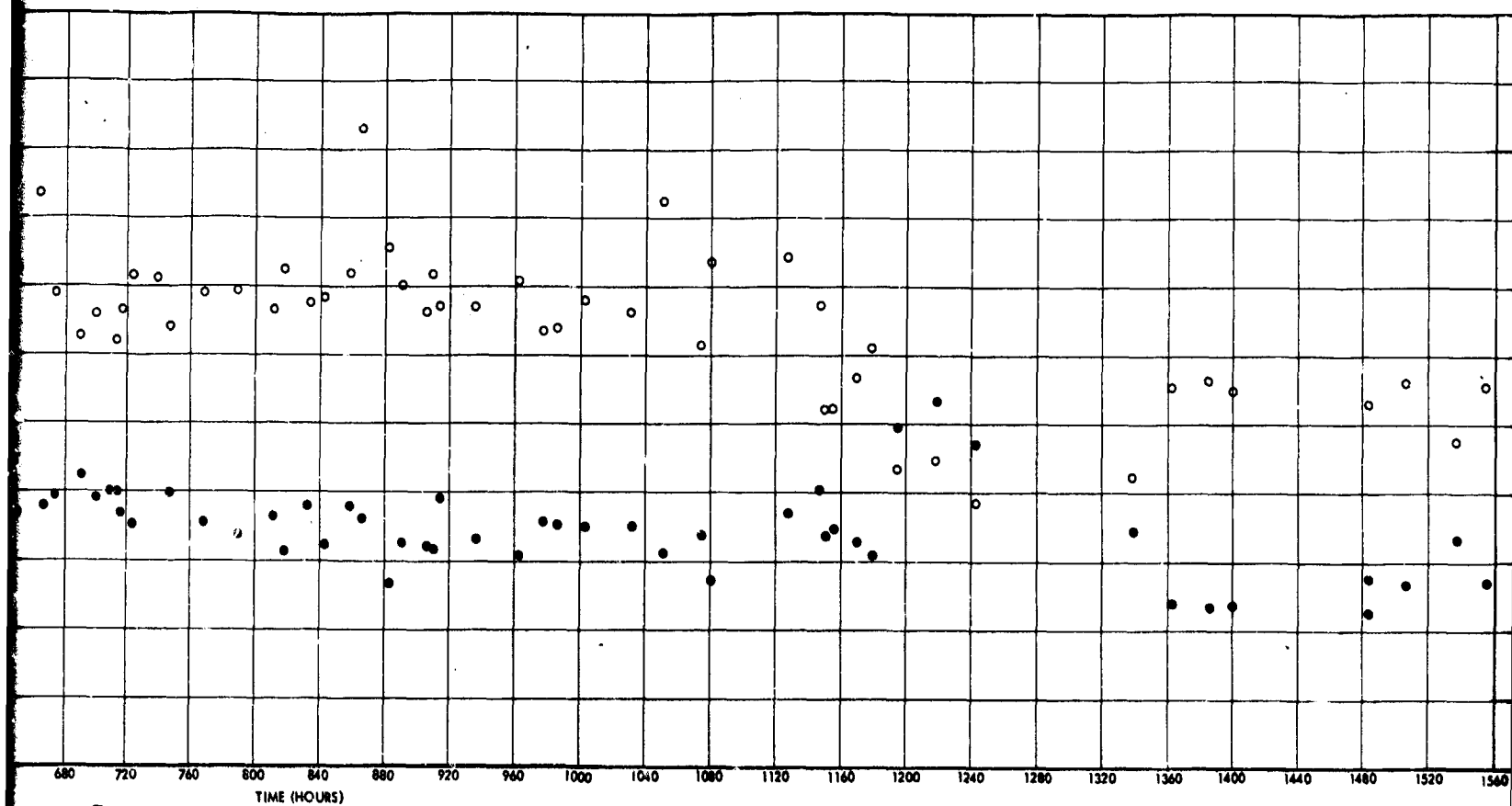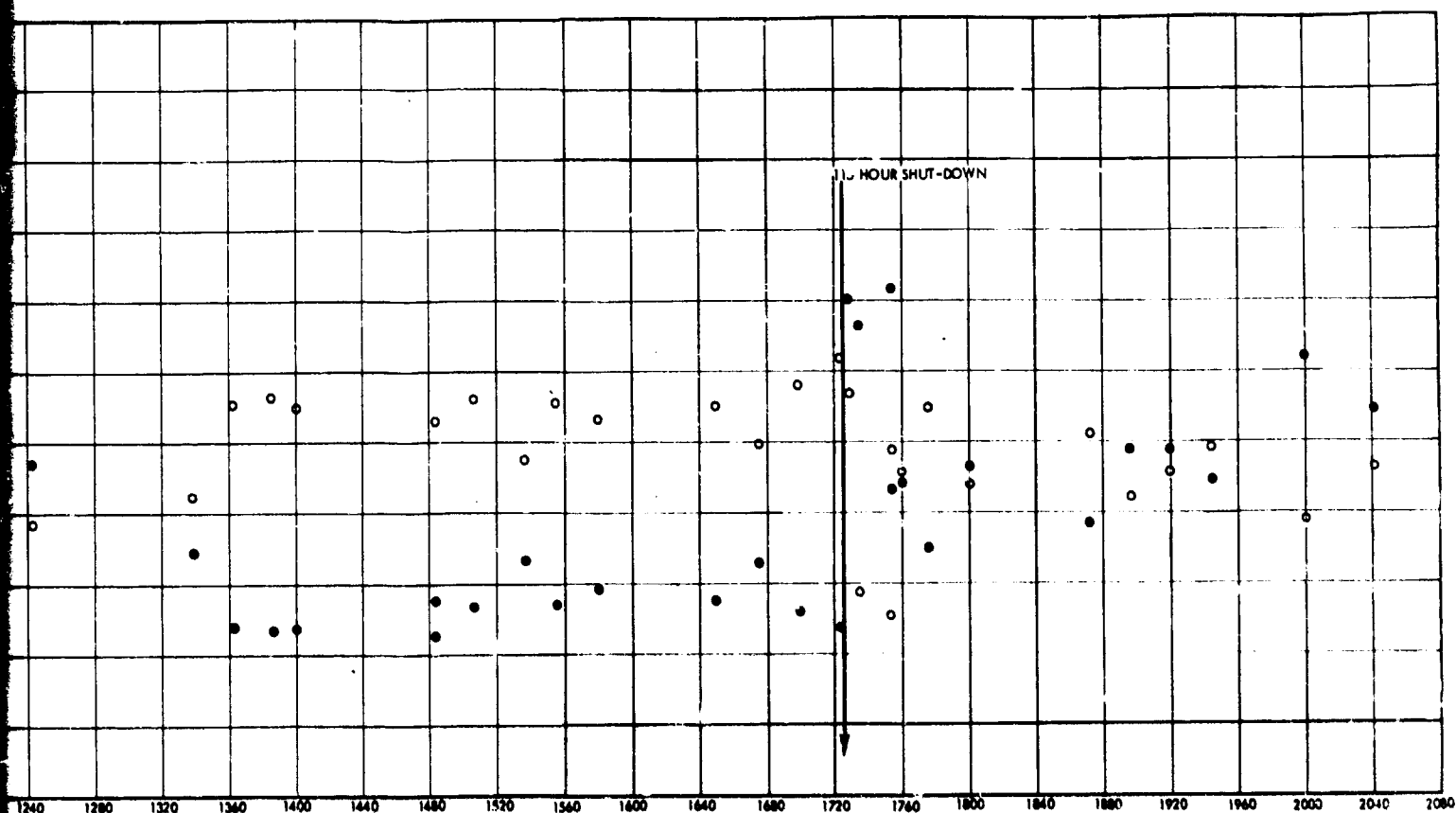
Figure 81. Run 710501: 1000 Hour
Life Test. Average
Coul/Kg x 10^3 and Mass
Flow Versus Time

At about 1955 hours in the test, another facility failure occurred when the test was unattended. The head gate closed on the vacuum system, but the voltages were not shut off. An overcurrent developed as a result of the high pressure build-up in the tank. There were no deflector currents; the drain was from source to extractor.

The test was recovered shortly; however, the gas generating activity had resumed in the meniscus, and this time could not be entirely quenched by lowering the source voltage to 13 kv. The gas generation continued for the remainder of the run.

Post-run examination showed that the resulting rim was uniformly covered with patches of solid contaminant of the order of 0.0005 inch thick. The deflector electrodes were also badly discolored, and had some patchy contamination. Figure 82 is a photo of the module, still mounted in place, immediately after the chamber was opened. The photo shows very clearly the dark area of the extractor where the heaviest bombardment of positive secondaries occurred. The effect was nearly identical to that seen in Run 710104.

2.6 DELIVERABLE ANNULAR THRUSTER

A single source annular emitter module was designed and fabricated as deliverable hardware under the current contract. The module included a thrust vectoring capability, a temperature control capability, and parts of the propellant feed system, including a filter.

The module design is discussed in Section 2.1. Design of the base-plate and filter holder was adapted from earlier design work done for an

Figure 82

Annular Thruster After
Conclusion of 2000-Hour
Life Test, Before Removal
from Facility

99

18-source module. Temperature control is achieved with a potted thermistor in conjunction with a radiant heater and controller. The radiant heater is not part of the deliverable hardware, but the controller and thermistor were supplied, along with calibrations.

A deflector electrode voltage controller assembly of the type discussed in Section 2.3 was also fabricated. It was voltage-tested to 18 kv before delivery. A circuit diagram is presented, and the design and use of this controller are also fully discussed in Section 2.3.

Complete performance testing of the module, without vectoring, was accomplished before delivery. Test results are included with the module.

2.6.1 Deliverable Hardware

The deliverable items are listed below. The module is shown in Figure 12. The YSI temperature controller is shown in Figure 83 and the deflector electrode voltage controller is shown in Figure 84.

- Module assembly, including baseplate, filter holder, source extractor, deflector electrodes, insulators and voltage connections

- An 8-micron pore size polyester propellant filter

- A Monel fitting to couple the module to the end of a glass propellant feed tube

- Two potted Yellow Springs Instrument Company thermistors with Teflon covered leads

- Calibration charts for the YSI thermistors

- A YSI temperature controller

- A deflector electrode voltage controller assembly, with current meters and recorder channel outputs

- Circuit diagram for the deflector electrode voltage controller

- Data sheet and plots of module performance.

2.6.2 Run 710601, Performance Test

The module was performance tested in a 6-inch pump station with a 1.4 meter time-of-flight distance. Prior to installation, the impedance was measured and found to be equivalent to approximately 0.72 inch of 0.004 inch ID hollow tubing (the standard). The rim-to-deflector spacing was set at 0.030 inch.

100

Figure 83.   Yellow Springs
Instrument Tem-
perature Controller
Unit
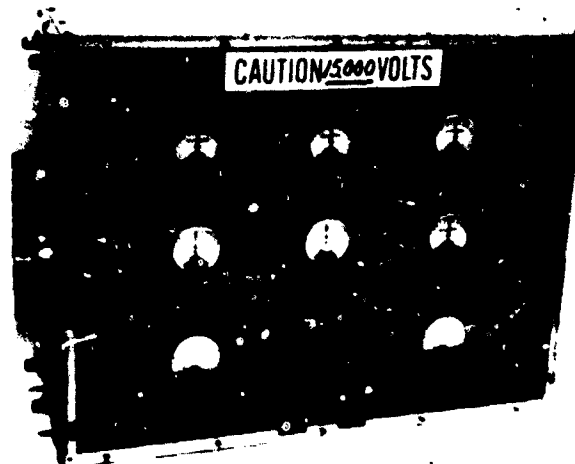
Figure 84.   TRW Annular Source
High Voltage Control
and Monitor Unit

Series of voltages and feed pressures were investigated with time-
of-flight measurements. Source voltage was varied from 13 to 16 kv,
and feed pressure was varied from 5 inches to approximately 11 inches
of mercury. The extractor was held at a potential of -2 kv, and the
deflectors were kept at -7 kv. The ambient pressure was approximately
1.6×10^{-5} torr.

Figures 85 through 89 show the results of the time-of-flight analysis.
All results are uncorrected for beam divergence and energy loss. No
systematic variation of mass flow rate with source voltage was noted for
constant feed pressure.

The source was run for a 48-hour period, with two overnight
periods. During the run, the beam was observed visually and with a
view-probe (grounded copper mesh inserted into the beam - see Sec
tion 2.2) and verified to be uniform and within ±15 degrees divergence
angle. The beam was also briefly vectored, and the action observed
to be normal, although no measurements were taken.
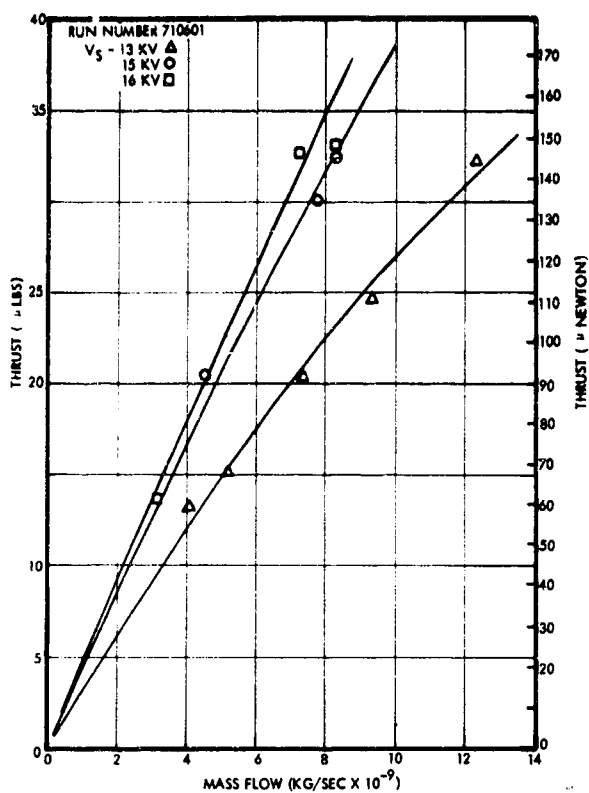
Figure 85

Run 710601 Performance Study —
Thrust Versus Mass Flow
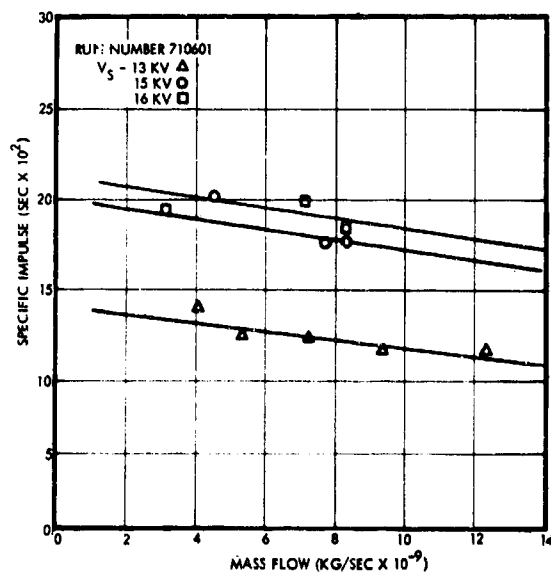
Figure 86. Run 710601
Performance Study —
Specific Impulse Versus
Mass Flow
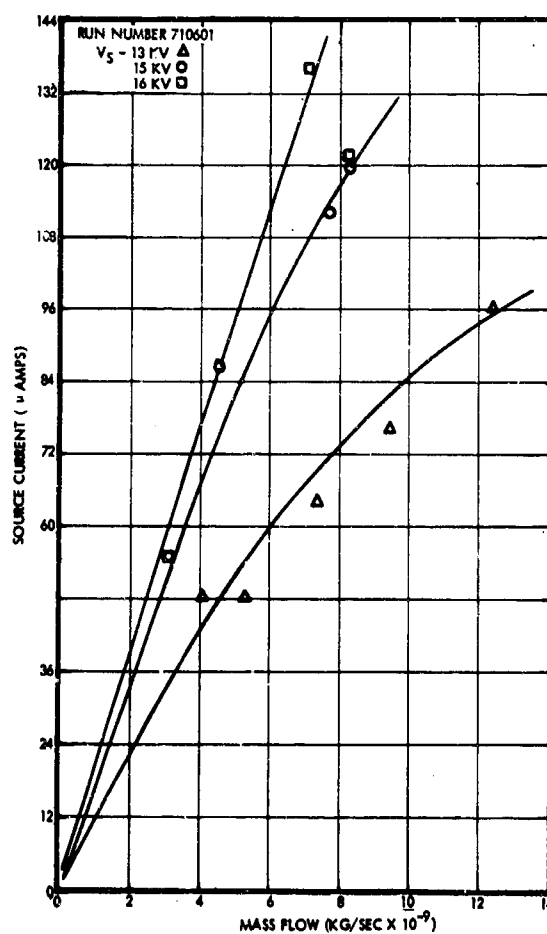
Figure 87. Run 710601
Performance Study —
Source Current Versus
Mass Flow

102
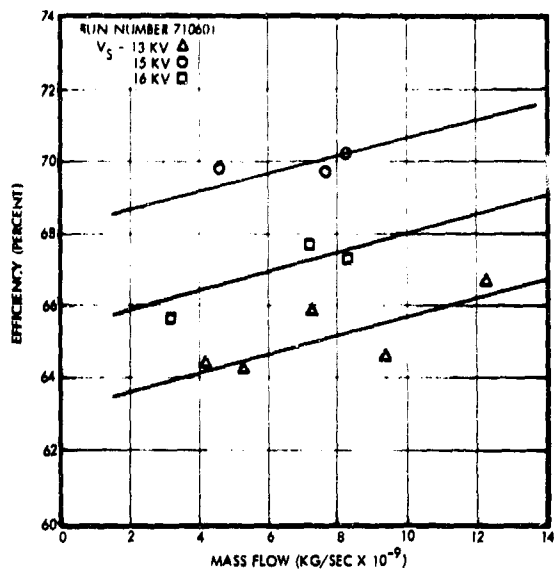
Figure 88

Run 710601 Performance Study —
Source Efficiency Versus
Mass Flow
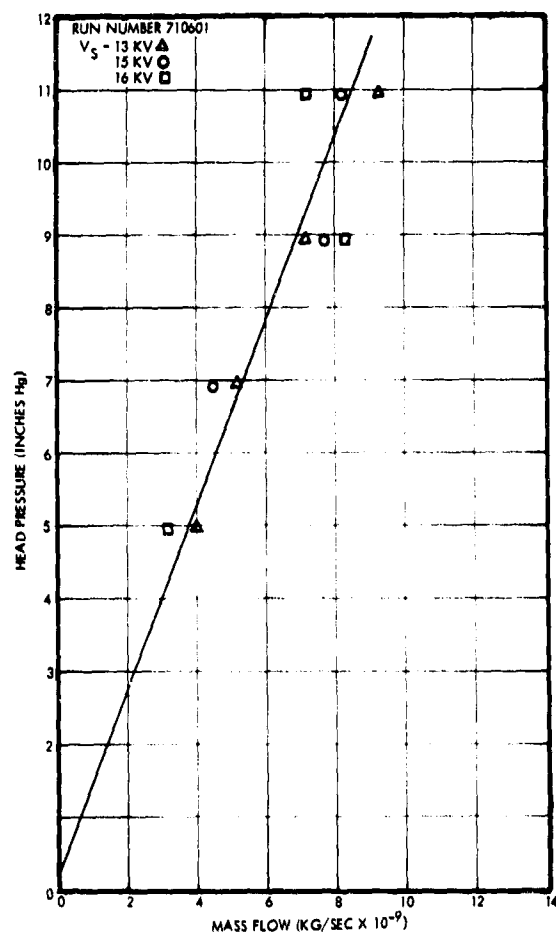
Figure 89

Run 710601 Performance Study —
Propellant Feed Pressure
Versus Mass Flow

103

3. PULSED OPERATION

The main purpose of this part of the program was to investigate and further develop pulsed colloid operation. Specific areas included power conditioning concepts, pulsed capillary needle and annular geometry operation, and the effects of shield electrodes on pulsed operation. Pulsing frequencies were in the range that would be required for spin-stabilized satellites; of the order of 1 pulse per second.

A laboratory breadboard pulsed power conditioning and control unit was designed and built using spacecraft-type components. It provides nominally 8-κv, 200 μa at 30 to 120 pulses per minute at 15 to 50 percent duty cycle when powered by a 28-volt dc input. This supply was successfully tested with a single needle for 1000 hours (> 3×10^6 pulses). Propellant wetting the sides of the needle was identified as a major problem and the shielded needle was shown to adequately handle this problem. A parametric study of the operation of this needle under various pulsing conditions was completed. Various larger ("annular") needles were pulsed and shown to initially possess the same characteristics as when continuously operated. However, these larger needles which were unshielded, also gradually wetted further around the rim exterior and increased the angle of emission.

3.1 BREADBOARD POWER CONDITIONER

The initial plan was to utilize the fact that the current of colloid needle can be completely stopped for a few seconds by reducing the voltage by less than 20 percent. This was to be accomplished by pulsing only one of two supplies connected in series. This idea was abandoned when it was found that the best commercially available supply used far too much power with no output load to allow it to remain on during the off time. Also, when the entire voltage was pulsed on and off, it was found that it was unnecessary to actively discharge the output high voltage, as had been originally planned. It was soon found that the major problem that had to be overcome was the high power dissipation associated with the charging and discharging of the distributed winding capacity of the high voltage transformer. Extension of conventional techniques, such as cascading many smaller voltages and using special winding geometries and methods, failed to achieve practical power efficiencies when operating at 200 μ a, 8 kv (1.6 watt) output level. Acceptable efficiencies (> 70 percent) were achieved by developing a transformer winding scheme using thin wafer windings in individually insulating bobbins and then doubling the output of each of these windings and connecting in series to obtain the high output voltage.

3.1.1 Development of Methods to Discharge Output Capacity

Early in the contract, when it was felt necessary to discharge the output capacity in order to interrupt the engine current sufficiently rapidly, various schemes were considered and the most promising method was built and tested. The original plan to use a series array of silicon controlled rectifiers (SCR's) was abandoned because of lack of appropriate SCR's. This method became increasingly unattractive when the entire 8 kv was to

be discharged. The discharge system that was built consisted of two Kryton tubes in series, fired by a small pulse transformer and an SCR. The Kryton is a unique gas-filled tube manufactured by EG&G which sustains a low level discharge and then upon being triggered allows electrons from the discharge to initiate a breakdown to the high voltage anode. This circuit performed well, had a good lifetime, was small and light, and consumed little power, making it an attractive spacecraft component. However, it was later realized that the circuit would not be needed in the final power conditioner which worked at sufficiently high frequency and low output capacity so that the 15 percent voltage reduction needed to turn off the thrust could be accomplished in a small fraction of the on-time by a small drain current which used negligible power. This bleeder current is drawn by a resistor which is also used for control purposes.

3.1.2 Unsuccessful Approaches

Early work commenced on a lightweight, efficient 8-kv 200 microampere pulser to be operated from 28 volts. A complete pulser was built to supply the correct voltage waveform, but it had an unacceptably poor power efficiency. This was because the minimum idling power required to achieve high voltage even at no load, represents a considerable power penalty relative to the total desired useful power output. This was especially true of the commercially available supplies which were used in this first pulser design.

Even with a vast improvement in this area, it was evident that a portion of the power supply could not be allowed to remain on during the long off-period, as originally planned. The next approach was to construct a single, efficient 8-kv supply, turn it completely on and off at the desired rate and duty cycle, and discharge the output at the beginning of the off-time with a series-connected pair of Kryton tubes.

The large minimum power required to achieve high voltage, even at no-load conditions, is essentially caused by the large capacitive currents associated with the winding capacity of the transformers. There are three potential approaches to solving this problem: (1) wind the transformer in a manner to reduce the distributed capacity, (2) lower the frequency at which the converter operates, and (3) use fewer windings in conjunction with multiplier circuits. The first two result in greater size and weight, so a compromise is necessary. The third technique can be implemented by inductive kick (ladling) and doubling to increase the dc voltage without increasing windings and capacity.

Addressing all these considerations, a new transformer was wound (two previous toroid transformers had too much capacity despite being progressively bank-wound) and was driven with a 75 percent on-time, 10 kc pulse applied to a single transistor. The efficiency was still inadequate. Further attempts to improve performance by resonating the distributed capacity were also not sufficiently successful.

3.1.3 Final Model

The desired high power efficiency was finally achieved by the use of cascaded voltage doublers and special transformer winding techniques.

105

The schematic of the unit is shown in Figure 90. Q_1 and Q_2 form a nonsymmetric, free running multivibrator at about 1 Hertz. The on and off periods are separately variable. The on current of Q_2 is amplified by Q_3, Q_4 and Q_5 and during the on-period allows most of +A to be applied across the driver transistors Q_6 and Q_7 and the push-pull 6.5 kc oscillator using Q_8 and Q_9. A+ is alternately switched across the two primary windings and an approximately 500-volt peak square wave is produced across each of the eight secondaries. The output voltage of each secondary is rectified and doubled and these voltages are cascaded to produce about 8 kv. This voltage is varied from 6 to 9 kv by varying the input voltage from 20 to 30 volts. A picture of the transformer is shown in Figure 91. The eight secondary windings are each wound on a separate slim bobbin less than 1/8 inch wide and more than 1 inch deep. The bobbin is thick enough and of such a material that it can insulate the full output voltage of 9 kv. The wire is scramble-wound from the bottom to the top with occasional polystyrene doping to prevent slippage of wire down the sides. The wire leading to the bottom windings is insulated and brought up the inside wall to the top of the bobbin. Distributed capacity of a single bobbin is small because of the large depth and small width. Side capacity between bobbins has no influence because an identical ac voltage exists on all bobbins. The capacity to the core and primary has no effect because the inner windings are at zero ac voltage. The transformer is homemade of readily available materials, is not potted, and uses larger than necessary, easily handled wire and so is excessively bulky. A professionally wound transformer using the same principles would be lighter and smaller.

Transistors Q_{10} and Q_{11}, incorporated in this laboratory model for life tests, allow the output voltage to be regulated a few percent below the open-circuited voltage to produce no overshoot of the voltage (if desired) with negligible loss of efficiency.

Figure 92 shows a typical current, voltage and time-of-flight trace taken with the breadboard pulser and the single needle during the flat portion of the on-time. The time scales for the photos are 0.1 sec/div and 10 μsec/div. The initial rise-time of the voltage is so fast it cannot be seen. Needle current is 11 μA at 7 kv.

3.2 IMPLICATION OF PULSING A FLIGHT-TYPE COLLOID HIGH VOLTAGE SUPPLY

Our experience with this supply and with the high voltage supply used in the Colloid Advanced Development Program suggests there are no major adverse effects of pulsing the high voltage power conditioning on a spacecraft. The most obvious fact is that the input power varies with time. The timing and synchronization signals would be straightforward and would add little to the complexity or weight and power consumption. Pulsed voltages have to be insulated more carefully than nonpulsed voltages and so the cabling might be a little heavier. If the output capacity is sufficiently small because of high frequency operation, the input drive to the high voltage conversion stage need merely be started and stopped. The voltage rise time will be shorter than the formation time of the jets. Accelerating the voltage decay rate with a small bleeder current will allow

Figure 90. Schematic of Breadboard Power Conditioner for a Pulsed Colloid Engine

107
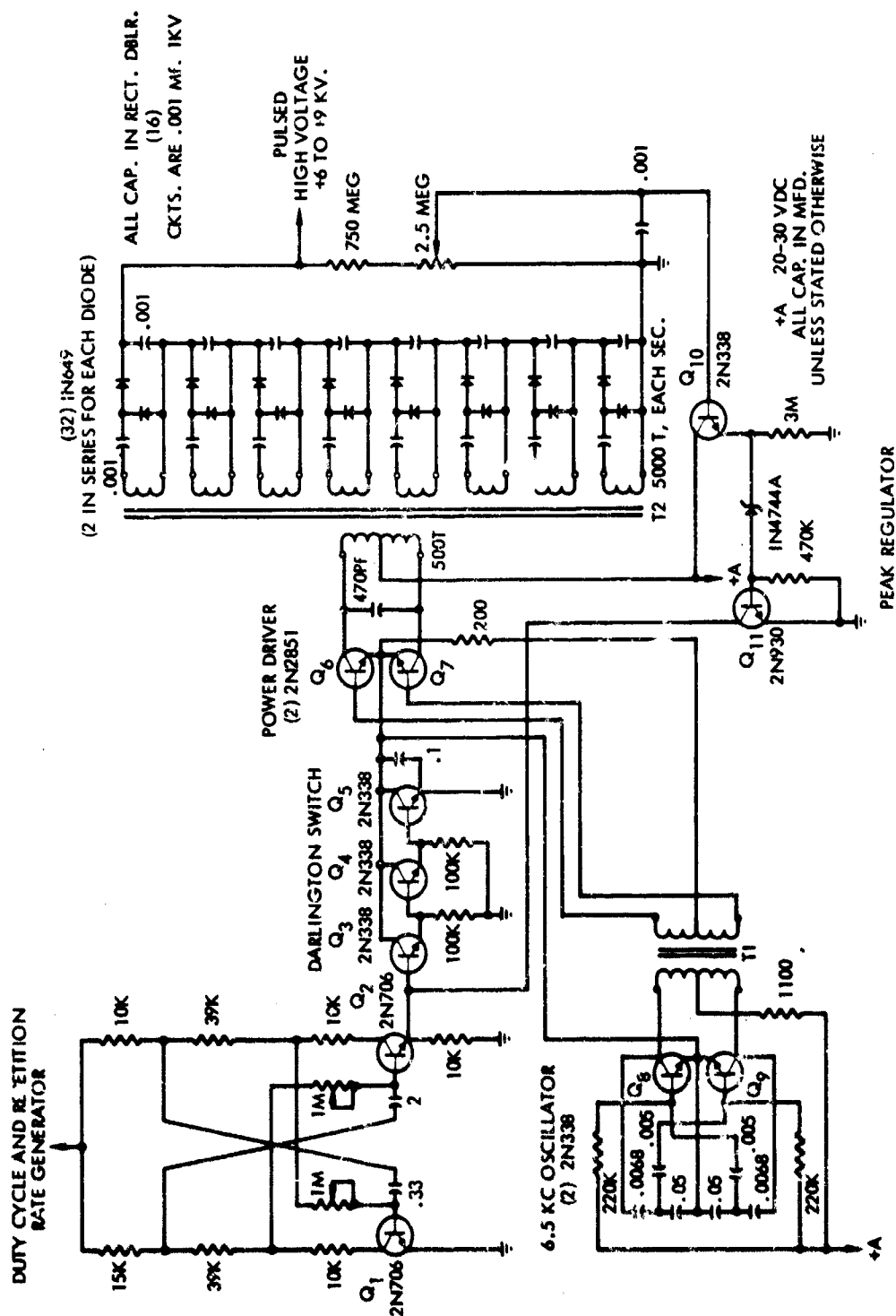
Figure 91. Specially Wound, Low Distribution-Capacity Transformer that allows high power efficiency, high voltage operation at low power levels.
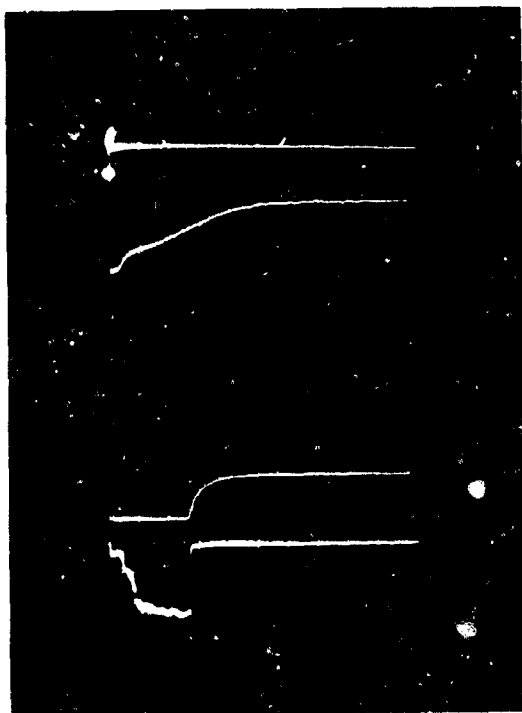
Figure 92. Pulsed Operation Using Breadboard Power Conditioner, Top trace, time-of-flight at 10 µs/div; bottom trace, voltage 5 kv/div and current 5 µa/div at 0. 1 sec/div. Top trace time-of-flight photo at 10 microseconds/cm horizontal sweep speed. Bottom trace shows needle voltage (top) at 5 kv/cm and collector current (bottom) at 5 µa/cm for 0. 1 second/cm sweep speed. (All traces are inverted with positive signals producing a downward deflection.)

sufficiently rapid turn-off for most envisioned satellite spin speeds. If faster turn-offs are required with less energy waste than used by a bleeder resistor, a discharge device discussed in Section 3.1.1 can be used.

3.3 LIFE TEST OF PULSED SINGLE 0.014-INCH OD PLATINUM NEEDLE

3.3.1 500-Hour Test Using Vacuum Tube Pulser

A platinum/10 percent iridium needle (0.014-inch OD) was life tested for 500 hours in the pulsed mode. The vacuum system employed a continuously trapped 600 liter/second oil diffusion pump. The thruster was positioned 30 centimeters from a spherical registered-hole time-of-flight collector. During the entire 500 hours, the pulse duration was kept constant at 0.25 second on and 0.75 second off at a constant feed pressure and needle voltage. The pulser supply was a vacuum-tube pulser built on a previous program. This supply used a shunt triode tube to lower the needle voltage during the off-period. It also allowed triggering a time-of-flight any time during the on-period.

Oscilloscope pictures were taken daily of the voltage and current waveform and representative time-of-flight traces during the current pulse. A typical photo is shown in Figure 93. The time scale is 0.1 sec/div in the lower trace and 10 microsed/div in the TOF traces. The voltage is on at 6.5 kv for 0.25 second. The current linearly increases to a peak of 2.4 microamps (this represents 12 microamperes needle current since the time-of-flight collector has 20 percent active collection area). This current pulse remained essentially constant throughout the test and was identical to the needle current as measured through a specially devised differential capacitive divider. The time-of-flight traces show approximately the same specific impulse and efficiency during most of the pulse,
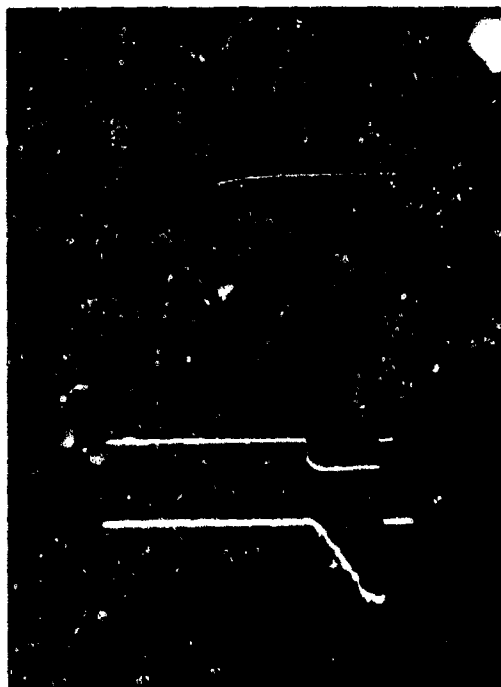
Figure 93. Current Voltage and Time-of-flight Traces of a Pulsed Single Needle During the 500-Hour Run. (Downward deflections)

including the increasing portion. During the entire run, the specific impulse was in excess of 1000 seconds and the efficiency in excess of 65 percent. The peak thrust was in excess of 2 micropounds.

The observed jet distribution was very uniform, increasing in prominence during the pulse and disappearing during the off-period. The angle of emission was good as judged by the jet position and the 100 percent collection on the collector.

The 500-hour life test of a pulsed single needle was successfully completed. It ran with no sign of degradation for 522 hours. One hundred percent of the current was within a 20-degree half angle. Peak time-of-flight thrust was 2.2 μlb at 12 μa and 7 kv. Efficiency during this peak thrust was 0.66 and the specific impulse was 1160 seconds.

3.3.2 Breadboard Pulser Life Test

After the successful 500-hour life test with a vacuum tube pulser was completed with no degradation of performance, an additional 650 hours were put on the same needle using the breadboard transistorized pulser at nearly the same voltage and duty cycle (7 kv, 0.3 sec on, 0.8 sec off). This was accomplished simply by changing the power supplies without any interruption in the vacuum, trapping, or feed system. During the last few days of operation it was found that the beam angle had increased. This showed first as a slight lowering of time-of-flight collector current, and was confirmed by a careful comparison of the needle current with the collector current. Also visual observations revealed fluorescence along the walls of the chamber where it was being struck by the beam. This interception of a portion of the beam on the stainless steel wall of the vacuum enclosure could be easily seen when the system was dismantled. The half angle exceeded 45 degrees.

When the operating needle was viewed through a microscope with blacklighting to see the jets, stationary light-scattering sites were seen. This suggested specks of dirt or tar distributed around the rim. However, the needle appeared clean when removed from the system and viewed with a microscope. Any foreign material on the rim might have been washed away by glycerol as the system was let down to atmosphere. The outside shank of the needle was covered by a layer of liquid perhaps 3 mils thick extending about 4 diameters from the tip. Since the feed system pressure was crudely adjusted in order to suck liquid back into the needle rather than expelling it when letting the system back up to atmospheric pressure, and since the shank of the operating needle appeared somewhat conical, it was concluded that the wide-angle operation might have been obtained when the outside of the needle had been wet with a bulging band of propellant around it.

In order to check this, the needle was chemically cleaned (but with no mechanical work or polishing) and operated again for an additional 350 hours (total needle time approximately 1500 hours). During this run, the needle was carefully observed for any signs of wetting on the outside. Also the total needle current was continually monitored and checked against

the collector current to be sure the angle was reasonably small. The first sign of trouble was a speck of crystalline material about 0.005 inch high on the lower side of the horizontal needle, about a needle radius back from the rim. Examination in the dark indicated a small jet shooting downwards at about 45 degrees. It seemed evident that liquid had seeped over the lower region of the rim and run to the crystal from which the glycerol evaporated leaving a growing NaI crystal behind. Also the collector current was slightly less than the needle current, indicating a widening beam. Time-of-flight results were still normal.

Before terminating the experiment, it was decided to carefully flood the needle and observe the wetting and the washing action of the fluid and the effects of liquid on the shank upon reapplication of the voltage. After a few minutes, the propellant began wetting the needle exterior with a small contact angle. If forced to advance too rapidly, the contact angle would reach approximately 90 degrees. When most of the propellant was drawn off by reapplication of high voltage and then reflooded with voltage off, the liquid would readily flow over the existing film but would slow down again as it started wetting the dry needle further from the tip. The liquid flowed more rapidly on the lower part of the needle and upon reaching the crystal, started dissolving it. By repeated flooding and reapplication of voltage, the crystal and its foreign material on the rim were cleaned off. It could be observed though that excess propellant on the needle shank at higher voltages would be pulled off as jets on any projections present, but thinner films at normal voltages could stably exist with near-normal operation at the needle tip.

The wetting of the outside of the needle does appear to be a potential problem associated with pulsed operation as it was with ac operation. The problem might not exist for higher voltage operation at lower feed rate especially if particulate matter is not present in the fluid. This run did not use a filter (although the propellant had previously been filtered) and the latter part was run at higher feed rate than the first 500 hours. Also, to allow close visual observation, the pulsed work was performed in a closely confined system, very near to glass view parts, whose surfaces tend to charge up to high potentials which can modify thruster operation.

An observation made at this time is worthy of note. With the light and the microscope arranged to see a reflection off the meniscus at a point where the surface of this liquid is about 25 degrees to the axis of the needle, it was observed that this point receded away from the rim about 0.1 second after the voltage was applied during the pulsing cycle, and advanced in about the same time after the voltage stopped. This observation is most easily explained by supposing that the liquid surface becomes convex (or less concave) near the metal interface as higher electric fields terminate on the liquid.

One wonders if the regenerative convexity gives rise to jets on the liquid away from the interface, or if the jets are pulled over to the interface where they anchor and the space charge from these jets reduce the field and prevent the liquid surface from becoming more convex and producing more jets.

111

3.4 PULSED "ANNULAR" NEEDLE RESEARCH

Four different 3/32-inch diameter needles were tested in the horizontal station with close viewing windows. The pulsing control was provided by the older vacuum-tube pulser. This device supplies current through a series resistance in order that the voltage can be lowered sufficiently to stop all needle current by temporarily introducing a relatively low series impedance to ground. The control also allows easy variation of pulse rate, duty cycle and imitation of time-of-flight experiment relative to any part of the on-time. The transistorized breadboard pulser could not be used at this high voltage (approximately 14 kv), as it was designed for the operation of 14 mil needles at 8 kv. (Straightforward alteration could extend its voltage output, but such effort was not budgeted into the present program.) These studies were of an exploratory nature and were coupled with the steady-state "annular" needle research to establish proper needle geometry and solve problems relating to wetting.

The first needle tested was configuration No. 6. The liquid well in this design was sufficiently shallow to prevent bubbling, but the outer surface produced a relatively wide beam. Typical operating conditions are illustrated in Figure 94. The lower trace is the collected current (50 microamp/div, 0.2 sec/div) with a 40 percent voltage-on duty cycle. The average current was 30 percent of the peak current. The upper curve is a time-of-flight trace taken at the end of the pulse. (Surprisingly, the efficiency and specific impulse were constant throughout the entire current pulse.) The time scale is 10 microsecond/div with the time-of-flight distance of 30 cm. This results in an efficiency of about 50 percent with a specific impulse of above 1500 seconds and thrust of the order of
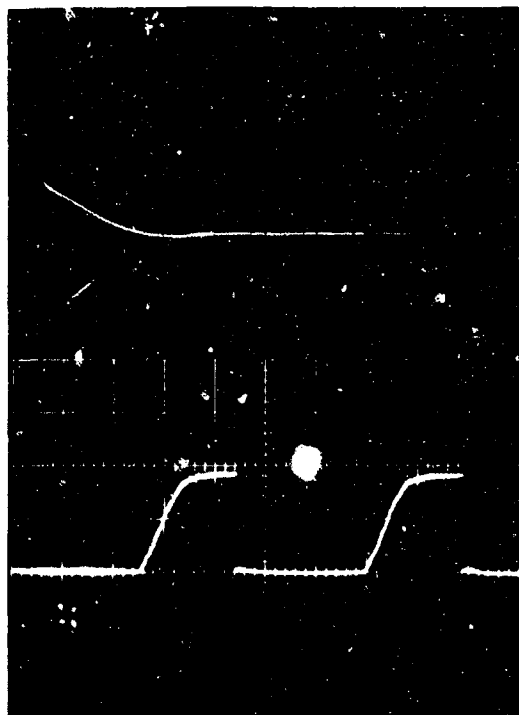
Figure 94. Time-of-Flight Trace (10 μsec/div at 30 cm) and Current Pulse (0.2 sec/div) for Pulsed Wide-Angle "Annular" Needle

20 micropounds. Feed pressure was 0.6 inch Hg, temperature approximately 24°C, voltage +11.5 K and -1500 v. The angle regretfully was large (20 percent of current in half-angle greater than 25 degrees) and increased with time of operation. A few jets exceeded 35 degrees for a brief period at the beginning of the pulse. Liquid propellant apparently would creep to the outside during the off-time and be pulled off at the beginning of the pulse when the voltage and field were highest because the current was still low.

This disagreeable tendency to increase the angle during long term operation was observed to some extent in all four tests. It is reminiscent of the same problem with pulsed smaller needles. This effect is not understood and has not been extensively studied. It is the major problem that must be solved to make pulsed colloids feasible. If this "super wetting" is not controlled, tar will prematurely develop, shortening life.

Next a configuration 7 source was tested. It worked well with peak beam currents of 100 microamps at 12.5 kv and -1.5 kv, with efficiencies of 75 percent at specific impulses greater than 1500 seconds. Again side jets at large angles developed and persisted for only the first part of the pulse.

A source of configuration 7-2 that had been giving trouble when tested with deflectors was then tested. The object was to compare results with the tests of the same needle in a different tank with different trapping and in a different electrode geometry. The source worked almost identically to the previous No. 7 configuration. These two No. 7 sources had an initial 20 percent step in the current and then a linear rise in 0.1 second to 80 percent and a rounding to the final current. As in previous pulsing experiments, the first step is fast particles that decay to mostly ions.

Source 7-1 was then reinstalled for further testing. Its performance was similar to previous operation and the opportunity was used to pretest the source prior to use with deflector geometry, as well as to test a new batch of propellant. All these tests with the annular needle were of short duration and showed the characteristic first initiation period followed by operation essentially identical to steady-state operation.

3.5 PULSED SINGLE SHIELDED NEEDLE

As stated in previous sections, one of the major concerns with pulsed and ac operation has been a tendency for the outside of the needle to wet during long-term testing. An obvious potential solution to this problem is the use of the shielded electrode configuration (that used in the Colloid Advanced Development Program). This design has already demonstrated an ability to recover from accidental flooding situations. Moreover the shield structure prevents sideward emission from the needle to the inner perimeter of the extractor hole. For these reasons, a test of a pulsed single needle shielded electrode configuration was started. This configuration is shown in Figure 95.

Figure 95. Shielded Needle

3.5.1 Parameter Study of Shielded Needle

During the course of the test, thruster performance was mapped at several operating points in order to obtain a better understanding of the overall pulsed operating characteristics. This is a considerably more complex operation than conventional steady-state performance mapping for the following reasons:

- The time-of-flight trigger must be synchronized to the proper time within the thrust pulse.

- The total needle current varies rapidly within the thrust pulse.

- In addition to variations in the normal colloid control parameters, such as voltage and mass flow, increased analytical complexity is introduced because, for each value of voltage and mass flow, the effect of varying pulse durations and repetition rate must be investigated.

- For any given set of operating conditions, a number of time-of-flight measurements must be made corresponding to various points within the thrusting cycle. The beam performance parameters for these individual points must then be plotted versus time to obtain a picture of the overall time-dependent thrusting profile. They must also be mathematically combined in an appropriate manner to calculate the overall thruster performance characteristics.

In order to simplify the task of performance mapping, the test matrix shown in Table 19 was utilized. The detailed time-dependent performance parameters are mapped in Figures 96 through 102. Approximate overall averages, as listed in Table 19, were then estimated from a visual inspection of these graphs.

Based on preliminary experimentation, 14.7 kv was selected as a base line operating needle voltage. The purpose of runs 1 and 2 in Table 19 was to determine what would happen if, for an approximately constant total period, the feed pressure and the on time were increased in the same ratio. One would expect, assuming mass flow to be strictly

114

Table 19. Pulsed Colloid Performance Test Matrix†

| | Control Parameter Matrix | | | | | Estimated Time-of-Flight Averages | | | | |
Run No.	Voltage (kv)	Feed Pressure (in. Hg)	Total Period (sec)	On Time (sec)	Q/M (C/kg)	ṁ (μg/sec)	Thrust (μlb)	Current (μamps)	Efficiency* (%)	Specific Impulse (sec)
1	14.7	1.3	0.575	0.19	5,000	3	6	14	70	1000
2	14.7	1.9	0.601	0.26	5,000	3	6	12	75	1000
3	14.7	0.95	0.6	0.23	5,000	2	5	10	80	1100
4	14.7	0.65	1.2	0.48	8,000	1.5	4	7	70	1300
5	14.7	0.65	1.2	0.24	5,000	3	6	12	75	1000
6	14.7	0.65	2.4	0.40	5,000	3	7	14	75	1000
7	14.7	0.65	2.4	1.0	9,000	1.5	4	11	75	1300

†These are estimates based on visual inspection of Figures 96 through 102. A more accurate calculation would involve a detailed computation of a mass flow weighted average throughout the on time.

*This is the observed average value of the instantaneous efficiency. We have not at this time taken into account the time integrated efficiency degradation caused by the time dependent variation of the I_{sp} during the pulse.
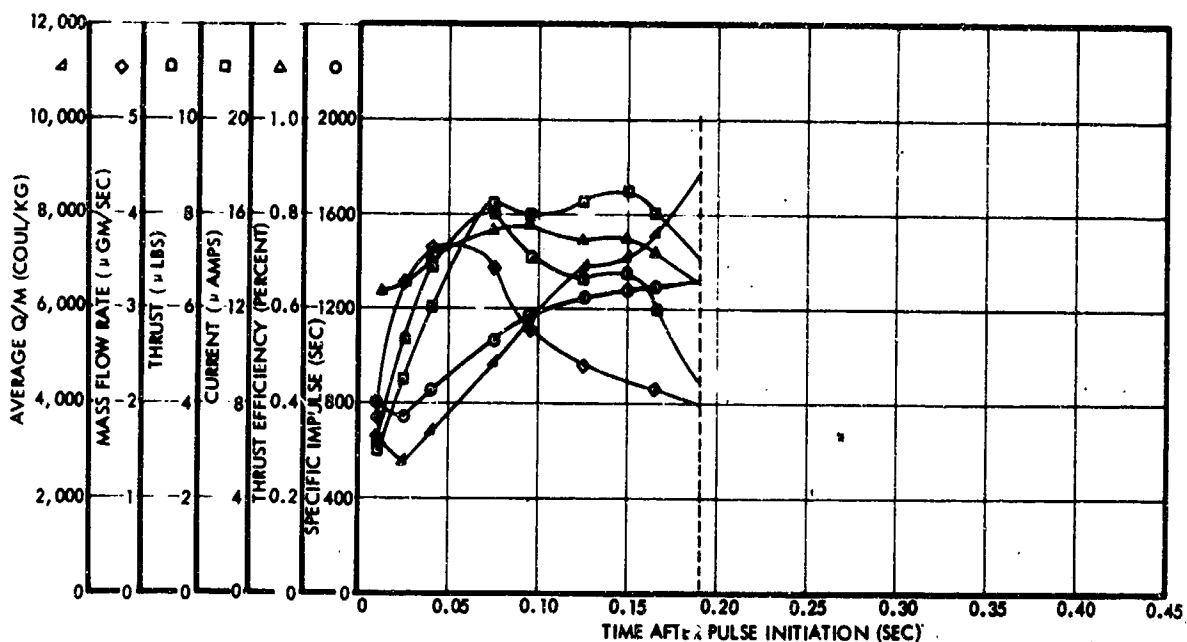
Figure 96.   On-Time Profile of Time-of-Flight Parameters
at V_N = 14.7 kv, 1.3 in. Hg, 0.575 second
total period, 0.19 second on time
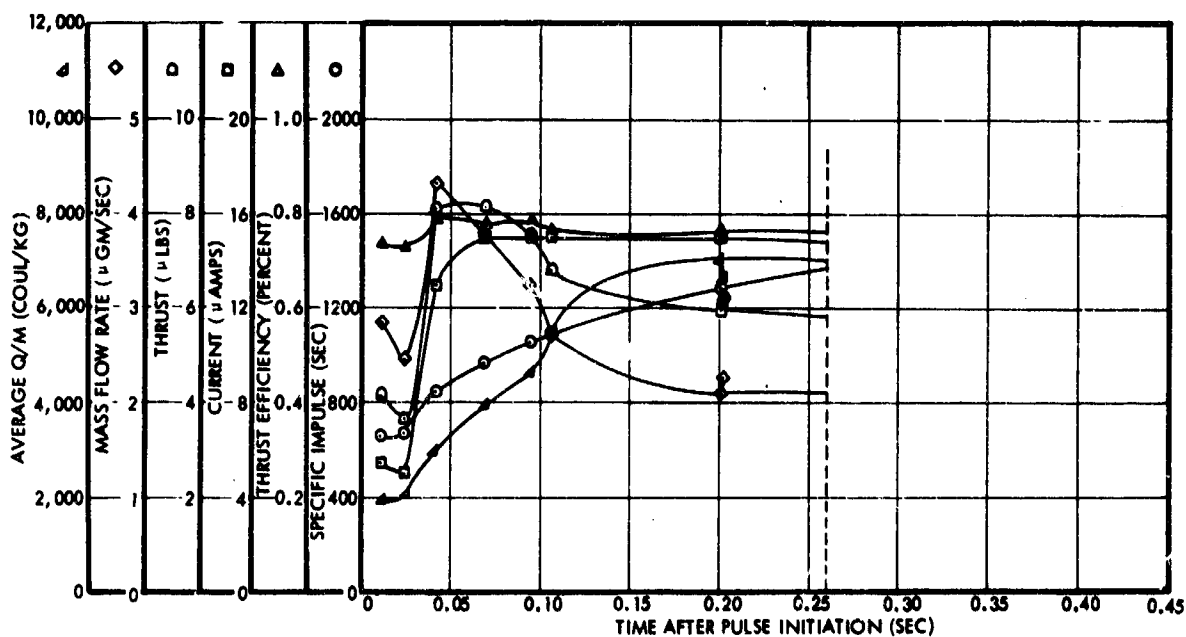
Figure 97.   On-Time Profile of Time-of-Flight Parameters
at V_N = 14.7 kv, 1.9 in. Hg, 0.601 second total
period, 0.26 second on time

116
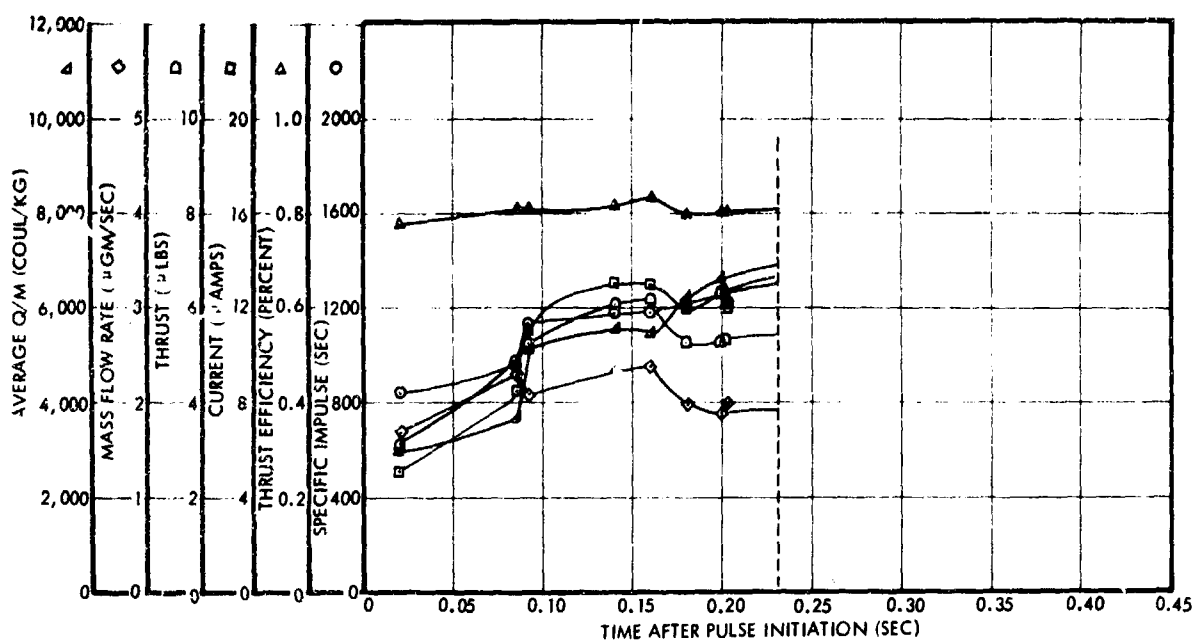
Figure 98. On-Time Profile of Time-of-Flight Parameters at V_N = 14.7 kv, 0.95 in. Hg, 0.6 second total period, 0.23 second on time
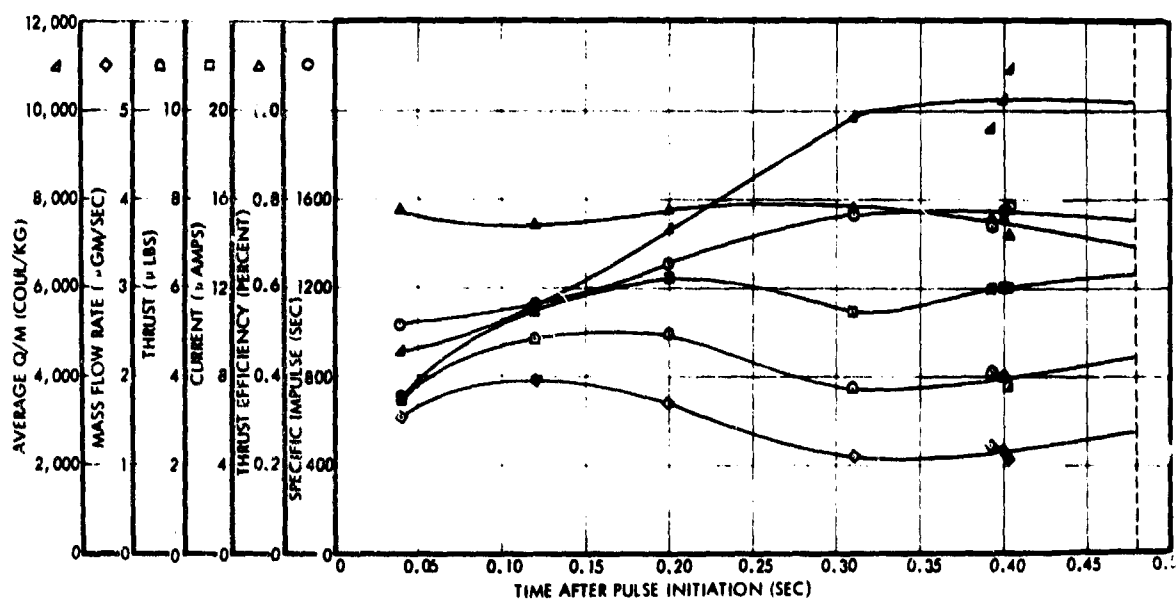
Figure 99. On-Time Profile of Time-of-Flight Parameters at V_N = 14.7 kv, 0.65 in. Hg, 1.2 second total period, 0.48 second on time

117
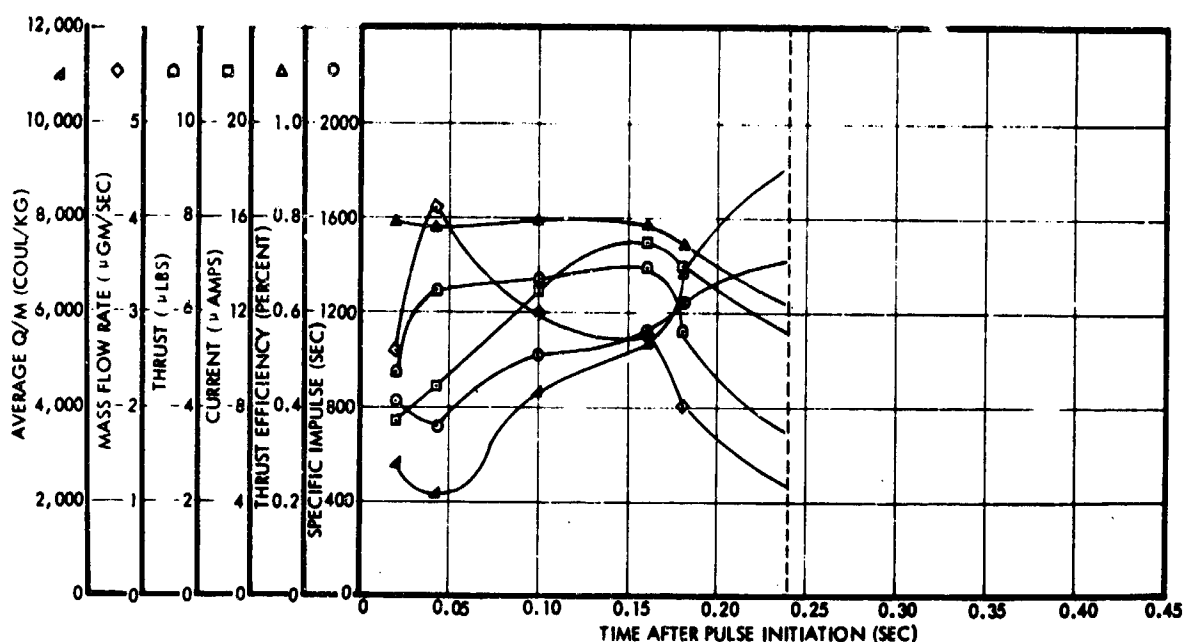
Figure 100. On-Time Profile of Time-of-Flight Parameters
at V_N = 14.7 kv, 0.65 in. Hg, 1.2 second total
period, 0.24 second on time
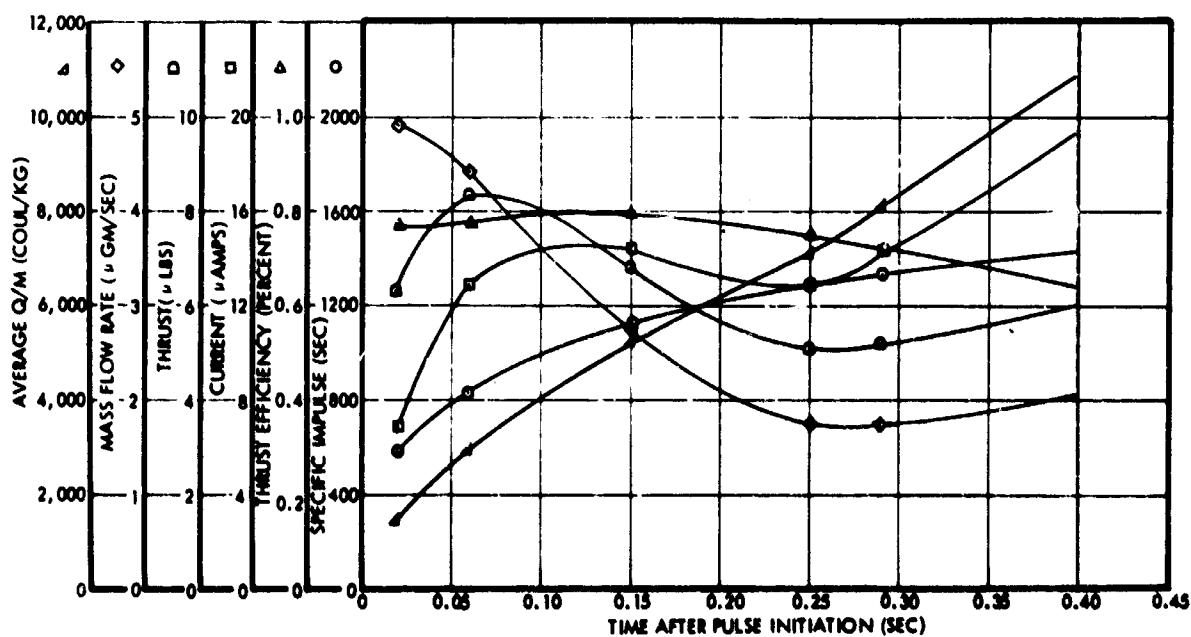
Figure 101. On-Time Profile of Time-of-Flight Parameters
at V_N = 14.7 kv, 0.65 in. Hg, 2.4 second total
period, 0.40 second on time

118
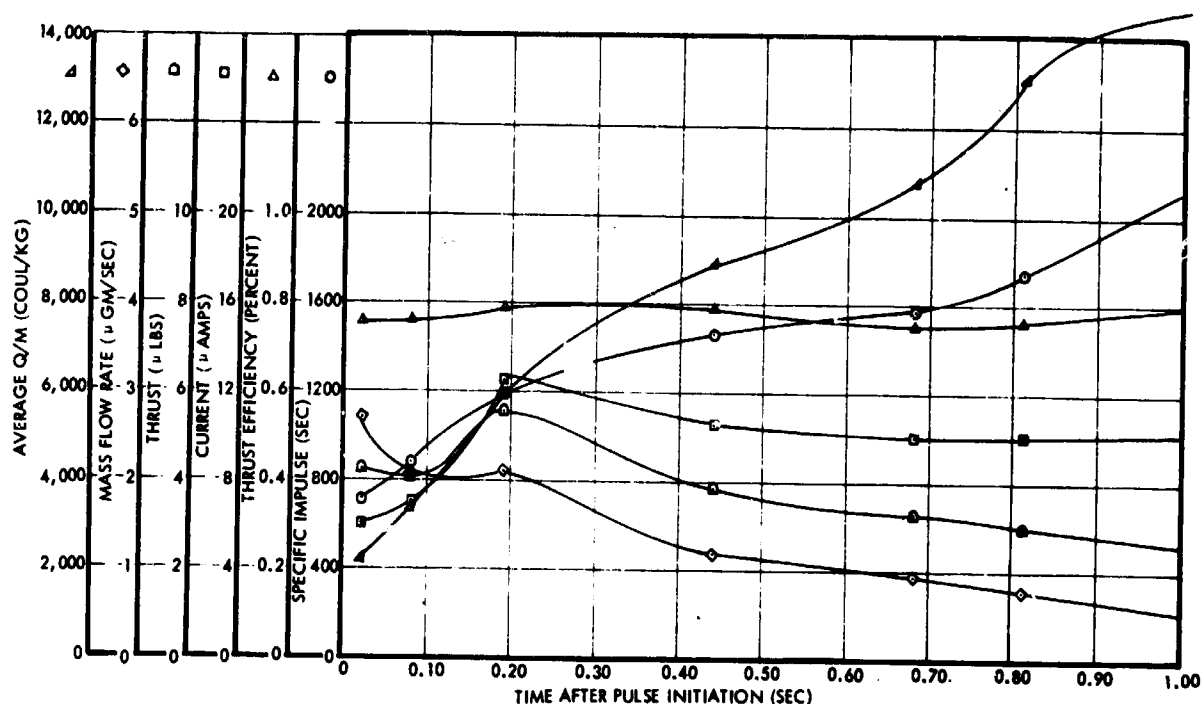
Figure 102. On-Time Profile of Time-of-Flight Parameters at V_T = 14.7 kv, 0.65 in. Hg, 2.4 second total period, 1.0 second on time

proportional to pressure, that the average mass flow during on time would be the same for the two runs; within the roughness of our estimates, this did appear to be true. Similarly the average thrust during the on time remained constant. Of course, since the total on time was greater in Case 2, the thrust averaged overall time would be correspondingly greater. For the problem of determining the total useful impulse delivered in an actual spinning satellite, the problems become slightly more complicated, since it is then necessary to average using the cosine of the satellite's instantaneous rotational angle. At the present, comparatively inchoate stage of the analysis, it suffices to state that the thruster behavior seems reasonable. One major surprise throughout the measurements, however, was the high instantaneous time-of-flight thrust that was usually observed.

Runs 2 and 3 were intended to show the effect of halving the feed pressure at constant repetition rate and pulse duration. There was some decrease in ṁ, thrust and current, but not as great as anticipated. Once again, we must remember that these calculations are approximate.

Runs 4 and 5 were designed to determine the effects of halving the on time, holding all other parameters constant. Here, the average ṁ changed as anticipated. Runs 5 and 6 show the effects of a 2:1 ratio in repetition rate at an approximately constant percentage on time. Here the average mass flow, thrust and current remained approximately constant. Runs 6 and 7 once again show the effects of an approximate 2:1 ratio in on time, holding all other parameters constant. The performance parameters behaved approximately as expected.

119

3.5.2 Pulsed Shielded Needle Life Test

The shielding needle was run for 500 hours during which the parametric study reported in the previous section was performed. The performance was satisfactory during this period with no degradation noted. The angle as determined from the distinct pattern on the collector, was quite low – half-angle less than 17 degrees. Unfortunately a power shortage removed voltage and flooding resulted, obscuring the visual evidence of the needle condition. The needle was in good condition after superficial cleaning and was put back in operation for an additional 300 hours.

During this time the needle was run at a high thrust and a low specific impulse (overfed). This was felt to be a severe test tending to accelerate the production of tar or outside needle wetting. During the 300 hours, no trouble was evidenced except the current would reduce with time from the initial well-wet condition induced by low voltage operation. This situation is reminiscent of contamination by pump oil, but the system was continuously trapped during the 300 hours. The operation at the end of 300 hours is shown in Figure 103. The time-of-flight trace indicates good efficiency (77 percent) and low ions (14.9 kv, 13.5 microamps, 6 micropounds, 1200 seconds, 2.3 micrograms/sec). The current on the bottom traces shows 0.55 second off, 0.33 second fully on at nearly a constant value, and about 0.08 second of erratic operation. This needle, upon examination after the test, was found to be clean around the rim but had liquid on its outside which in no way affected its operation. Without the shield electrode, this material might have caused tar as it crept around the rim or at least would have come off at a large angle and bombarded the accelerator and initiated arcing. The needle geometry with the shielded electrode cupped around it does indeed seem quite capable of long-term pulsed operation.
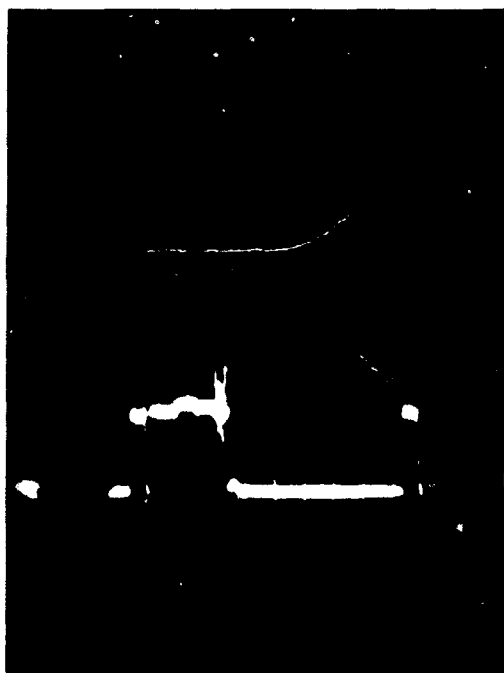
Figure 103. Current (vertical) vs Time (hori ontal)—Top Trace 10 μsec/div, 5 μamp/div, Bottom Trace 0.1 sec/div, 5 μamp/div—0.014 inch Platinum Needle with Shielded Electrode After 800 Hours (300 hours since cleaning)

4. FEED SYSTEM

The feed system task consisted of designing, fabricating, and testing a high voltage isolation valve. The function of this valve is to interrupt propellant flow and simultaneously provide an electrically insulating section in the propellant flow passage capable of withholding, at low leakage current, the high operating voltage of a colloid thruster. This type of valve has several potential applications. One application allows independent operation of more than one thruster from a common propellant supply system, shown schematically in Figure 104. When the valve of one of the thrusters is closed, both the propellant and current paths to that thruster are broken.

A second application isolates a thruster unit that has failed by shorting to ground. The shorting path would then be isolated from the rest of the propulsion system.

A third application uses the valve as part of a propellant ladling system. Shown schematically in Figure 105, the propellant required for the entire mission is stored in a central supply vessel that is at ground potential. Each thruster has its own individual propellant supply vessel, capable of sustaining thruster operation for several hours or days. The individual vessels are refillable from the central supply when the thruster is not operating. In this application, the isolation valves are located in the interconnecting propellant supply lines.

4.1 DESIGN APPROACH

To perform the isolation function in the several applications, the valve must meet a series of design criteria. These include:

- Positive propellant shut-off

- A sealing action that will expel propellant from the seat area

- Nonconductive (electrically) sealing materials

- A valve sealing surface of sufficient length to limit current and prevent electrical breakdown

- All materials in contact with the propellant must be compatible with the propellant.

The valve's performance goal for this program was of a capability of isolating 15 kv with less than 10 μ amp leakage current when situated in a line filled with propellant. In practice, a leakage current of 2.5 μ amp was achieved. The 15-kv
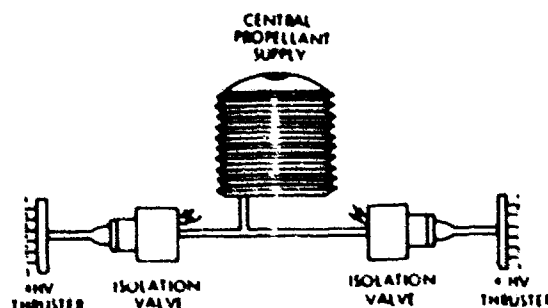
Figure 104. Thruster Isolation Schematic

121
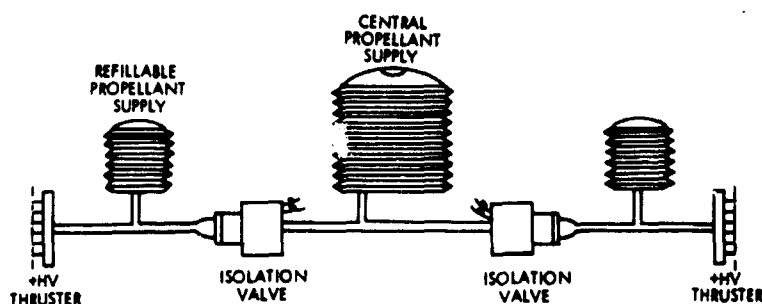
Figure 105. Propellant Ladling Schematic

level was selected as the operating point because it is compatible with
a large class of operational thrusters. The upper limit of 10 μ amp leak-
age current is somewhat arbitrary. This value would produce an
extremely small power drain during isolation of a failed thruster; 0.15
watts at 15 kv. However, gas generation resulting from the current leak-
age could be a problem. The electrolytic gas production rate resulting
from this leakage current is proportional to the current. A current of
10 μ amp would generate 1.16×10^{-6} cc of H_2/sec at standard pressure
and temperature. Implications of this gas generation rate are discussed
in Section 4.5.

The positive shut-off feature of the valve is a requirement for two
reasons: 1) Propellant leakage through the valve could result in flooding
the thruster to which it is coupled during off periods; and 2) A propellant
leakage path would represent a current leakage path. Residual propellant
in the seat region also could represent a current leakage and electrical
breakdown path.

The valve seat region must be fabricated from nonconducting mate-
rials with sufficiently high dielectric strength to withstand the electric
fields where the conducting path is interrupted. The length of the valve
seat must be sufficient to limit surface conduction and to restrict the
intensity of the electric field.

The propellant, NaI doped glycerine, is corrosive; therefore, the
selection of materials with which it is compatible is limited. One of the
main problems associated with corrosion in the propellant is that of hydro-
gen gas generation. Only a small corrosive attack on the valve assembly
materials can produce a relatively large volume of gas. This gas can
nucleate into bubbles that degrade thruster performance. An additional
requirement is that the valve materials have low gas absorption and per-
meation properties or be easily outgassed. Excessive absorbed gas
diffusion from the structural material can also nucleate bubbles in the
propellant.

122

4.2 PRELIMINARY VALVE DESIGN

Preliminary tests were performed on mockup versions of several isolation concepts. These concepts included:

- Collapsing of elastomeric tubing
- Sealing of glass body valves with Teflon poppets.

The tests indicated that high voltage isolation could be achieved by either of these means. The technique of collapsing an elastomeric tube would be the simplest to implement; however, it would not have the reliability required for spacecraft application because of permanent deformation of the tubing in the collapsing area and aging of the tubing when located in a vacuum environment. The valve seat/poppet concept could be implemented in a manner similar to that used in ordinary solenoid valves. However, a glass valve body would be fragile and present problems in making structurally sound transitions to metal components and/or economically maintaining dimensional tolerances. Teflon is not suited for long term operation as a poppet seat because it has a tendency to cold flow under the extremely high seating pressures required to remove propellant from the seat region. In addition, Teflon is extremely difficult to outgas.

For these reasons, a test program was initiated to determine the propellant compatibility moldable resins and elastomers for use as the valve seat and poppet materials. As part of the program, a series of five different elastomers, which could be used for seat sealing material, were formulated and molded into test specimens. These elastomers were:

- Viton A, a low hydrocarbon, fluorocarbon elastomer containing MgO as a curative, an acid acceptor, and a carbon black reinforcing agent

- Ethylene-propylene terpolymer (EPT) elastomer with Hystl resin as a reinforcing agent and a silica and methyl group as a surface conditioner

- Fluorosilicone elastomer with a silica reinforcing agent

- A high acrylonitrile-butadiene elastomer with a silica reinforcing agent

- Polyisobutylene-low isoprene elastomer with a polytetrafluoroethylene filler.

In addition to these elastomeric seat materials, nonreinforced and both silica and alumina reinforced Hystl resins were formulated and molded into test specimens. As a result of these tests, alumina filled Hystl resin and the EPT compound were found to be satisfactory materials. The test specimens were inserted in the sealed leg of a glass U-tube and outgassed in an ambient pressure of 10^{-6} torr. The tubes were then

filled with outgassed propellant and sealed under vacuum. Photographs of test samples are shown in Figures 106 and 107.

The glass U-tubes had reduced diameter tube sections at their closed ends, which were filled with void free propellant at the start of the tests. The samples were stored vertically as shown in Figure 106. If gas was liberated from a test specimen due to either outgassing or reaction, gas would accumulate in the closed end of the U-tube in the form of a bubble. One test sample in Figure 107 contains EPT with silica as a reinforcing agent and a peroxide curative and the other contains an alumina filled Hystl resin. The propellant in the closed end of the U-tube is under tension when positioned as shown in Figure 107 because the sample was sealed under vacuum. As can be seen, no void or bubble is apparent in the closed end section. The photograph was taken after 16 months of test time. These materials were selected for the seat and isolation portion of the valve body and poppet.

4.3 VALVE DESIGN

The valve design for the high voltage isolation was solenoid actuated. The components of the valve included:

- Seat
- Poppet
- Body
- Magnetic field coil
- Spring.

Figure 106. Test Samples Stored in Vertical Position

A schematic of the valve with its various components identified is shown in Figure 108. Photographs of the valve components and of the assembled valve are shown in Figures 109 and 110.

The major difference between the high voltage isolation valve and a conventional flow control valve lies in the seating action of the poppet into the seat port and the non-conducting materials of construction of these parts. The valve seating region has a truncated conical shape. The included cone angle of the seat is 90 degrees, while that of the elastomeric tip of the poppet is 88 degrees. During valve closing contact is first made between the

Figure 107. Test Samples of EPT with Silica and Alumina Filled Hystl Resin

124

Figure 108. Isolation Valve Design

SEAT SURFACE

TUBE MONEL K 500

FLANGE HYST

SEAT E PT

SUPPORT HYST

LINER MONEL

ARMATURE 430F

BODY 430F

SPACER 347SS

COIL

SPRING INCONEL 718

TUBE MONEL K 500

125

Figure 109. Valve Assembled

SEAL

SPRING   POPPET

SEAT

BODY AND COIL

0 *TRW* 1   2   3   4   5   6

Figure 110. Valve Components

seat and poppet at the larger diameter end of the conical section. As pressure is applied to the poppet by the valve spring, the elastomeric tip of the poppet deforms, causing the contact surface area between the poppet and seat to increase in a uniform manner toward the apex of the conical section. At full closure, the contact length between the seat and poppet is 0.075 inch, which is sufficient to withstand the electric field. The closing action of the valve is designed to allow sweeping of residual propellant from the seating interface. If the valve closing action allowed simultaneous initial contact of the entire seating area, a propellant film or isolated pockets of propellant could be trapped in this region. A propellant film on the seating surface would provide a relatively low electrical resistance path. Isolated pockets of propellant in the seating area could serve as terminal points for an electrical breakdown path. Either condition would cause an electrical short through the valve. The valve sweeping action during closure avoids these problems by forcing propellant out of the growing seat contact area. In this way, residual propellant film in the seat area is minimized and the presence of propellant pockets is virtually eliminated.

The valve was designed as onlatching to allow concentration on the seat design. An operational valve would be latching to conserve power.

4.3.1 Valve Seat

The valve seat is one of the components that produces the discontinuity in the current path when the valve is closed. A sketch of the valve seat is shown in Figure 111. The valve seat was molded of alumina filled Hystl. The Inconel X750 extension tube, on the seat was positioned initially in the mold and became an integral part of the seat assembly during the molding process. A thin (0.0005-inch thick) layer of silica

Figure 111. Valve Seat Assembly

127

reinforced ethylene-propylene terpolymer elastomer was deposited on the tube in the area to be covered with Hystl prior to the molding process. This layer formed the bond and seal between the metal tube and the resin seat. A photograph of the mold and finish seat is shown in Figure 112. The O ring groove for sealing the seat to the valve body is molded directly into the seat. The O ring used was molded from silica reinforced EPT.

4.3.2 Valve Poppet

The valve poppet contains the deforming portion of the valve seat assembly and the armature for activating the valve with the magnetic field as well as being part of the current path discontinuity. A schematic of the valve poppet is shown in Figure 113. The poppet armature is fabricated from annealed type 430F stainless steel, required for its magnetic
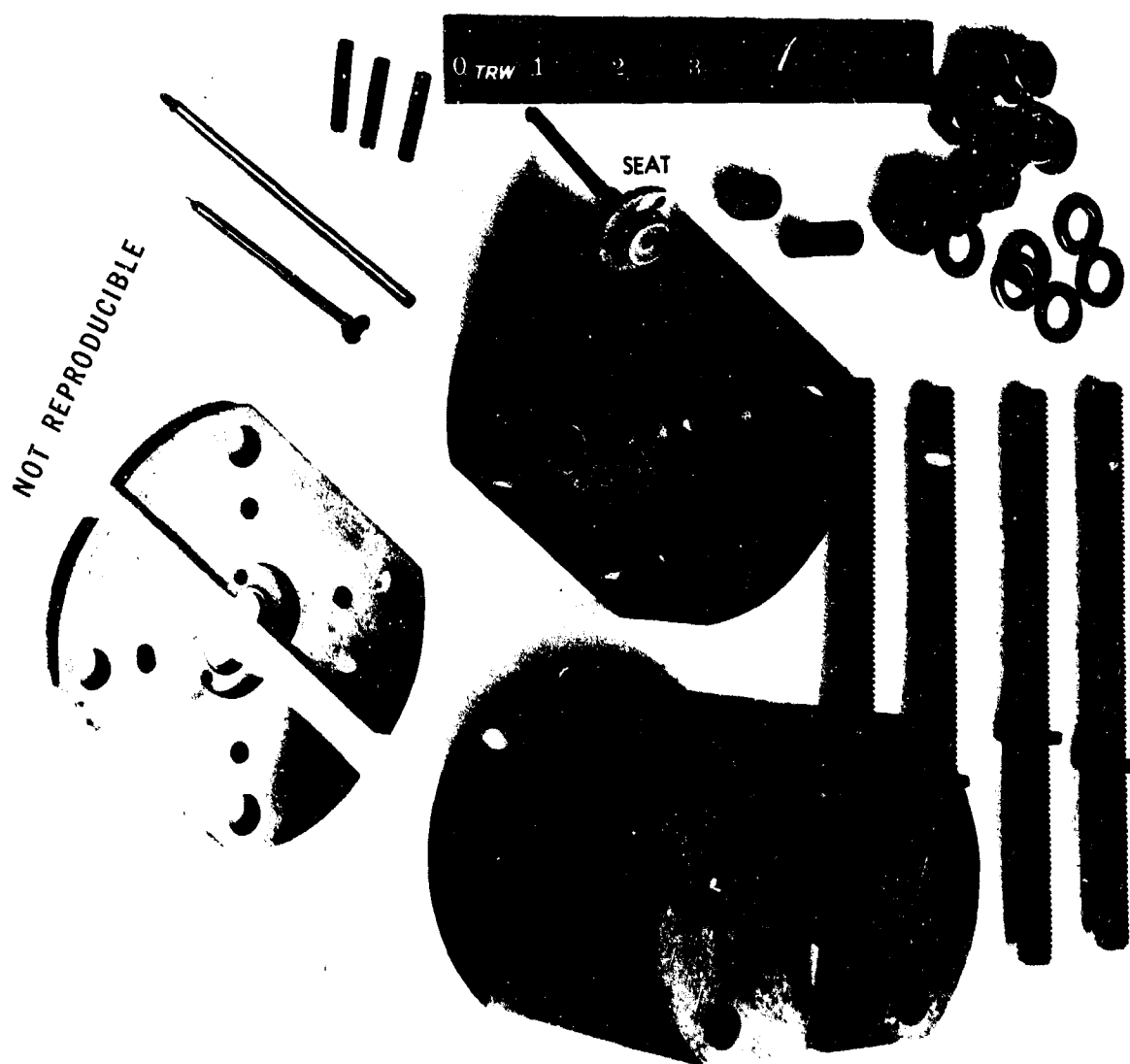
Figure 112. Seat and Mold
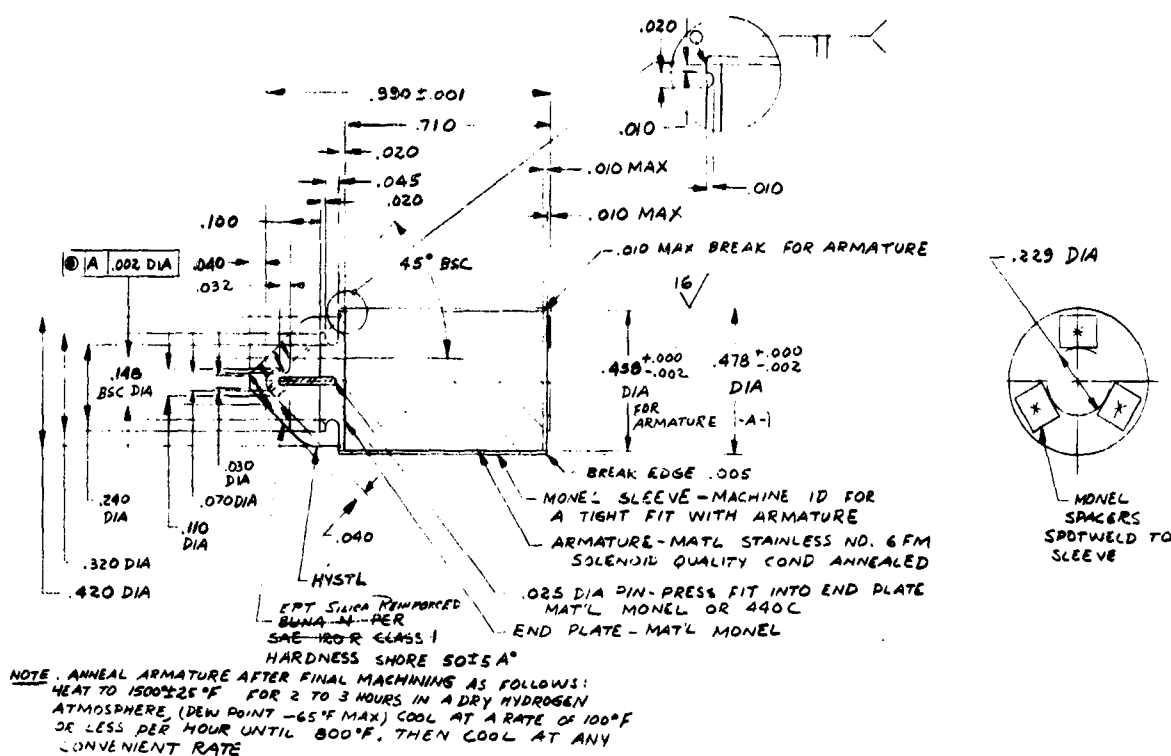
Figure 113. Poppet Assembly

properties. However, since it is not compatible with the propellant, the armature is encapsulated in a Monel K-500 can.

To reduce the size and thickness of the elastomeric sealing tip of the poppet, a portion of the tip was fabricated of Hystl polyimide. The material that actually performed the sealing operation was the silica reinforced EPT. The Hystl was molded to the poppet armature cladding at an interface that allowed mechanical retention of Hystl to the cladding. The EPT elastomer was molded to the Hystl.

The molding of the Hystl and EPT is a two-step process. In the first step, the Hystl is molded to the armature clad and then partially cured. The mold end is then replaced with one holding the EPT compound. After positioning the EPT mold face, both the EPT and Hystl are cured. During this curing process, a chemical bond is formed between the EPT and Hystl at the interface and is sufficient to hold the EPT tip to the poppet. A photograph of the poppet mold and a finished poppet is shown in Figure 114.

4.3.3 Valve Body

The valve body contains the propellant flow passage, the magnetic field coil, the magnetic circuit path, the poppet well, and the seat attachment point. The valve body sketch is shown in Figure 115. The main structural portion is fabricated from type 430F stainless steel because

129
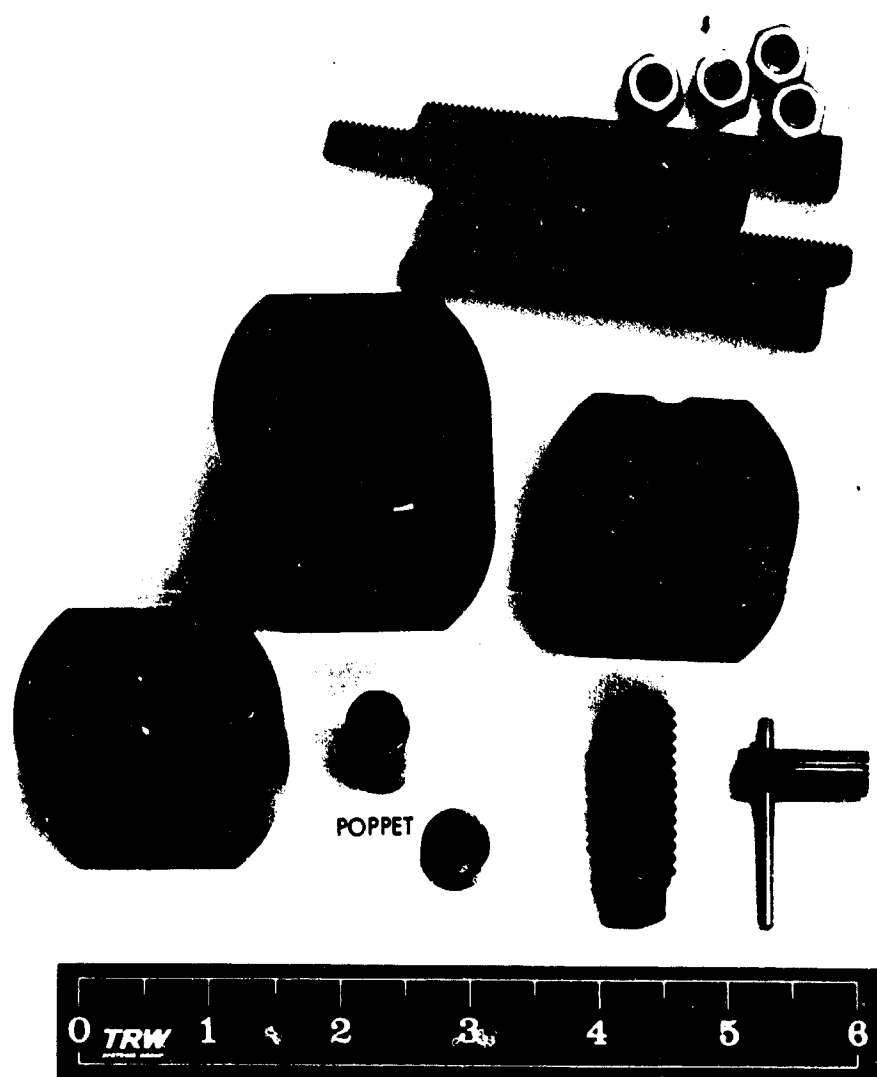
Figure 114. Poppet and Mold

of its magnetic properties. The valve body inner liner is fabricated from Monel K-500 since this region contacts the propellant.

4.3.4 Magnetic Field Coil

A schematic of the magnetic field coil, positioned on the valve body with the outer jacket for completing the magnetic circuit, is shown in Figure 116. The coil contains 1640 turns and has a resistance of 26 ohms.

4.3.5 Valve Spring

A sketch of the valve spring is shown in Figure 117. The spring was fabricated from Inconel X750 and has a spring rate of 63 lb/in^2. With no shimming of the spring, the seating pressure of the valve was 90 psi. Shims can be placed under the spring to increase the seating pressure to 360 psi.

CHAMFER 45°x.010 +.005 -.000
FOR -2,-4,AND -5
TYP

.312 REF

.0790±.0005 FOR -2
.0760±.0005 FOR -4

.030 .005 -.000

.551±.001 DIA
FOR -2 AND -5

.558 +.001 -.000 DIA FOR -4
.557±.001 DIA FOR -2

.185

.005 +.005 -.000 R
TYP

FULL R

.188

.140

1.400

.590
.100
.025

.025

1.50

1.175

.020 R MAX

-4 SLEEVE

B

.025

.025

.610 +.000 -.005 DIA

.125 DIA

.020

.094 R

3

1.375 +.000 -.001 DIA

.010 R MAX

FLANGE -5

.060

1.114 ± .001

.010 MAX

1.814

4 AFTER BRAZING AND FINAL MACHINING ANNEAL AS FOLLOWS:
HEAT TO 1500°±25°F FOR 2 TO 3 HRS IN A DRY HYDROGEN
ATMOSPHERE (DEW POINT 65°F MAX) COOL AT THE RATE OF
100°F OR LESS PER HR. UNTILL 800°F, THEN COOL AT ANY
CONVINIENT RATE (FOR -2 AND -5 PAR S ONLY)

3 BRAZE PER MIL-B-7883 IN A VACUUM OF LESS THAN 10⁻⁴ TORR
USING BRAZE ALLOY PER ASTM-B 260 (BAU-4)

2 MACHINE DIAMETERS TO OBTAIN A TIGHT FIT OF -3 WITH -2 AND -5

1. IDENTIFICATION MARKING PER PR 13-1
TYPE_____CLASS_____PART NUMBER_____

NOTES: UNLESS OTHERWISE SPECIFIED

A

Figure 115.   Valve Body

~ 12° LONG LEADS

SK 406946 JACKET

SK 406945 BOBBIN ASSY
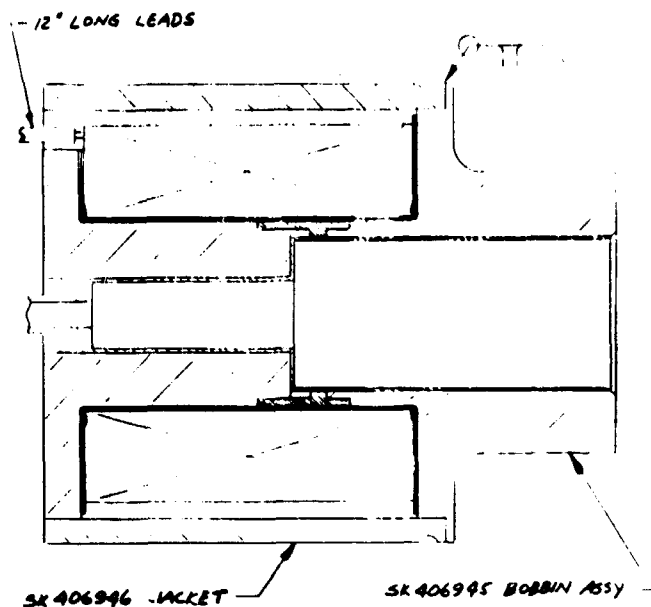
1. INSULATE BOBBIN WITH 2 LAYERS OF .005 THICK MICA SHEET

2. WIND COIL WITH NO. 29 AWG SINGLE ML MAGNET WIRE PER MIL-W-583 TYPE M CLASS 220 TO 1640 +6/-0 TURNS AND 26 ± 1.5 OHMS AT 70°F. LAYER WIND A MINIMUM OF 1/2 TOTAL TURNS

3. NO. 25 AWG LEADWIRES PER MIL-W-16878 TYPE E SHALL BE SOLDERED TO COIL ENDS. INSULATE JOINTS.

4. SECURE LEADS AND O.D OF WINDINGS WITH UNTREATED FIBRE GLASS YARN PER MIL-Y-1140 C CLASS C FORM 1, COVER ENTIRE COIL O.D USE OF 1/4 IN. WIDE X .006 FIBRE GLASS RIBBON IS OPTIONAL

5. PROTECT FLANGES OF BOBBIN FROM VARNISH AND VACUUM IMPREGNATE THE COMPLETE COIL WITH DC 997 SILICONE VARNISH. CURE VARNISH IN AN AIR CIRCULATING OVEN AT 150°F ± 25°F FOR 1 HOUR THEN AT 400°F ± 25°F FOR 4 HOURS.

6. ASSEMBLE JACKET OVER BOBBIN ASSY. AND INSTALL TEFLON TUBING OVER LEADS

Figure 116. Solenoid Assembly

~ 270° ± 30°

.803 FREE LENGTH (REF)

.712 MINIMUM WORKING LENGTH (REF)

.207 O.D +.005/-.000 (BODY)

.207 OD +.005/-.000 (INACTIVE COILS)
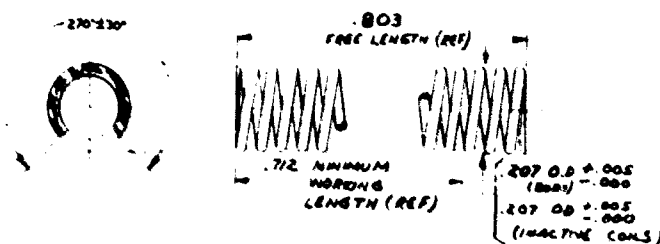
CLOSE ENDS, GRIND SQUARE WITH AXIS ± 1° AND REMOVE BURRS
14 ACTIVE COILS, 1 INACTIVE COIL EACH END
16 TOTAL COILS, REF
63.4 LBS PER INCH, RATE (REF)
4.5 LBS ± .2 LBS LOAD WHEN COMPRESSED TO .712 LENGTH
5.77 LBS ± .2 LBS LOAD WHEN COMPRESSED TO .712 LENGTH
SPRING MUST DEFLECT TO .669 LENGTH (MAX SOLID HEIGHT) WITH 9.33 LBS LOAD MAX WITHOUT PERMANENT SET
.219 DIA HOLE FOR TEST
DIRECTION OF COILING OPTIONAL

MATERIAL INCONEL X750 WIRE .04 DIA PER AMS 5699 SPRING TEMPER

Figure 117. Valve Spring

4.4 VALVE TEST PROGRAM

After assembly, the valve was subjected to a series of tests to determine its operating characteristics. These tests included:

- Power requirements
- Leak
- Low voltage resistance
- High voltage.

Several modifications were made to the valve throughout the course of the test program. These modifications were primarily changes in the molded components to improve the voltage isolation characteristics and the closing valve time. The results and implications of the changes are discussed in the individual test sections.

4.4.1 Power Requirements

Although the main objective was to develop a seat configuration that would produce adequate high voltage isolation through an electrical conducting fluid, some effort was expended in developing a total operational configuration. The valve seat was packaged and actuated with a solenoid. The main difference between this valve and a typical solenoid valve was the method used to meet the compatibility requirements. In the high voltage isolation valve, the armature and interior of the valve body were clad with nonmagnetic Monel K500 for compatibility with the propellant. This cladding produced gaps in the valve magnetic circuit, which could result in a high valve power requirement. The first test performed on the valve, and checked throughout the entire test program, was the determination of the valve "pull-in" power. This power was found to vary between 2.6 and 5.0 watts for a seating pressure range of from 90 to 360 psi. The nominal holding power was 1 watt. These values were consistent throughout the entire test program and did not vary with the valve modifications. These power levels are not excessive and the results of these tests indicate that cladding can be used to achieve compatibility in a solenoid valve.

4.4.2 Leak Test

The high voltage isolation valve was subjected to a helium leak check after its assembly and various seat modifications. In all cases, no leaks were detected through the valve seat or through the external surface of the valve using a leak detector having a sensitivity of 2×10^{-10} std cc He/sec-div.

4.4.3 Low Voltage Resistance Test

After valve assembly and completion of the preliminary tests, the valve was installed in a test assembly and filled with propellant. A schematic of the test assembly including the valve is shown in Figure 118. Prior to the high voltage tests on the first series of valve seat/poppet configuration tests, the valve was subjected to a series of low voltage
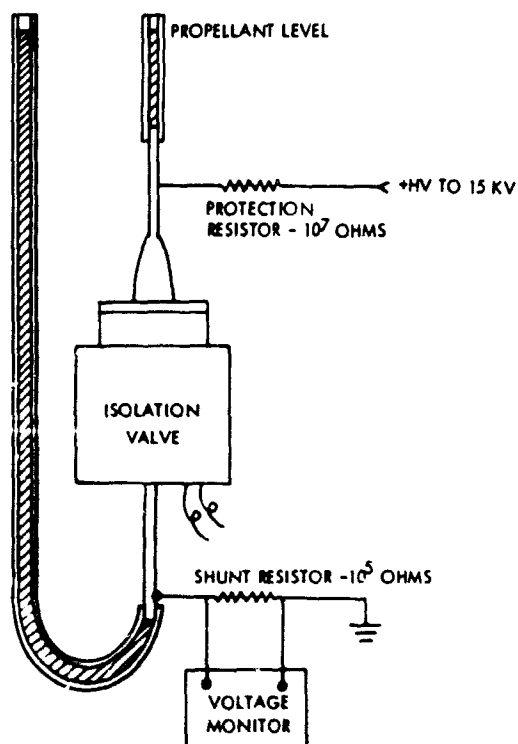
Figure 118. High Voltage
Test Schematic

(50 to 500 volts) tests to measure its closing times and its resistance characteristics. The resistance across the valve was always checked before charging with pro- pellant. Across the dry seat, the resistance was greater than 10^{12} ohms for all configurations. This was the sensitivity limit of the low voltage test unit. When charged with propellant, the low voltage tests performed on the valve indi- cated that the conductance through the valve seat decayed as an expo- nential with time. The initial resist- ance across the valve seat at valve closure was 10^8 ohms. The resist- ance would increase with time, the rate of which was a function of the seating pressure used on the poppet and changes in the seat configura- tion. In the initial seat configura- tion, a resistance value of 8×10^{10} ohms across the seat was reached 4 hours after valve closure. The poppet had a seating pressure of 200 psi during this test. After these tests, the valve was disas- sembled and the seat and poppet were inspected. The results of the inspection indicated that the conical elastomer section of the poppet was slightly concave due to differential shrinkage of the molded elastomer during the curing process. The elas- tomer mold was then modified to correct this differential shrinkage, which was caused by material thickness variations. The poppets molded after the modification had a straight conical shape.

The time for the valve to reach a resistance of 8×10^{10} ohms after closure with the modified poppet was 3 hours with a seating pressure of 200 psi and 2 hours with a seating pressure of 360 psi. The low voltage checks of this poppet indicated a resistance of greater than 10^{12} ohms 12 hours after valve closure.

4. 1.4 High Voltage Tests

The high voltage tests were performed on the valve in a step man- ner in the assembly shown in Figure 118. Initially, the valve was tested with 10 kv across the seat. In the first series of seat and poppet config- urations, the leakage current across the valve was 0.17 μamp at 10 kv at a lapse time of 1 hour after valve closure. This appeared to be the steady-state value. The leakage current at 10 kv, 30 minutes after valve closure, was 0.6 μamp. The leakage current increased to 0.2 μamp at 12 kv; however, breakdown occurred after several minutes at the 12-kv level. This breakdown occurred, in some cases, through the Hystl seat,

135

and in other cases, through the elastomeric material. The breakdown through the Hystl would originate at the tip of the metal tube molded into the Hystl and extend into the seating area. The breakdown through the elastomer would originate in the seating area and extend to the Hystl sublayer. The path would then move along the Hystl elastomer interface into the propellant.

The seat and poppet configuration was modified slightly to eliminate these breakdown paths. The seat was modified by moving the metal tube back from the sealing region to increase the thickness of Hystl along the breakdown path. The poppet was modified by eliminating a portion of the Hystl sublayer to increase the thickness of elastomer between the seating area and the Hystl interface. The valve was reassembled with the modified seat/poppet configuration and subjected to a high voltage test. The valve had a leakage current of 2.8 μamp at a voltage of 15 kv; the current remained at this level for a period of 29 hours. The voltage was applied 30 minutes after valve closure.

This same seat/poppet configuration was then subjected to 15 kv at a lapse time of 10 minutes after valve closure. The initial leakage current was 80 μamp, then decayed to 35 μamp over a 5-minute period. At this time, there was electrical breakdown through the valve. The valve was disassembled and examined; and an eroded track that extended across the entire seating region was found in the Hystl seat. This result indicated that applying high voltage without allowing sufficient time for the propellant to be expelled from the seating area would result in a failure. A typical threshold leakage current of 15 μamp was determined to be a safe upper limit to prevent damage to the seat and poppet.

Two subsequent seat and poppets were molded and tested. In these tests, voltage was applied 30 minutes after valve closure. The leakage current for these combinations was 2.5 μamp at 15 kv and appeared to be the steady-state value. The individual tests were extended for 40-hour periods.

Although the modified seat/poppet configurations were capable of withstanding a higher potential than the original ones, the leakage current through the seats was larger, apparently caused by roughening of the mold surface during usage. This roughness appeared as irregularities, and, though extremely small, caused an increase in the propellant film thickness in the seating area.

4.5 CONCLUSIONS

The final valve design demonstrated the capability of isolating 15 kv with a leakage current of 2.5 μamp, which is within the specifications outlined for the program. The valve material appeared to have adequate compatibility with the propellant; during the 16 month storage test period, there was no (or, at most, negligible) reaction between the alumina reinforced Hystl and the silica filled, Hystl reinforced, ethylene-propylene terpolymer. These materials also exhibited the capability of being outgassed to an acceptable level for use with the propellant. The

136

concept of cladding the valve armature and internal surfaces to achieve compatibility with the propellant proved to be satisfactory for use in a solenoid actuated valve. Although no effort was made to optimize the valve magnetic circuit, the "pull-in" power requirement for the valve was less than 5 watts.

The leakage current of 2.5 µamp corresponds to a power drain at 15 kv of 37.5 mw, which is an acceptable value when the valve is used for isolation of a failed thruster. A leakage current of 2.5 µamp, however, could represent a gas generation rate of 3×10^{-7} cc H_2/sec at standard temperature and pressure. At a nominal feed pressure of 1.0 psi, this corresponds to a generation rate of 4.5×10^{-6} cc H_2/sec or a total of 1.62×10^{-2} cc of H_2 in a 10-hour period. This amount of hydrogen is close to the solubility limit if dispersed in 1 cc of propellant. Therefore, it would be necessary for the valve to be actuated at frequent intervals and for sufficient propellant to be purged through the valve during the open period to avoid accumulation of gas bubbles. Formation of gas bubbles in the line of a failed thruster would not cause a problem; however, it would be a problem in the line of an operational thruster, e.g., if the valve was used for the operation of more than one thruster from a single propellant supply system or for operation with a propellant ladling system. A knowledge of the operational duty cycle would be required to define an acceptable current leakage level. However, a level of one-tenth that achieved in the final valve configuration would probably be adequate to eliminate the gas generation problem for most applications. Tests on the valve during the early part of the program (when the voltage was limited to less than 12 kv) indicated that leakage currents of this level could be achieved. The higher leakage currents measured during the latter part of the program were attributed to roughness of the seat and poppet tip surface. This roughness was due to wear in the mold, which could be reduced by using different surface treatment techniques, such as Teflon coating. A Teflon coating technique would require a complete redesign and refabrication of the molds used for this program.

137

5. NEUTRALIZATION

Colloid thruster neutralization involves slightly different considerations from the neutralization of the relatively high current, low-voltage ion thruster:

- Current levels are too low to warrant the use of discharge neutralizers

- Low-power colloid thrusters require correspondingly lower power neutralizers if overall system efficiency is to be maintained high

- The propellant can poison high efficiency cathodes.

These considerations have led to the development of an electron gun type neutralizer which can be positioned further away from the thrust beam than a more conventional space charge coupled neutralizer in order to minimize the risk of cathode poisoning by the thruster exhaust. In actual flight use, the gun current would be adjusted to provide a slight excess of electrons, thus driving the spacecraft slightly positive, in order to allow the excess negative current to be compensated by electrons drawn from the ambient space plasma.

Two basic electron gun cathode concepts were experimentally investigated in this program. One used a 0.032-inch-diameter porous tungsten plug impregnated with a barium, strontium, calcium aluminate. This plug was heated by a tungsten filament encased in alumina, which provided thermal connection to the cathode. The other source type employed a conventional Raytheon production cathode, designed for use in a 1B3 rectifier tube. This is a 1/2-inch-long spiral of 0.0019-inch-diameter tungsten/1.5% rhenium wire coated with Ba/Ca/Sr carbonates in a nitrocellulose binder. As long as the cathode is not fired and the binder is retained, it is stable with respect to atmospheric contamination.

The latter source was the more successful of the two, providing on the order of milliamperes of current for less than 1/3 watt. In addition, several life tests still in progress have demonstrated its ability to operate for time durations of 10,000 hours or more.

In addition to the experimental program, Section 5.3 describes a theoretical investigation to determine if an electron gun neutralizer can be positioned sufficiently far from the source so that only one neutralizer will be required for several colloid thrusters on board the same spacecraft. While this problem was not completely solved, the results to date indicate that this concept can be valid.

5.1 ELECTRON GUN DEVELOPMENT

5.1.1 Porous Plug Neutralizer

Two porous plug designs were investigated. The first design is shown in Figure 119a. It was mounted on an arm that could move the neutralizer parallel to the thruster beam axis or rotate it through an 8-inch circle. The neutralizer was mounted so that, when facing up, moving it parallel to the beam axis positioned it either closer to or further

138

from the diverging beam. Unfortunately, the beam divergence was greater than anticipated. This made it impossible to turn the neutralizer up without the beam striking it. For this reason the floating potential of the neutralizer beam was not measured. Beam off-performance data were obtained with the neutralizer 2 inches away from the front tub. Only 18 percent of the emitted current reached the collector at saturation; the remainder was collected by the anode. The greatest collector current measured was 200 μamp. The anode was kept at +25 volts relative to the cathode. No attempt was made to achieve higher currents because it was felt the nickel anode grid would melt at higher currents.

The second porous plug design is shown in Figure 119b. The anode was modified by removing the nickel grid and reducing the anode hole from 60 to 30 mils. Two layers of 1.5 mil tantalum sheet were wrapped around the emitter to reduce the radiated power loss. The end of the heat shield extended 5 mils beyond the cathode surface to focus electrons through the smaller anode hole. This geometry improved the gun perveance so that 30 percent of the emitted current reached the collector at saturation. Up to 6 milliamperes of current were collected from this neutralizer.

The neutralizer test circuit is shown in Figure 120. The can shield and can top are part of the neutralizer. The can shield was grounded. Both the can top and collector were 10 inches in diameter. The can could be connected by a switch to either the cathode or the anode. The can top and anode were in the same plane. The collector was mounted directly opposite and parallel to the can top. A 60 cycle ac voltage was applied to the collector through an isolation transformer. This same ac signal was applied to the horizontal input of the oscilloscope. The signal of the neutralizer current through a resistor to ground was displayed on the oscilloscope as a function of the ac voltage. A trace taken with the anode +150 volts relative to the grounded cathode and can top is shown in Figure 121. The collector was 1.25 centimeters away from the neutralizer. Following the trace from left to right, the collector potential sweeps from -100 to +100 volts. Between 0 and 57 volts the neutralizer current to the collector closely follows a $V^{3/2}$ curve. Above 57 volts, the current saturates with only a small increase with voltage. Figures 122 through 125 were taken under the same conditions as Figure 119 except that each was taken for a different anode voltage.

Figures 126 through 128 show how the neutralizer current varied with position. The traces were taken at 1, 3, and 5 cms. The collector-cathode voltage required to produce the same cur̲ ̲ach trace shows an X^n relationship where $3/4 < n < 1$. For this part of the experiment the anode voltage was kept constant, the cathode emission current was kept constant, and the can top was at cathode potential.

A hysteresis and a shift in the zero current point are apparent in Figures 126 and 127. Both effects were caused by the charging of an insulating film on the collector. This charge varied with time and with the energy and amount of the electrons. Upon removal of the collector for inspection, this film could be seen where it was discolored by electron bombardment. After the collector was cleaned and replaced, these effects were eliminated. Later, after an accidental overpressure permitted backstreaming of the

ELECTRON GUN NEUTRALIZER NO. 1
POROUS TUNGSTEN CATHODE IMPREGNATED WITH Ba, Sr, Ca, ALUMINATE
PLACED 0.015" BELOW Ni SCREEN

SPOTWELD

0.010" THICK S. S.
0.250" DIAMETER

GLASS BEAD

ANODE SUPPORT AND ELECTRICAL LEAD

ANODE

CATHODE SUPPORT
AND LEADS

CATHODE HEATER LEADS
SPOTWELD

0.060" HOLE COVERED WITH
250 MESH Ni SCREEN

SPOTWELD

GLASS BEAD

FRONT VIEW   SIDE VIEW

ELECTRON GUN NEUTRALIZER NO. 2
(CONSTRUCTION IDENTICAL TO NO. 1 EXCEPT WHERE NOTED)

ANODE

0.030" HOLE

2 LAYERS OF 0.0015" THICK TANTALUM SHEET EXTENDING 0.005" BEYOND FACE
OF IMPREGNATED TUNGSTEN CATHODE. FACE OF CATHODE PLACED 0.015"
BELOW EDGE OF 0.030" HOLE.

Figure 119. Electron Gun Neutralizer Designs using a porous tungsten
cathode impregnated with a barium, strontium, calc m
aluminate

VARIAC

V_{FIL}

COLLECTOR

I_{FIL}

CAN SHIELD

ANODE

CATHODE

HEATER

ISOLATION
TRANSFORMER

BIAS
SUPPLY

$I_{CATHODE}$

I_{ANODE}

CAN TOP

VARIAC

I_{COL}

2

S_1

$I_{CAN\ TOP}$

$10^3 \Omega$

1

HORIZ
INPUT

SCOPE
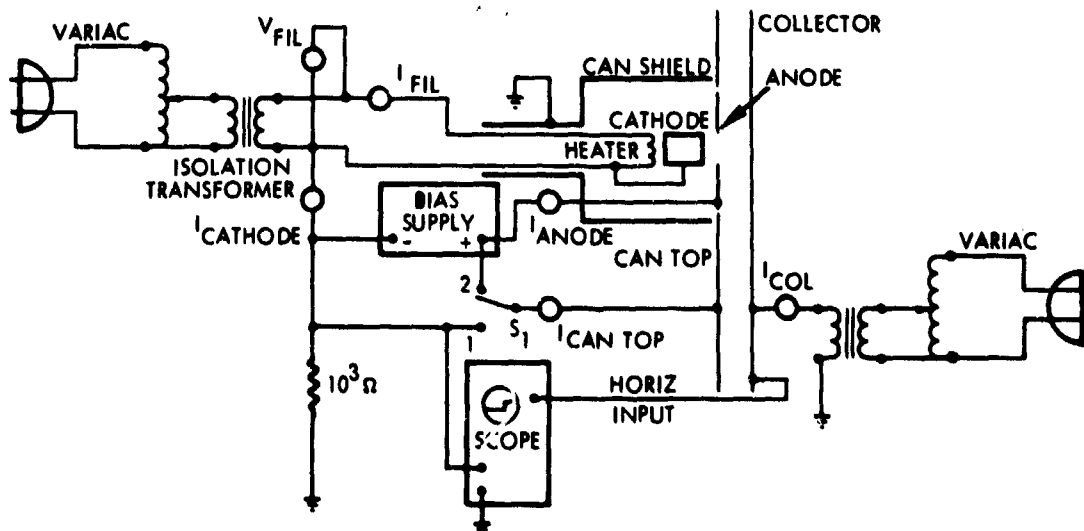
Figure 120. Neutralizer Test Circuit

140

Heater Power   = 1.44 watts

V_{anode} = +150 volts

$V_{cathode}$ = 0

$V_{can\ top}$ = 0

$I_{cathode}$ = 14.3 milliamps

Collector   = 1.25 cm from
                     neutralizer

Vertical Scale   = 1 milliamp/cm

Horizontal Scale = 20 volts/cm
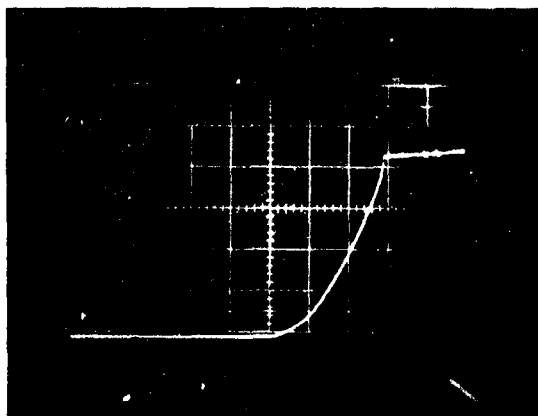
Figure 121. Emitted Neutralizer Current as Seen Across
             a 1 KΩ Resistor vs. a 200 v P/P Signal
             Applied to the Collector (-100 on left,
             +100 on right of trace)

Heater Power   = 1.44 watts

V_{anode} = +50 volts

$V_{cathode}$ = 0

$V_{can\ top}$ = 0

$I_{cathode}$ = 5.4 milliamps

Collector   = 1.25 cm from
                     neutralizer

Vertical Scale   = 1 milliamp/cm

Horizontal Scale = 20 volts/cm

Figure 122. Emitted Neutralizer Current as Seen Across
             a 1 KΩ Resistor vs. a 200 v P/P Signal
             Applied to the Collector (-100 on left,
             +100 on right of trace)

141

Heater Power   = 1.44 watts

V_{anode} = 15 volts

$V_{cathode}$ = 0

$V_{can\ top}$ = 0

$I_{cathode}$ = 7.6 milliamps

Collector   = 1.25 cm from
                     neutralizer

Vertical Scale   = 1 milliamp/cm

Horizontal Scale   = 20 volts/cm
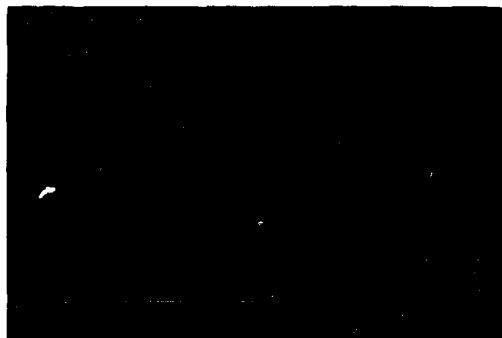
Figure 123. Emitted Neutralizer Current As Seen Across
a 1 KΩ Resistor vs. a 200 v P/P Signal
Applied to the Collector (-100 on left,
+100 on right of trace)

Heater Power   = 1.44 watts

V_{anode} = 100 volts

$V_{cathode}$ = 0

$V_{can\ top}$ = 0

$I_{cathode}$ = 11.2 milliamps

Collector   = 1.25 cm from
                     neutralizer

Vertical Scale   = 1 milliamp/cm

Horizontal Scale   = 20 volts/cm
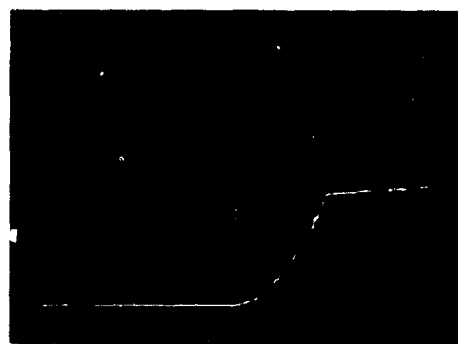
Figure 124. Emitted Neutralizer Current As Seen Across
a 1 KΩ Resistor vs. a 200 v P/P Signal
Applied to the Collector (-100 on left,
+100 on right of trace)

Heater Power   = 1.44 watts

V_{anode} = 125 volts

$V_{cathode}$ = 0

$V_{can\ top}$ = 0

$I_{cathode}$ = 13.4 milliamps

Collector   = 1.25 cm from
                     neutralizer

Vertical Scale   = 1 milliamp/cm

Horizontal Scale   = 20 volts/cm
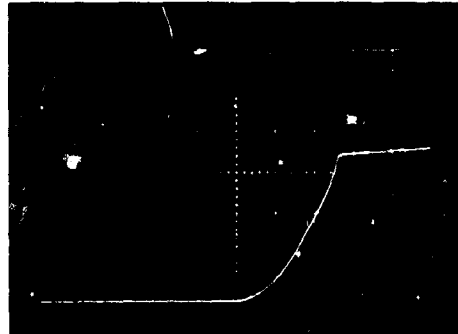
Figure 125. Emitted Neutralizer Current As Seen Across
a 1 KΩ Resistor vs. a 200 v P/P Signal
Applied to the Collector (-100 on left,
+100 on right of trace)

Heater Power   = 1.32 watts

V_{anode} = 150 volts

$V_{cathode}$ = 0

$V_{can\ top}$ = 0

$I_{cathode}$ = 6.4 milliamps

Collector   = 1.0 cm from
                     neutralizer

Vertical Scale   = 0.5 milliamps/cm

Horizontal Scale   = 20 volts/cm
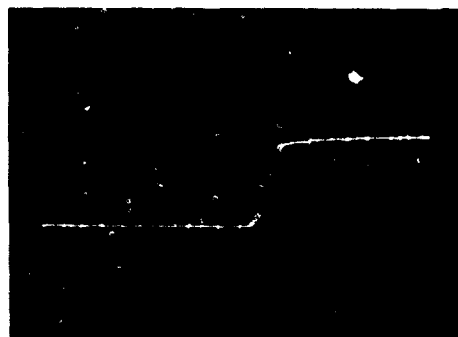
Figure 126. Emitted Neutralizer Current As Seen Across
a 100Ω Resistor vs. a 200 v P/P Signal
Applied to the Collector. This Figure plus
Figures 127 & 128 show how the neutralizer
current varied with collector distance.

143

Heater Power   = 1.32 watts

V_{anode} = 150 volts

$V_{cathode}$ = 0

$V_{can\ top}$ = 0

$I_{cathode}$ = 6.7 milliamps

Collector   = 3 cm from
                      neutralizer

Vertical Scale   = 0.5 milliamps/cm

Horizontal Scale   = 20 volts/cm
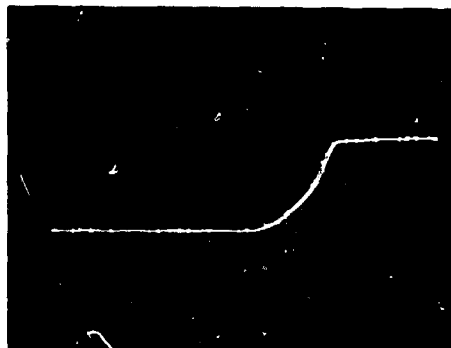
Figure 127. Emitted Neutralizer Current As Seen Across
a 100Ω Resistor vs. a 200 v P/P Signal
Applied to the Collector. This Figure plus
126 and 128 show how the neutralizer current
varied with collector distance.

Heater Power   = 1.32 watts

V_{anode} = 150 volts

$V_{cathode}$ = 0

$V_{can\ top}$ = 0

$I_{cathode}$ = 6.8 milliamps

Collector   = 5 cm from
                      neutralizer

Vertical Scale   = 0.5 milliamps/cm

Horizontal Scale   = 20 volts/cm
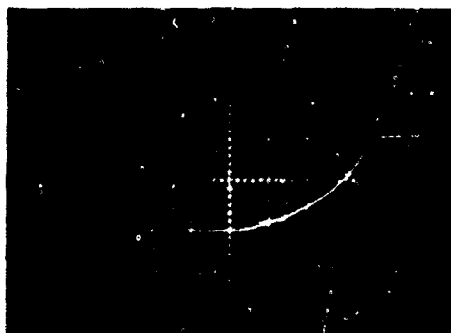
Figure 128. Emitted Neutralizer Current As Seen Across
a 100Ω Resistor vs. a 200 v P/P Signal
Applied to the Collector. This Figure plus
126 and 127 show how the neutralizer current
varied with collector distance.

diffusion pump, these same effects returned indicating that the pump oil was the source of the film.

It was felt that the perveance could be increased by connecting the can top to the positive anode. This would be equivalent, in space, to running the cathode negative relative to the spacecraft skin (the can top simulates the spacecraft skin). Figures 129 through 131 were taken in this configuration. The traces were badly distorted by secondary electron currents when the collector was negative relative to the can top. Figure 129 was taken with the anode-can top +25 volts relative to the cathode. There is only a small secondary electron effect here, but in Figure 130 the secondary electron current from the collector virtually cancels out the current to it from the neutralizer until the collector becomes more positive than the +50 volt anode-can top potential. Figure 131 shows the same effect with the anode-can top at +100 volts. Despite the secondary electrons, when the collector was just slightly above the can top potential, all of the current was collected. Obviously this is much better perveance than when 50 to 100 volts were required to collect all the current while the can top was at cathode potential.

A reduction in the transmissivity of the electron gun occurred some time between Figures 123 and 124. This drop from 30 to 18 percent in net output current was caused by a shift of the cathode to one side. The normal operating vacuum of 5×10^{-7} mm Hg had no effect on cathode current output but exposure to either oxygen or acetylene at pressures of 5×10^{-7} poisoned the emitter. The poisoning effect of oxygen could be reversed by a brief exposure to acetylene, but prolonged exposure would again poison the emitter. The acetylene poisoning could be reversed by a brief exposure to oxygen. Obviously, too much carbon or too much acetylene will adversely affect emission from this type (barium, strontium, calcium aluminate) of coating.

Heater Power	= 1.37 watts
V_{anode}	= 25 volts
$V_{cathode}$	= 0
$V_{can top}$	= 25 volts
$I_{cathode}$	= 1.4 milliamps
Collector	= 5 cm from neutralizer
Vertical Scale	= 0.5 milliamp/cm
Horizontal Scale	= 20 volts/cm

Figure 129. Emitted Neutralizer Current Plus Secondary Electron from Collector as Seen Across a 100Ω Resistor vs. a 200 v P/P Collector Signal (-100 volts on the left and +100 volts on the right). Anode and can top now connected.

145

Heater Power   = 1.37 watts

V_{anode} = 50 volts

$V_{cathode}$ = 0

$V_{can top}$ = 50 volts

$I_{cathode}$ = 3.1 milliamps

Collector   = 5 cm from
                    neutralizer

Vertical Scale   = 0.5 milliamp/cm

Horizontal Scale = 20 volts/cm

Figure 130. Emitted Neutralizer Current Plus Secondary
             Electron from Collector as Seen Across
             a 100Ω Resistor vs. a 200 v P/P Collector
             Signal (-100 volts on the left and +100 volts
             on the right). Anode and can top now
             connected.

Heater Power   = 1.37 watts

V_{anode} = 100 volts

$V_{cathode}$ = 0

$V_{can top}$ = 100 volts

$I_{cathode}$ = 6.7 milliamps

Collector   = 5 cm from
                    neutralizer

Vertical Scale   = 0.5 milliamp/cm

Horizontal Scale = 20 volts/cm

Figure 131. Emitted Neutralizer Current Plus Secondary
             Electron from Collector as Seen Across a
             100Ω Resistor vs. a 200 v P/F Collector
             Signal (-100 volts on the left and +100 volts
             on the right). Anode and can top now
             connected.

The data accompanying Figure 121 indicate that in order to get 4.5 milliamps to the collector 1.25 cms away it took 3.17 watts (1.44 watts heater power, 1.47 watts dissipated on the anode, and 0.26 watts injection loss). There are several ways of reducing this power. The transmissivity of the gun could be increased through improvements in the electrode design. This would decrease the power wasted because of emission current being intercepted by the anode. A second method of reducing the power required would be to improve the perveance of the interior part of the gun (150 volts were necessary to get 4.5 milliamperes through this gun).

5.1.2 1B3 Neutralizer

A third way of reducing the power required would be to use a more efficient emitter. For this reason the design was modified to employ coated 1B3 filaments which are capable of emitting as much as 30 milliamperes for only 1/4 watt. As previously stated, this cathode has the further advantage that as long as it is not activated and the binder retained, it is stable with respect to atmospheric contamination.

Figures 132 and 133 are, respectively, a schematic and photograph of the experimental design. The filament is mounted on a glass tube base, as received from the manufacturer. It is partially enclosed within a tubular shield which is kept at the filament potential. An accelerating anode is placed outside of and just in front of the shield. This configuration allows a large current to be drawn out of the structure with minimal anode current.

All tests were run in an ion pumped glass bell jar and it soon became apparent that any insulating surfaces which were allowed to charge negatively would confuse the experimental data by returning electrons to the anode. Because of this, it was necessary to place a grounded copper screen liner in the bell jar.

The accelerating injection voltage was obtained by applying a negative bias to the filament while holding the anode at ground potential, thus simulating the spacecraft skin. Total emission and anode currents were monitored as a function of negative bias, using a two-pen x-y recorder.

Figures 134 through 136 show the results obtained during an early test. The data in Figure 134, taken at the beginning of the test, are extremely impressive. With well under 1 watt heater power it was possible to obtain 2-1/2 ma total current at 50 volts injection voltage and 4 ma at less than 70 volts. In the course of approximately 180 hours the performance decreased to where 1.4 ma were obtained at 50 volts and 75 volts were needed to obtain 2 ma. In all cases, the anode current was of the order of tens of microamperes. A slight hysteresis was observed in that the curve going up in voltage was always slightly below the down-going curve. It is suspected that this was probably caused by the remaining insulating surfaces charging up, since the effect was much more pronounced before the grounded screen was added to the system. However, it is also possible that there is a slight effect caused by ohmic heating of the oxide coating by the emission current. From 154 to 211.7 hours the neutralizer performance remained essentially constant.

147
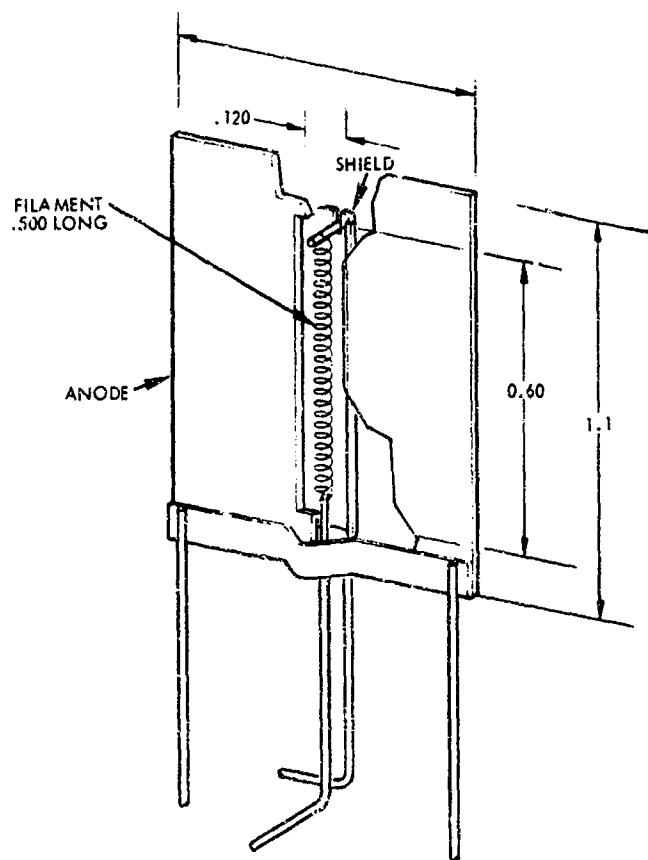
Figure 132. Filament Source Gun Neutralizer Schematic
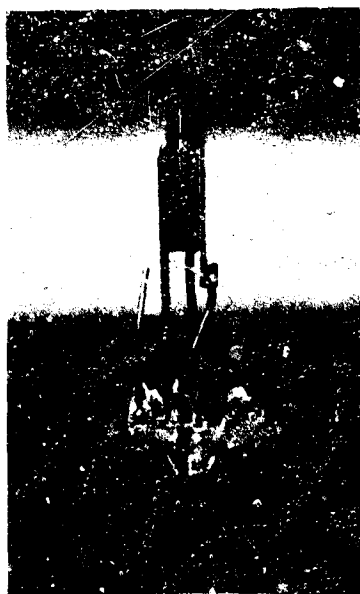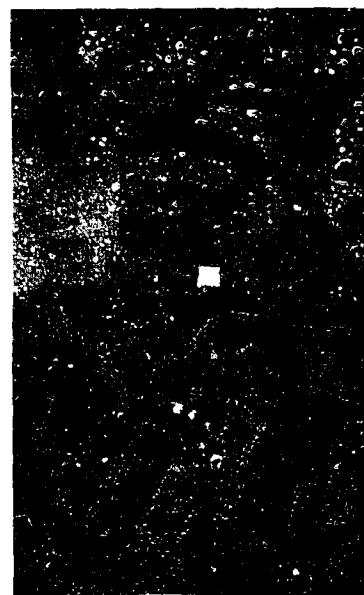
(a) Side View   (b) Front View

Figure 133. Filament Source Gun Neutralizer

148
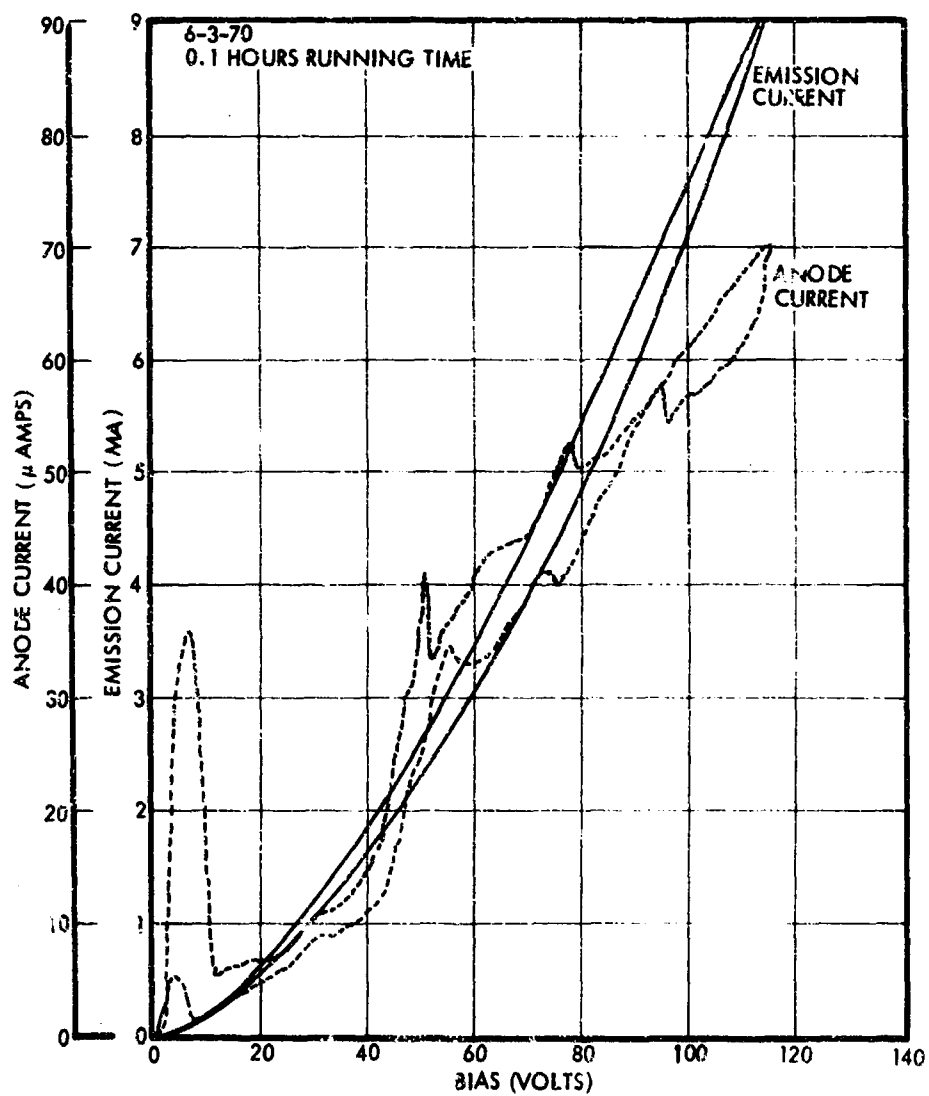
Figure 134. Electron Gun Performance at Start of Test
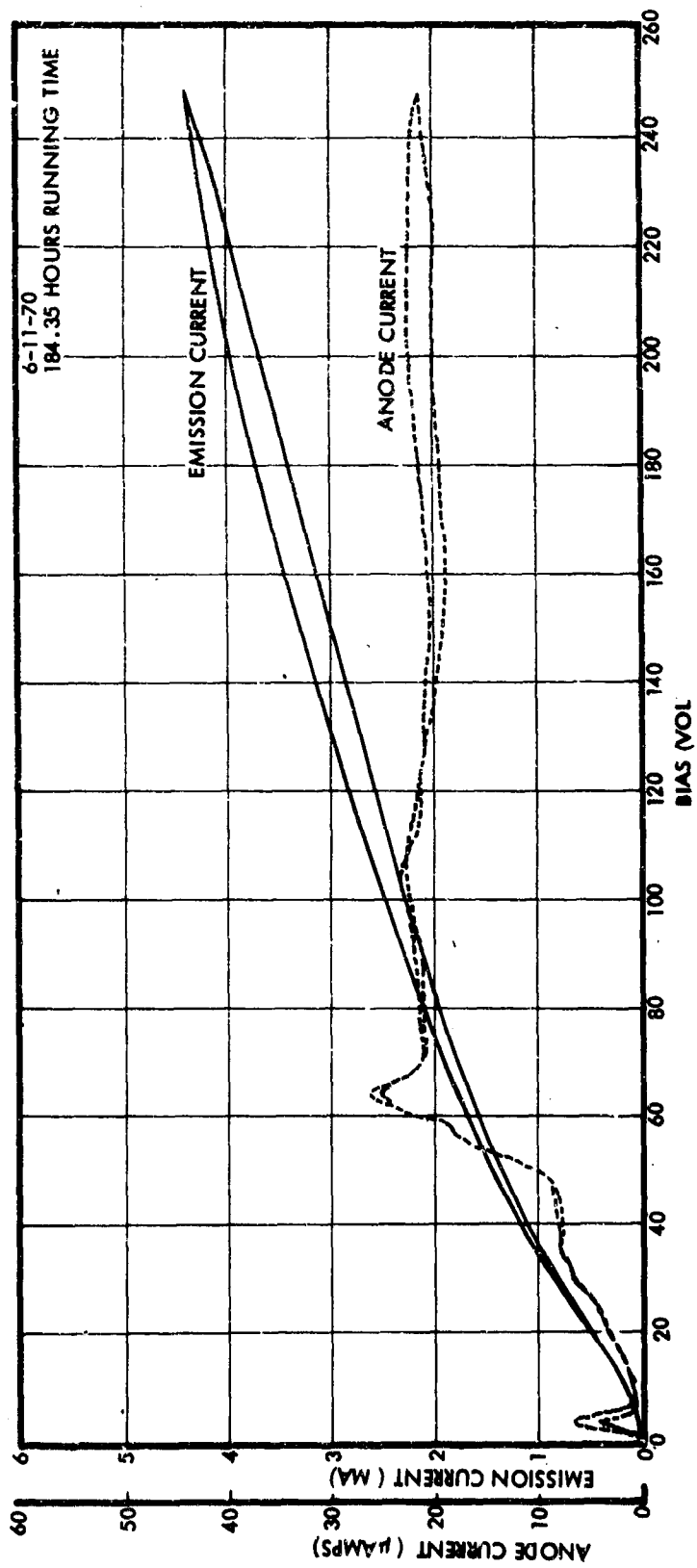
Figure 135. Electron Gun Performance After 184 Hours
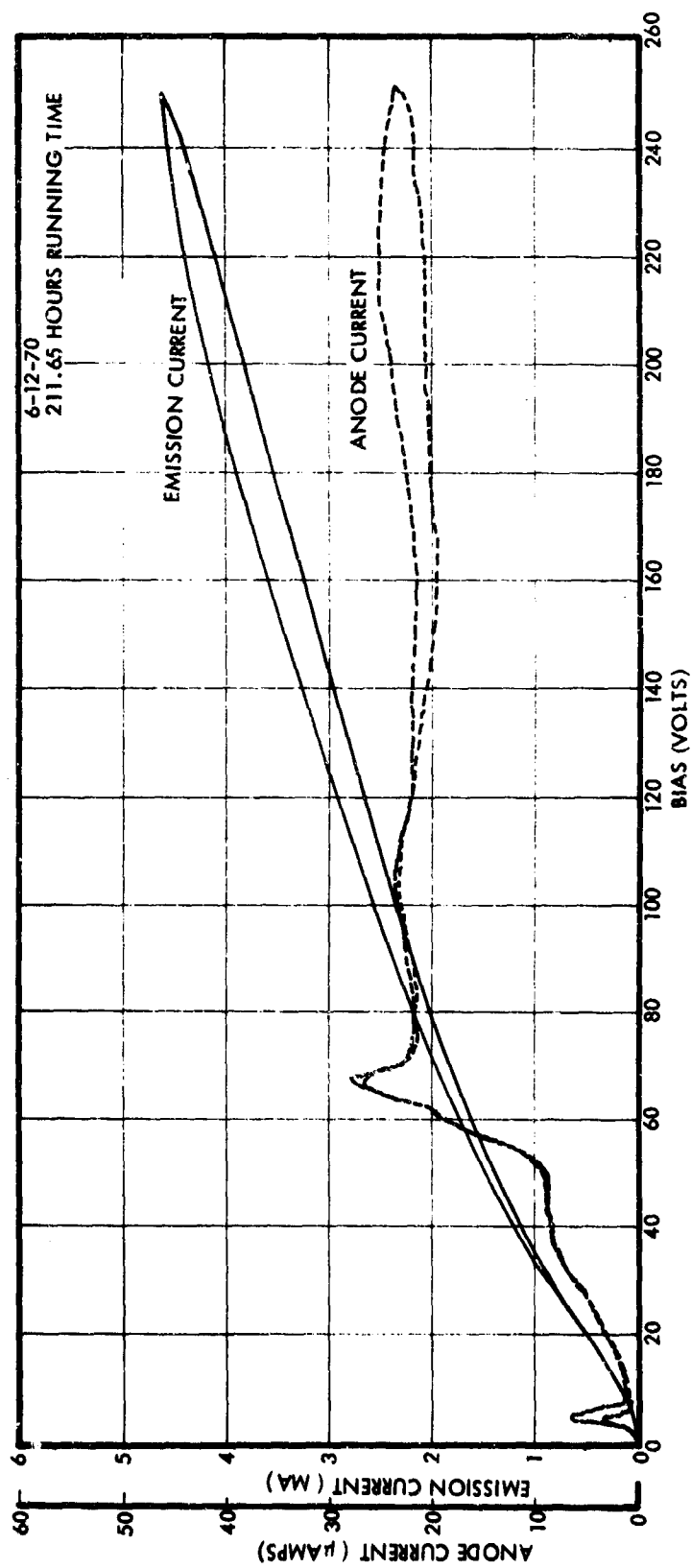
Figure 136. Electron Gun Performance After 211 Hours

151

At this time an experiment was performed to determine if further activation procedures could improve performance. The procedure followed at the beginning of the experiment consisted of slowly raising the cathode temperature to 1.25 volts, at a sufficiently slow rate of temperature rise to maintain the system pressure below 2×10^{-5} torr. Later information obtained from the manufacturer described the production line activation sequence. These procedures included briefly raising the cathode to much higher temperatures than previously employed in our experiments. Specifically, the manufacturing activation process included RF heating the surrounding anode to a white hot temperature while raising the filament heating current to 0.38 ampere. After this information had been obtained, it was decided to briefly raise the cathode heater current in the laboratory test to 0.4 ampere to ascertain if an improvement in emission could be obtained. After this was done, the emission current dropped to zero and all further attempts to reactivate the cathode failed. In retrospect, what probably happened is that the higher temperature desorbed materials from the adjacent electrodes, thus poisoning the cathode. For this reason future experiments involved going through the full high temperature cycle at the beginning of the activation period before the carbonates had completely decomposed.

5.2 LIFE TESTS

One of the goals of the present program was to life test several neutralizers for more than 5,000 hours. The approach taken here was to begin a preliminary test with a single neutralizer; if this gave evidence of testing a long time, then a simultaneous test would be instituted with three other neutralizers.

The single gun test has been operated at 95 volts injection voltage and approximately 0.3 watt heater power. Figure 137 shows the time history of the test for the first 6285 hours of steady operation at which time the emission current was very slowly decaying and had dropped to 1.35 ma. At this time a timer was installed to cycle the neutralizer on-off continuously. Figure 138 shows a strip chart record of a typical period of performance during the cycling operation. It can be seen that at the end of each on period the neutralizer has not quite reached its steady-state equilibrium performance. The test is still running and has accumulated a total 10,082 hours of on time and 50,268 on-off cycles. The emission current is currently at 1.30 ma and is still slowly dropping off.

After the single gun test had accumulated 2000 hours, it was felt that enough data had been acquired to justify starting a simultaneous test of three neutralizers. Figure 139 is a photograph of the ion pump test station. The basic test circuitry is shown in Figure 140. Essentially the same activation procedure as used for the single gun test was followed. It was originally planned to activate all three neutralizers simultaneously, but it was found that this generated too high a gas load on the system. It was therefore decided to activate one filament at a time, in succession. It is believed that this caused a slight poisoning of neutralizer number 1, the first one to be activated, since its emission current is slightly below that of the other two.

152
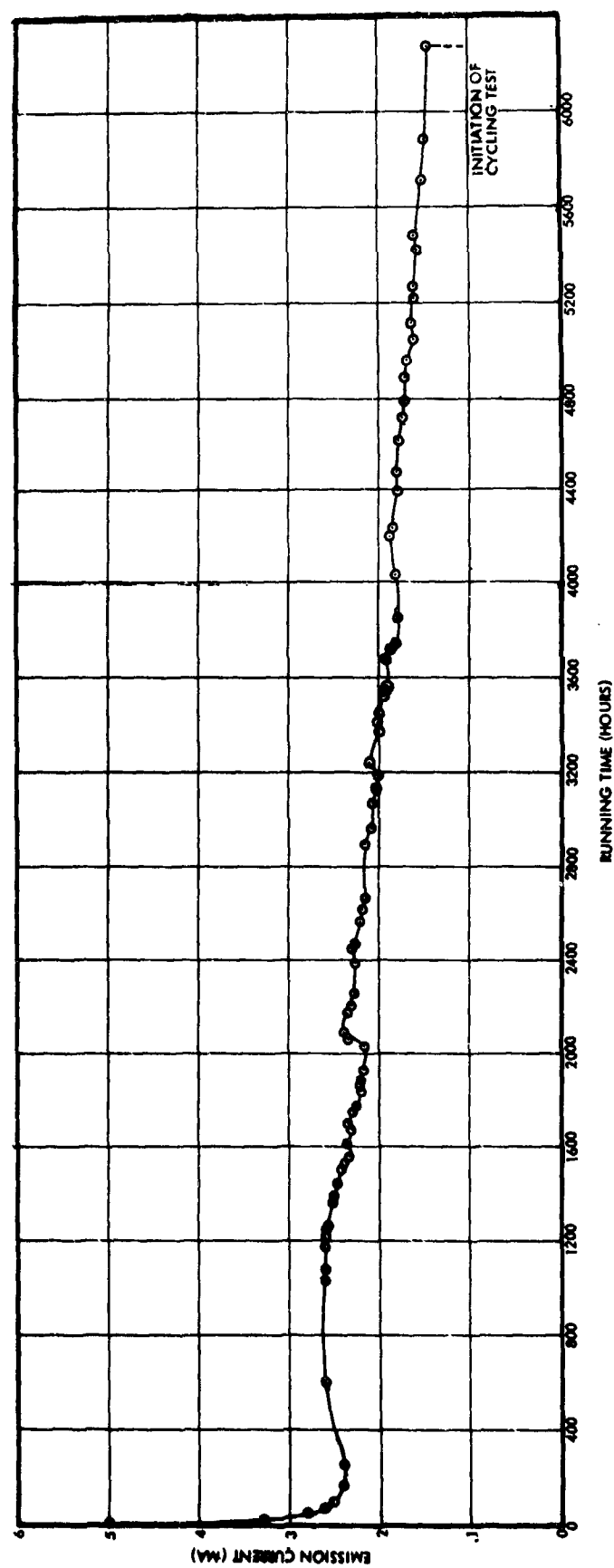
Figure 137. Single Neutralizer Life Test Performance Data

153
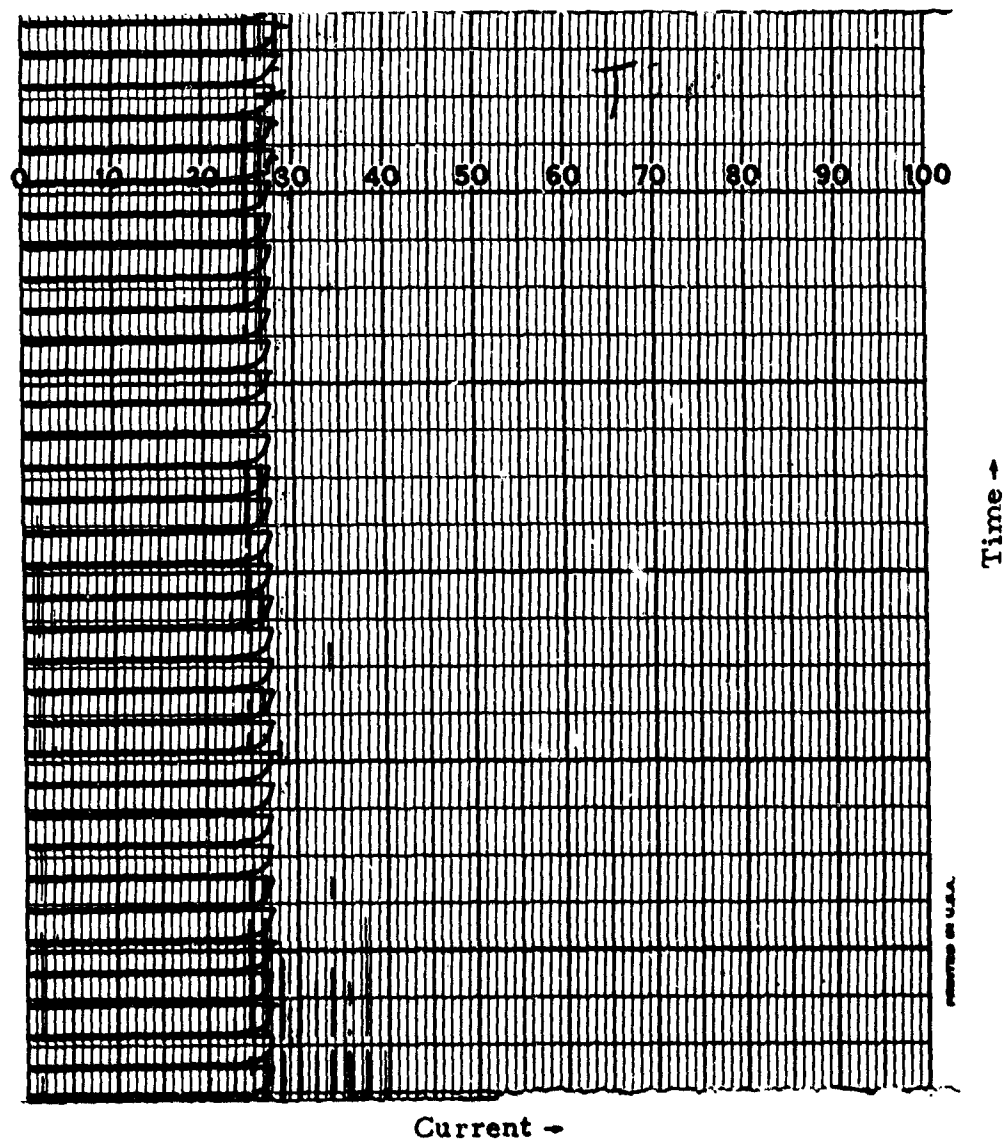
Figure 138. Strip Chart Record of Emission Current as a
Function of Time During Electron Gun
Neutralizer Cycle Life Test. Horizontal axis
is 5 milliamperes full scale, vertical scale
is 7.5 minutes/division.

154

TEST CHAMBER

STRIP CHART RECORDER

TEST CIRCUITS
AND
METER MONITORS

HEATER
SUPPLY
VARIACS

TOTAL TIME INDICATOR

SOLA TRANSFORMER
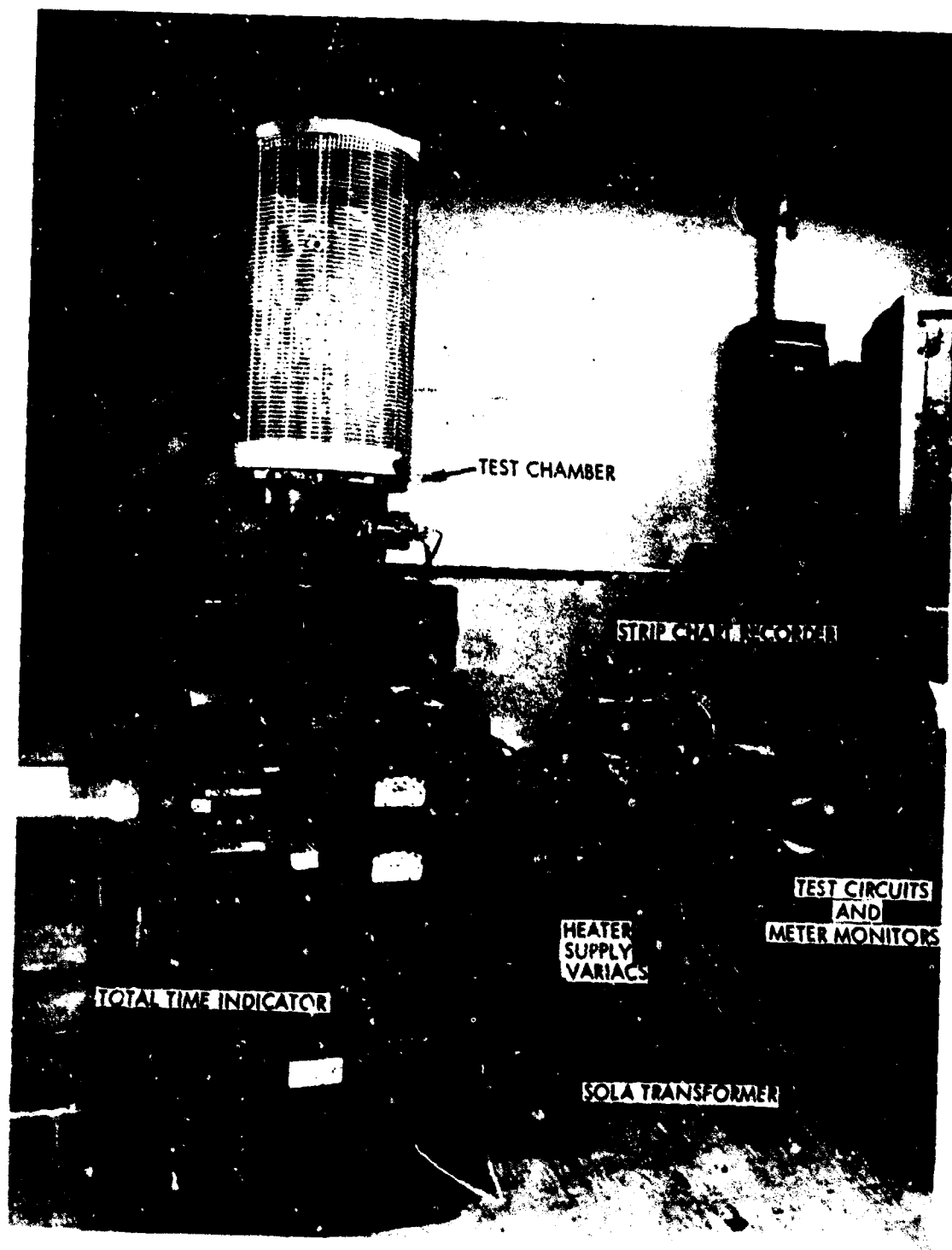
Figure 139. Neutralizer Life Test Station
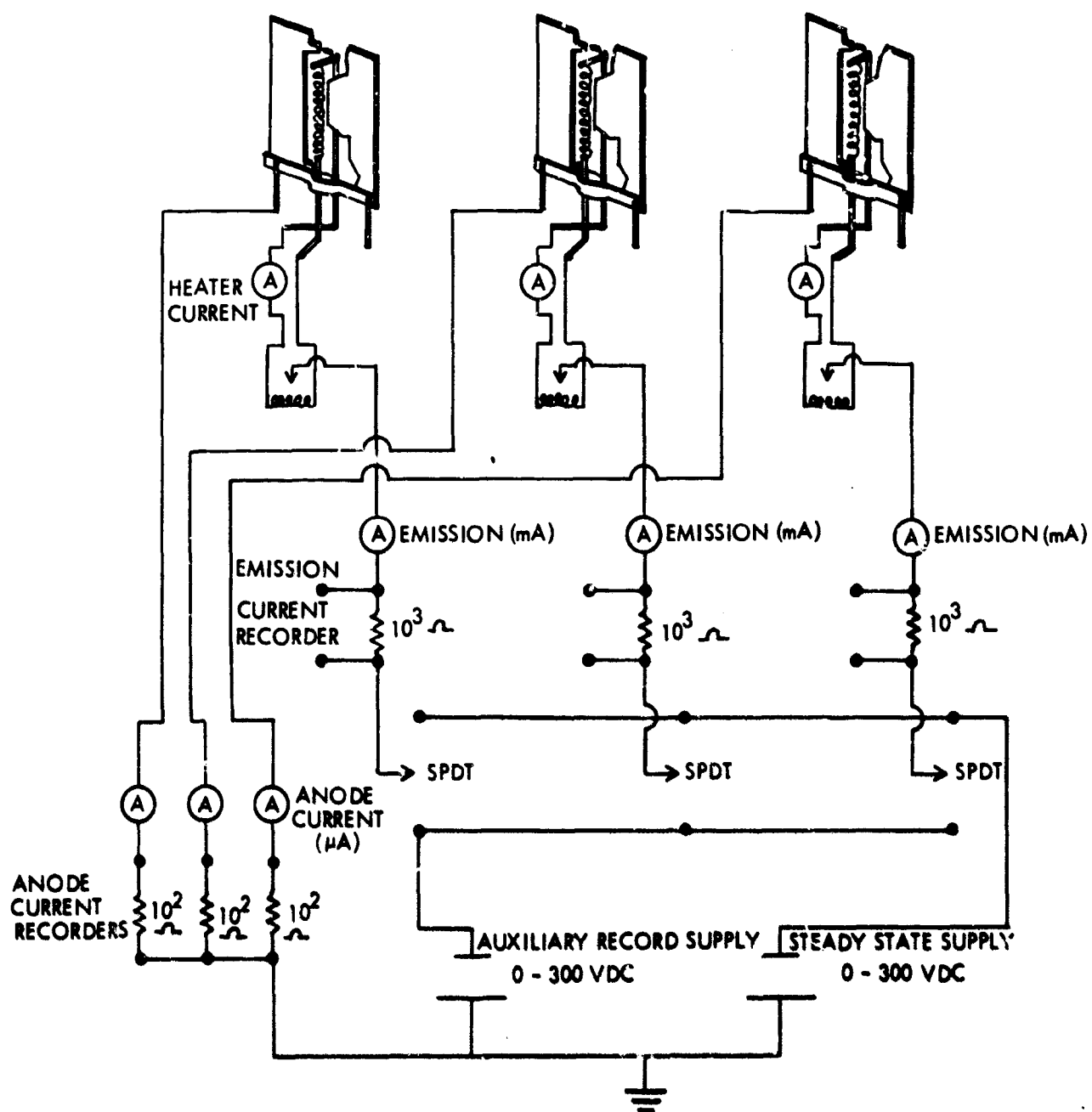
Figure 140. Circuitry for Three Gun Life Test

In normal operation the filaments are biased at -95 volts by a single steady state supply. An auxiliary record supply is also provided to allow a volt-amp curve to be plotted on any one neutralizer while holding constant operation for the other two neutralizers. In addition to series ammeters, load resistors and pickoff points are provided for continuous current monitoring.

The effect of the gas load on the 100 liter/second ion pumped system can be appreciated from the fact that although the system pressure was 4.8×10^{-8} torr before the test (as indicated by the ion pump current) it quickly rose to 10^{-4} torr when simultaneous activation was attempted. The steady-state test pressure is currently 1.2×10^{-6} torr. In retrospect, it appears that the high gas load was caused by evaporation of the nitrocellulose binder, rather than the actual activation reaction; perhaps in future tests it would be better to first evaporate the binder from all three filaments before proceeding to the higher temperature activation phase. However, this problem would not exist on an actual spacecraft.

The initial performance levels (after 310 hours) are shown below:

	Filament			Emission	Bias
	vac	amps	watts	ma	volts
Neutralizer No. 1	1.34	0.201	0.27	3.81	95
Neutralizer No. 2	1.34	0.200	0.27	5.79	95
Neutralizer No. 3	1.35	0.200	0.27	5.38	95

The test is still in progress after having passed 8446 hours. The test history is shown in Figure 141. Approximately 350 hours were required before the filaments leveled off at their steady-state levels. Since these levels were considerably higher than the 1.5 ma program goal, the emission currents for neutralizers one and three were reduced to a more conservative 2 ma in order to increase the probability for a successful long-term test. The currents for these two neutralizers drifted upward slightly and after approximately 2150 hours neutralizer 1 was again reduced to 2 ma. The present performance levels are shown below.

	Filament			Emission	Bias
	vac	amps	watts	ma	volts
Neutralizer No. 1	1.12	0.182	0.204	1.75	95
Neutralizer No. 2	1.09	0.206	0.364	4.10	95
Neutralizer No. 3	1.07	0.170	0.182	2.02	95

157
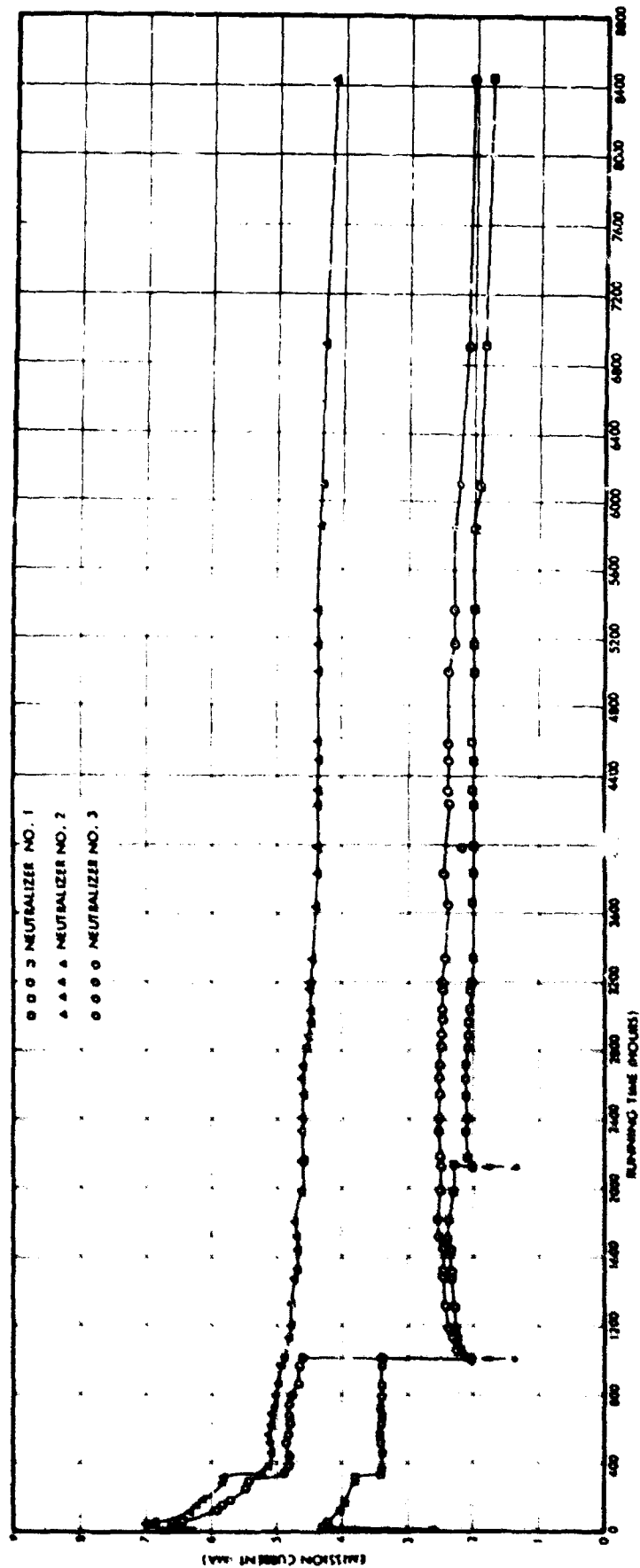
Figure 141. Three Neutralizer Life Test Performance Data: (a) neutralizer 1 and 3 heater inputs reduced to obtain 2 ma emission; (b) neutralizer 1 heater input further reduced to 2 ma emission

158

5.3 NEUTRALIZER INTERACTION WITH ANNULAR THRUSTER

Two neutralizers were investigated during the program's thruster life-test phase. An electron gun neutralizer whose cathode was expected to rapidly poison in the test environment was included to demonstrate its ability to function satisfactorily prior to poisoning. A tungsten wire neutralizer was used to provide neutralization throughout the remainder of the test, thus demonstrating that long-term laboratory testing, as far as the thruster is concerned, is compatible with neutralization.

The tungsten neutralizer consisted of an 0.003-inch-diameter, 0.750-inch-long non-sag tungsten wire spot welded to 0.030-inch-diameter nickel support rods. This neutralizer ran for a total of 2086.9 hours. This was longer than the actual thruster operation since it was allowed to remain on during a period in which the thruster was turned off for several days following a circuit breaker failure after approximately 1700 hours. During the course of the test, the neutralizer resistance increased from 2.3 to 4.0 ohms and the required heater power remained relatively constant at approximately 2 watts.

Although the gun neutralizer poisoned rapidly because of the hydrocarbon background within the test chamber, it was possible to obtain an understanding of its interaction with the thruster. Figure 142 shows the emission current and collection Faraday cage floating potential as a function of gun bias. The data are what would be expected for this high impedance source. At low injection bias (< 10 volts), the electron current is less than the beam current and the collector is driven highly positive, triggering a limiting neon bulb* at approximately 60 volts. At -11 volts, the electron current equals the beam current and the floating potential is approximately zero. As the bias is raised further, the floating potential continues to track approximately 11 volts more positive than the gun bias. Thus, floating potential versus gun bias is a straight line in this region until the neon safety bulb is once again triggered at approximately 65 volts. The electron current increase with voltage in this region is probably caused by an increase in gun accelerating electrode drain and leakage through the large (24-inch diameter) pumping port in the Faraday cage wall. The latter leakage is energetically favorable when the plasma potential within the cage is negative with respect to the grounded external pumping ports.

Figure 143 shows similar data for the tungsten wire neutralizer which was in operation throughout the test. The data are characterized by a relatively high injection voltage of the order of 70 volts. For positive floating potentials, a neutralizer emission plateau of 88 μamps was observed, indicating that probably some electrons from other sources are finding their way into the cage. As with the gun neutralizer, at negative floating potentials excess electrons must be supplied to compensate for leakage to the grounded components of the vacuum system. The main difference between the low impedance of the space charge coupled tungsten wire and the high impedance of the gun lies in the positive floating potential region of the two curves. The wire automatically delivers the current required to hold a constant floating potential. The gun is not influenced by

---

*The neon bulb is connected between the collector and ground to prevent the accidental build-up of excessively high potential on the floating collector.
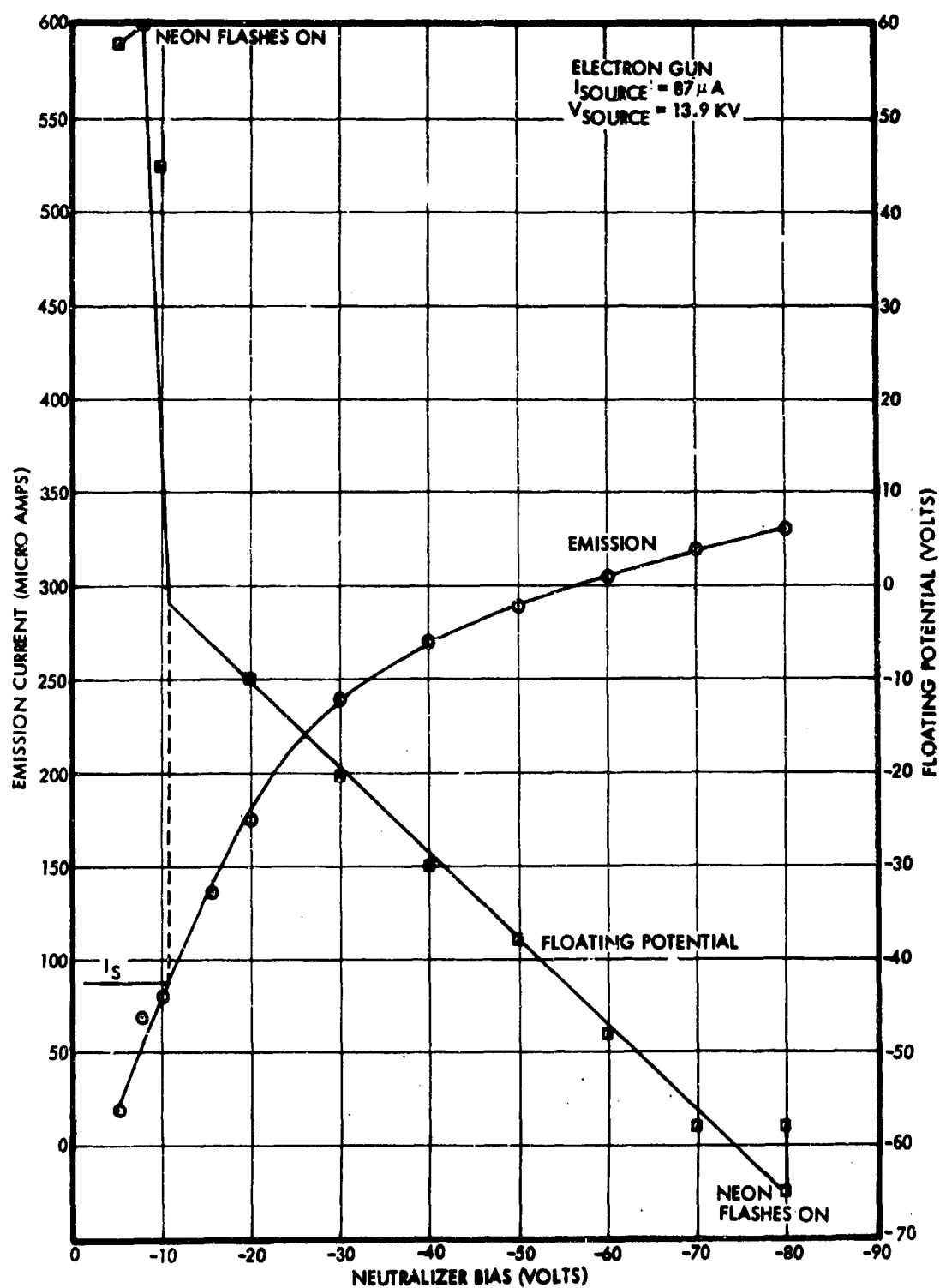
Figure 142. Electron Gun Neutralizer Ireraction with Annular
Thruster (I_S = Source Current)

160
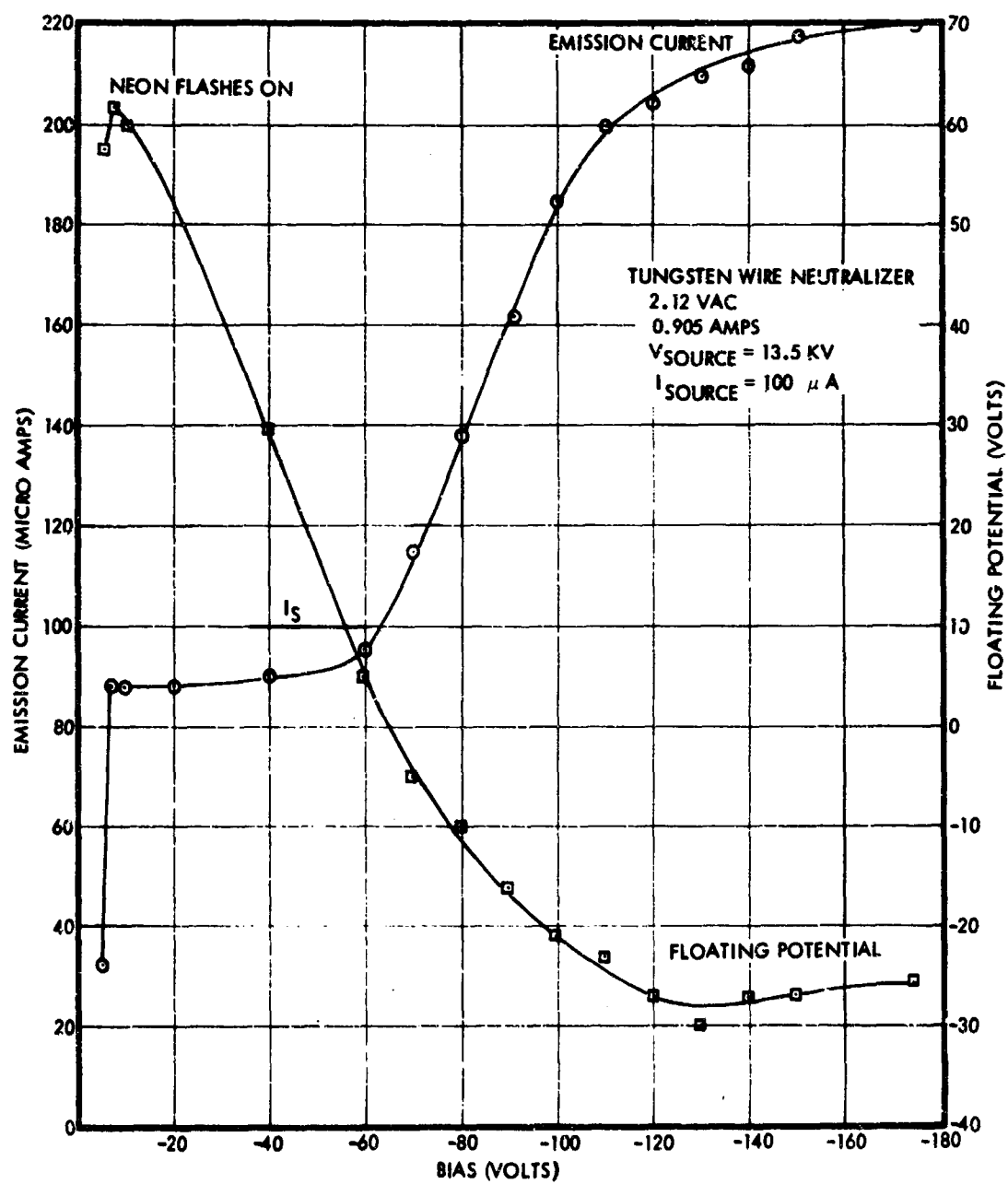
Figure 143. Tungsten Wire Neutralizer Interaction with Annular Thruster (I_S = Source Current)

161

external conditions and, hence, allows the potential to rise to the neon breakdown point without providing compensating electrons. This illustrates the fact that a gun must always be biased to provide excess electrons for effective neutralization to take place. Once this condition is met, it is easy to control floating potential by adjusting the gun bias.

5.4 NEUTRALIZATION OF AN ELECTROSTATIC THRUST BEAM BY ELECTRONS FROM AMBIENT SPACE PLASMA

The role of the neutralizer is a dual one: first, to maintain zero net current from the spacecraft and second, to provide the electrons which accomplish point-to-point neutralization of positive space charge within the thrust beam. In the case of colloid thrusters, in particular, where currents are relatively small and potentials relatively high, it may be possible for the electrons in the ambient space plasma to provide the space-charge neutralization. If the neutralizer is not needed for space-charge neutralization only, a significant simplification of the neutralizer system can be realized.

A theoretical study of this problem has been undertaken. This section describes the objectives of this study, the overall approach to the problem, a detailed derivation of the basic mathematical statement of the problem, the current state of the problem solution, and provides an outline of the steps to be taken to complete the study. Some details of the numerical techniques used in related calculations are set forth in an appendix.

5.4.1 Objective of the Study

The primary objective is to establish that the exhaust from a colloid thruster can be neutralized by the ambient plasma that exists in the environment in which these thrusters will be operating and that the only requirement for a neutralizer is to release enough electrons into space to provide a zero net flow of current from the spacecraft, but without the necessity of any coupling between these electrons and the beam.

This will allow an electron gun neutralizer to be located at a point on a spacecraft which is remote from the thruster, and therefore not subject to any deterioration caused by a reaction between the expellant material and the neutralizer filament. This also implies that one neutralizer could neutralize an arbitrary number of thrusters. At the level of currents required for colloid thrusters the electron gun power can be regarded as almost independent of current; that is 10 ma of electrons can be supplied with only slightly more gun power than the 1 ma required for a single small thruster.

With these advances the problem of making a satisfactory neutralizer would become relatively trivial, and the degradation of overall efficiency caused by the neutralizer power would be reduced to an insignificant level.

A complete examination of the feasibility of this concept requires the calculation of detailed information about potentials and charge densities everywhere in the exhaust. While not a primary goal of this program, this information will also assist in calculating what interference might exist between the thruster and other spacecraft subsystems.

162

The main point of the mathematical analysis, however, is to demonstrate the existence of a physically realizable solution to the problem. If, on the other hand, subject to the boundary conditions and environmental constraints of a typical synchronous satellite application of this concept, no self-consistent stable charge and potential distribution can be found, then we can suspect that the proposed neutralization concept is not valid. That is, the proof of the feasibility of the concept will depend on our ability to solve the analytical problem it presents.

5.4.2 Outline of the Analysis

There are several broad aspects to the analysis of this problem: one is finding an equilibrium solution; others involve questions of accessibility and stability of the equilibrium solution, and the range of applicability of the solution. If physical paths to the equilibrium solution can be demonstrated, and the solution is shown to be free from instabilities that would tend to drive electrons out of the beam, then an equilibrium solution can be obtained.

5.4.2.1 Equilibrium Solution

In this problem it is assumed that the space plasma is a thermally equilibrated plasma and remains at thermal equilibrium even in the center of the beam. For a typical colloid thruster accelerating voltage, the maximum potential to be expected within the neutralized thrust beam has negligible effect on the trajectories of the directed positively charged particles.[*] This fact makes possible the assumption of a positive charge density profile that is independent of the potential distribution in the beam. The electron charge density function is completely defined by the requirement of thermal equilibrium, and the problem is a well-defined one, which, together with the boundary conditions of zero potential at the vehicle surface and within the space plasma, has an unique solution. Finding this solution is the first task of the analysis and is covered in Section 5.4.3.

5.4.2.2 Accessibility and Stability of the Solution

The next questions which must be raised are the parallel questions (1) as to the processes by which electrons get trapped and thermalized inside the beam, and (2) whether there are instabilities for the derived distribution function which tend to drive electrons out of the equilibrium potential well which is formed.

It is easy to enumerate many mechanisms by which electrons are trapped in the beam, e.g., electron-ion, electron-electron and electron-atom collisions. However, the total rate at which trapping collisions occur has not yet been determined. Although it can be a complicated problem to include details of electron orbits in the complicated field of the beam, no difficulties are anticipated in making approximate calculations based on estimated trajectories and known values of inelastic scattering

---

[*]This is not quite true for the relatively low voltages and high current densities which exist in ion engines.

cross sections (with atoms) and coulomb scattering cross sections (with electrons and ions).

From the electron distribution function and the ion velocity distribution, which is known from the time-of-flight laboratory data, estimates of two-stream instability can be made. If regions of instability exist, then growth rate must be compared with damping rates and with the rate at which particles leave and enter the regions of instability.

5.4.2.3 Comparison of Colloidal and Ion Thrusters

Finally, it is important to be able to refine the ideas so that they can be used for a wide range of charge-to-mass ratios. It is clear from several elementary considerations that colloid thrusters will be neutralized by the space plasma with much greater ease than Cs^+ or Hg^+ ion beams, but it remains to be shown that there is some q/m value below which it is possible to depend on the space plasma and above which one must depend on the closely coupled neutralizers commonly regarded as necessary.

5.4.3 Mathematical Statement of the Problem

It is normally supposed that space charge neutralization of ion engine or colloid thruster beams is accomplished by the electrons drawn from the neutralizer. It is not clear to what extent it is necessary to depend on these, especially in the case of colloid thrusters where currents are relatively small and voltages relatively high. If the necessity of space charge neutralization can be avoided, while still maintaining zero total spacecraft current, there is a simplification of the neutralization problem. Electrons can be ejected, for example, at the opposite end of the vehicle where there is no cathode contamination problem. By controlling the ejection, t e vehicle potential can be made to assume the desired potential relative to space.

In the analysis being undertaken in this program, all electrons but those coming from the ambient plasma are ignored. In effect it is assumed that electrons ejected from the vehicle escape into space in such a way that they maintain the vehicle at zero potential but otherwise play no role in the neutralization. It would be equally simple to solve this problem for a vehicle potential different from zero.

The problem is illustrated in Figure 144. Relative motion between the vehicle and the ambient plasma is ignored. The thrust beam space charge tends to make the potential, V, positive in the vicinity of the beam. Accordingly, the electron density

$$n_e = n_o \exp(eV/kT)$$

becomes greater than n_o, where n_o is the equilibrium, zero potential, space plasma electron density and T is the electron temperature. Space charge
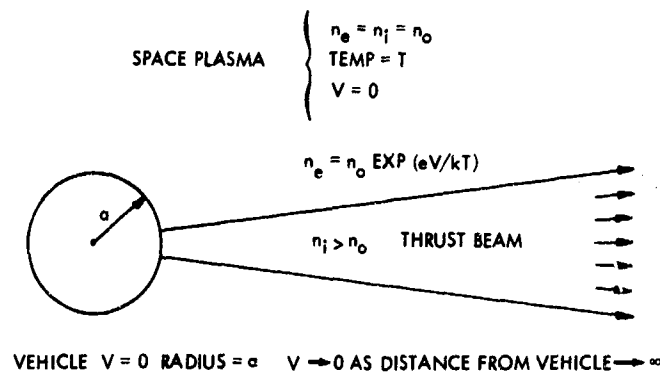
Figure 144. Assumed Problem Geometry

neutralization is achieved by this increased electron density. Let us see from the start what sort of potential might be required. At synchronous orbit altitude one can expect large variations in n_0, and T, but values of $n_0 = 10^2$ cm^{-3} and kT/e = 2 volts are typical. If the densities in the thrust beam near the exhaust plane are 10^8 electronic charges per cm^3, which is typical, then perfect neutralization requires

$$\exp(V/2) = \frac{10^8}{10^2}$$

which gives

$$V = 2\ln(10^6) \approx 28 \text{ volts}$$

This is so small compared to the accelerating voltage (12,000 volts) as to produce negligible charged particle deflection.

In view of the low voltage found above, which would be an upper limit to the voltage within the beam, it can be assumed that the ion velocity and trajectories are independent of the potential. As a first step then, we assume a beam density that resembles a real exhaust and is independent of the final form of the neutralized space charge potential distribution.

The beam density profile generally is not flat, falling suddenly to zero at a beam boundary, but, rather, the density at the beam edge falls gradually to zero. We represent this in cylindrical coordinates (r, z) by a Gaussian cross section of width w(z) which increases with distance

$$n_+ = I \exp(-r^2/w^2)/(\pi evw^2)$$

165

where I is the total current, e the electron charge, and v the exhaust velocity. The w^2 in the denominator is required by continuity, i.e., when the beam area increases, the current density function must decrease so that the total current through any cross section remains constant. It will be noted that n_+ is normalized in the sense that

$$\int_0^\infty (n_+ ev) 2\pi r \ dr = I$$

Beam divergence is described by the functional form of w. Let us choose w to be given by

$$w = w_o \left[1 + (z/z_o)^2 \right]^{1/2}$$

This gives a beam shape (to the 1/e density contour) which is shown in Figure 145. The smallest beam radius is w_o, and $z_o = w_o \cot \theta_B$ (where θ_B is the beam divergence angle far downstream) is the distance over which the beam stays essentially parallel.

The density of plasma ions is $n_o \exp(-eV/kT)$ and of plasma electrons is $n_o \exp(eV/kT)$. The difference between these is equal to the density of beam ions. The total charge density is then

$$\rho = -en_o \left[\exp\left(\frac{eV}{kT}\right) - \exp\left(\frac{-eV}{kT}\right) \right] + \frac{I \exp(-r^2/w^2)}{\pi v \, w^2}$$

so that Poisson's equation $\nabla^2 V = -\rho/\epsilon_o$ becomes

$$\nabla^2 V = \frac{2en_o}{\epsilon_o} \sinh(eV/kT) - \frac{I}{\pi \epsilon_o v} \ \frac{\exp(-r^2/w^2)}{w^2}$$

The handling of these quantities will be facilitated by making the following changes to dimensionless variables. Let

$$\eta = eV/kT$$

$$\lambda = \lambda_D = \left(\frac{\epsilon_o kT}{n_o e^2}\right)^{1/2} = \text{Debye length}$$

$$\omega = w/\lambda$$

166
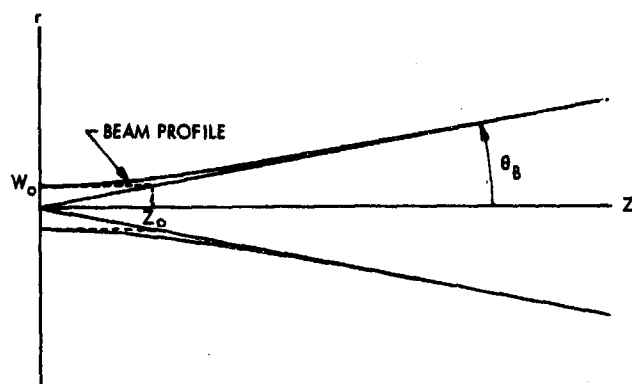
Figure 145. Beam Profile
Function w(z)

$$\gamma = r/\lambda$$

$$\zeta = z/\lambda$$

$$K = \frac{I}{\pi w_o^2 \eta_o ev} = \frac{n_i(0, 0)}{n_o}$$

This leads to

$$\nabla^2 \eta = 2 \sinh \eta - \frac{K \exp(-\gamma^2/\omega^2)}{(\omega/\omega_o)^2} \quad (1)$$

which is a statement of the equilibrium solution. The computational task posed by Equation (1) is finding the potential distribution function which satisfies the boundary conditions representing potentials (assumed zero) on the vehicle surface and at large distances from the vehicle within the ambient plasma. The first term on the right of Equation (1) is descriptive of charged particle densities from the ambient plasma which are contributing to neutralization of the thrust beam ion densities described in the second term. Inasmuch as a rise in potential is expected within the beam, and this rise in turn serves to maintain the enhanced electron density within the beam over that in the ambient plasma, the two terms of Equation (1) are never exactly equal, except in the limit of infinite distance from the vehicle. On the other hand, along the beam axis and near the beam exit plane, the ratio K is a large number and Equation (1) requires that both terms be almost, but not exactly equal. As will be seen, this behavior makes severe demands on computational precision.

5.4.4 Mathematical Approach

Considerable insight into the solution of Equation (1) is gained by first solving a simpler mathematically one-dimensional approximation. The procedure is to examine several cross sections of the approximately conical beam, considering each section as a simple cylindrical slab. By this means the effects of the partial derivatives with respect to the axial dimension are neglected. A set of solutions for various axial locations then comprises an approximate three-dimensional solution. The solution thus obtained can then be applied to the larger problem by using it as an initial approximation to the potential distribution function.

The second term in Equation (1) is equal to the positive charge density within the thrust beam:

$$\rho_+ = \frac{K \exp(-\gamma^2/\omega^2)}{(\omega/\omega_o)^2} = \frac{K \exp(-\gamma^2/\omega^2)}{1 + (\zeta/\zeta_o)^2}$$

167

Equation (1) is simplified by holding ζ fixed and assuming no axial dependence. For example, at $\zeta = 0$, $\omega = \omega_o$ and η is a function of (γ/ω). Thus, Equation (1) becomes

$$\nabla^2 \eta = 2 \sinh\eta - K \exp(-\gamma^2/\omega_o^2) \tag{2}$$

A first step in solving this equation is to critically examine the numerical constants of the problem and select values to be used in the calculations. Of principal importance is the electron temperature T to be encountered at the altitude of a synchronous earth satellite orbit. Various estimates are available, all much lower than 10 volts equivalent. Recent probe data have all been troubled by an uncertainty in spacecraft potential because of the unknown contribution caused by photo-electron emission. A meaningful measurement would require that the measuring satellite carry an electric field meter which would verify that the spacecraft potential was equal to that of the ambient plasma .t the time the electron temperature data were taken. The best estimates to date are to the effect that the electron temperature gives kT/e on the order of 2 volts. If one takes a value of 1.309 volts, and a number density of 100 ions and electrons per cm^3, this leads to a Debye length of 1.0 meter — a convenient number for normalization of other parameters, and one which is as realistic as can be determined.

The following typical values of thruster design and operating conditions have been chosen for the first calculations:

- 288 μA beam current

- 4 in.^{2} exhaust aperture

- 15,000 meter/sec exhaust velocity ($I_{sp} \approx 1500$ sec)

- 1 meter vehicle radius

- 10 degrees beam divergence angle

Putting these numbers into the various relationships, a maximum value is obtained for the zero order approximation to the plasma potential on axis at the exhaust plane of about 23.4 volts, K ($= n_i (0,0)/n_o$) = 4.24×10^5, and the initial value of η_o on axis at the exhaust plane ($= \log_e (k)$) = 12.95. Characteristic values derived from beam diameter and divergence angle are $\omega_o = 0.03$ and $\zeta_o = 17$.

Initially the Math-Oriented On-Line Computer System[*] (OLC-UCSB-OLS system using MOL language) was first used for the solution of this problem. Several operating consoles communicate with an IBM 360-75

---

[*]An extension of the Culler-Fried system.

computer at the University of California in Santa Barbara over voice-grade telephone lines in a time-sharing mode. Each console consists of two typewriter-like keyboards and a cathode-ray tube display unit. One keyboard represents data storage locations. The other keyboard represents the entry points of computer subroutines and may be thought of as a library of mathematical operators. The significance of the keys on each keyboard varies from one "level" to another (e.g., Real Level I: each storage key represents the location of one number, Level II: each represents the location of a vector of n components (i.e., a function), Complex Level II: each key represents the location of two related vectors of n components, etc.). Each user may define his own operators by storing lists of button pushes under operator keys in any of several user levels, e.g., to generate "differentiate" or "integrate" operators. Built-in operations include computations on vectors such as basic arithmetic operations, trignometic, exponential, logarithmic, and certain data handling functions. The machine normally displays vectors optimally scaled for display in the interval $-1 \gtrless x \gtrless 1$, $-1 \gtrless y \gtrless 1$.

One of the purposes of developing the OLC and its MOL language was as an aid in the iterative solution of integral equations of the form

$$f_{n+1}(x) = \int dx' \ F(f_n(x'))$$

where the symbol $\int dx'$ is a generalized integral operator, and f_n, f_{n+1} are consecutive terms in a converging sequence of functions. Equation (2) may be cast into this mold by letting $F(\eta) = 2 \sinh \eta - \rho_+$ and integrating with the inverse Laplacian operator. Thus, one has in cylindrical coordinates,

$$\eta_{n+1}(\gamma/\omega) = \int_0^\gamma d\gamma'' \frac{1}{\gamma''} \int_0^{\gamma''} d\gamma' \ (2 \sinh \eta_n - \rho_+)(\gamma') \tag{3}$$

This is a one-dimensional integral version of the desired equilibrium solution.

From the nature of the problem, it is obvious that while the charge density on the beam axis is several orders of magnitude greater than within the ambient plasma, maximum potentials within the neutralized beam will be small. Therefore, the term to the left of the equals sign in Equation (2) is always small and represents the difference between two large and nearly equal terms on the right. Accordingly, it is reasonable to assume that a good "zero-order" approximation to the potential function is given by

$$\eta_o = \sinh^{-1}\left(\frac{\rho_+}{2}\right) \tag{4}$$

169

At fixed z, the radial dependence of this function is given by

$$\eta_{or} = \sinh^{-1}\left[\frac{K}{2}\exp(-\gamma^2/\omega^2)\right] \quad (5)$$

whereas, putting $\gamma = 0$, gives the axial dependence of the "zero-order" approximation:

$$\eta_{oa} = \sinh^{-1}\left[\frac{K/2}{1 + (\zeta/\zeta_o)^2}\right] \quad (6)$$

5.4.4.1 Solutions Obtained Using a CRT Terminal

Figures 146 and 147 show machine-generated displays of the axial and radial dependence of the ρ_+ term in Equation (1) as given above and of the corresponding η_o function of Equations (5) and (6) (before proceeding to the one-dimensional case). In Figure 146, the abscissa is (γ/ω_o) from 0 to 10, the smaller curve is ρ_+ with an initial value of 4.24×10^{-5}, the larger curve is η_o with an initial value of 12.958. For Figure 147, the abscissa is (ζ/ζ_o) from 0 to 10 with the same initial values for the ρ_+ and η_o curves.
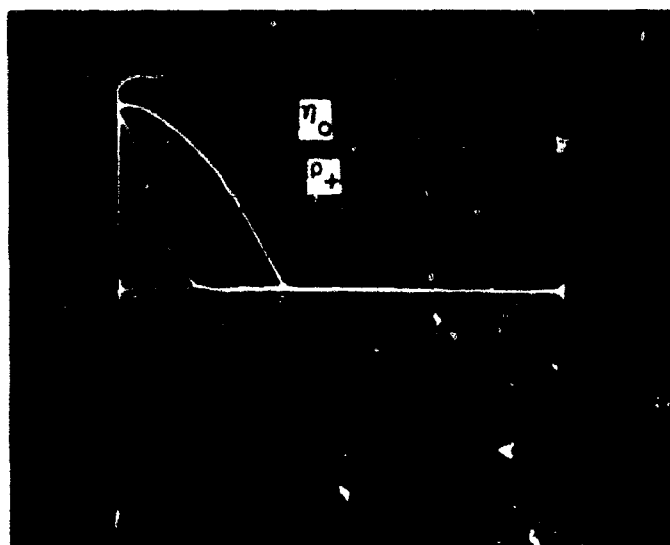
Figure 146. Machine-Generated Plots of the ρ_+ Term in Equation (1) and η_o Equation (2) Evaluated at $\zeta = 0$ and Photographed From the Cathode-Ray Display Tube. The horizontal axis is (γ/ω_o) from 0 to 10, zero at left. Initial values of the curves a $\rho_+(0) = 4.24 \times 10^5$, $\eta_o(0) = 12.958$.
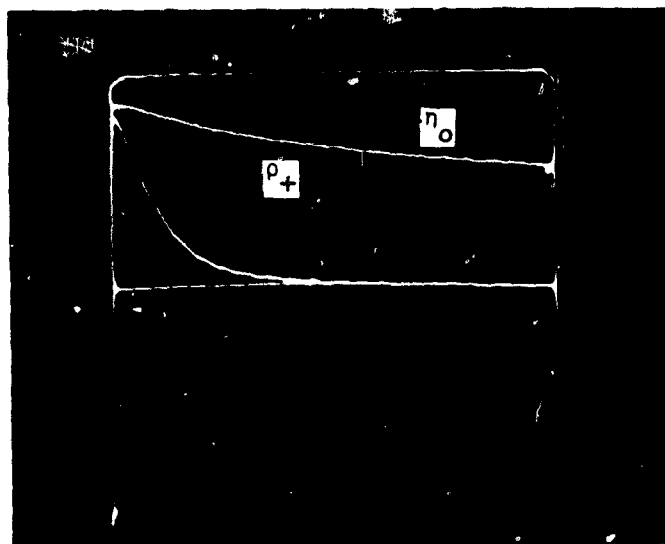
Figure 147. Plots of ρ_+ and η_0 evaluated at $\gamma = 0$. The horizontal axis is (ζ/ζ_0) from 0 to 10, zero at left. Initial values are the same as in Figure 146.

If one inserts η_{0r} from Equation (5) into Equation (3), the integrand is identically zero, giving $\eta_1 = 0$ plus two constants of integration. These are chosen to give zero electric field on axis and zero potential at infinity so that η_1 is identically zero everywhere. Putting $\eta_1 = 0$ into the integral expression gives only the $-\rho_+$ term as the starting point for the next iteration. Figure 148 shows the results at each step in the performance of this calculation. Note that the scales of these curves are not all the same. One may identify the curves from top to bottom in the figure reading to the right of that portion of the frame in which curves cross. The curve (second down) which most rapidly approaches the zero axis is the ρ_+ starting function. The next curve down is $\gamma\rho_+$ starting at $(0,0)$ The first integral curve is the bottom one in the figure; when multiplied by $(1/\gamma)$ it becomes the next curve up from the bottom. The computed value of η_2 is the uppermost curve. Its initial value is displayed in numerals in the corner of the frame, and is orders of magnitude too large for a final solution, but this is not surprising. The shape of the curve is much different from that of η_0 in Figure 146 and begins to resemble that of the final solution.

In Figures 146 and 148, the independent variable consists of 100 equally spaced points in the interval 0 to 10, i.e.,

$$x_i = (0.0, \ 0.1, \ 0.2, \ \ldots, \ 10.0).$$
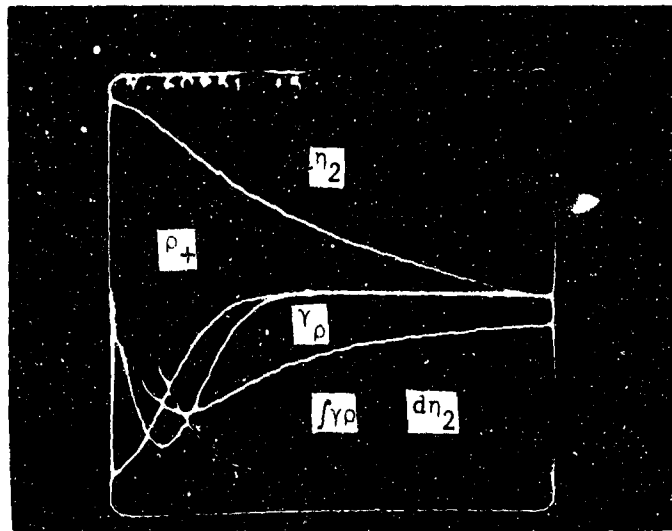
Figure 148. Machine-Generated Plots Showing Successive Steps in Computation of Equation (3) Using the Single Term $-\rho_+$ as the Starting Function (see text). In order of computation, the curves are $\rho_+, \gamma\rho, \int\gamma\rho$, $1/2\int\gamma\rho = d\eta_2$, η_2. Scaling of the curves is automatically adjusted by the computer to optimally display the functions in the x-y intervals from -1 to +1. The initial value of the η_2 curve is given by the numerals in the corner of the frame. Two integration constants equal to zero are introduced by forming the first integral from left to right and the second from right to left.

In order to use a greater range, and at the same time achieve better resolution near zero, this was then changed by computing successive x_i from the equation

$$x_i = 100 \left[(i - 1)(0.01)\right]^2 \quad (i=1, 2, \ldots, 101)$$

$$= (0.0, 0.01, 0.04, \ldots, 98.01, 100.00)$$

For display purposes, however, the linear scale is still used, giving a distorted but readable view of the functions. (Note: the computer connects points on the curves with a continuous line.) The effect of this change may be seen by comparing Figure 148 with its counterpart, Figure 149.

A two-step iterative procedure leading to an approximation of the solution proceeds as follows: In storage one has the current η function (η_k)

172
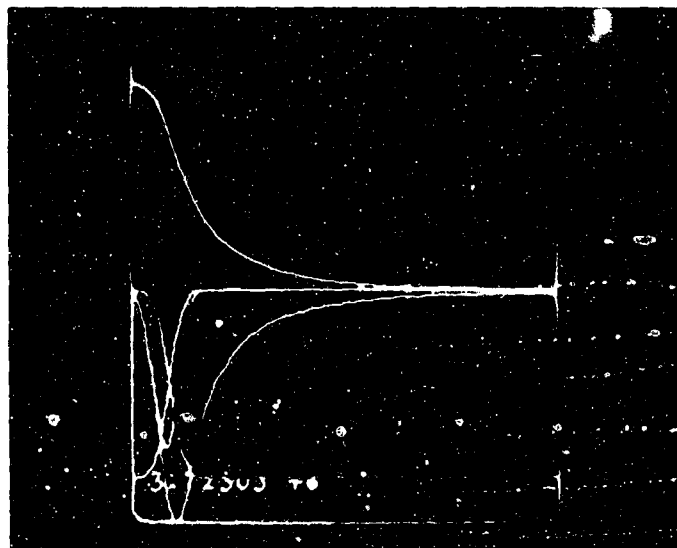
Figure 149. Curves Displaying Results at Each Step in the Operation
of the "Inverse Laplacian Operator" Described Above. In each
curve, 101 points are equally spaced across the display tube and
connected with continuous lines. Point values are computed from
unequally spaced values of the independent variable as described
in the text, giving a distorted appearance to the curves. The
curves are a) $-\rho_+$ negative, non-zero initial point, b) $\gamma\rho$ short
negative spike, c) $\int\gamma\rho$ step function, d) $(1/\gamma)\int\gamma\rho = d\eta/d\gamma$, tall
negative spike, and e) η positive curve.

and the ρ function (ρ_k) from which it was calculated using the integration
(inverse Laplacian) operator. Step one computes the next ρ function
from

$$\rho_{k+1} = [(2 \sinh \eta_k - \rho_+) - \rho_k] (1 \times 10^{-6}) + \rho_k \tag{7}$$

and step two computes the next η from

$$\eta_{k+1} = \iint_{cyl.} (\rho_{k+1}) \tag{8}$$

173

In principle, as the current values of η and ρ approach the exact solutions to the problem, the bracketted quantity in (7) should approach zero. If not, the convergence factor of 1×10^{-6} would cause the ρ function to change very slowly from one iteration to the next in the proper direction to improve the approximation. In practice, the algorithm was stable for over 65 iterations in the sense that each iteration produced an approximation from which a succeeding approximation could be calculated using the same algorithm. On the other hand, the process was "noisy" in the sense that a given approximation was not always a closer approximation than some previous one had been. This latter result seemed to be the effect of the size quantizing steps in the machine. [Compare the approximately 7-decimal-digit precision of the machine with the (1×10^{-6}) convergence factor.] Accordingly, a given set of η and ρ functions were considered to be "good" solutions if the immediately preceding and subsequent solutions were close to the same. A solution set (iteration 36) is shown in Figure 150. The η curve is uppermost in the figure, and is slightly larger than the "best" obtained. The input ρ function is the jagged curve at the bottom of the figure. These curves may be interpreted in terms of the neutralization problem which they attempt to represent, somewhat as follows: The input ρ function represents the difference between the input positive charge density function and the corresponding electron-density function. This difference has a maximum absolute value less than 5 parts in 10^6 of the magnitude of the input function at the point where the maximum difference occurs. The maximum difference represents an excess of ions (negative maximum is an excess of "$-\rho_+$") and occurs at the "shoulder" in the potential function. Close examination of the ρ function also shows a low-amplitude positive excursion extending several beam "diameters" outward from the beam "edge." Finally, Figure 151 is a comparison between another η solution (iteration 66) and the "zero-order" approximation $\eta_0 = \sinh^{-1}(\rho_+/2)$ displayed in Figure 146. Also plotted is the difference between the two curves.

In view of the "noise" referred to above and the reasonableness of the solutions obtained, no further iterations were carried out.

5.4.4.2 Precise Solution Obtained Using More Powerful Techniques

More precise solutions to the two-dimensional equation were then obtained using the method described in Appendix A. The method consists of expressing the potential function as nodal values in a mesh with systematically varying mesh spacing, writing the system of inter-mesh equations in band-matrix form, and solving the system using a library subroutine with a special driver program on the CDC 6500 computer at TRW. More mesh points were used in each case (up to 1000) and the CDC machine carries about 15 decimal digits in normal precision.

174
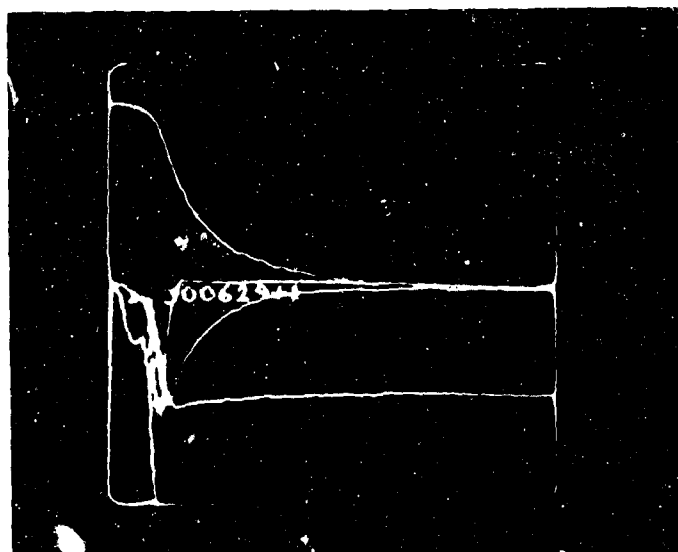
Figure 150. Upper Curve is an Approximate Solution to the
One-Dimensional Equation $\nabla^2\eta = 2 \sinh\eta - \rho_+$ Obtained
After 36 Iterations as described in the text.
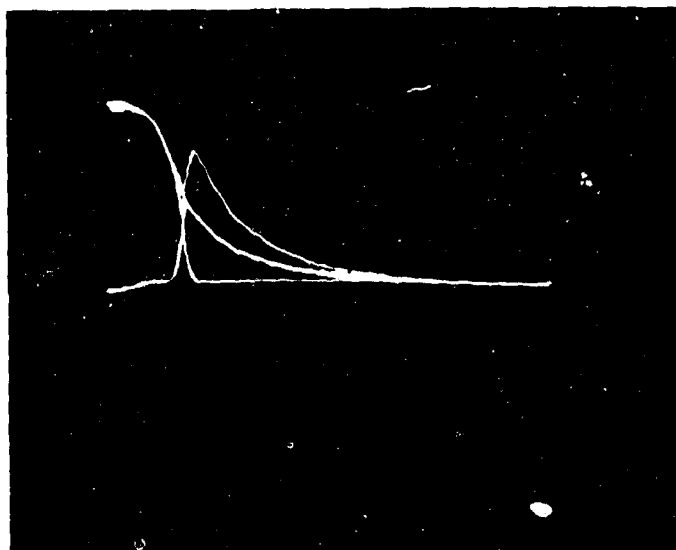
Figure 151. Comparison Between a Solution Obtained After
66 Iterations and the "Zero-Order" Approximation. The
third curve in the figure is the difference between the two
others (at twice the scale), and represents the modifica-
tion computed in the iteration process.

The cylindrical geometry method used in the calculations is potentially extendable to the three-dimensional (axisymmetric and thus mathematically two-dimensional) case that will yield values for the potential field surrounding both the thrust beam and the spacecraft which emits it. Details of how this may be done are given in Section 5.3.5.1.

Radial solutions were obtained for ion densities corresponding to those expected at axial distances from the exhaust plane over the range of $\zeta = 0$ to $\zeta = 17$. This set of solutions gives the potential and net charge distribution which will match the three-dimensional case (mathematically two-dimensional since the variables show no azimuthal dependence) except for: (1) the second partial derivative in the axial direction, expected to be small except near the vehicle; and (2) the boundary conditions at the vehicle, that will have a profound effect on the potential and space charge over distances of the order of the vehicle dimensions or the Debye shielding length corresponding to the space plasma, whichever is smaller.

These solutions show the manner in which beam density, charge distribution and potential merge into the ambient plasma environment. Overall features thus presented are in qualitative agreement with the experimental results obtained by Sellen, et al[1] from detailed mapping of the beam from a 1-inch-diameter ion source in the 25-foot-diameter by 80-foot-long vacuum chamber at the NASA Lewis Research Center. Essential differences between the premises for the mathematical model and that experiment are that the experimental beam was operated in vacuum, not in an ambient plasma and was neutralized by electrons from a 2500° K hot wire, resulting in an axial gradient in electron temperature.

The previously derived normalized equation for potential is:

$$\nabla^2 \eta = 2 \sinh \eta - \rho_+$$

[1] J. M. Sellen, R.R. Kemp and R. Hieber, "Observations of Neutralized Ion Thrust Beams in the 25-Meter NASA Testing Chamber, "Section III. G., Final Report NAS 8-1560, 1964.

where

$$\eta = \frac{eV}{kT_e}, \quad V = \text{local potential}$$

$$\rho_+ = \left(\frac{n_+(0,0)}{n_0}\right)\left(\frac{\omega_0^2}{\omega^2}\right) \exp -\left(\frac{\gamma^2}{\omega^2}\right)$$

$n_+(0,0) = $ axial charge density in thrust beam

$n_0 = $ charge density in ambient plasma

$$\left(\frac{\omega}{\omega_0}\right)^2 = \left(1 + \frac{\zeta}{\zeta_0}\right)^2 \text{ describes beam divergence}$$

$\gamma = r/\lambda \qquad$ radial $\quad\Bigg\}$ dimensions normalized

$\zeta = z/\lambda \qquad$ axial $\quad$ to Debye length.

For the specific example, $n = 10^8$ electric charges/meter^3, $T_e = 1.809$ volts, $\lambda = 1.$ meter, $\omega_0 = 0.03$ meter, $z_0 = 0.17$ meter. Hence, for a 360 μA beam with velocity $= 15 \times 10^3$ m/sec, $(n/n_0) = 529834.11$.

The ρ_+ term describes thrust beam charge density (given), and the $2 \sinh \eta$ term describes the required electron density to provide charge neutralization of the beam. The difference between the two terms is the net charge density required to support the potential function which holds the electron charge within the thrust beam. At any fixed value of the axial coordinate, the potential and charge densities are functions of the radius only. The approximate expression for this case is

$$\nabla^2\eta = \frac{\partial^2\eta}{\partial\gamma^2} + \frac{1}{\gamma}\frac{\partial\eta}{\partial\gamma} = 2 \sinh \eta - \rho_+$$

Cases for which solutions have been obtained are summarized in Table 20. Note that the net charge density on axis - $(2 \sinh \eta - \rho_+)$ indicates a little less than 1 percent deficiency of electrons for all cases. Plots of the η function for $\zeta = 0$, and $\zeta = 15$, together with plots of net charge density at the same radial scale for each case are presented in Figures 152 through 155. It is interesting to compare the location of the zero-crossing of the net-ρ curve with the inflection point of the η curve. Also, the net-ρ curves are particularly interesting in another sense: The shape of the curves is consistent with the notion of a "trapped" electron cloud within the beam in which electrons are in oscillatory motion across the axis of the beam. As such one would expect a local decrease in density where velocities are highest, with a corresponding increase in electron densities (above the ion densities) at the regions where electrons are being reflected by relatively large electric fields.

177

Table 20. Summary of Computer Runs for One-Dimensional Equation

ζ	Axial Values			No. of Mesh pts	No. of Iterations
	+	Netρ	η		
0.	529854.11	4520.0	13.176	500	50
1.	14882.67	125.0	9.6015	250	57
3.	1695.97	14.3	7.429	300	25
4.	955.32	8.05	6.8548	300	20
6.	425.01	3.57	6.0453	200	18
8.	238.15	1.99	5.4698	200	11
10.	153.08	1.26	5.0234	200	9
12.	106.32	0.89	4.6587	200	8
15.	68.05	0.573	4.212	1000	6
17.	52.98	---	3.9622	200	5
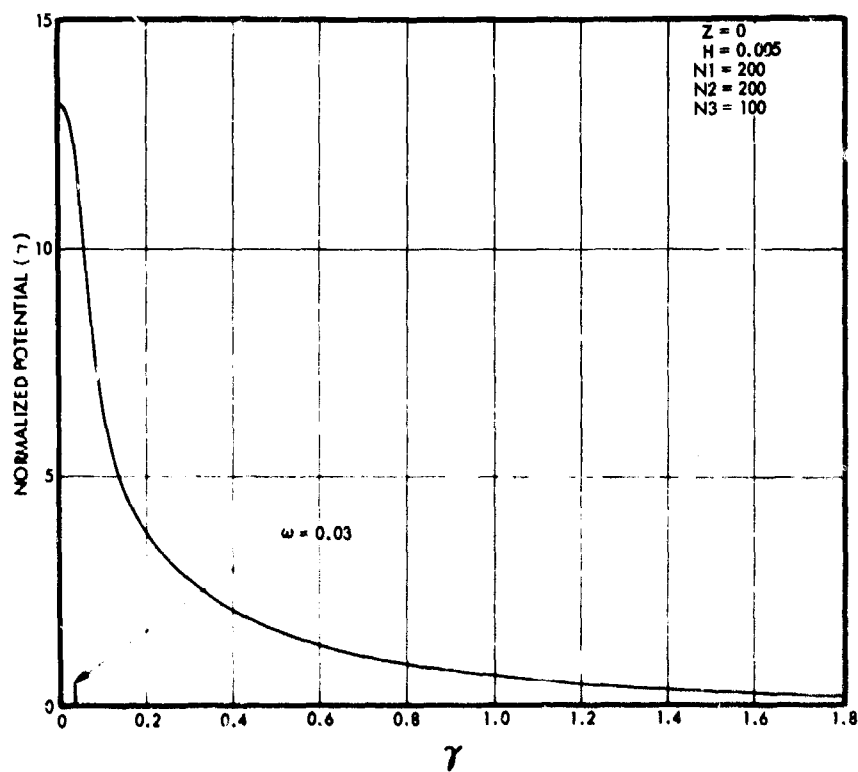
Figure 152. Normalized Potential as a Function of Normalized Radius at Z = 0

178
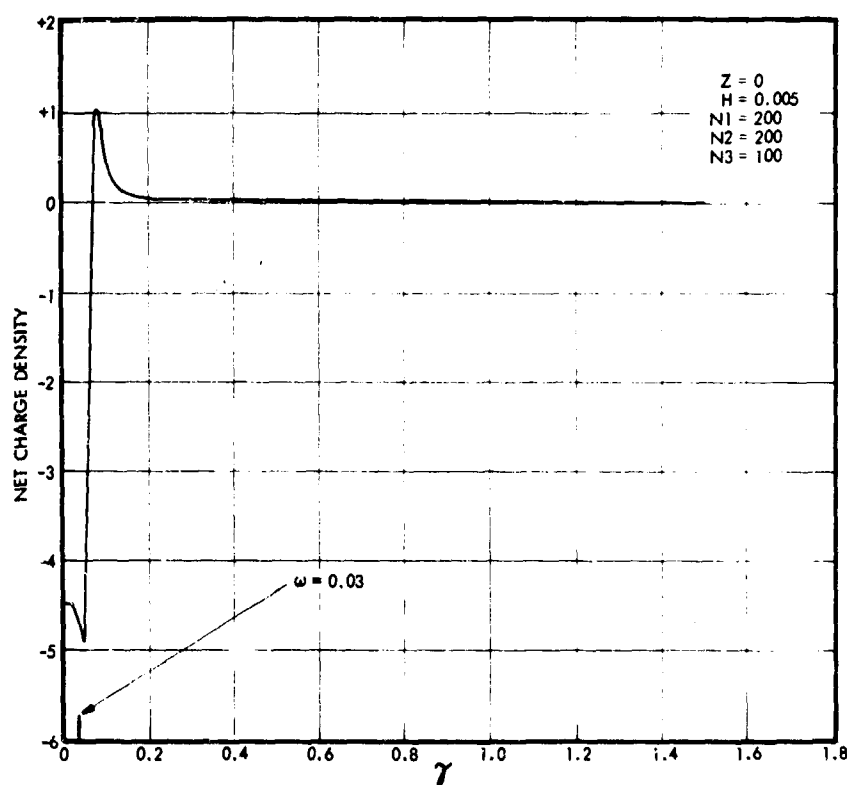
Figure 153. Net Charge Density as a Function of Normalized
Radius at Z = 0

Given a description of a thrust beam charge density in terms of a
"well-behaved" mathematical expression, consistent electron density
and potential functions were found which provide solutions to the Poisson
equation for the given expression. It is i esting that the solution of
Poisson's equation, subject to the auxiliar, conditions (1) that the ion
trajectories are unaffected by potential variations in the beam, and (2)
that the electron density follows a Boltzmann distribution equilibrium
with the space plasma, displays the behavior which has usually come to
be expected for ion beams neutralized by an electron emitter. Specific-
ally, we obtain almost complete neutralization of the space charge
within the main part of the beam, and a cloud of excess electron density
surrounding the beam. This type of behavior was also experimentally
observed, as previously mentioned. These are positive implications as
to the feasibility of space charge neutralization by ambient electrons,
providing only that current neutralization of the spacecraft is achieved;
however, further conclusions await completion of the more general
three-dimensional case.

5.4.5 Completing the Equilibrium Solution

The partial differential equation which th potential function satis-
fies has been cast in spherical polar coordinates and, by standard pro-
cedure, difference equations derived therefrom. At the present time

179
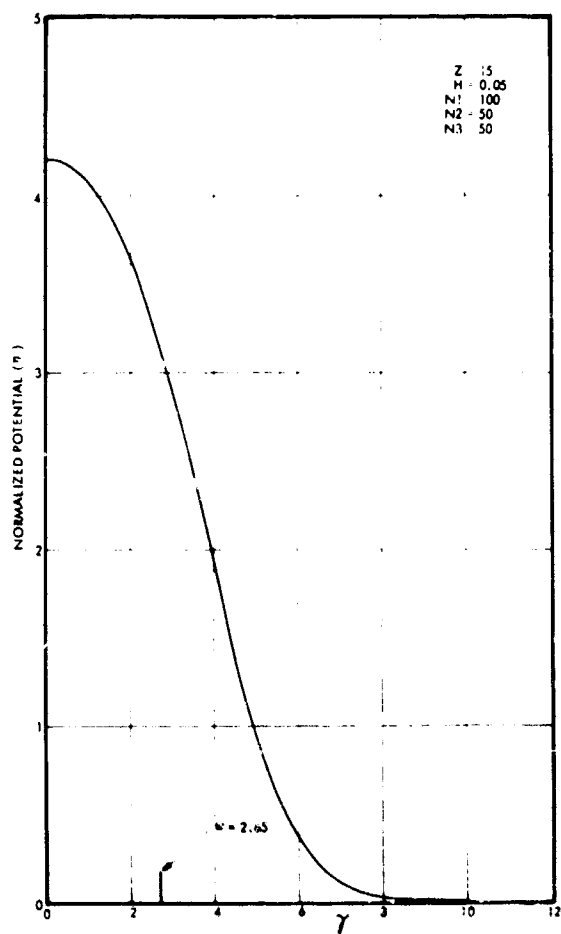
Figure 154.
Normalized Potential as a
Function of Normalized
Radius at Z = 15
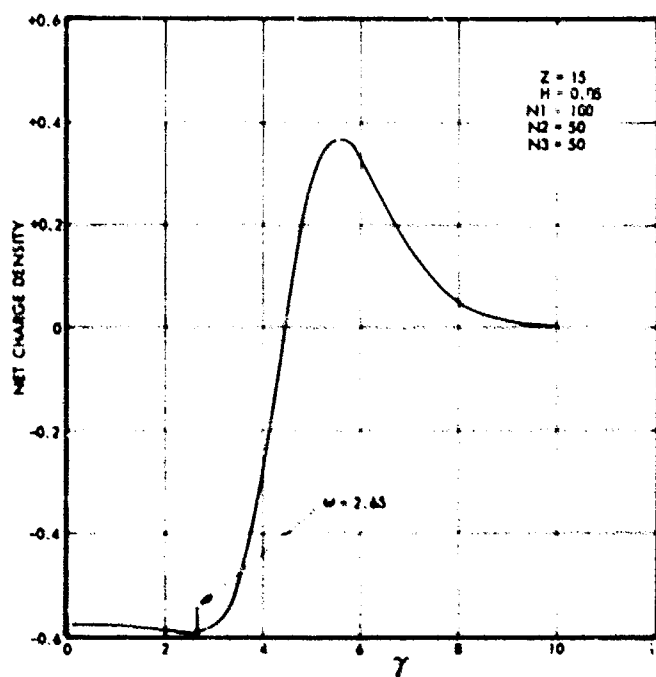
Figure 155.   Net Charge Density as a Function
of Normalized Radius at Z = 15

180

this system of difference equations is being arranged in different patterns so that the eventual numerical solution of these equations may be accomplished efficiently.

The system of difference equations is, in fact, nonlinear. It is anticipated that Newton's method will be used to solve them. This requires the repeated solution of large order systems of linear equations. The number of times that these large order systems are solved determines, essentially, the computer costs to obtain a particular potential function (solution). The number of times these equations are solved may be limited by finding a suitable initial guess for the potential function. With this in mind, some time has been spent in consideration of various schemes for producing such an initial "guess."

On the one hand, a z-independent solution was obtained which is easily changed to a z-dependent solution which is a good approximate solution at distances from the vehicle large compared to the vehicle radius. On the other hand, we believe we have techniques for yielding an exact solution if we have an approximate solution. There remains the problem of finding an approximate solution that is valid in the important region in the vicinity of the spacecraft. One method we propose is as follows:

(1) Take $V_0(r, z)_{z>0}$, where $z = 0$ at the exit grid, from the z independent solution.

(2) Extend this to $z<0$ by using hemispherical equipotential surfaces. It can be shown that this is equivalent to writing $V_0(r, z)_{z<0} = V_0(r^2 + z^2, 0)$.

(3) Transform to spherical coordinates with origin at the center of the sphere and polar axis in the beam direction. Obtain the potential at a distance "a" equal to the vehicle radius, call this $f(\cos \theta)$.

(4) Write this as a sum of Legendre Polynomials, i.e., $f(\cos \theta) = \Sigma\ a_n P_n(\cos \theta)$ for which the a_n are easily evaluated.

(5) The solution

$$V_1 = V_0(r, z) - \sum \frac{a_n P_n(\cos \theta)}{R^{n+1}}$$

where R is the spherical radius is expected to be close to the desired solution because the first term approximately satisfies Poisson's equation and the second term satisfies Laplace's equation; the sum therefore approximately satisfies Poisson's equation and the match to the boundary conditions are assured by the method used for finding the coefficients a_n.

181

As a matter of fact, it is not necessary to go through the analysis recommended by Brooks to get an exact solution. It would be enough to verify by using Poisson's equation (Equation 1) that our approximate solution is quite good, i.e., that the left and right hand sides of this equation are fairly close together in the critical region which is the region of the beam between the vehicle and a distance from the vehicle of a few beam diameters.

5.4.6 Summary and Conclusions

An equation has been derived from the basic assumption of thermal equilibrium within a charged-particle thrust beam, which describes the equilibrium potential and charged-particle distribution within the beam. An approximation of this equation has been solved by two somewhat different computational means, yielding radial distributions at different axial positions within the beam. The largest number of solutions, and those having the greatest precision, were computed numerically on the CDC 6500 computer. Taken together these solutions tend to present a complete three-dimensional concept of the neutralized beam which is consistent with laboratory measurements on neutralized ion beams. As such, these results tend to support the conclusion that neutralization of colloid beams by electrons from the ambient plasma (which become trapped within the potential well of the beam) would occur, provided that current neutralization of the spacecraft were achieved otherwise.

An approach has been devised for computing a full-blown three-dimensional case including the boundary conditions on the spacecraft surface. Results from the one-dimensional solutions presented here will provide an excellent first "guess" required for this approach, everywhere except within short distances of the spacecraft surface.

182

6. CONTAMINATION STUDIES

Long term or erratic operation of a colloid thruster in a vacuum chamber often results in the build-up of a foreign substance coated on various thruster and facility surfaces. This substance, which may be characterized as "tar-like," is usually dark brown in color and has a consistency that ranges from solid to viscous fluid. Because the presence of this contaminant on critical thruster surfaces may influence thruster performance and/or lifetime, experiments performed determined its exact composition. When it was established that the substance was decomposed propellant, efforts were made to evaluate the effectiveness of adding chemicals to inhibit the decomposition. Experiments with the inhibitors were not successful.

The analytical and remedial experiments are described in the following sections. In addition, efforts to determine the influence of collector geometry and vaccum pressure on the rate of contaminant build-up are reviewed, and the possibility that the presence of excessive iodine leads to contaminant build-up is discussed. Also, a brief review of the problem of dissolved gases in the propellant is given as well as the studies made of the effect of background pressure on the rate at which dissolved gases will nucleate and escape from the propellant. An important conclusion of this study is that there is a threshold ambient pressure below which such nucleation does not occur.

6.1 ANALYSIS OF PARTICULATE FORMATIONS

A chemical analysis was made of the various contaminating substances found on colloid thruster and test facility surfaces. Contaminants found on the walls of the test facility and on the emitting rim of the thruster after a long period of slightly unstable operation were analyzed separately. To obtain contaminants of the type formed in catastrophic accidents, a "tar-maker" was fabricated and run. This device and the contaminants it generated are described below in Section 6.1.2.

The following analysis techniques were used to determine the atomic and molecular structure of the various types of residue.

6.1.1 Sample Preparation

Altogether, five different samples of contaminants were analyzed. These were of the two types mentioned above, from the walls of the test facility and from the emitting edge of a source.

After a 1000-hour test of the 36-needle (capillary needle) thrust vectorable module, tar samples were scraped from the vacuum tank wall at the entry port to the hi-vac valve and from the cold wall. The total weight of these two samples was more than 100 mg. The test facility was evacuated with a 24-inch Edwards diffusion pump.

Three tar samples were taken from colloid emitter surfaces and weighed approximately 105 mg.

1. One sample taken from the tar-maker (described in the next section) consisted of whitish salt crystals and a large quantity of solid, very dark brown material.

2. The second sample was taken from needles and annular emitters involved in vacuum accidents and long term runs, including the two long runs of the six-needle annular module. The consistency of this substance was more tarry than solid, and it was somewhat lighter in color than the previous sample.

3. The third sample was a small chunk of tar taken directly from the needle tip after run 700504 (the first in the vertical test station) was terminated.

6.1.2 A Tar-Making Device

This device consisted of a 1/2-inch-diameter double-rimmed circular slit. The center extractor was removed and replaced with a large stainless steel button that completely filled the center area and was held at emitting potential (see Figure 156). The propellant was allowed to flood the center button where electron back bombardment formed tar. To facilitate the flooding process, the inner rim was set about 5 mils behind the outer rim. The extractor and annulus support structure were modified to withstand higher voltages and heavier heat loads.

The device operated in a 2 x 4 foot chamber with a 6-inch diffusion pump. The first runs were short lived and were terminated by high voltage breakdown or component failure due to overheating. However, a small amount of tar was obtained from these runs.

Due to the large radius of the annulus and its modification to a center button at high voltage, the electric field from this device varied from that originally intended. The direction of highest field strength tended to be radial with respect to the axis of the annulus with the result that nearly all the emitted current went directly to the extractor and led to a high local power density on both annulus and extractor, and, consequently, overheating.

Two very successful runs were made; one run lasting over 4 hours and the other overnight. These runs produced the majority of the tar collected from the emitters. The region of heaviest tar formation was directly on the rim. The vacuum environment was on the high 10^{-5} scale. The contaminant contained a good deal of crystalline salt from one of the annulus runs, probably as a result of rapid propellant evaporation. The device was very unstable during the run; because it was emitting to the extractor it was carefully watched. The extractor was run at ground potential for these runs, serving only as an extractor and not as an electron barrier generator.

6.1.3 Analysis of Contaminants From Test Station Walls

The two samples taken from the test facility surfaces were analyzed quantitatively for metallic constituents, sodium, iodide, carbon, and

184
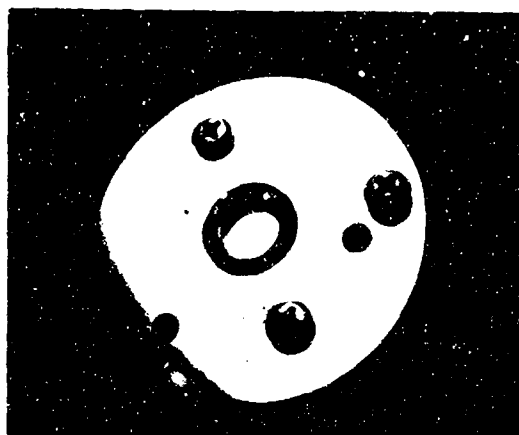
a. Tar-Maker Showing Extractor, Emitting Rim, and Steel Button In Center
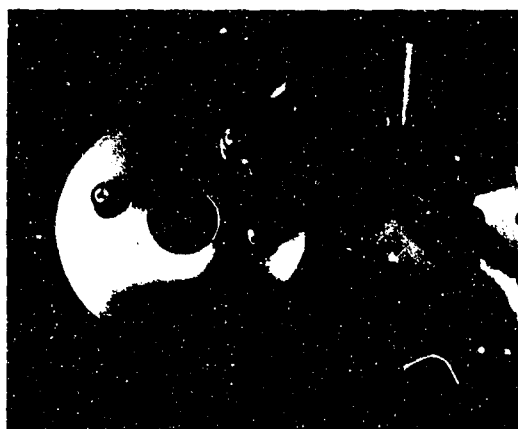
b. Disassembled Tar-Maker, Extractor to Left, Outer Rim and Feed Tube at Bottom Right. Top right is the inner rim with spiral feed channels. Inner rim contains center button, which is not visible.

Figure 156. Tar-Making Device

hydrogen content. In addition, analyses were conducted to elucidate the structures of the organic constituents. The results showed that both samples contained considerable concentrations of metallic species, primarily copper. Analysis for sodium iodide content showed the salt to be present in the cold wall sample, with considerably less being found in the hi-vac sample. In addition, both samples were found to contain silica. Structural elucidation of the organic constituents, which represented 65 to 80 percent of the sample, has shown the major component to be a polymeric glycerol compound containing more than three glycerol structural units.

A mass spectral analysis was also performed on the volatile constituents of the first sample and the results indicated that the volatile content of the sample represents a complex mixture of chemical constituents, including furans, alcohols, polyols, and iodine bearing compounds.

6.1.3.1 Experimental

The techniques used were:

● Metallic species were identified qualitatively on a GE XRD-5 X-ray Spectrometer, by X-ray fluorescence techniques. Quantitative determination of metallic species was obtained by a Perkin-Elmer Model 290 Atomic Absorption Spectrophotometer.

● Sodium content was measured quantitatively by atomic absorption spectroscopy.

- Iodide content was measured by an aqueous titrimetric procedure.

- Carbon and hydrogen contents were measured by a standard micro-analytical combustion method while oxygen content was calculated by difference. The carbon and hydrogen analysis was performed by an outside service laboratory (Elek Micro-analytical Laboratory).

- Organic constituent identification and structure elucidation were conducted by the following procedures. Infrared spectra were obtained on a Perkin-Elmer Model 521 Grating Spectro-photometer. Nuclear magnetic resonance spectra were obtained on a Varian A-60-A NMR Spectrometer.

- Mass spectra were obtained on a Hitachi RMU-6E Mass Spectrometer. Gas chromatographic-mass spectral analysis employed a Perkin-Elmer Model 881 Gas Chromatograph connected in series with the Hitachi Mass Spectrometer. Gas chromatographic separation was conducted under the following conditions:

Sample temperature:	50° C
Inlet temperature:	70° C
Column temperature:	70° C for 5 minutes 6° C/min to 125° C
Column:	50 ft capillary: Carbowax 20M
Carrier gas:	He
Carrier flow rate:	5 cc/min

6.1.3.2 Results and Discussion

Elemental Analysis

Quantitative analysis of the metallic species yielded the following concentrations, by weight (% w/w):

	Hi-Vac (% w/w)	Cold Wall (% w/w)
Cu	3.9	9.4
Cr	0.05	<0.01
Ni	0.07	0.02
Fe	0.16	0.02
Zn	0.04	0.01
Totals	4.22	9.46

186

During the preparation of the samples for atomic absorption analysis, an acid insoluble white crystalline solid was found in each contaminant. The solid was recovered quantitatively and identified by infrared as silicon dioxide (silica-SiO_2); the cold wall sample contained 1.5 percent w/w, while the hi-vac sample contained 8.1 percent w/w. The silicon dioxide probably came from the diffusion pump oil.

The sodium and iodide content of the samples was found to be:

	Hi-Vac (% w/w)	Cold Wall (% w/w)
Na	1.07	6.40
I	6.90	17.0

The iodide analysis will not distinguish between iodine (I_2) and iodide (I^-) and the reported values represent total concentrations as iodide.

The following values for hydrogen, carbon, and oxygen content of the samples were determined:

	Hi-Vac (% w/w)	Cold Wall (% w/w)
C	32.56	23.71
H	6.80	5.10
O	40.35	36.83

The oxygen values are calculated by difference, with all identified constituents having been considered. Assuming the carbon, hydrogen, and oxygen values to be representative of organic compounds plus water, 79.36 percent of the hi-vac sample and 65.64 percent of the cold wall sample are organic or water constituents.

The determined elemental concentrations for both samples are:

	Hi-Vac (% w/w)	Cold Wall (% w/w)
SiO_2	8.1	1.5
Cu	3.9	9.4
Cr	0.05	<0.01
Ni	0.07	0.02
Fe	0.16	0.02
Zn	0.04	0.01
Na	1.07	6.40
I	6.90	17.0
C	32.56	23.71
H	6.80	5.10
O	40.35	36.83

Structural Characterization

The techniques of infrared, nuclear magnetic resonance, and mass spectroscopy were employed to define organic chemical constituents and elucidate compound structures where possible. Infrared spectra of the contaminants were produced by the thin film technique. Additionally, a sample of the hi-vac contaminant was dried and a KBr pellet was used to produce an infrared spectrum.

The spectrum obtained from the cold wall sample corresponds to a spectrum of glycerol with some notable spectral changes. A spectral comparison is given below:

Observed Absorption Bands

Cold Wall Sample	Glycerol	Remarks
$3380 \ cm^{-1}$	$3360 \ cm^{-1}$	OH stretch
$2940, \ 2830 \ cm^{-1}$	$2940, \ 2880 \ cm^{-1}$	CH stretch and CH_2 and CH
1580^{-1}	Absent	Unidentified
$1500\text{-}1250 \ cm^{-1}$	$1500\text{-}1150 \ cm^{-1}$	OH in plane bend, CH_2 symmetrical bend
1100 (shoulder), $1020 \ cm^{-1}$	1105, 1035, 980	C-O bend combination of primary and secondary alcohols
Absent	920	CH_2 deformation
Absent	850	Unassigned

The spectral differences may possibly be explained by the production of polymeric glycerol structures such as those formed by the following condensation reactions:

$$
\begin{array}{c}
\qquad\quad \overset{OH}{|} \quad \overset{OH}{|} \quad \overset{OH}{|} \; \longrightarrow \; \overset{OH}{|} \qquad \overset{OH}{|} \qquad\qquad\qquad \overset{OH}{|} \quad \overset{OH}{|} \\
1) \quad 2\ CH_2 - CH - CH_2 \qquad CH_2 - CH - CH_2 - O - CH_2 - CH - CH_2 + H_2O
\end{array}
$$

Glycerol (A)   Diglycerol (B)

$$2) \quad A + B \rightarrow \underset{\displaystyle |}{\underset{OH}{CH_2}} - \underset{\displaystyle |}{\underset{OH}{CH}} - CH_2 - O - CH_2 - \underset{\displaystyle |}{\underset{OH}{CH}} - CH_2 - O - CH_2$$

$$- \underset{\displaystyle |}{\underset{OH}{CH}} - \underset{\displaystyle |}{\underset{OH}{CH_2}} + H_2O$$
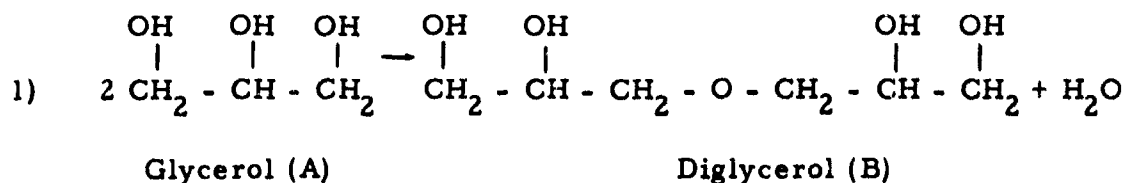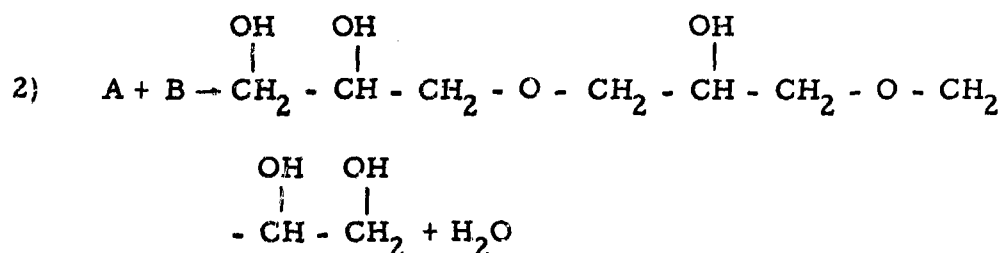
<p style="text-align:center">Triglycerol</p>

The major spectral differences occur in the 1100-980 cm^{-1} region; in the spectrum of the contaminant, the 1100 cm^{-1} peak has been reduced to a shoulder of the more intense peak at 1020 cm^{-1}, while the 980 cm^{-1} peak has disappeared. The three peaks at 1105, 1035, 980 cm^{-1} in the glycerol spectrum are assigned to the C-O stretch for the primary and secondary alcohol groups. The 1105 cm^{-1} and a portion of the 1035 cm^{-1} are attributed to a secondary alcohol structure, and the 980 cm^{-1} and a portion of the 1035 cm^{-1} absorption are attributed to the primary alcohol structure. In triglycerol, the number of primary alcohol structural units has been greatly reduced, as have the secondary units. However, the secondary-to-primary ratio in glycerol of $1/2$ has changed to $3/2$ in triglycerol. In addition, this region should be changed due to C-O stretch in the polymeric ether linkages. The second major spectral change is the appearance of a strong band at 1580 cm^{-1} which is absent in the glycerol spectrum. Presently, this band is unidentified; however, it does appear in the spectrum of triglycerol. The peak is also absent in diglycerol and appears to grow in intensity with the number of glycerol structural units added. The infrared spectrum of the cold wall contaminant suggests that the major organic constituent is a high molecular weight polyol, constructed by reactions similar to the condensation reaction presented above.

A spectral comparison of the hi-vac sample and glycerol is:

Hi-Vac (cm^{-1})	Hi-Vac (Dry) (cm^{-1})	Glycerol (cm^{-1})
3360	3420	3360
2940, 2830	2920, 2950	2940, 2880
1625	1580	Absent
1500-1300	1420	1500-1150
1250	1250	Absent
1100 (shoulder) 1010	1105, 1030	1105, 1035, 980
Undefined	790, 720, 695	920, 850

The same general structural considerations apply to the hi-vac sample as those given previously for the cold wall contaminant. The dried and undried hi-vac samples show a strong band at 1250 cm^{-1}, which presently can not be assigned. The complex hi-vac sample appears to be related structurally to that found on the cold wall; however, differences in the spectra imply that the hi-vac sample may be more of a mixture of

compounds and rigorous interpretation is not possible. The peaks at 790, 720, and 695 cm^{-1} found in the dry hi-vac sample yield some interesting possibilities because this region is characteristic of substituted aromatic rings, carbon-halogen bonds, and other organic and inorganic compounds. The possibility of iodinated organic compounds cannot be excluded.

Nuclear magnetic resonance spectra were obtained on the samples in dimethyl sulfoxide solution. Spectral comparisons are:

Cold Wall (ppm)	Hi-Vac (ppm)	Glycerol (ppm)	Remarks
3.30	3.20	3.52	CH, CH$_2$ protons
	7.30	4.25	OH protons

The resonances obtained in the glycerol are sharp, while those obtained for the contaminants are broad, unresolved absorptions charac-teristic of polymeric compounds. For the contaminants, the hydroxyl, methylene, and methine protons are not resolved. The NMR spectra do, however, eliminate from major structural consideration aromatic, olefinic, and methyl groups. The results of the NMR spectra support the conclusions drawn from the infrared spectra. The absorption at 7.30 ppm in the spectrum of the hi-vac sample may be indicative of olefinic groups. The presence of additional organic constituents in the hi-vac sample also supports the conclusions drawn from the infrared spectra, i.e., the hi-vac samples appeared to be more complex.

Mass Spectral Analysis

The volatile constituents of the contaminant were analyzed directly by mass spectrometry with the sample maintained at 50°C. The resulting spectrum revealed the volatile constituents to be a complex mixture with the 50°C volatiles containing compounds with molecular weights up to 205. To enhance mass spectral identification of the constituents, the volatiles were subjected to gas chromatographic separation on a Carbowax 20M column prior to introduction into the mass spectrometer.

Gas chromatographic analysis of the volatiles showed a minimum of 14 components; but mass spectral analysis showed this separation to be incomplete and indicated that significantly more constituents are present. Because of the incomplete separation on the gas chromatograph, mass spectra analysis was unable to identify specific constituents. However, several structural considerations may be obtained from the results.

A marked similarity of the fragment patterns in the mass spectra of the constituent mixtures, which eluted from the gas chromatograph dur-ing the initial 4 minutes of the run, led to a basic structural assignment of substituted furans for these compounds. The following compounds are indicated in the mass spectra; 2-methylfuran, 3-methylfuran, 2,5-dimethylfuran, 2-furaldehyde, and 2-acetylfuran. The furan consti-tuents appear to be the major portion of the highly volatile components.

190

The distinctive odor of furan compounds correlates with the odor of the contaminant and would be expected to contribute significantly to the contaminants malodorous content.

Mass spectra of components eluting from the chromatograph between 10 and 15 minutes after injection appear to be alcohols and polyols. The compounds show high water peaks and high 31 peaks (CH_2OH) generally associated with alcohols. Additionally, the organic skeleton appears to be five to seven carbons in length with some indication that they are cyclic (i. e., substituted cyclohexanes, cyclopentanes, etc.).

An additional component eluting from the chromatograph after 30 minutes gave intense peaks with a mass difference of 126, indicating loss of an iodine molecule. The scan was complicated by additional components and identification of this component was not possible.

6.1.3.3 Conclusions

The presence of metallic species arising from the corrosion of chamber materials of construction has been verified. A significant finding was the identification of appreciable quantities of silica in the contaminant samples. Quantitative analysis for the sodium and iodide content of the residue samples revealed that the ratio of sodium to iodide in the hi-vac sample was lower than would be expected, while the ratio in the cold wall residue was higher. One explanation of these phenomena may be the volatile nature of I_2, which (when formed during propellant electrolysis) would have a tendency to be condensed on chamber walls rather than impinged on a receiver sheet.

The organic products have been characterized partially and appear to be primarily a polymeric form of glycerol. The difference in composition betwee the cold wall and hi-vac samples may be explained by the volatility of the organic compounds. The higher molecular weight materials are essentially nonvolatile and tend to remain concentrated on the spot of impingement, whereas the lighter, more volatile components are more easily dispersed to other chamber walls.

Mass spectral analysis has helped to elucidate the chemical reaction occurring in the chamber. The volatile components of the Edwards hi-vac contaminant represent a mixture of chemical species of greater than 14 components. An outstanding constituent of the lower molecular weight compounds appear to be substituted furans. These compounds may also be responsible for the malodorous content of the contaminant. In addition to the furan constituents, alcohols, polyols, and iodine bearing molecules are also present. A complete determination of the chemical species present would be essential in elucidating the chemical reactions occurring in the vacuum chamber. However, without going into this further detail, it is already apparent that the variety of products manufactured and scattered back in the test chamber is sufficiently great such that the only sure protection for the thruster is the utilization of well planned test chamber geometries in order to minimize backscattering.

6.1.4 Analysis of Contaminants Taken From Emitters

The emitter contaminant samples analyzed to determine chemical constituents are identified as:

1a. A mixture of black and white solid materials (solids) recovered from tar-maker runs

1b. A black-brown semisolid (tar) recovered from several engine experiments

2. A contaminated capillary needle was preserved for residue analysis. Microscopic examination revealed the residue to be brown-black semisolid plus a clear viscous liquid (needle residue).

The solid sample (1a) was analyzed by X-ray fluorescence for identification of metallic species. All samples were analyzed by infrared and nuclear magnetic resonance spectroscopic techniques.

The results of analysis of the needle residue (2) has identified the viscous liquid as being glycerol. The semisolid component of the needle residue could not be identified because of the strong contribution of the glycerol absorption bands to the infrared spectrum. Analysis of the solid (1a) and tar (1b) contaminant indicates that polymeric forms of glycerol, similar to compounds found in the vacuum chamber sample (Section 6.1.3) are present; however, evidence was obtained indicating the presence of additional components presently unidentified. The analyses are described below in more detail.

6.1.4.1 Experimental

The instruments used were:

- X-ray fluorescence spectra were run on a GE XRD-5 X-ray Spectrometer.

- Infrared spectra were obtained on a Perkin-Elmer Model 521 Grating Spectrophotometer.

- Nuclear magnetic resonance spectra were obtained on a Varian A-60-A NMR Spectrometer.

6.1.4.2 Results and Discussion

The X-ray fluorescence spectrum of the solid sample (1a) indicated the presence of iodine with trace amounts of copper. The iodine (undifferentiated from iodide) content of the residue has several possible origins: a) sodium iodide residue resulting from propellant vaporization, b) ionic iodine species resulting from chemical reactions within the propellant feed system, c) elemental iodine produced in electrolysis and trapped during residue formation, and d) organic iodine containing compounds produced by propellant chemical reactivity.

The observed infrared absorptions are presented in Table 21. The spectrum of the needle residue correlates well with that of glycerol and indicates that the clear viscous liquid portion of the residue is undegraded propellant. The notable exception to this correlation is the peak at 1630 cm⁻¹. This peak is indicative of a high water content in the sample, which is to be expected, considering the hygroscopic nature of glycerol.

The solid residue yielded a poor infrared spectrum from which little structural characterization is possible. The most noteworthy portion of the spectrum are the two bands at 600 cm⁻¹ and 470 cm⁻¹. The region is characteristic of carbon halogen bonds and, with frequencies this low, indicates carbon-iodine bonds. Absorptions in this spectral region are not definitive however, because the region is also characteristic of some aromatic hydrocarbons, sulfur-oxygen bonds, and metal oxygen bonds.

The tar sample (1b) shows reasonable correlation with the poly-alcohol structure typified by glycerol. In addition, the absorption at 1605 cm⁻¹ has been associated previously (Section 6.1.3) with the formation of glycerol polymeric forms. The appearance of two absorption bands at 3880 cm⁻¹ and 2000 cm⁻¹ present interpretive difficulties. Absorption bands in either region are rare and no compound correlations were possible with the materials present in the colloid microthruster engine. The peak at 2000 cm⁻¹ is very strong while the peak at 3880 is weak and may be an overtone of the former. The region of 2000 cm⁻¹ is typical of carbon oxygen bonds in simple di- and triatomic molecules such as carbon monoxide and carbon dioxide. In addition, the region is characteristic of amine hydrochloric salts, carbon-nitrogen triple bonds (i.e., isocyanides and inorganic cyanides), and some inorganic species such as bicarbonates, thiosulfates and perchlorates.

The results of nuclear magnetic resonance spectrometric analysis are given in Table 22. The tar and solid samples show single broad resonances similar to those found in the Edwards vacuum chamber contaminants. These types of resonances have been associated with polymeric molecules. The needle residue shows two peaks as in glycerol; however, the chemical shifts have moved up-field. In addition, the chemical shift difference is less than that noted for glycerol. Additional NMR spectra have eliminated temperature and solvent effects as possible causes of the observed shifts. No explanation is available for the observed spectrum.

6.1.4.3 Conclusions

The needle contaminant could not be identified because of the residual glycerol content of the sample. The solid and tar contaminant samples show polymeric characteristics similar to those found in the vacuum system contaminants (Section 6.1.3). However, evidence of additional components is present but they have not been identified.

6.2 RADICAL INHIBITORS

Particulate contamination studies have confirmed the presence of polymeric forms of glycerol, including polyols and iodine bearing compounds. A tenable hypothesis is that these forms are glycerol type

Table 21. Observed Infrared Absorption

Solid Residue (cm⁻¹)	Tar (cm⁻¹)	Needle Residue (cm⁻¹)	Glycerol (cm⁻¹)	Remarks
3400	3880			Unassigned
	3420	3360	3360	OH stretch
	2930, 2880	2940, 2880	2940, 2880	CH_2 stretch for CH_2 and CH
	2000			Unassigned
1615	1605	1630		Unassigned
		1500-1150	1500-1150	OH in plane bend CH_2 symmetrical bend
1100 1035	1080 1038 975	1100 1030 985	1105 1035 980	C-O bend combination of primary and secondary alcohols
	905	910	920	CH_2 deformation
	840	845	850	Unassigned
600				Unassigned
470				Unassigned

194

Table 22. Nuclear Magnetic Resonance Spectral Data

Solid Residue (ppm)	Tar (ppm)	Needle Residue (ppm)	Glycerol (ppm)	Remarks
3.60	3.50	3.00	3.52	CH, CH_2 protons
		3.25	4.25	OH protons

radicals, caused by bombardment of glycerol atoms by high energy negative secondaries, which migrate through the propellant until they bond with another favorable radical or molecule. One tentative solution is to introduce a radical inhibitor into the propellant that would quickly deactivate the offending radical by joining with it to form a harmless, stable substance that would be assimilated into the propellant. The following list of radical inhibitors contains one representative of each major class of compounds used for this purpose:

Compound	Type
2,2-diphenyl-1-picrylhydrozyl	stable radical
p-benzoquinone	quinone
trinitrobenzene	nitroaromatic
2-aminonaphthalene	aromatic amine
4-phenylphenol	substituted phenol
sodium sulfide	inorganic
thianaphthalene	aromatic thiol

A sample of p-benzoquinone was obtained and experiments were initiated to evaluate its potential for preventing propellant tar formation. A test station was set up to bombard propellant samples with electrons to evaluate the effects of candidate additives. The station included a small semifocused electron source capable of delivering up to several milliamperes at 5 to 15 kv. The material to be bombarded was spread thinly over the bottom of a 2-inch-diameter aluminum cup placed 6 inches below the source. Several normal colloid propellant samples were bombarded to provide a comparison standard. It was found that eventually, long term bombardment in a vacuum led to the formation of a solid iodine-colored residue. This residue was highly deliquescent and, upon exposure to the atmosphere, soaked up enough water to turn completely liquid. The residue is most probably a mixture of sodium-iodide and iodine that remains after the glycerol has been driven off by bombardment-induced decomposition and evaporation. There is a good probability that this same process initiates particulate formation on operating thrusters.

A 5 percent solution of p-benzoquinone in propellant (80 grams of propellant to 4 gms of additive) and a normal propellant sample were

195

placed side by side and bombarded at 8 kv, at 200 and 150 µamps, respectively. Due to a slight asymmetry in the electron beam profile, the currents were not exactly equal. Two cc of outgassed fluid were used for each sample. Immediately upon initiation of the bombardment, the modified propellant bubbled vigorously compared to the relatively low bubble generation rate in the normal sample. Bombardment was continued until the samples were converted into slushy residues. From the photographs of the samples after bombardment (Figure 157), it is apparent that the normal propellant resulted in much less residue than the modified sample. As a result of the comparative behavior of the two samples during the experiment, it is concluded that the addition of p-benzoquinone does not reduce the deleterious effects of electron bombardment but, on the contrary, enhanced both gas formation and residue volume. Samples of the other candidate additives were obtained but work was discontinued because of their hazardous nature.

6.3 BACKSCATTERING EXPERIMENTS

Experiments were performed to investigate techniques for minimizing the effect of backscattering of material from the collector and other surfaces during vacuum chamber life testing of colloid thrusters. To accomplish this experiment, the 24-inch diffusion pumped 4 x 8 foot chamber was outfitted with a special aluminum "venetian blind" baffle positioned directly in front of the honeycomb collector. The baffle was controlled from outside the tank during thruster operation, thus providing different geometric collector configurations. The main objective of this experiment was to determine if changes in the collector geometry could serve as an effective technique for reducing the arrival rate of backscattered particles in the vicinity of the thruster. The ability to produce these changes without having to shut down the test and open the chamber guaranteed constant thruster performance during the comparison.

Three different backscattering detection devices were placed in the vicinity of the thruster: (1) a quartz crystal microbalance (QCM), (2) a current measuring probe, and (3) an ionization gauge. These probes were individually rotatable so that their response to the general test chamber background could be compared to the signals obtained when looking directly into the backscattered efflux.

Figure 158 is a photograph of the test chamber taken from the thruster end of the system. The ion gauge detector, the QCM, and current probe assembly can be seen in the immediate foreground. These, as well as the other detectors shown, were mounted on externally rotatable support rods so that readings could be made either when looking directly into, or away from, the backscattered flux. In this figure the venetian blind baffle is open, affording a full straight-on view of the honeycomb collector. Figure 159 is the same view with the baffle partially closed and Figure 160 is a view through the baffle from the other end of the tank. The 36-needle module can be seen in the center of the far end of the tank.

When the baffle was closed, it simulated a flat-plate backscattering target; when fully open, it was essentially transparent and allowed the
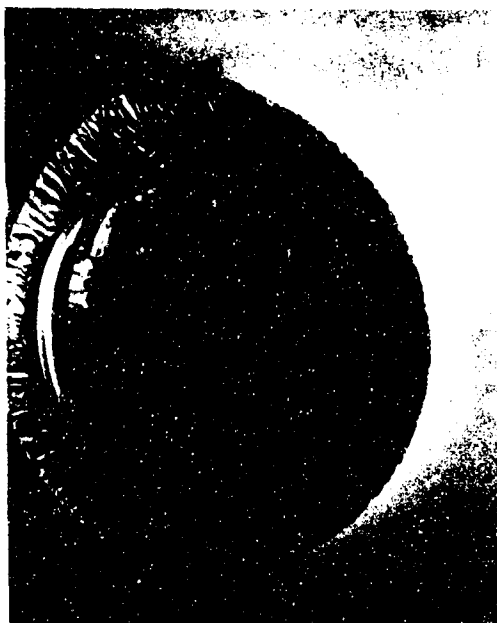
a. NaI + Glycerine

b. NaI + Glycerine +
P-Benzoquinone

Figure 157. Samples After
Electron Bombardment

colloid beam to impinge directly on the honeycomb collector; and, in the intermediate positions, the resultant geometry was an optically opaque chevron baffle with a central vertical axis of symmetry. This last feature was necessary to ensure that both sides of the diverging thruster beam could see an equally opaque baffle.

The quartz crystal microbalance used the mass dependence of the resonant frequency of a vibrating quartz crystal to determine mass changes caused by the deposition of arriving material. Thus, as backscattered material was deposited on the face of the crystal, the resonant frequency was progressively lowered. A strip chart recorder plotted the frequency as a function of time, thus providing a continuous indication of the rate of deposition of backscattered material. The crystal was mounted directly behind an electromechanical shutter and collimating aperture. The assembly was normally positioned with the crystal directly to the side of the thruster module, 7 inches from the center of the thruster module, and looking directly back at the collector. To verify that the crystal response was due to backscattering, observations were periodically made with the crystal shutter closed and/or the crystal facing the side of the vacuum tank. During the measurements, the thruster was operated at a needle potential of 10 kv with 9.2 kv on the deflector electrodes and -1.6 kv extractor voltage. The feed pressure was varied between 1 and 1.6 inch Hg. Early in the experiment, it was determined that the current probe and ionization gauge detectors were too insensitive to pick up changes in the backscattering rate. The ionization gauge's response to the backscattering was too small compared to the signal produced by the background pressure (approximately 3×10^{-6} torr) within the
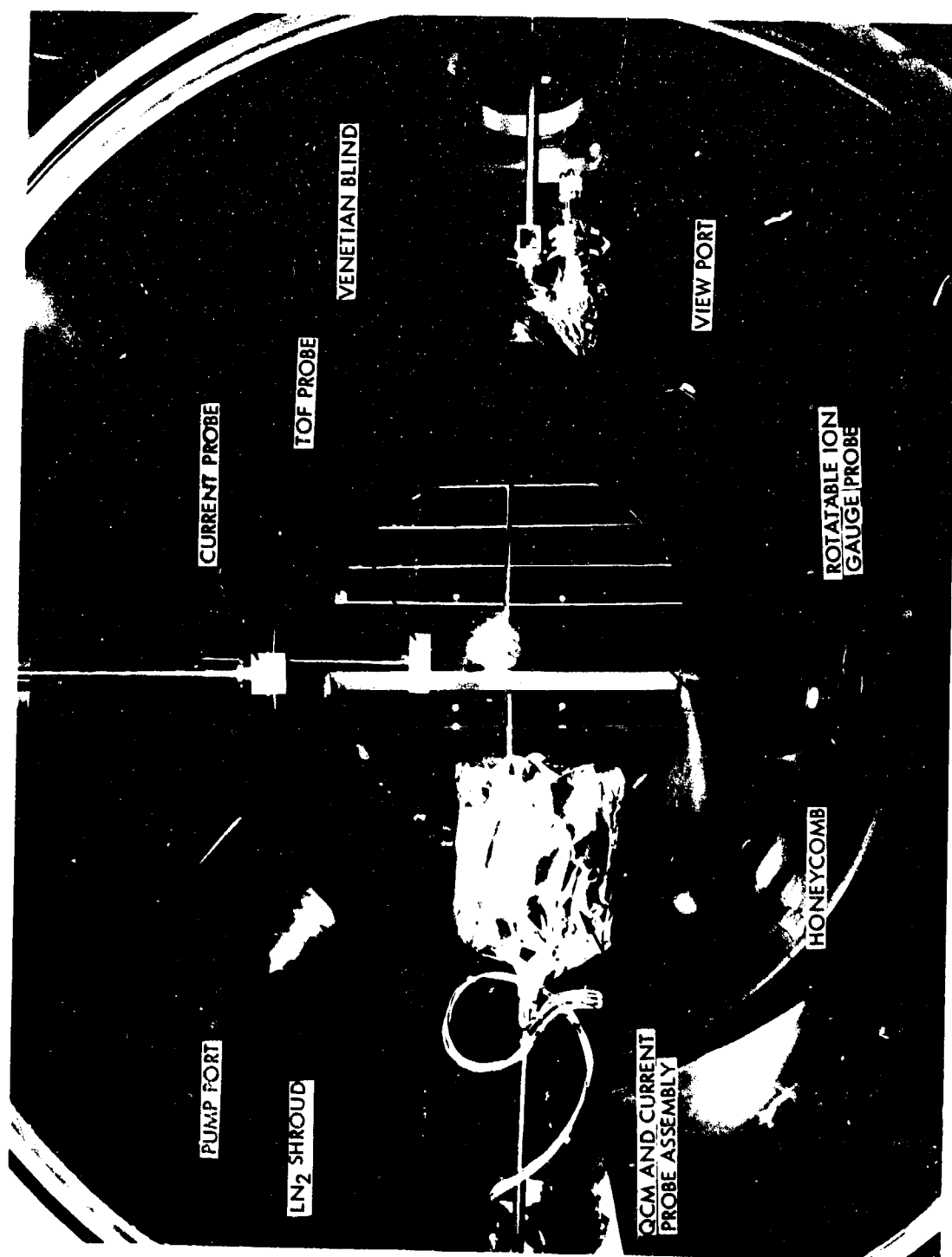
Figure 158. Backscattering Experiment Viewed from Thruster End of Chamber With Venetian Blind Baffle Open
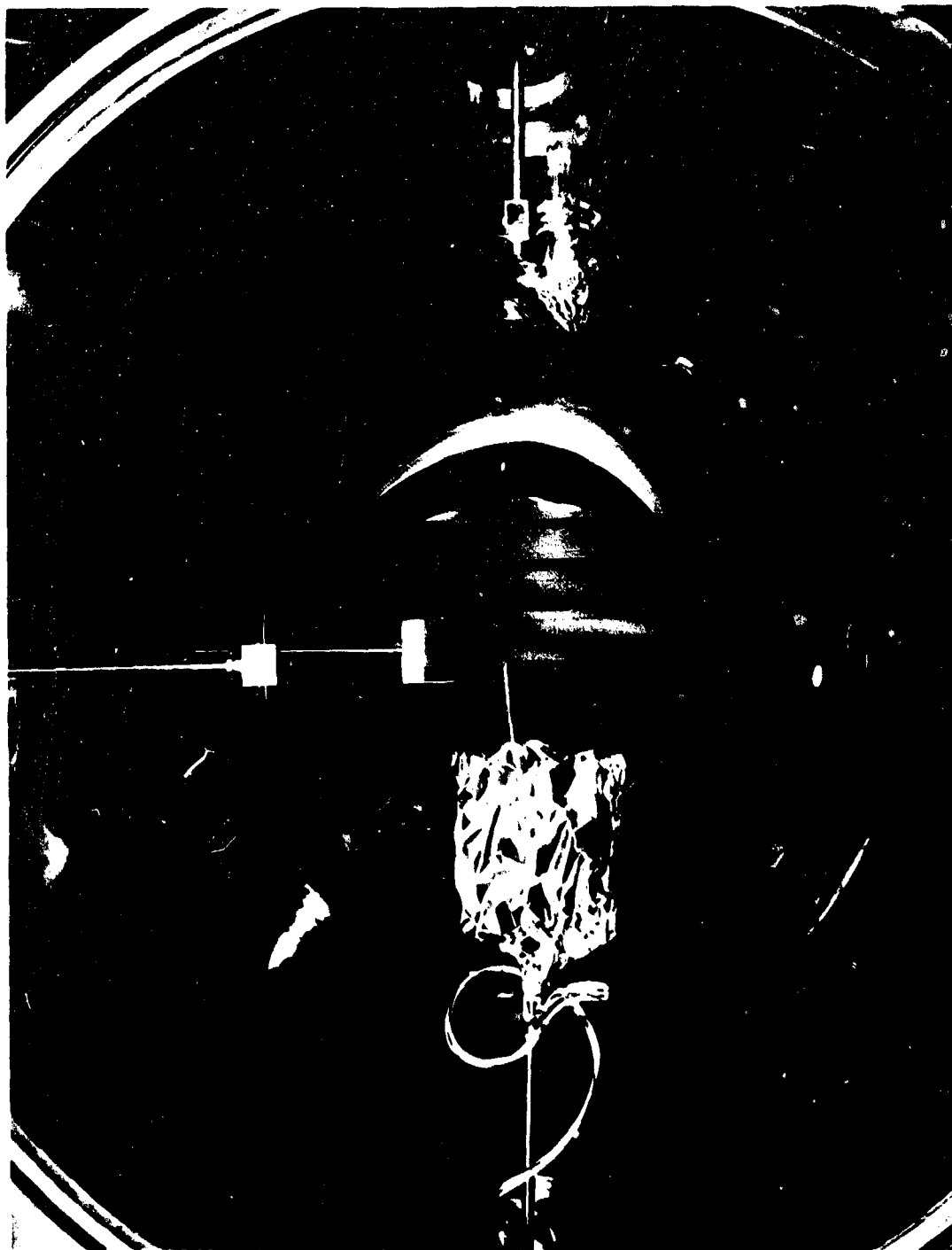
Figure 159. Backscattering Experiment Viewed From Thruster End of Chamber With Venetian Blind Baffle Partially Closed

Figure 160. Backscattering Experiment Viewed From Collector End of Chamber Through Open Baffle (Note 36-Needle Module at Far End of Tank)

vacuum chamber, e. g., the gauge reading was affected very little by rotation of the pointing direction. At zero bias, the current probe reading seemed to be caused by the chamber's ambient plasma. At other biases, the response was completely dominated by extraneous leakage currents. The quartz crystal microbalance was able, however, to provide sensitive measurements of the backscattered current throughout the course of the experiment.

The following table shows the QCM results for three different venetian blind baffle angles, where 0 degrees corresponds to fully open and transparent (i. e., looking at the honeycomb collector) and 90 degrees corresponds to fully closed (i. e., flat plate collector).

Run of 8/28/70			
P = 1 in. Hg, I_N = 270 μamp, I_{sp} = 1680 seconds, $\dot{M}$ = 13. 7 microgram/sec, Q/M = 19, 700 C/kg, T = 50. 7 μlb, QCM at Room Temperature			
Baffle Angle	0	45	90
Detected backscatter (microgm/cm^2/hr)	0. 0885	0. 1416	0. 239

Thus, the backscatter for the honeycomb geometry was 37 percent of that for the flat plate. After being shut down for the weekend the test was resumed the following Monday. This time the QCM was cooled to -50° C, to see if the observed trends would be changed at the lower temperatures. The following results were obtained in this case:

Run of 8/31/70			
I_N = 265 μamp, no time-of-flight data taken			
Baffle Angle	0	45	90
Detected backscatter (microgm/cm^2/hr)	0. 177	0. 294	0. 428

In this case, the honeycomb response was 41 percent of the flat plate backscattering.

An additional run was then made on September 3 at various angles between 0 and 75 degrees (Figure 161). These data were taken at time-of-flight beam parameters of I_N = 310 μamp, I_{sp} = 1505 seconds, thrus' 65. 5 μlb, $\dot{M}$ = 19. 6 microgm/sec, η = 68. 5 percent, q/m = 15, 820 C/kg

201
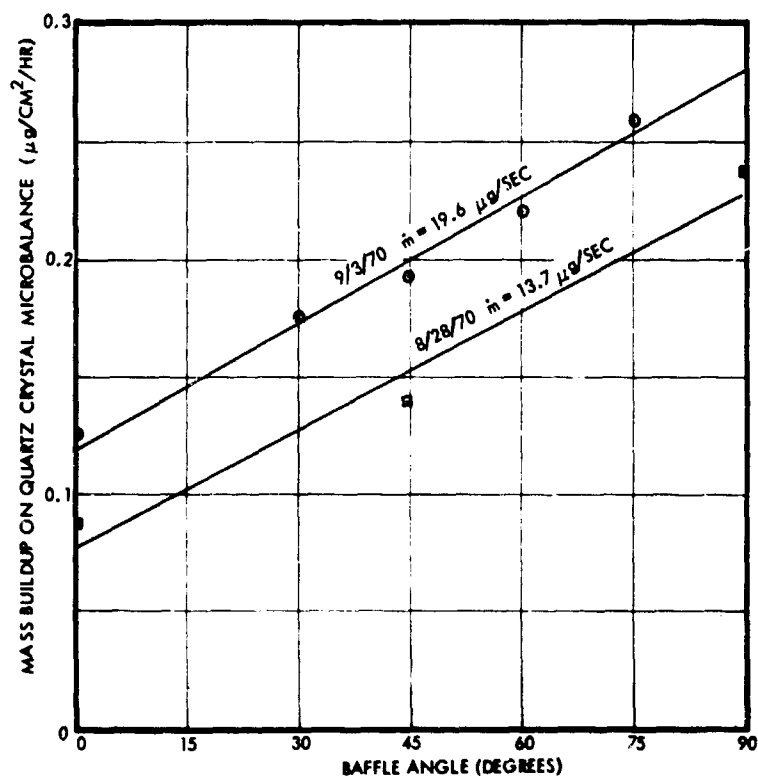
Figure 161. Quartz Crystal Microbalance
Response as a Function of Baffle Angle
for Two Different Thruster Mass Flows

at P - 1. 4 in. Hg. Comparison of the data for 8/31/70 and 9/3/70 shows, as one would expect, that the backscatter is approximately proportional to the total mass flow. The ratio of the time-of-flight thruster mass flow of the first run to that of the second was 0. 7. This was also the ratio of the mass buildups.

The effect of background vacuum pressure on QCM mass buildup was investigated. The QCM response was measured at system pressures of 2.8×10^{-6}, 9×10^{-6}, and 2.8×10^{-5} torr. These data were taken at time-of-flight beam parameters of $P = 1.4$ in. Hg, $I_{sp} = 1480$ seconds, $T = 68.0$ μlb, $\dot{M} = 20$ μlb/sec, $Q/M = 14,900$ C/kg.

Run of 9/9/70 - Background Pressure Effects			
Background Pressure (torr)	2.8×10^{-6}	9×10^{-6}	2.8×10^{-5}
Detected backscatter (microgm/cm^2/hr)	0.0974	0.0974	0.0407

202

The above table indicated that the apparent backscatter was independent of pressure for the two lower readings, but decreased to 42 percent of its value at the highest pressure, 2.8×10^{-5} torr. The apparent decrease in the backscatter at the highest pressure is most probably caused by the mean free collision path being of the order of the test system dimensions. This shows up in two ways; first, particles scattered from the back wall now become attenuated before reaching the QCM, and second, the primary beam slightly attenuates before it reaches the back wall. The latter effect is believed to be the lesser of the two since there was no observable reduction in collector current for the higher pressure. An increase is expected in the collision rate with gas molecules directly in front of the thruster; but, since the QCM was 7 inches off to the side of the module, these collision products would not be able to deposit on the QCM, and therefore as far as collisions with the background gas are concerned, the QCM is not a good indicator of the resultant deposition on the thruster.

6.4 EFFECT OF AMBIENT BACKGROUND PRESSURE ON GAS GENERATION

This experiment consisted of microscopically observing bubble generation rates within the emitter tip as a function of needle current and vacuum tank background pressure. The test was run with a number 4 type source with a partially clogged impedance. Because of this impedance, the beam current was down to 30 μamp at 14 kv and 4-inch Hg feed pressure. The time-of-flight traces showed an ion peak containing nearly 70 percent of the current and an abnormally low mass flow. The study showed, not unexpectedly, that bubbling rate was an increasing function of ambient (tank) pressure and needle current. Data taken for the needle operating at three different currents are plotted in Figure 162.

The curves in Figure 162 show that, for each needle current, there is an ambient pressure below which no bubbling occurs. This minimum pressure, which is rather well defined, is shown in Figure 163 as a function of needle current.

The zero bubbling rate point was studied extensively at the 38 μamp needle current level. This is the only level at which the mass flow rate was low enough so that the system pumping capacity could bring the ambient pressure below the bubbling threshold. The other two curves for 75 and 85 μamp had to be extrapolated to zero bubbling rate. The curve in Figure 163 is thus based on the extrapolations (shown in Figure 162) for these higher currents.

Based on this data, zero bubbling rates for a 90 to 100 μamp needle would require a vacuum in the low 10^{-5} torr or high 10^{-6} torr range.

A time-of-flight summary shown in Table 23 gives the relevant needle performance parameters during the bubble-counting sequences. Data are given for a source voltage of 14 kv (at which voltage all bubble counting experiments were performed) and for the 38- and 85-μamp beam currents. Time-of-flight information for the 75-μamp current turned out to be invalid due to a transient in performance; however, it is expected to be close to the 85-μamp performance.
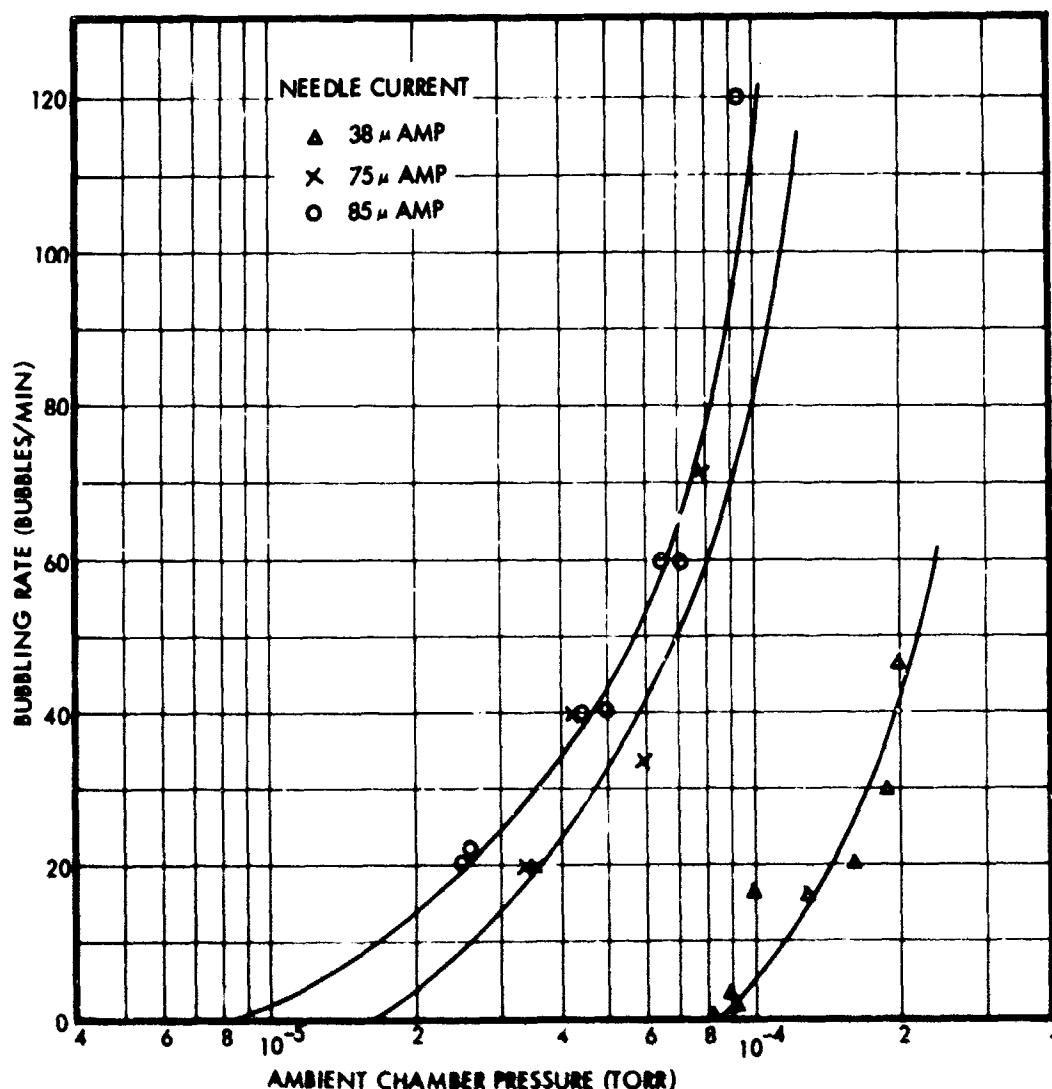
Figure 162. Bubble Formation Rate in Center Fed,
Open Meniscus ANG, as a Function of
Beam Current and Ambient Pressure

The time-of-flight information for the 38-μamp beam current was
obtained at the ambient pressure where onset of bubbling occurred. For
85 μamp, it was obtained at the lowest achievable ambient pressure.
Both 75- and 85-μamp beam current bubbling data were obtained with a
feed pressure of 1 atmosphere; and the current increase was caused only
by a change in rim wetting conditions, achieved by going to a "source-
voltage-off" condition for 90 seconds.

6.5 POSSIBLE IMPLICATION FOR HIGH CHARGE-TO-MASS RATIO FOR COLLOIDS

The hypothesis that the colloid propellant is charged by neutraliza-
tion of iodine ions implies that the maximum charge-to-mass ratio should
be influenced by the solubility limit of iodine in glycerine. Since a single
electronic charge is 1.6×10^{-19} coulombs, equivalent to 6×10^{18}
electrons/coulomb, a charge-to-mass ratio of 10^4 coulcmb/kilogram
requires the removal of 6×10^{22} electrons/kilogram of propellant.

204
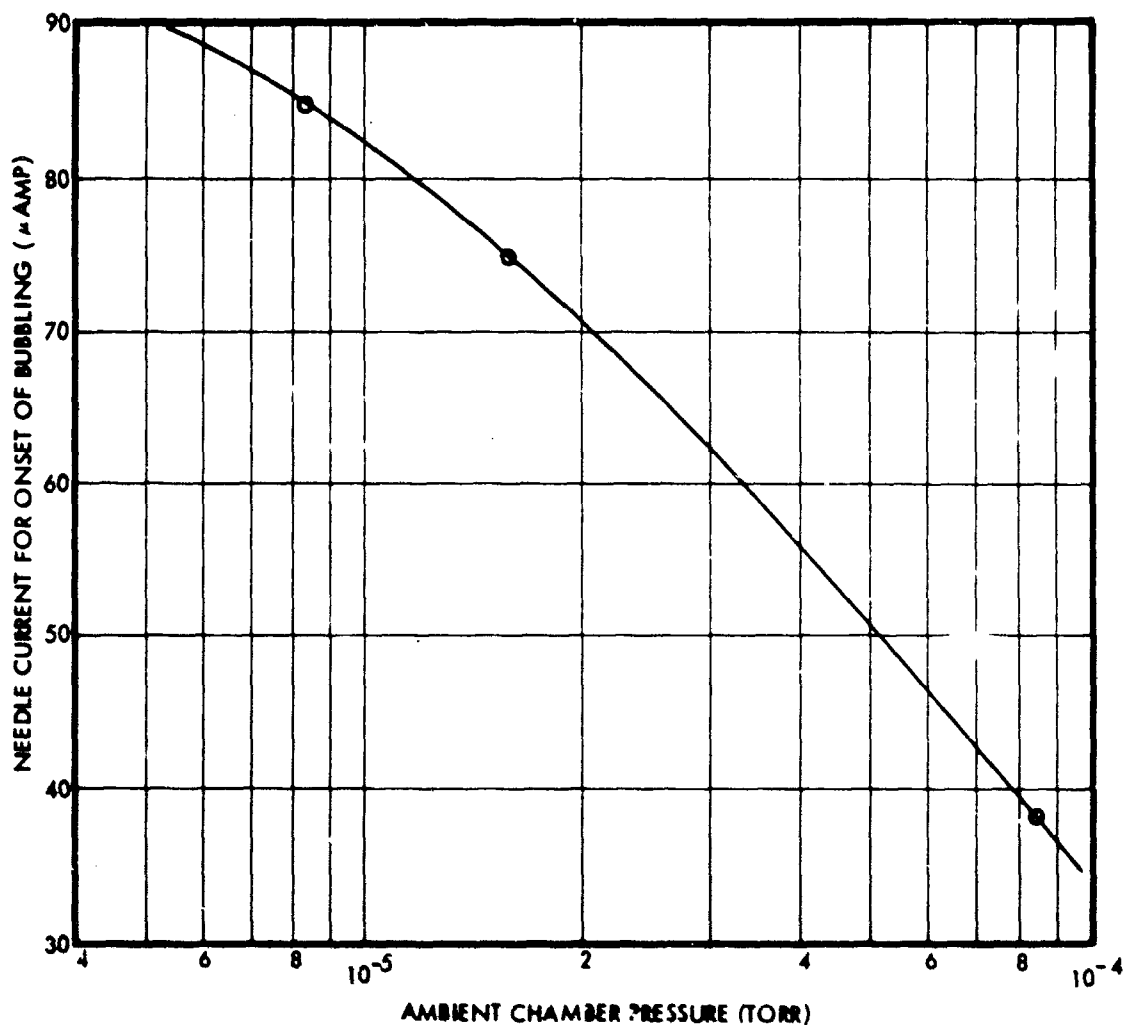
Figure 163. Minimum Bubble Generating Beam Current as a Function of Ambient Pressure. Bubbling occurs above the curve. Below the curve, the meniscus is quiescent.

The atomic weight of iodine is 127 amu. Since each electron neutralizes one iodine ion, and remembering that $N_o = 6 \times 10^{23}$ molecules/mole, 12.7 grams of iodine ions can be neutralized per 1 kilogram of propellant, i.e., 1 27 parts per 100 by weight. On the other hand, the published solubility of iodine in glycerol is only 2 parts per hundred.[1] Thus, in this charge-to-mass ratio range the solubility limit can be closely approached assuming no other mechanisms are operating. However, it is a well-known fact that, for aqueous iodine solutions, the presence of excess iodine ions, such as would be available from dissolved

1. "Physical Properties of Glycerine and its Solutions," Glycerine Producers' Association, New York, New York.

205

Table 23. Uncorrected Time-of-Flight Data for Bubble-Counting Experiments

Beam Current (μamp)	Feed Pressure (in. Hg)	Ambient Pressure (torr x 10^{-5})	Thrust (μlb)	Flow Rate (μgm/sec)	Thrust Efficiency (%)	I_{sp} (sec)	$\overline{q/m}$ (coul/gm)
38	5.0	8.5	4.3	0.723	48	2712	52.6
85	30	2.4	10.6	1.26	73.4	3810	67.9

Suppressor voltage: -45 v

Screen voltage: 50 v

Time-of-flight distance: 1.95 m

sodium iodide, provides a means of readily dissolving additional iodine,[2] accomplished by the formation of triiodide ions; $I^- + I_2$ (aq.) = I_3. Possibly, a similar mechanism occurs in glycerol. If not, excessively high charge-to-mass ratios would produce gaseous iodine evolution and/or precipitation (the vapor pressure of I_2 is 0.4 torr at 20° C). This, of course, could result in tar formation initiated by iodine precipitation, gas evolution and glow discharge. Similarly, for a nonuniformly emitting rim, this effect could then lead to difficulties on portions of the rim that are emitting at excessive charge-to-mass ratios.

---

[2] Principles of Chemistry, Latimer and Hildebrand, 5th ed., 1949, p 168.

7. DIAGNOSTICS

This section provides a discussion of several new techniques developed to diagnose performance of colloid thrusters. Section 7.1 describes an automatic data acquisition system which was developed to perform automatic digital recording and read-out of time-of-flight data. The system is coupled into the TRW Timeshare computer system to provide on-line computer analyses of the data. Section 7.2 is a discussion of the results of time-of-flight probe experiments to determine the angular distribution of propellant emission from the thruster. In addition to the mass flow angular distribution, specific impulse, thrust, current and charge-to-mass ratio distributions were also measured. The effect of these distributions on the accuracy of single collector time-of-flight experiments was analyzed for flat plate and spherical collectors. It was found to be of the order of 3 percent for typical annular source beam profiles. As a further check on the validity of the time-of-flight technique, experiments were performed to correlate direct mass flow measurements with time-of-flight computed mass flows for both annular sources and multineedle modules. These experiments, described in Section 7.3, showed that the time-of-flight mass flows were usually a few percent lower than directly measured flows. However, the data scatter was too great to allow a specific interpretation of the differences between the two techniques.

7.1 AUTOMATIC DATA ACQUISITION SYSTEM FOR TIME-OF-FLIGHT MEASUREMENTS

A new electronic system has been developed to greatly improve the convenience with which time-of-flight measurements can be made. It also should improve the accuracy of the data. As a result, the number of traces taken during a colloid thruster test may be expected to increase two- or threefold, with a consequent improvement in the overall understanding of thruster performance.

The colloid thruster automated time-of-flight data acquisition system (ADAS) is shown in Figure 164. A standard thyratron shorting system for the high voltage is shown, in which a 300-volt pulse applied to the grid triggers a discharge, instantaneously shorting the source voltage. A transient from this discharge is used to trigger the digital transient analyzer, which digitizes and stores the input signal current. A parallel oscilloscope is available for inspection of the signal. The transient analyzer is the input element of the total system described below.

The total system comprises three segments, two of which are electronic units; the digital transient recorder and the digital scanning recoder. The third is a standard teletype remote computer terminal. Both the terminal and the electronic system are on casters so that the electronics can be connected to any of the several colloid thruster test facilities, and the terminal can "talk" to the computer through its acoustic coupler and the nearest telephone handset.

207
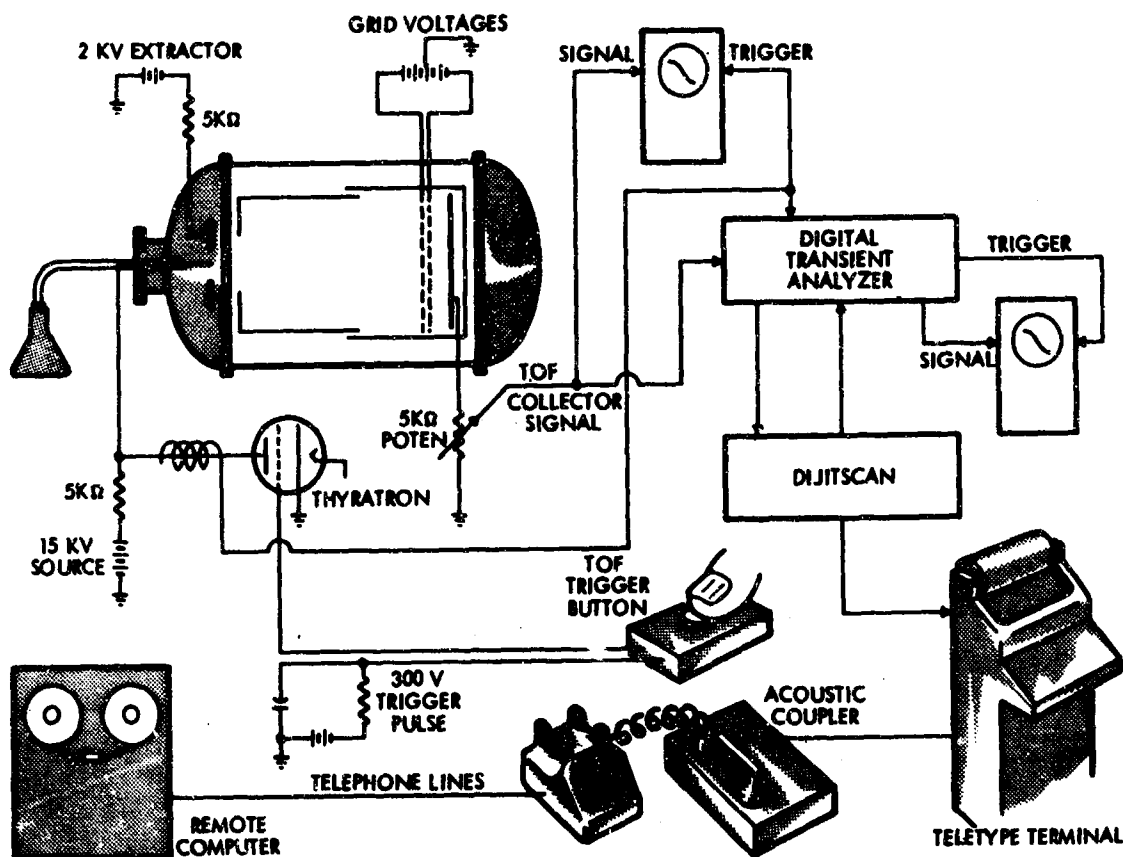
Figure 164. Schematic of Time-of-Flight Automated Data
Reduction System

The first of the electronic items is the transient recorder* which,
upon receipt of a trigger pulse, samples, digitizes, and stores 128 values
of the input analog voltage during the subsequent "sweep" period.   The
internal memory of the transient recorder is a solid-state, recirculating
shift register, and the recorded transient may be repetitively (continu-
ously) displayed on a monitor oscilloscope.   During the first recirculation
following a recording sweep, the contents of the shift register are gated
to the digital output bus as a sequence of binary words.   The second
unit, a digital scanning recoder,** accepts the binary words from the
transient recorder, recodes each one into two-digit decimal numbers, and
outputs these numbers to the teletype machine, together with proper punc-
tuation and line formatting.   During this playback of the recorded transient,
the teletype is used to make both a printed record of the transient and a
punched paper tape record which is suitable for subsequent input (from the
same terminal) to the computer.

---

*Biomation, Model 610

**Pivan Data Systems, Dijitscan

Heretofore, the typical procedure for time-of-flight data acquisition involved making a Polaroid photograph of an oscilloscope trace, reading a sequence of values from the trace, and punching the paper tape from the keyboard of the terminal. The current procedure involves only punching the identifying and auxiliary data by hand, and then pushing the trigger button to complete the paper tape preparation automatically. Tapes prepared either automatically or from hand-reading of photographs are equally compatible with the computer program which analyzes the time-of-flight traces.

Although the automatic system was acquired principally because of its convenience (hence, increased number of traces per te), it now appears that a considerable improvement in consistency in the data will result from its use, and possibly an improvement in accuracy as well. The transient recorder uses 64 quantizing levels (each internal 1.5625 percent of full scale), which can be expected to give precision comparable to the reading of photographs with the unaided eye (assuming absence of non-linearity and parallax in the photograph). The sampling intervals are derived from a quartz crystal oscillator, assuring much greater precision in the time base than is possible with the oscilloscope-photograph method. Studies are continuing of means to achieve the maximum accuracy with the automatic time-of-flight data acquisition system.

The time-of-flight equations have been programmed in Fortran, for use in the TRW timeshare computing system. This system is built around a CDC 6400 computer. A copy of the program listing and a sample case are given in Appendix B.

Several studies were undertaken to compare time-of-flight results calculated with the automatic system and calculated by hand. The studies mainly concentrated on mass flow rate comparisons, and were done in conjunction with direct mass flow rate measurements (Section 7.3). The studies showed no significant difference between the two methods of calculation.

Early in run 7104-02, during a 433-hour annular emitter run with direct mass flow measurements, a series of time-of-flight mass flow rate measurements were taken in close succession. These measurements were used primarily to seek a correlation between mass flow rate and gas generation activity on the propellant meniscus (see Section 6.4). They were also used to obtain a comparison between time-of-flight results using hand measured data from Polaroid photos and automated acquisition data.

Figure 165 shows the resulting scatter diagram for the data set. The 45-degree line is indicated as the line along which perfect data should lie. A least-squares straight line was fit to the data with two degrees of freedom. The two parameters found were the slope, 0.8245, and the "M-hand" axis intercept, 0.8561 μgm/sec. The calculated standard deviation of the data about the least squares line was 0.264 μgm/sec, and the resulting uncertainty band is shown in the figure. The least-squares line and the 45-degree line are within a standard deviation of each other over the range of the data, so that the difference is not statistically significant.

209
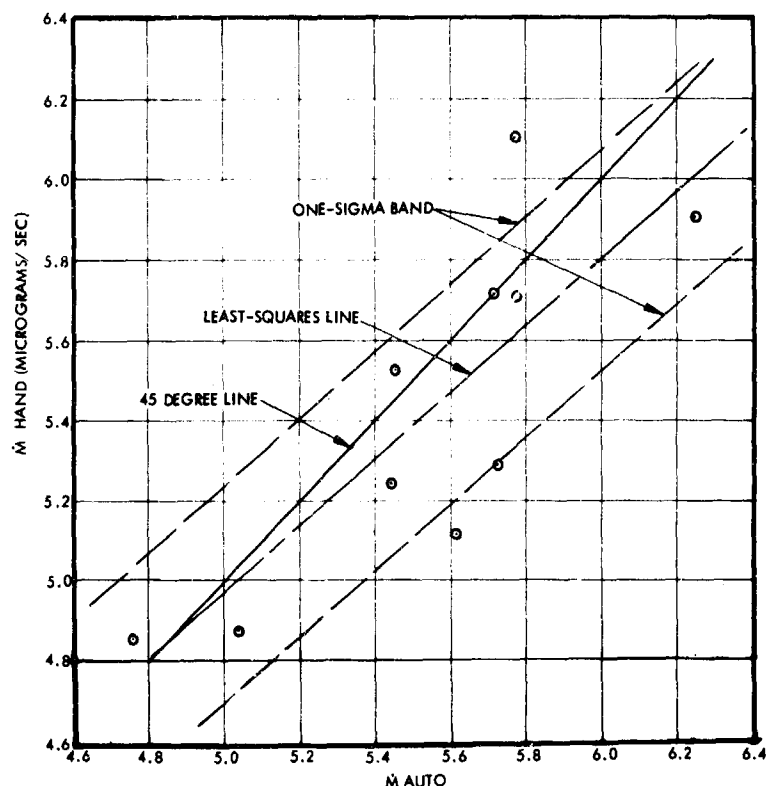
Figure 165. Comparison of Hand and Automatic
TOF Mass Flow Calculations:
Run 7104-02: Gas Generation
Correlations

A series of time-of-flight correlations was also taken during life test 7101-04, to compare hand and automatic calculations. This earlier test also showed no significant difference between the two, although a complete statistical analysis was not included in the test plan.

7.2 ANGULAR DISTRIBUTION OF EXHAUST BEAM MASS FLOW

Small movable time-of-flight collector probes were used to determine the angular distribution of mass flow rate, charge-to-mass ratio and other time-of-flight parameters in the colloid exhaust beam. These were installed in the 4- by 8-foot vacuum test chamber and were used to scan across the horizontal and vertical cross-section axes of the beam (Figure 166).

In addition to many runs in which beam current profiles were measured, a total of ten time-of-flight profile scanning experiments were measured during the course of six separate runs. Two were performed with a vectored beam. In the aggregate, these experiments showed a single-peaked distribution in mass flow, maximum in the direction of net thrust. Ninety percent of the beam was contained in a 12-degree half-angle cone. The time-of-flight probe results for these experiments are discussed in this section according to run number. Further results for each run may be found in Section 2.

210

Figure 166

Two Time-of-Flight Probes
Mounted to Measure Beam
in Orthogonal Directions

An analysis has been made of the effects of finite beam spread on time-of-flight measurement accuracy. These effects were evaluated by using a mass flow distribution function which is dependent on emission angle as well as charge-to-mass ratio. The results were then simplified in order to use the experimental probe results to estimate the errors caused by these effects. The result was an error of the order of 3 percent in thrust, flow rate, efficiency (neglecting thrust misalignment) and average charge-to-mass ratio. However, the specific impulse was affected only to second order by these effects.

7.2.1 Probe Design

A small, movable time-of-flight collector probe must have a small collection area whose size has been optimized to provide sufficiently localized measurement within the exhaust beam while still maintaining adequate collector current signal-to-nois' ratio. The probe should have a high internal impedance and a fast time response, in order to provide an accurate time-of-flight record. Good shielding will also enhance the signal-to-noise ratio. In the past, the most serious noise sources for these small collectors were displacement currents caused by the rapidly varying ambient plasma potential and radiated electromagnetic noise generated when the thruster voltage was suddenly shorted for time-of-flight initiation. For this reason, adequate shielding was an important design consideration.

Figure 167 is a schematic diagram of the probe design. It is a total current, registered-hole, collector (i.e., the sum of suppressor and collector current is read at the output). The slots are champhered to accept up to 20 degrees divergence without interception on the suppressor. Extra precautions against radiated electromagnetic noise included complete shielding of all leads, enclosure of the probe within a grounded 100 mesh external screen grid, and use of deep shield slots to attenuate fields penetrating the grid.
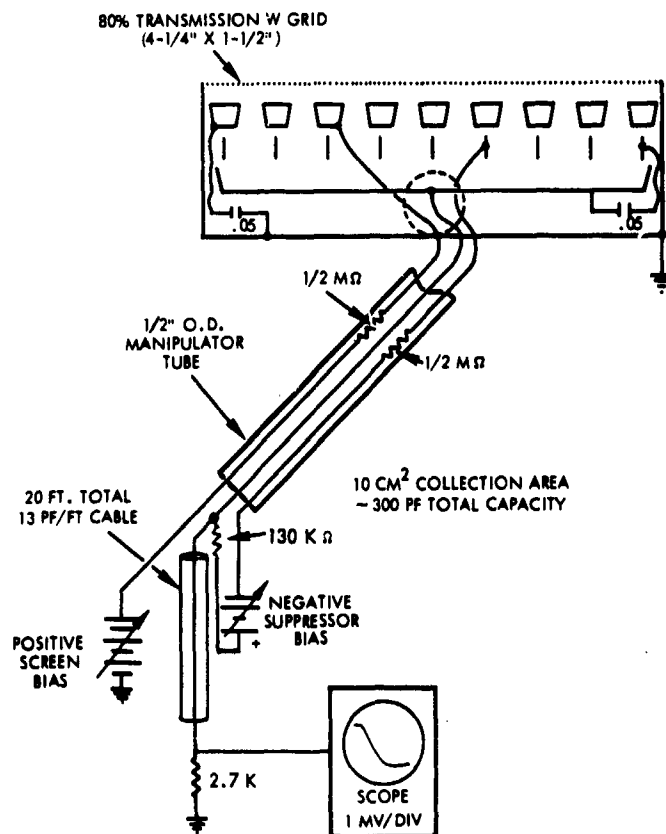
Figure 167. Time-of-Flight Probe Design

Former designs, which employed a field effect transistor input, used the shield biases to provide transistor bias voltages. This prevented the possibility of independently varying the shield biases to optimize collector performance. The new design has no such restriction.

A short RC response time (which is needed for accurate time-of-flight measurements) is assured by the device's low capacitance (C) to ground. This allows the use of a relatively high value of collector load resistance (R) while still maintaining a low RC product. Thus, an adequate voltage drop will be obtained for relatively low currents on the small collector area. When used as the input to a Tektronix 1A7 high gain, wide-band plug-in amplifier, the probe signal can be amplified for recording and digitizing by the automatic time-of-flight data acquisition system. Figure 168 shows a typical time-of-flight current trace taken with one of these probes.

The first five scanning experiments discussed in this section were performed with a probe screen voltage of 60 volts, obtained from a small regulated dc power supply, and a suppressor voltage of -60 volts, which was obtained from an unshielded battery. For the remainder of the experiments, the screen and suppressor voltages were reduced to ±30 volts. The battery was replaced with a small shielded 30-volt cell which was built into the cable connector.
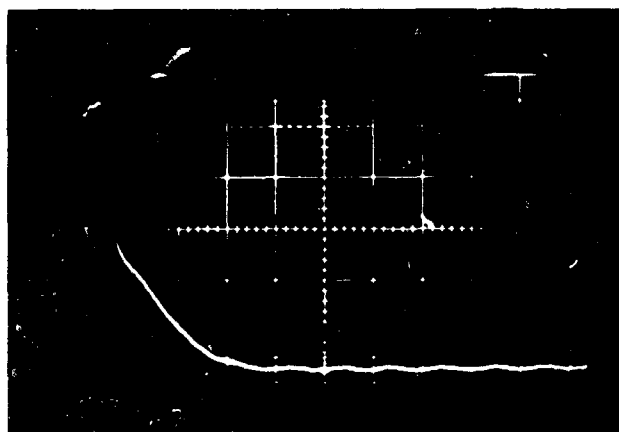
212

A typical set of probe measurements consisted of a probe position
measurement made on the outside portion of the probe manipulator rod; a
probe current measurement, either made directly or obtained from the
voltage drop across the 2.7K resistor; and a set of time-of-flight data
readings obtained either by hand or from the automatic data acquisition
system. These measurements were generally repeated for 1 inch incre-
ments of probe position, corresponding to about 1.5 degrees of beam angle.

The current density and time-of-flight distance are obtained for each
measurement by applying the following equations.

$$\theta = \arctan \frac{x - x_o}{r} \quad : \quad \text{probe angle} \tag{1}$$

x is the probe position (meters)

x_o is the probe centerline position (meters)

r is the distance from thruster to probe plane (meters)

$$D = r/\cos \theta \quad : \quad \text{time-of-flight distance} \tag{2}$$

$$\omega = \frac{A \cos \theta}{D^2} \quad : \quad \text{solid angle subtended by the} \tag{3}$$
$$\text{probe at the thruster}$$

A is the probe frontal area, 0.001 square meter

$$J = I/\omega \quad : \quad \text{beam current density} \tag{4}$$
$$\text{(microamps/ster)}$$

I is the collected probe current (microamps)

213

The value of r was typically a little less than 1 meter, and would vary from one test facility to another. A time-of-flight distance D is calculated for each probe setting using Equation (2). In Equation (3), the cos θ factor takes account of the reduction in effective area seen by the probe when it moves off axis. The beam current density given by Equation (4) can be converted to area current density at a distance d from the thruster by multiplying with $4\pi/D^2$. Solid angle current density is convenient to work with since the thruster is very nearly a point source in relation to the other distances involved. Therefore, the beam current density given by Equation (4) will be a constant along radial lines extending from the thruster as a center.

7.2.2 Time-of-Flight Probe Results

Ten time-of-flight beam scanning experiments were conducted in six different runs. Each experiment consisted of a horizontal scan and a vertical scan through the entire measurable beam, with data points at 1.5 to 3 degree intervals. The experiments are summarized in Table 24.

In run 700405 only, the beam was probed while vectored. Once it was established that a current density profile alone was enough to determine vectoring response, the time-of-flight calculations were dispensed with. Run 700405 yielded three separate scanning experiments. In one, the beam was unvectored. In each of the others, the beam was vectored in two orthogonal directions. Complete results for this run were presented in Section 2.3.

The time-of-flight probe data for run 701002 were not analyzed. The probe scan was taken under normal operating conditions with the beam unvectored. The current densities were computed and integrated over the entire beam, in order to obtain a check on the time-of-flight probe transmission factors. At this time, the actual effective collection area was found to be a little less than 10 cm^2 or about 35 percent of the total frontal area of the probe. This is, in fact, the designed open area of the screen. This normalization factor was again checked during run 710104.

Table 24. Summary of Time-of-Flight Beam Probing Experiments

Run No.	Source Type
700405	A
700904	7
701002	7-3
710104	7BM2
710402	6BM3
710501	6BM

214

Probe results for the remaining experiments are given in Figures 169 through 174. The results show mass flow and thrust densities that are generally symmetrical, but sometimes markedly asymmetrical across the beam direction. They always possess a single maximum near the direction of the net thrust vector, and, with only three exceptions, the entire distribution was contained within a 15-degree half-angle. Asymmetries which were observed could not be related in any way with the orientation of the source.

The distributions of average charge-to-mass ratio, average velocity (specific impulse) and local thrust efficiency were generally uniform with a random scatter, but sometimes markedly asymmetrical or antisymmetrical across the beam direction. The asymmetries that were detected could not be associated in any way with thruster orientation, but were probably caused by propellant wetting nonuniformities.

During the 2000-hour life test, three separate beam scans were made at widely spaced time intervals. Comparison of these three indicated no serious change in character of the exhaust beam throughout the test.

7.2.3 Effect of Finite Beam Spread on Time-of-Flight Measurement Accuracy

The uncorrected time-of-flight equations are normally written for a spherical collecting surface, such as S in Figure 175. In practice, time-of-flight measurements are often made with a flat collecting surface such as C. The time-of-flight distance, denoted by D, is typically about 1.8 meters for a large 4- by 8-foot test station. The collector radius is denoted by r. Tests conducted in TRW facilities have used one 3-foot and one 4-foot diameter collector.

The uncorrected time-of-flight equations used as a standard are written as follows.

$$\langle V \rangle = \frac{D}{2} \frac{\int i_c \, dt}{\int i_c t \, dt} \qquad \text{mean velocity, m/sec} \qquad (5)$$

$$\langle v^2 \rangle = \frac{D^2}{2} \frac{I_s}{\int i_c t \, dt} \qquad \text{mean square velocity, m/sec} \qquad (6)$$

$$\eta = \frac{\langle v \rangle^2}{\langle v^2 \rangle} \qquad \text{source efficiency} \qquad (7)$$

$$F = \frac{2 I_s V_s \eta}{\langle v \rangle} \qquad \text{thrust, newtons} \qquad (8)$$

$$\dot{M} = F / \langle v \rangle \qquad \text{mass flow, kg/sec} \qquad (9)$$

$$I_{sp} = \langle v \rangle / g \qquad \text{specific impulse, sec} \qquad (10)$$

$$g = 9.80 \ \text{m/sec}^2$$

215
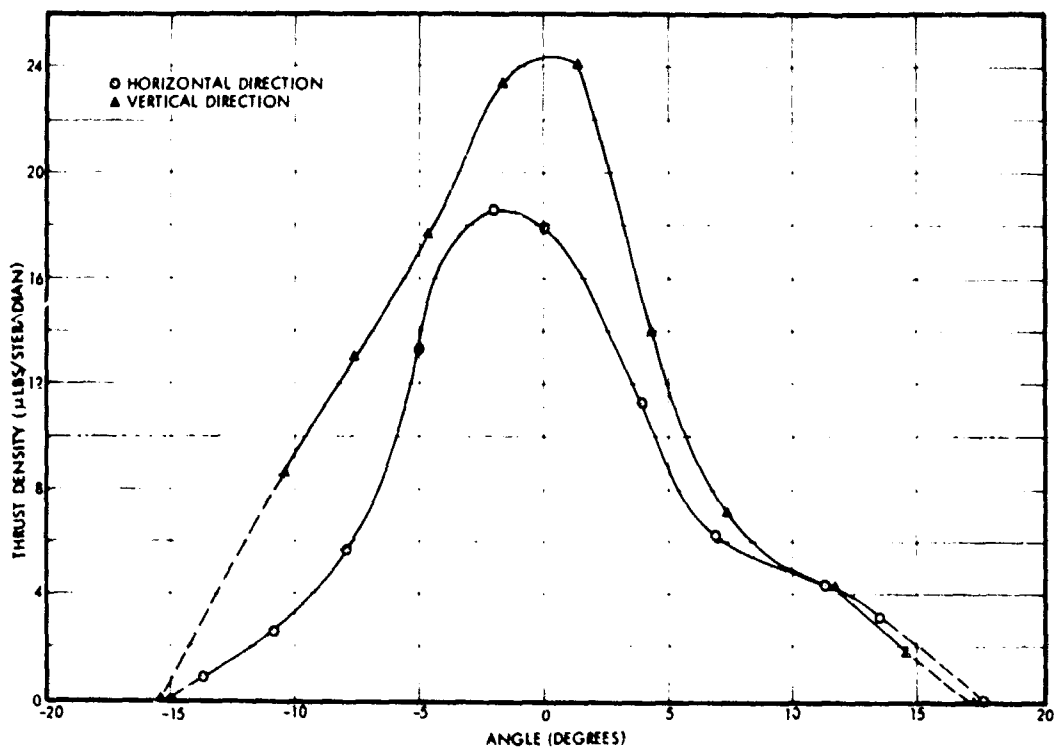
Figure 169a. Horizontal and Vertical Thrust Density Profiles for
Annular Source 7, From Time-of-Flight Probe
Data. Negative angle corresponds to upward
direction. Run 700904
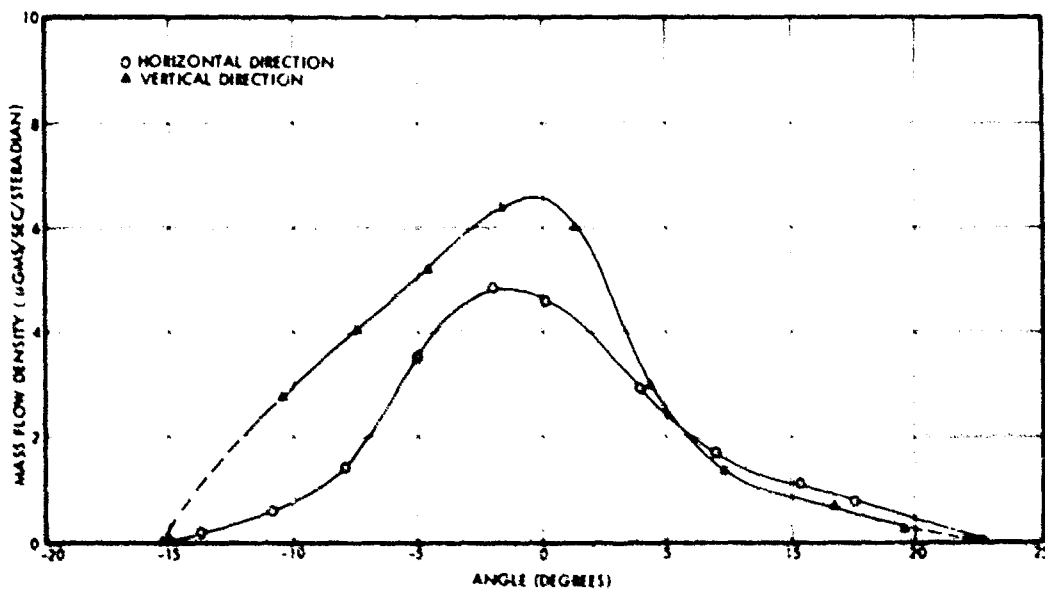
Figure 169b. Horizontal and Vertical Mass Flow Density. Profiles
for Annular Source 7, From Time-of-Flight Probe
Data. Negative angle corresponds to upward
direction. Run 700904.
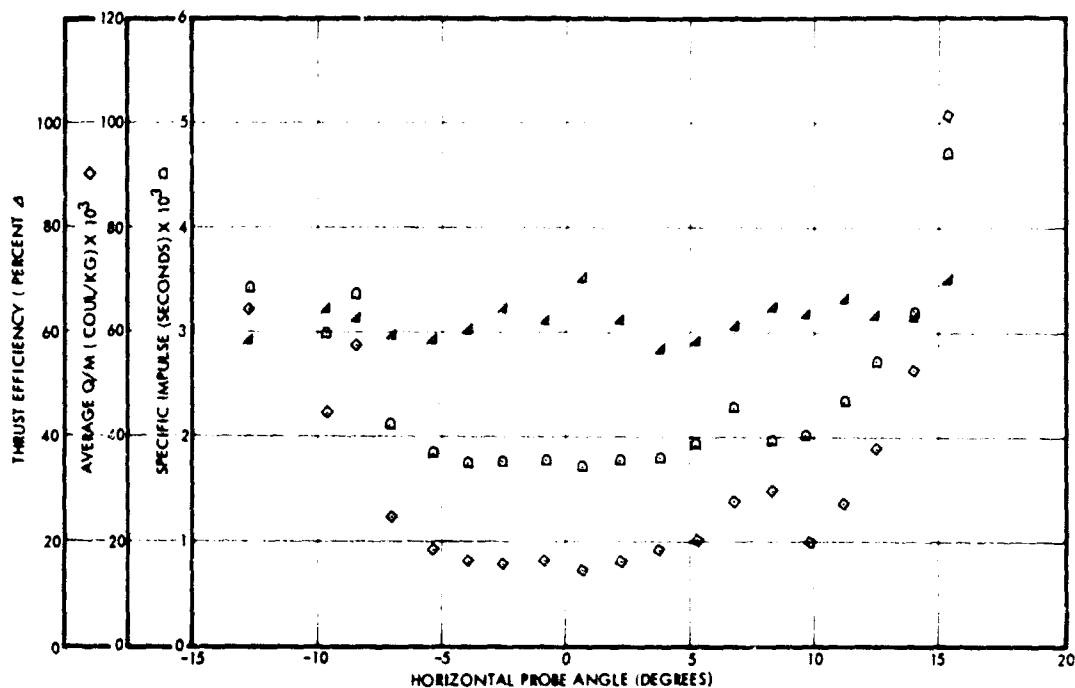
Figure 170a. Run 7101-04, Uncorrected Time-of-Flight Probe Data, in Horizontal Plane, for Unvectored Beam; Thrust Efficiency, Average Charge-to-Mass Ratio and Specific Impulse Versus Angle
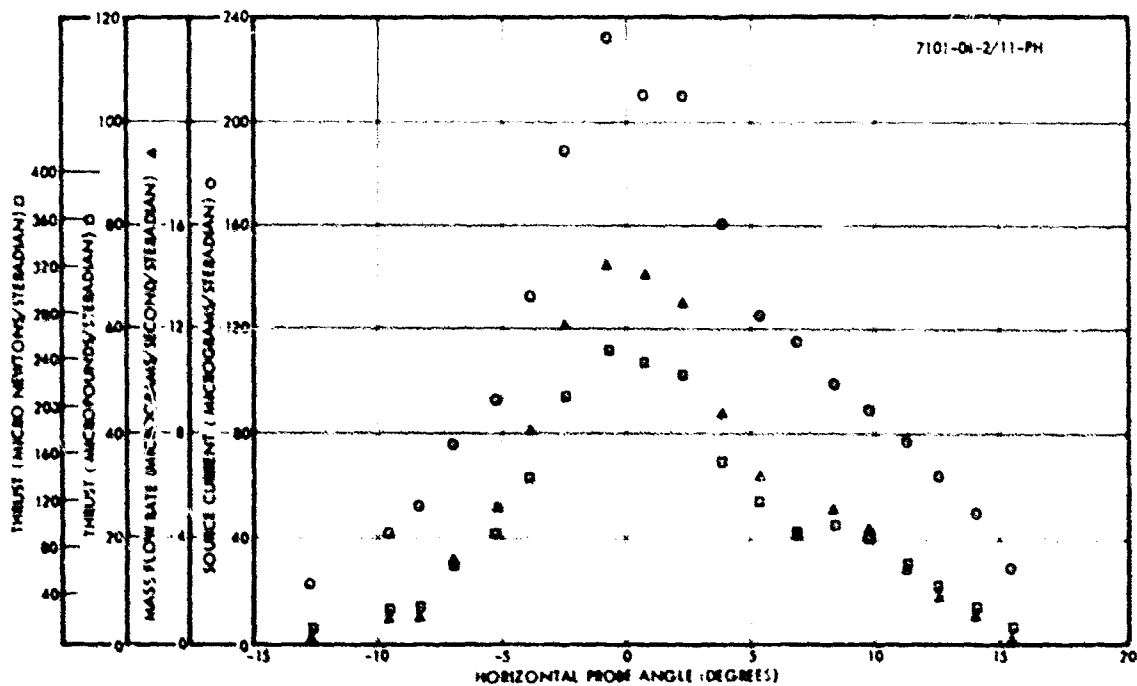
Figure 170b. Run 7101-04, Uncorrected Time-of-Flight Probe Data, in Horizontal Plane, for Unvectored Beam; Thrust, Mass Flow and Current Densities Versus Angle

217
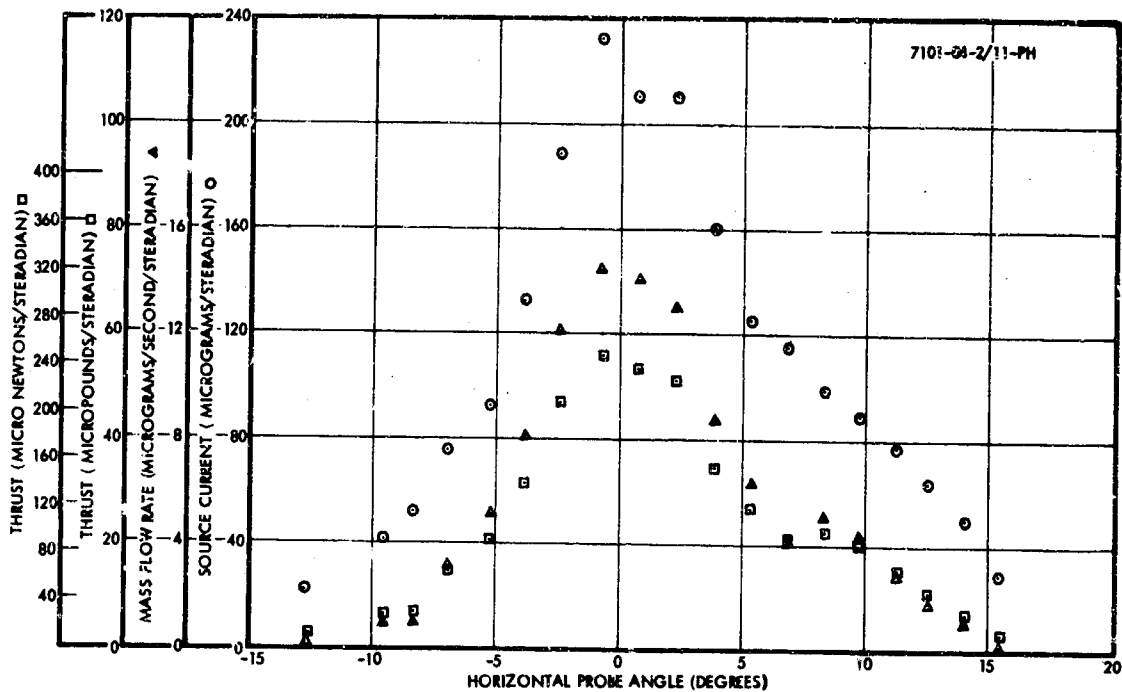
Figure 170c. Run 7101-04, Uncorrected Time-of-Flight Probe Data, in the Vertical Plane, for the Unvectored Beam; Thrust, Mass Flow and Current Densities Versus Angle. Gravity in Direction of Negative Angle
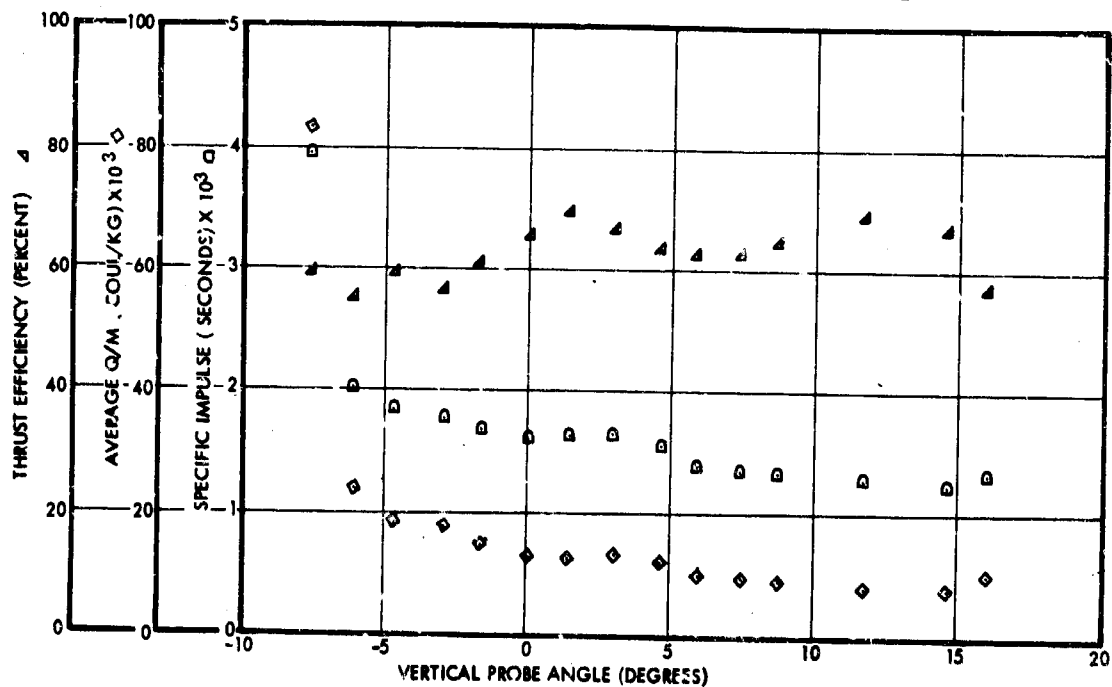
Figure 170d. Run 7101-04, Uncorrected Time-of-Flight Probe Data, in the Vertical Plane, for the Unvectored Beam; Thrust Efficiency, Average Charge to Mass Ratio and Specific Impulse Versus Angle. Gravity in Direction of Negative Angle.
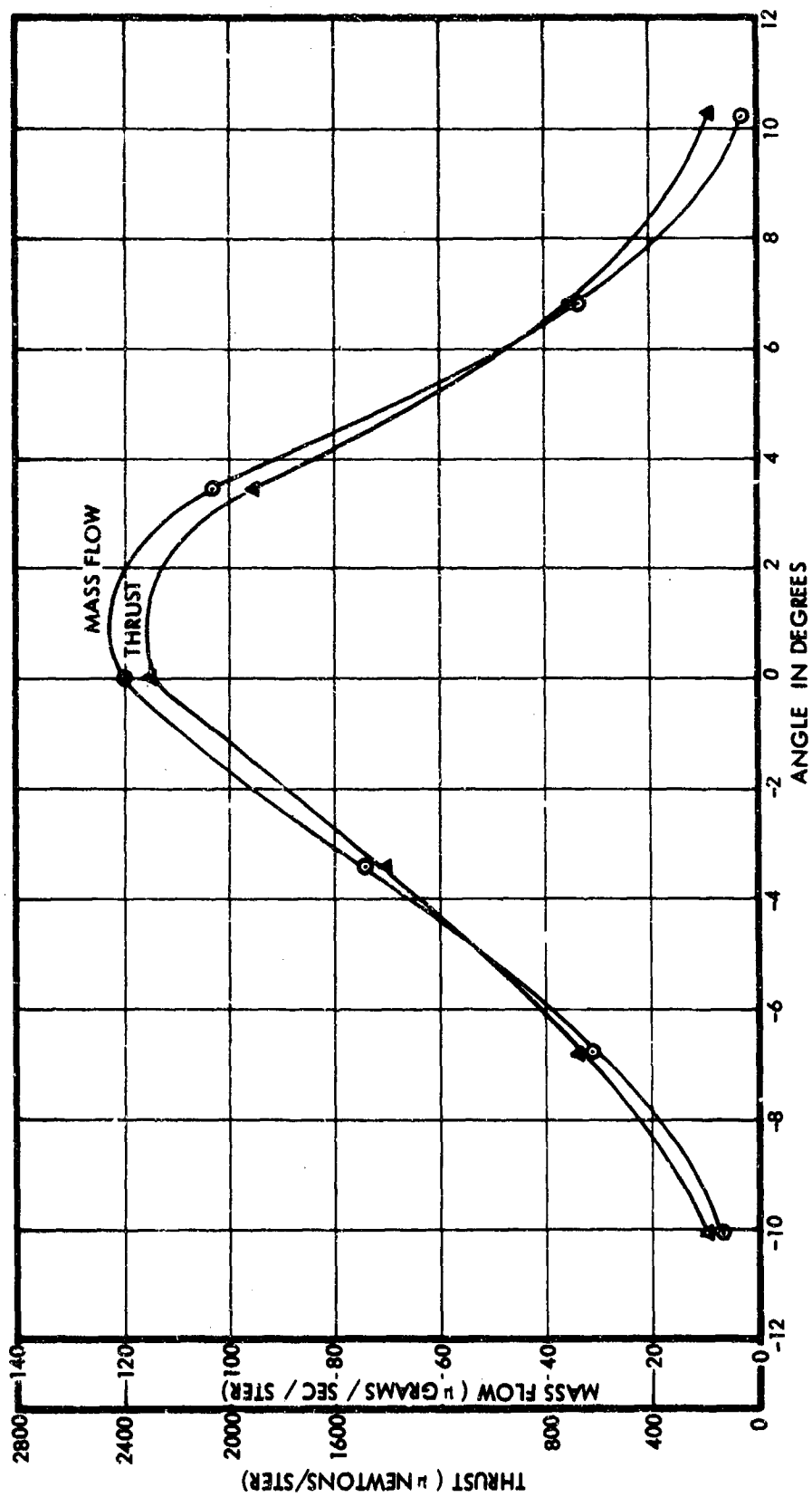
Figure 171a. Run 7104-02; Time-of-Flight Beam Probe, Horizontal
Probe of Thrust and Mass Flow. Uncorrected for
energy loss.

219
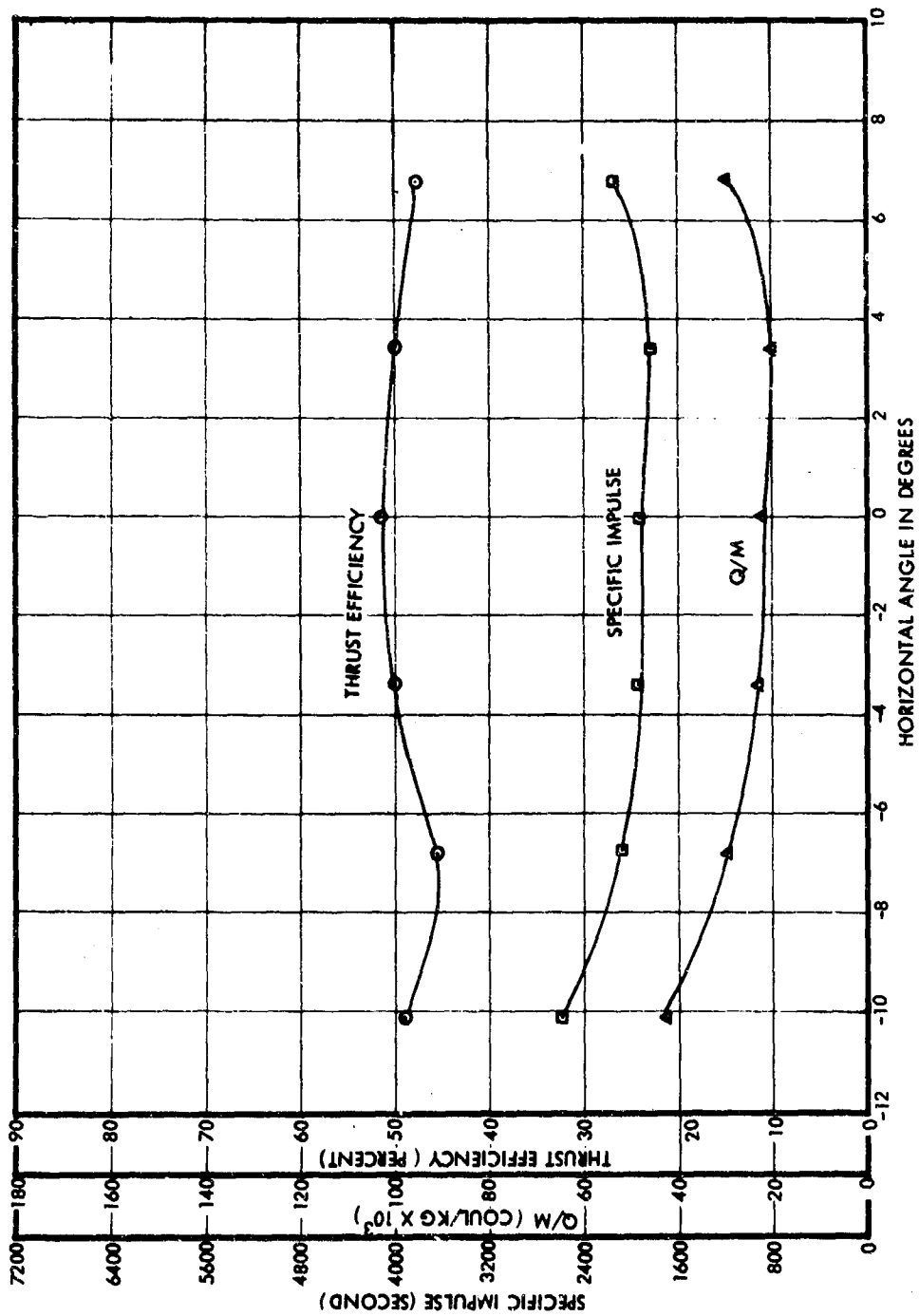
Figure 171b. Run 7104-02; Time-of-Flight Beam Probe, Horizontal Probe of Specific Impulse, Average Cha͟r͟g͟e-to-Mass Ratio and Thrust Efficiency. Uncorrected for en͟e͟r͟gy loss.
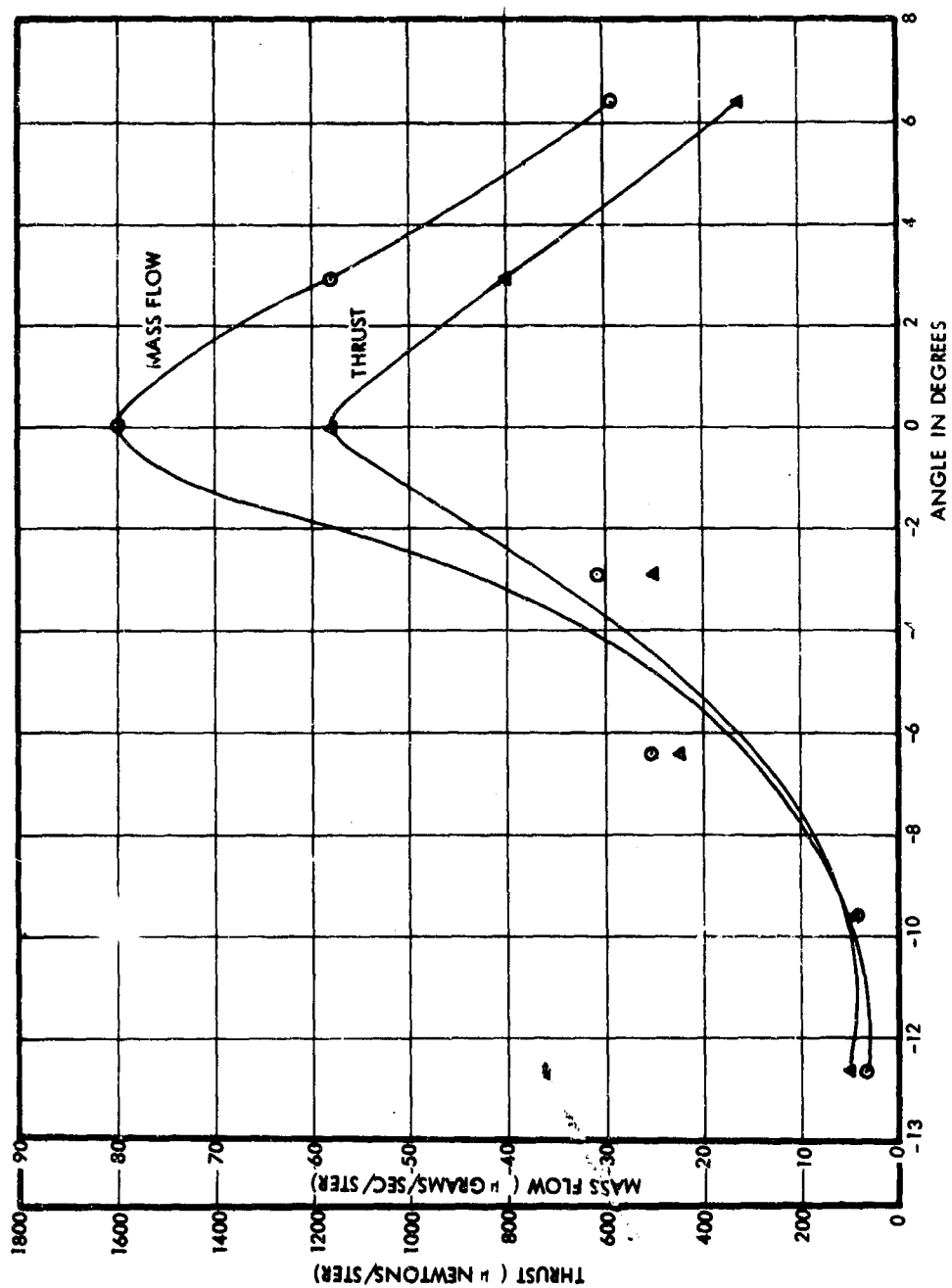
Figure 171c. Run 7104-02; Time-of-Flight Beam Probe, Vertical Probe of Thrust and Mass Flow. Uncorrected for energy loss. Negative angles correspond to downward direction.

221
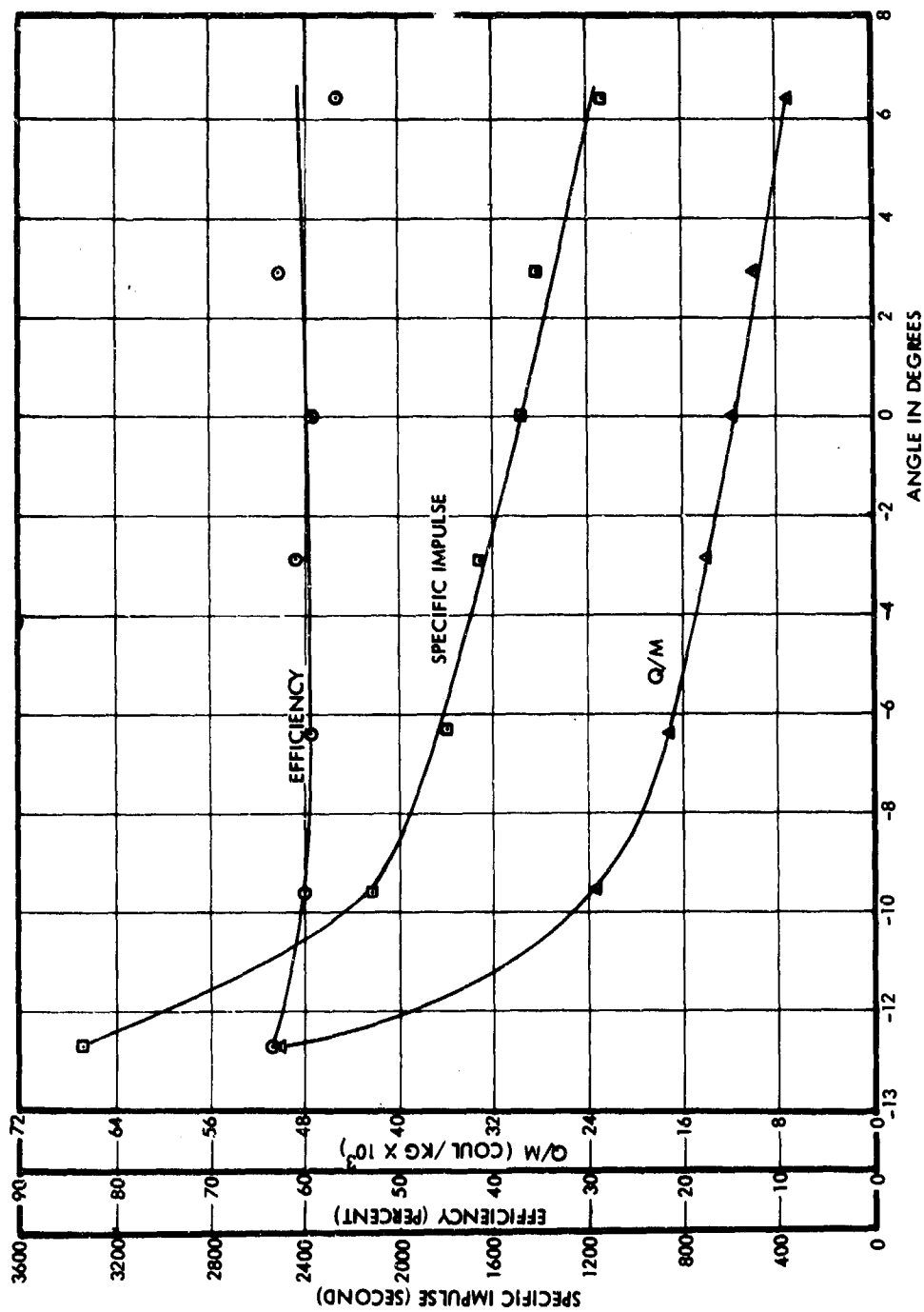
Figure 171d. Run 7104-02; Time-of-Flight Beam Probe; Vertical Probe of Specific Impulse, Average Charge-to-Mass Ratio and Thrust Efficiency. Uncorrected for energy loss. Negative angles correspond to downward direction.

222
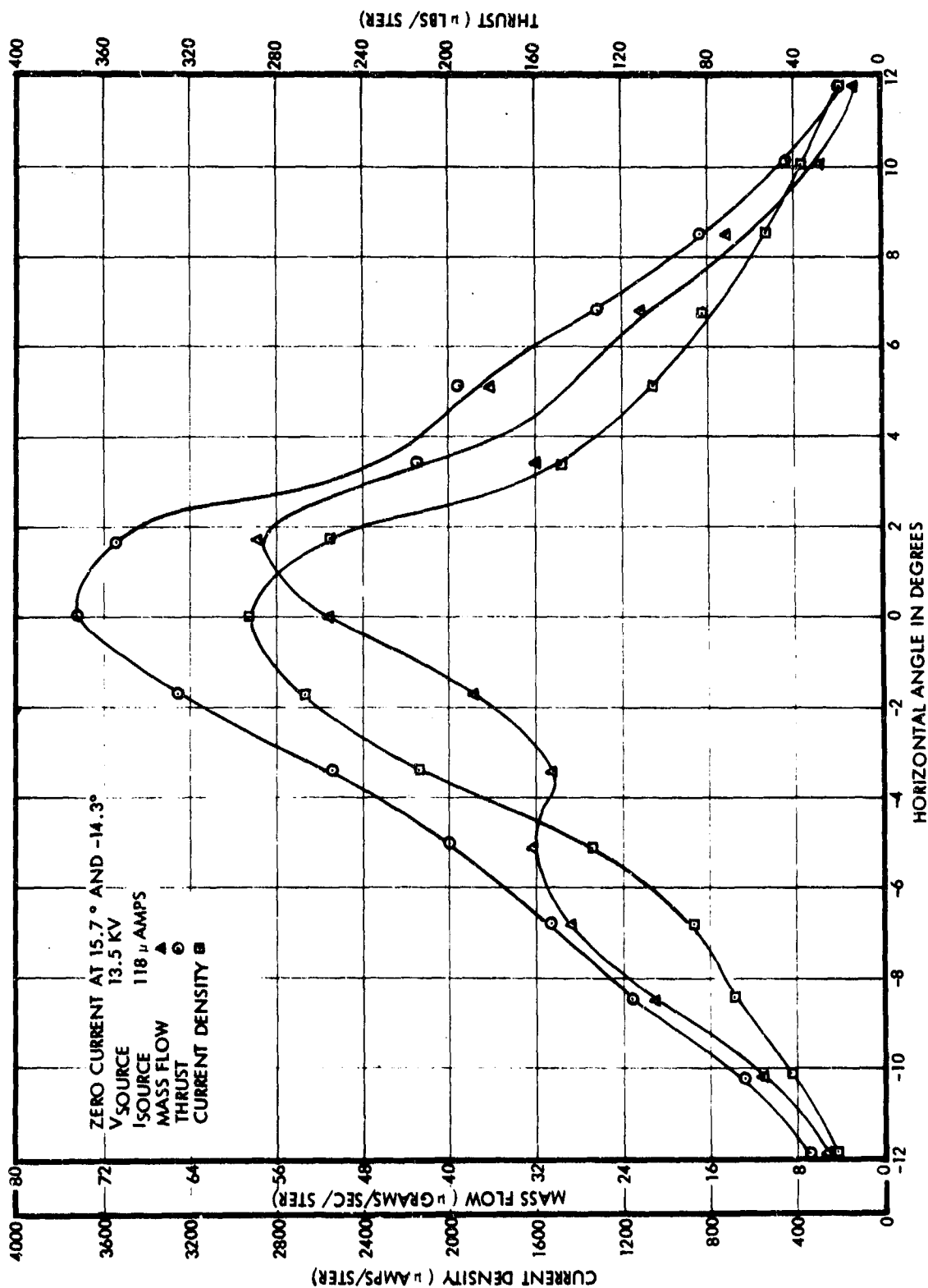
Figure 172a. Run 7105-01; Time-of-Flight Probe Data After 240 Hours — Thrust, Current and Mass Flow Densities for Horizontal Scan

223
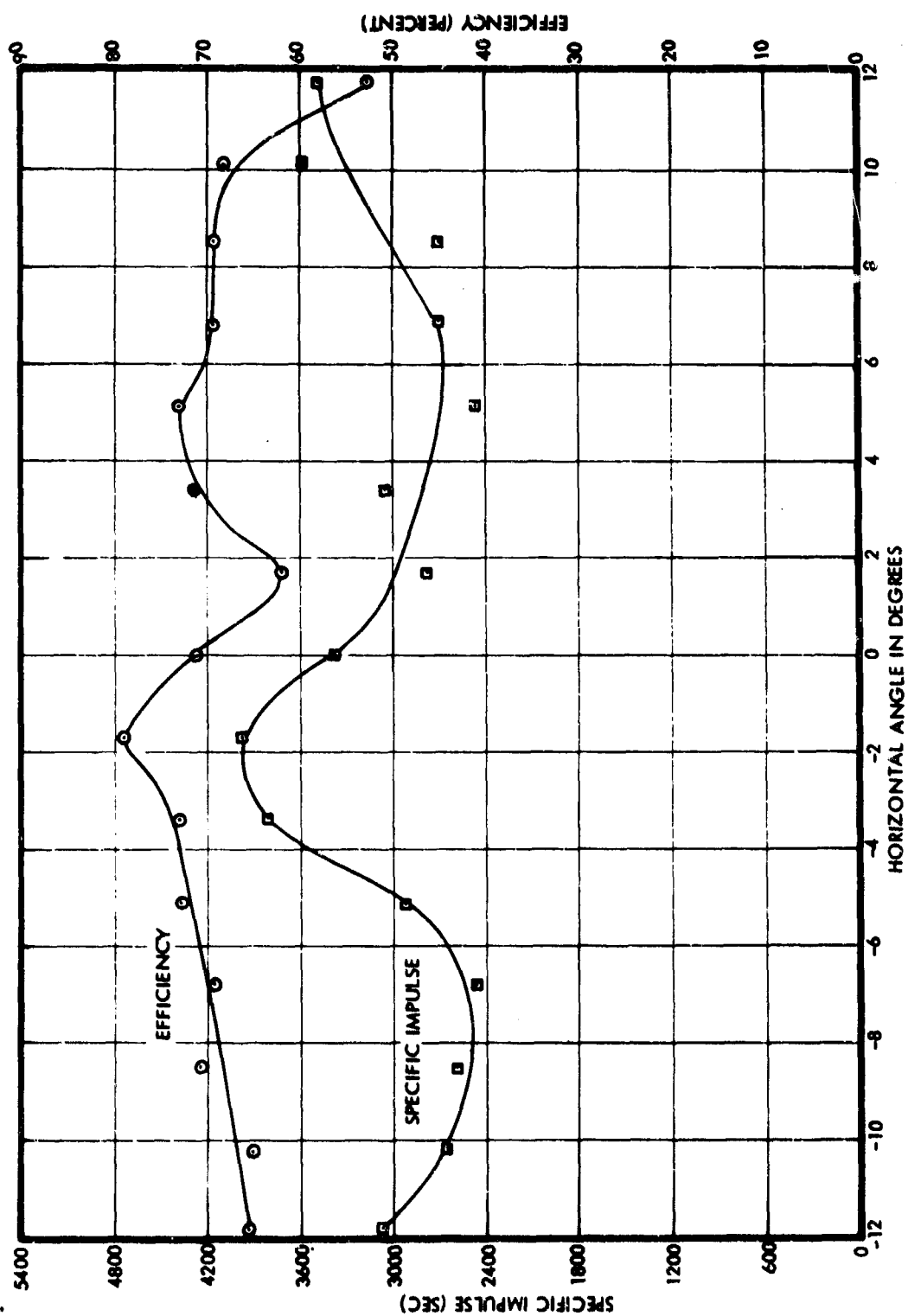
Figure 172b. Run 7105-01; Time-of-Flight Probe Data After 240 Hours—Specific Impulse and Thrust Efficiency for Horizontal Scan

224
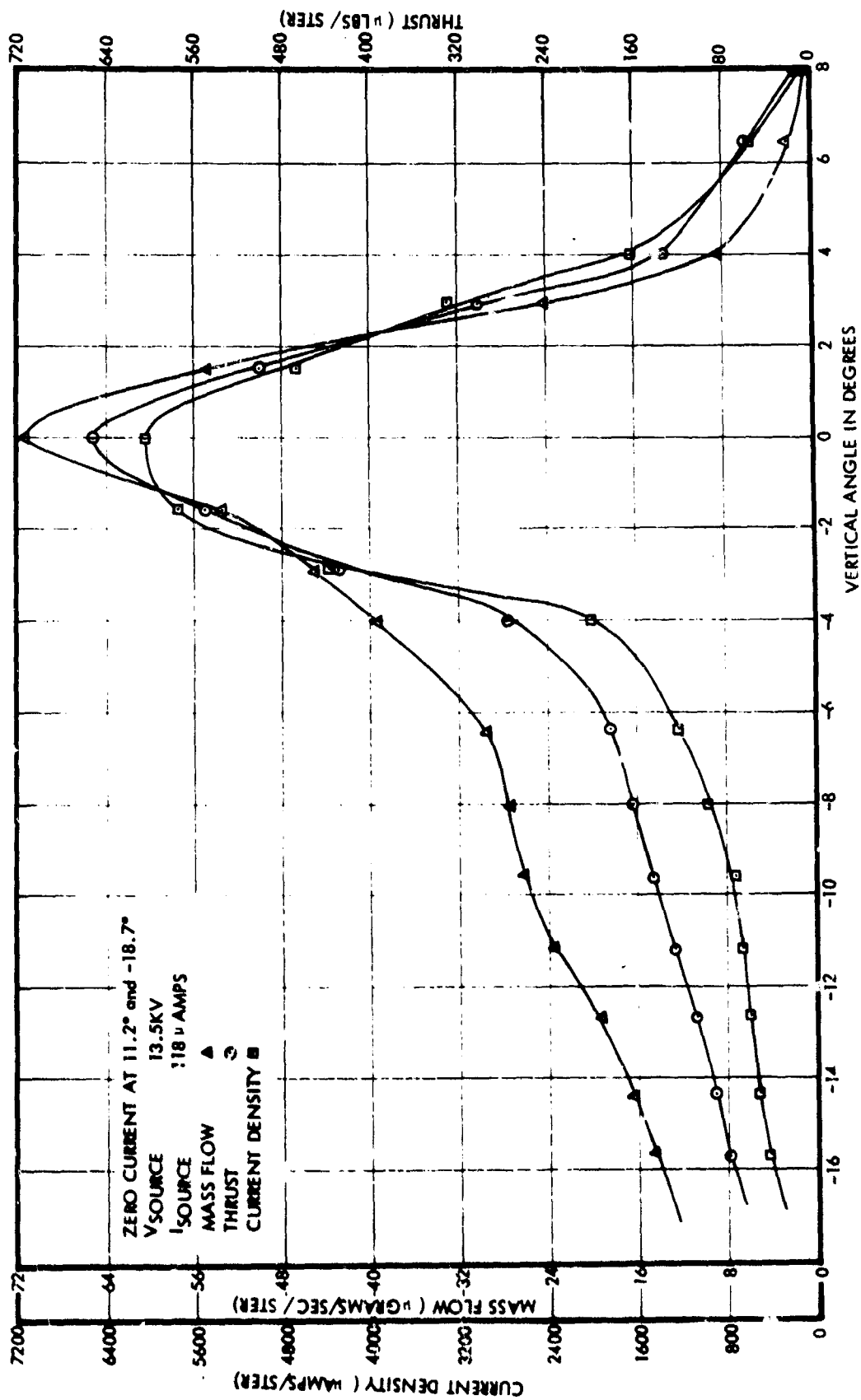
Figure 172c. Run 7:05-01; Time-of-Flight Probe Data After 240 Hours — Thrust, Current and Mass Flow Densities for Vertical Scan
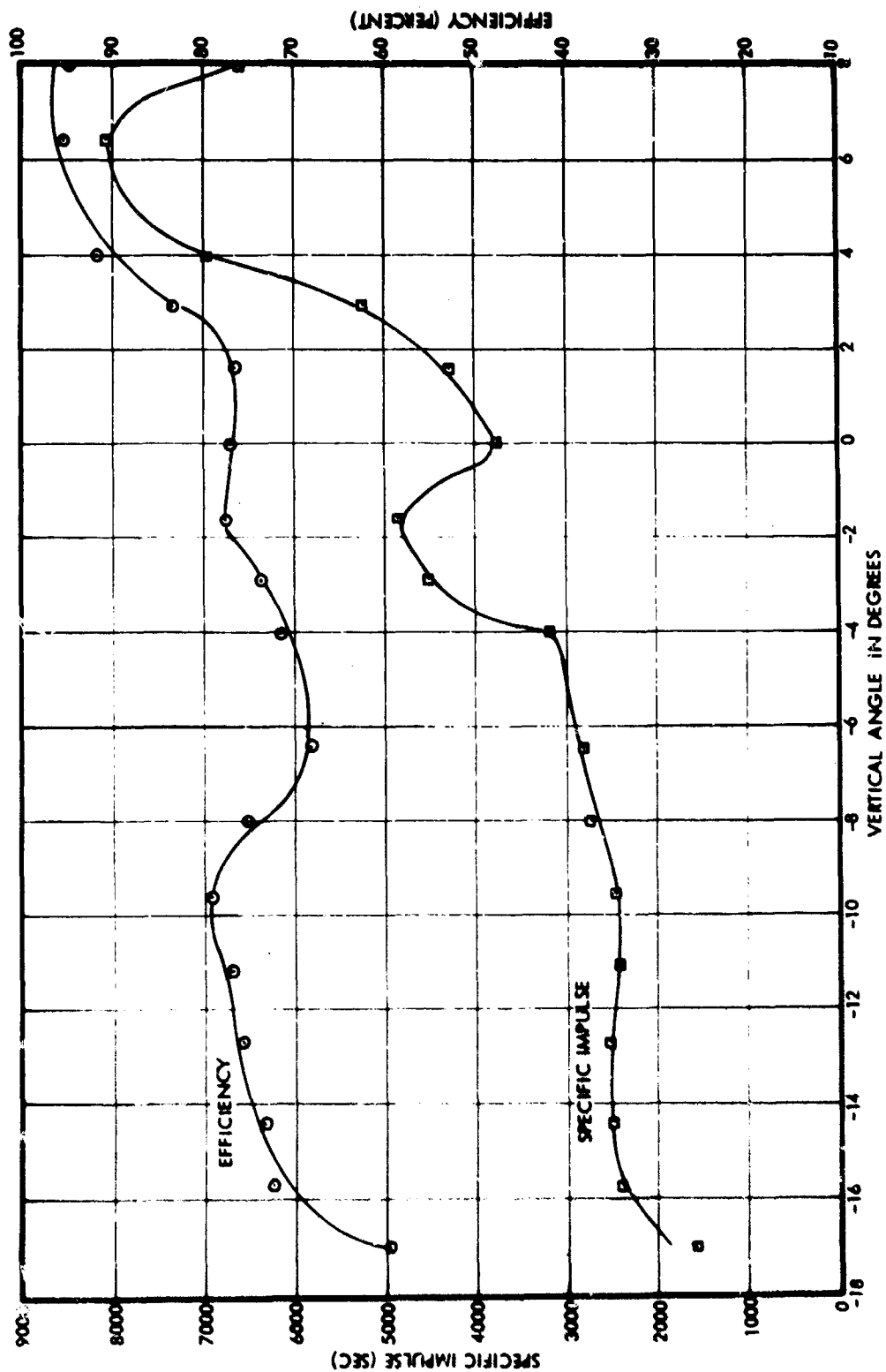
Figure 172d. Run 7105-01; Time-of-Flight Probe Data After 240 Hours—Specific Impulse and Thrust Efficiency for Vertical Scan
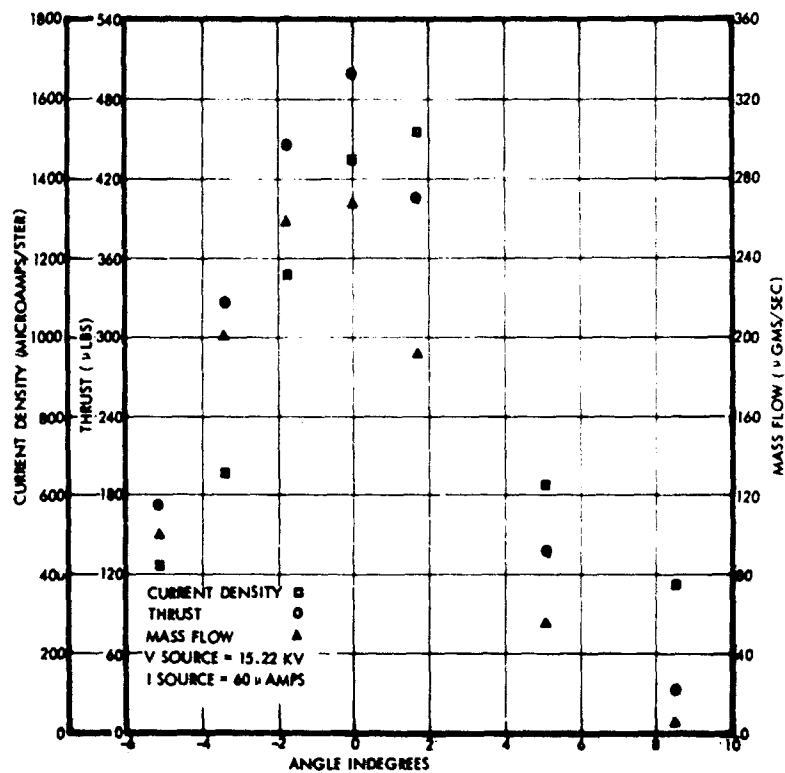
Figure 173a. Run 7105-01; Time-of-Flight Probe Data After 1010 Hours—
Thrust, Current and Mass Flow Densities for Horizontal
Scan
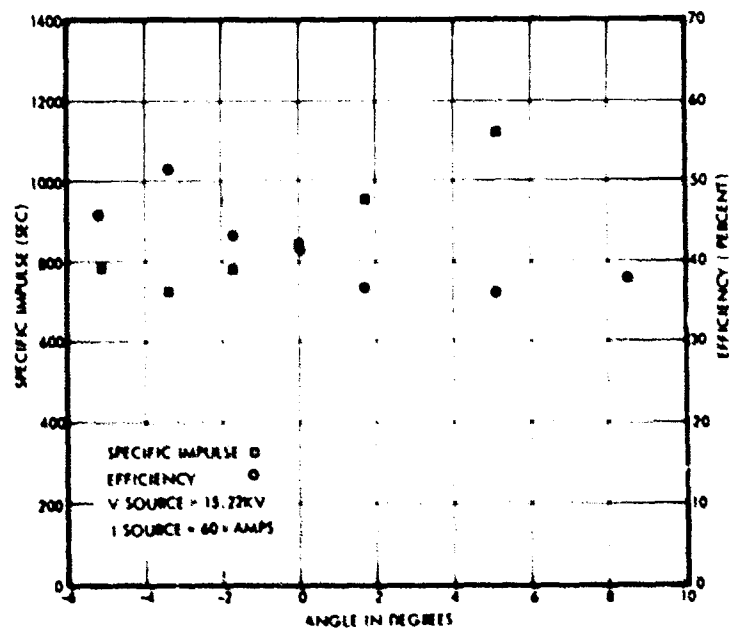
Figure 173b. Run 7105-01; Time-of-Flight Probe Data After
1010 Hours—Specific Impulse and Thrust
Efficiency for Horizontal Scan

227
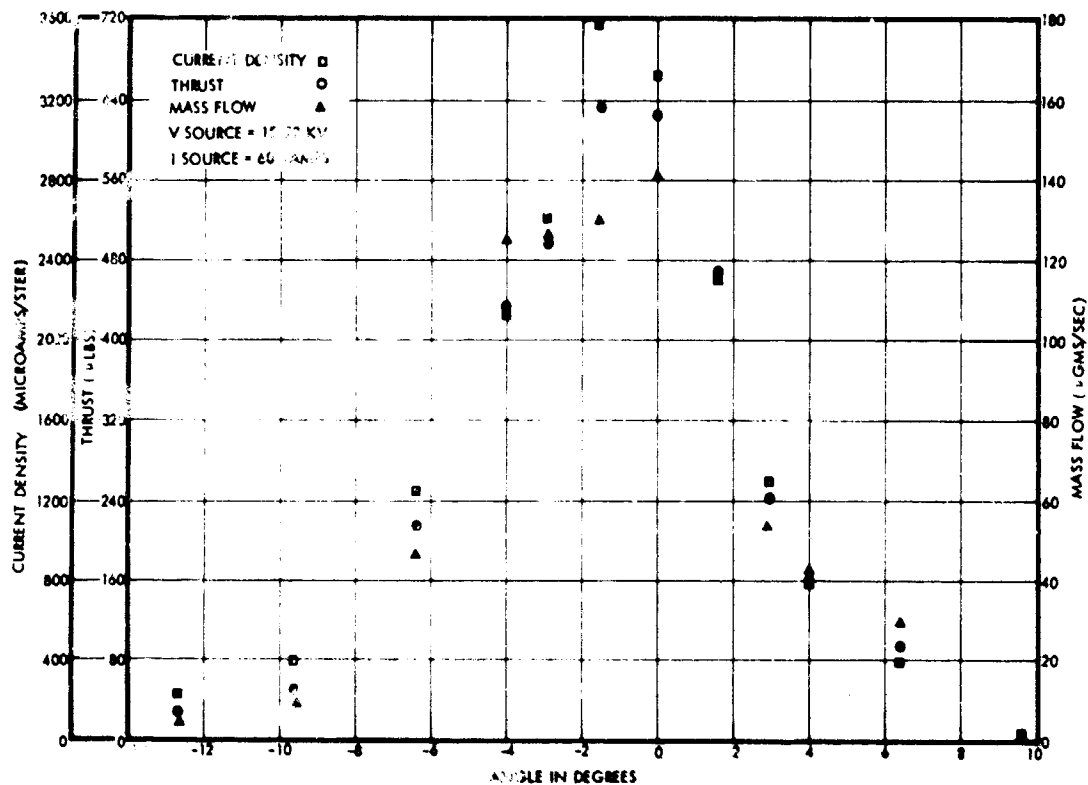
Figure 173c.   Run 7105-01; Time-of-Flight Probe Data After 1010 Hours —
Thrust, Current and Mass Flow Densities for Vertical Scan
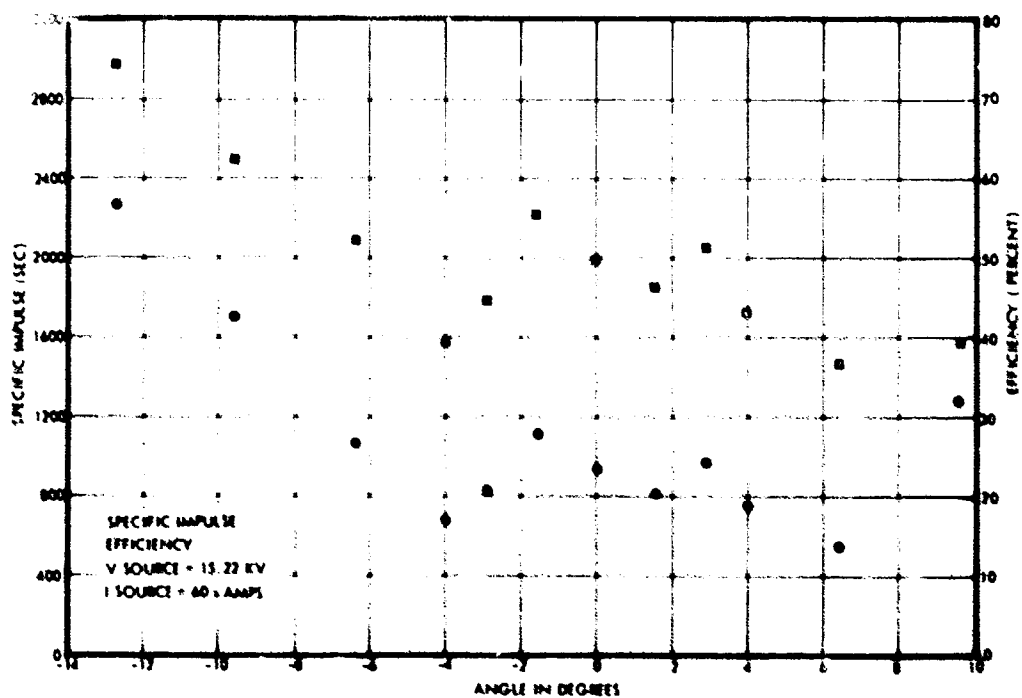
Figure 173d.   Run 7105-01; Time-of-Flight Probe Data After 1010 Hours —
Specific Impulse and Thrust Efficiency for Vertical Scan
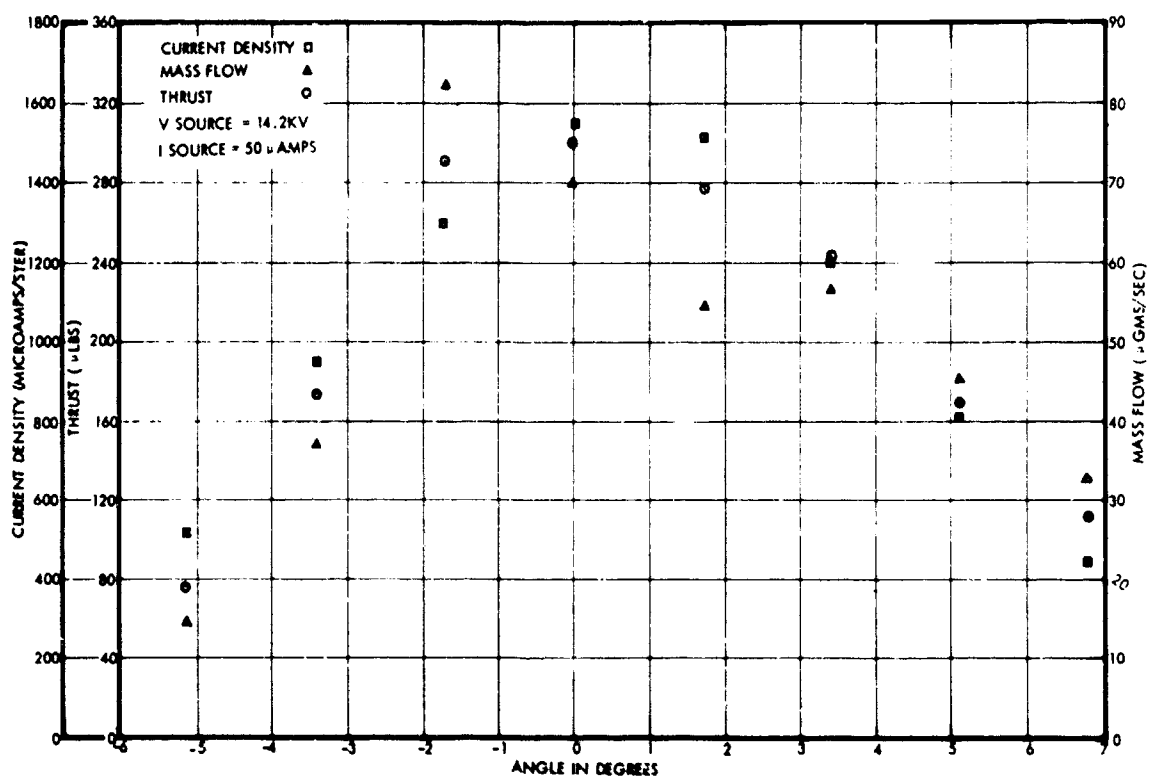
Figure 174a. Run 7105-01; Time-of-Flight Probe Data After 1898 Hours—
Thrust, Current and Mass Flow Densities for Horizontal Scan
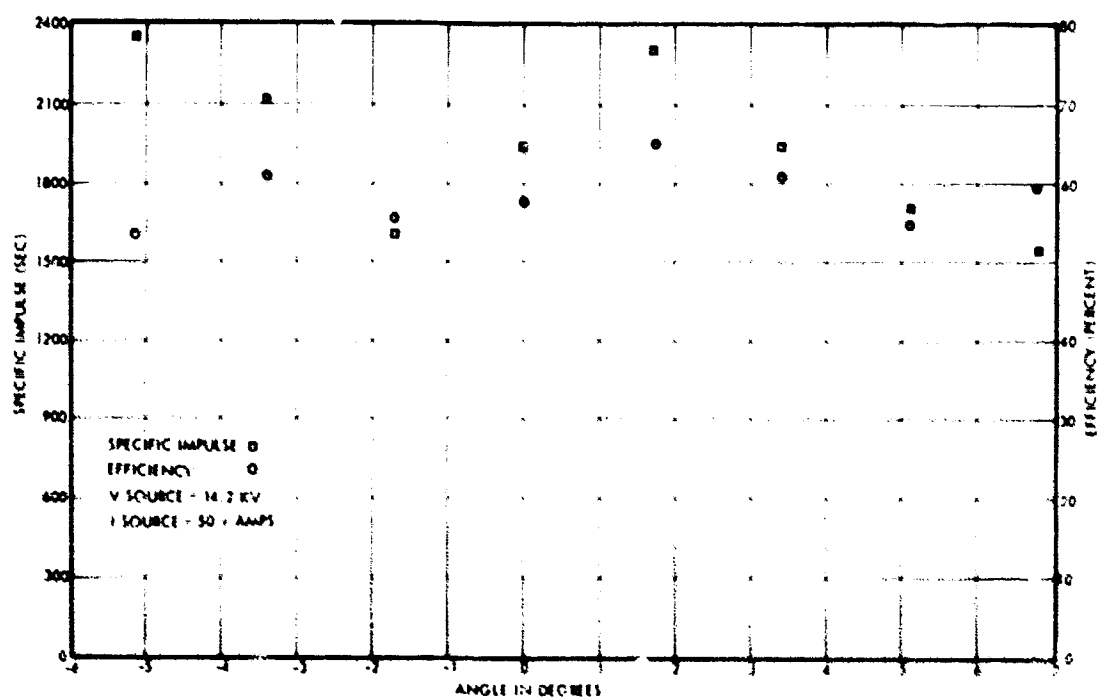
Figure 174b. Run 7105-01; Time-of-Flight Probe Data After 1898 Hours—
Specific Impulse and Thrust Efficiency for Horizontal Scan

229
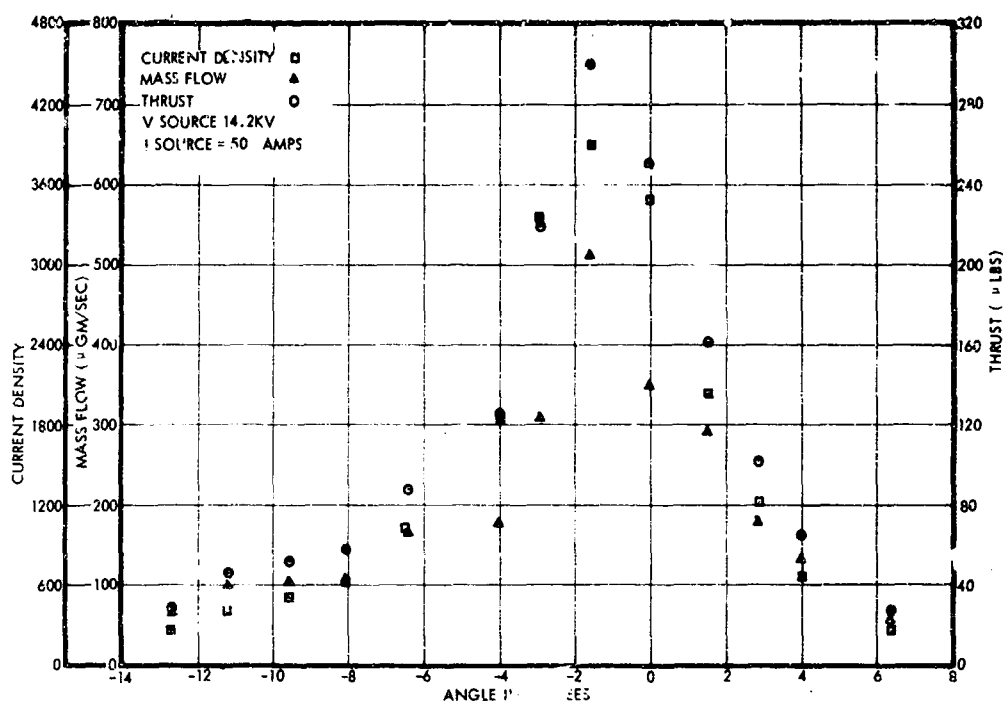
Figure 174c. Run 7105-01; Time-of-Flight Probe Data After 1898 Hours—
Thrust, Current and Mass Flow Densities for Vertical Scan
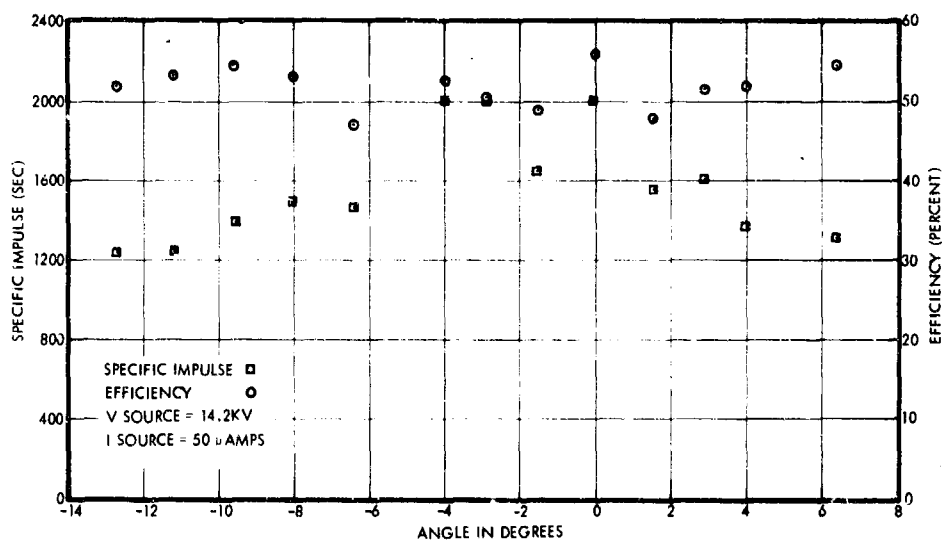
Figure 174d. Run 7105-01; Time-of-Flight Probe Data After
1898 Hours—Specific Impulse and Thrust
Efficiency for Vertical Scan

230
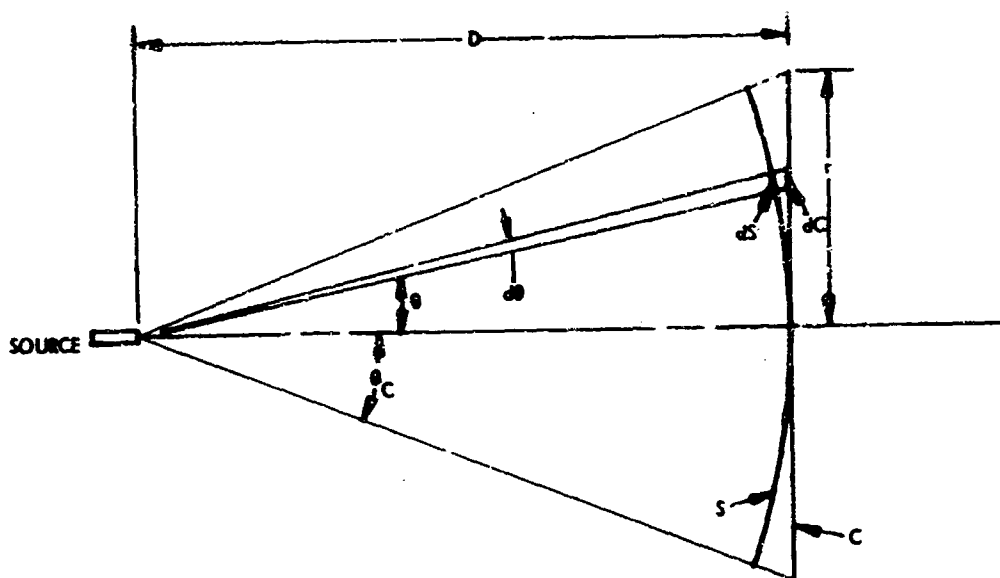
Figure 175. Time-of-Flight Geometry Used in Calculating Corrections for Flat Time-of-Flight Collecting Surfaces

$$I_{sp} = <v>/g \qquad \text{specific impulse, sec} \qquad (10)$$

$$g = 9.80 \text{ m/sec}^2$$

$$<q/m> = I_s/\dot{M} \qquad \text{average charge to mass ratio,} \qquad (11)$$
coul/kg

$$I_s = \text{source current, amperes}$$

$$V_s = \text{source voltage, volts}$$

These equations are valid for a nondivergent beam which strikes the collecting surface at a single point. They involve two basic current integrals, which are seen in Equations (5) and (6) and define the characteristic velocities of the beam. Each integral has, in its integrand, the time-of-flight collector decay current i_C which is initially equal to I_s at time $t = 0$, when the instantaneous grounding (Zap) occurs, and which decays to zero with increasing collector arrival time t.

There are three types of errors which occur in these equations when they are used in a beam of finite spread. For particle trajectories with a nonzero divergence angle θ, only the axially directed velocity component is effective in producing thrust. Also, such trajectories have an actual time-of-flight distance equal to $D/\cos \theta$, as may be seen in Figure 175. Thus, particles arriving on C at larger θ are delayed or retarded in time relative to those arriving at smaller θ. Finally, the effect of beam particles having a divergence angle greater than $\tan^{-1} (r/D)$ will not be measured at all by the time-of-flight collector.

Let $d\dot{M}$ be the element of mass flow in the beam carried by particles with a charge-to-mass ratio between q/m and q/m + d (q/m), and leaving the source along a linear trajectory in an element of solid angle of $d\Omega = \sin \theta \, d\theta \, d\phi$ with polar angles θ, ϕ.

231

The element of current carried by such particles is

$$di = q/m \, d\dot{M} \tag{12}$$

The element of axial thrust contributed by the particles is

$$dF = v \cos \theta \, d\dot{M} \tag{13}$$

where v is the magnitude of their velocity, and is related to the charge to mass ratio by

$$q/m = \frac{1}{2V_s} v^2 \tag{14}$$

An averaging operation is defined over the mass flow rate distribution as

$$<y> = \frac{1}{\dot{M}} \int y \, d\dot{M} \quad ; \quad \dot{M} = \int d\dot{M} \tag{15}$$

the above equations may be integrated to obtain

$$I_s = <q/m> \dot{M} \tag{16}$$

$$F = \dot{M} <v \cos \theta> \tag{17}$$

$$<q/m> = \frac{1}{2V_s} <v^2> \tag{18}$$

in which $<v^2>$ is the mean square velocity magnitude.

The source efficiency is defined as the ratio of the kinetic beam power for an ideal thruster to the actual beam power. This definition does not include power conditioning losses or other thruster system losses not associated with the source itself. It does include (a) power losses due to a finite particle velocity distribution, (b) beam divergence losses, (c) energy loss due to the electrostatic spraying process, and (d) efficiency losses due to propellant evaporation at the source meniscus. Electrostatic spraying energy loss mechanisms include viscous resistance to fluid motion and ohmic resistance to charge transport at the droplet emission sites. This energy loss has been measured by Huberman,[1] and results in a reduction

---

[1] Huberman, M. N., "Measurement of the Energy Dissipated in the Electrostatic Spraying Process," J. A. P. 41, 578 (1970).

of effective source voltage of 400 ±200 volts, independent of source voltage. Evaporation losses have been estimated by means of direct mass flow measurements (see Section 7.3). These measurements show an apparent discrepancy of 5 percent in mass flow, but were accurate to only ±10 percent.

In the mathematical development which follows, we will concern ourselves only with velocity distribution and beam divergence effects on source efficiency. Then we may write as follows:

$$\eta = \frac{F^2}{2\dot{M} I_s V_s} \tag{19}$$

Integrating over the actual kinetic beam power, gives

$$I_s V_e = \frac{1}{2}\dot{M} <v^2>$$

in which $<v^2>$ is defined as before. It follows that

$$\eta = \frac{<v\cos\theta>^2}{<v^2>} \tag{20}$$

Eliminating mass flow from the equation for thrust, gives

$$F = \frac{2 I_s V_s \eta}{<v\cos\theta>} \tag{21}$$

Finally, specific impulse is found from

$$I_{sp} = \frac{F}{\dot{M}g} = \frac{<v\cos\theta>}{g} \tag{22}$$

All performance parameters are now expressed in terms of two velocity integrals over the $\dot{M}$ distribution, similar to Equations (5) and (6). All corrections for beam divergence are accounted for by one difference, that $<v>$ is replaced by $<v\cos\theta>$.

To account for the flatness of the collecting surface, we must now allow the current distribution to be a function not just of q/m, but also of the polar angles θ and ϕ. Defining

$$di = dj(\theta, \phi) d\Omega \tag{23}$$

233

so that dj is an incremental current density, in amperes per steradian, being carried through the stream tube $d\Omega$ at θ, ϕ by particles having a charge-to-mass ratio of q/m. These particles have a velocity v satisfying Equation (14). They reach the collecting surface C in Figure 175 after a time t satisfying.

$$v = \frac{D}{t \cos \theta} \tag{24}$$

Using Equations (12), (14), (23) and (24), the averaging operation defined by (15) may be rewritten as an integral over current distribution, involving collector arrival time.

$$\langle y \rangle = \frac{2v_s}{\dot{M} D^2} \int y\, t^2 \cos^2\theta\, dj\, d\Omega$$

$$\dot{M} = \frac{2v_s}{D^2} \int t^2 \cos^2\theta\, dj\, d\Omega \tag{25}$$

For both velocity integrals, y is dependent on t and $\cos\theta$. In each case an integration by parts may be accomplished, to interchange t and j as the variables of integration. As an illustration, the integration of $\dot{M}$ is as follows.

$$\frac{D^2}{2v_s} \dot{M} = \int_{\Omega_B} \left\{ t^2 j \Big|_{j=0}^{t=0} - \int^{t=0} 2jt\, dt \right\} \cos^2\theta\, d\Omega$$

$$= 2 \int_{\Omega_B} \int_{t=0}^{\infty} j(\theta, \phi, t)\, t \cos^2\theta\, dt\, d\Omega$$

in which j is now a function of collector arrival time, and Ω_B is a sector of solid angle within which the entire beam is contained.

234

Integration is done over all solid angle containing nonzero current density, and over all time of the current decay. Following this method, we obtain

$$<v \cos \theta> = \frac{D \int j \cos^2\theta \, dt \, d\Omega}{2 \int jt \cos^2\theta \, dt \, d\Omega} \qquad (26)$$

$$<v^2> = \frac{D^2 I_s}{2 \int jt \cos^2\theta \, dt \, d\Omega} \qquad (27)$$

Equations (16), (17), (20), (21), (22), (26) and (27) now constitute the complete and correct set of equations for time-of-flight analysis. Equations (26) and (27) are not yet usable for single collector time-of-flight analysis, however, since they require a knowledge of the entire beam current density distribution, and this is not always available. In addition, an integration is made over the entire beam width, and if the entire beam is not collected a further error will occur.

Both of these expressions contain integrals of the form

$$W_n = \int_{\Omega_B} d\Omega \int_0^\infty dt \, j(\theta, \phi, t) \, t^n \cos^2\theta : n = 0, 1$$

where t^n is a function only of collector arrival time. This integral may be rewritten as follows:

$$W_n = \int_{\Omega_C} d\Omega \int_0^\infty dt \, (jt^n) + \int_{\Omega_{B-C}} d\Omega \int_0^\infty dt \, (jt^n) - \int_{\Omega_B} d\Omega \int_0^\infty dt \, (jt^n \sin^2\theta) \qquad (28)$$

Here, Ω_C is the solid angle sector subtended by the collecting surface C, and $\Omega_{B-C} = \Omega_B - \Omega_C$. The first term in this expression can be integrated over Ω_C only to obtain the usual time-of-flight approximation:

$$\int_{\Omega_C} d\Omega \, j(\theta, \phi, t) = i_C(t) \qquad (29)$$

235

in which $i_C(t)$ is the total collector current as a function of collector arrival time. A similar integration can be performed over Ω_{B-C} in the second term, to obtain an integrand which is a function of total currents rather than current density. If $i_B(t)$ is the total current passing through the infinite plane containing the collector at time t after the zap, then Equation (28) becomes:

$$W_n = \int_0^\infty dt\, i_C t^n + \int dt\, (i_B - i_C) t^n - \int_{\Omega_B} d\Omega \int dt\, j\, t^n \sin^2 \theta \qquad (30)$$

These integrals, for n - 0 and n = 1, contain all the corrections required for a flat collector of finite size collecting some portion of a divergent beam.

The first term in Equation (30) is the usual, uncorrected, time-of-flight approximation. The other two integral terms are correction terms.

The first term is an integral of total collector current, $i_C(t)$, multiplied by a function of collector arrival time and integrated over that time. The total current may consist of moving charged particles with some nonuniform distribution of local charge-to-mass ratio and thrust efficiency[*] which depends on the local angles θ and ϕ. Effects of such nonuniform distributions are partially accounted for in the integration over current density which was performed in Equation (29). The total collector current, $i_C(t)$ is a directly measurable quantity and contains information pertinent to the angular distribution of charge-to-mass ratio and thrust efficiency. These will be factors determining the total t dependence of $i_C(t)$.

The second integral term in Equation (30) is an integral over all currents not striking the collector. The variation with angle of the time dependence of these currents would in any case, not be measurable with a single collector. Because of variations in angular distribution of charge-to-mass ratio and thrust efficiency, the time dependence of $i_B(t)$ will generally be different from that of $i_C(t)$. This effect must be taken into account when considering corrections to the time-of-flight integrals caused by uncollected current ($i_B(t) - i_C(t)$).

The third integral term in Equation (3) depends in part on the fact that the collector is flat. If the beam were perfectly collimated, then, of course, this term would vanish for both n = 0 and n = 1, regardless of whether the collecting surface were flat or spherical. If the beam has a finite divergence and a spherical collector is used, then the correction for n = C becomes $2 \sin^2(1/2) \theta$ instead of $\sin^2 \theta$. For n = 1 the correction vanishes. Because of the presence of the $\sin^2 \theta$ in the integrand, a direct integration to obtain total current cannot be made. However, an average angle, θ_n, can be defined by the formula

---

[*] The term thrust efficiency is used to discern the local beam efficiency at angles θ, ϕ from the overall source efficiency.

236

$$\int_{\Omega_B} d\Omega \int_0^\infty dt \, jt^n \sin^2 \theta = \sin^2 \theta_n \int_0^\infty dt \, i_B t^n \tag{31}$$

Again, as in the other two terms, the time dependence of $j(\theta, \phi, t)$ will be influenced by nonuniform angular distributions of charge-to-mass ratio and thrust efficiency. These must be taken into account in some way. They may influence the weighting of $\sin^2 \theta$ in such a way as to affect the value of θ_n.

A convenient assumption regarding the current density function is that it displays a uniform angular charge-to-mass ratio and thrust efficiency distribution. This model has the advantage of being analytically tractable, and of allowing investigation of the effects of small deviations from uniformity of thrust efficiency and charge-to-mass ratio.

Let the current density be described by

$$j(\theta, \phi, t) = I_s \, f(\theta, \phi) \, g(t) + \delta j(\theta, \phi, t) \tag{32}$$

such that

$$\int_{\Omega_B} d\Omega \, f(\theta, \phi) = 1$$

$$g(0) = 1; \, g(\infty) = 0$$

$$\delta j(\theta, \phi, 0) = \delta j(\theta, \phi, \infty) = 0$$

and δj is a small variation in the current caused by nonuniform charge-to-mass ratio and thrust efficiency distributions. By the above model, the steady-state current density is given by

$$j(\theta, \phi, 0) = I_s \, f(\theta, \phi)$$

Now consider the following definitions of local thrust efficiency $e(\theta, \phi)$ and charge-to-mass ratio $X(\theta, \phi)$.

$$e(\theta, \phi) = \frac{\cos^2 \theta}{2} \frac{(\int j \, dt)^2}{j(\theta, \phi, 0) \int jt \, dt} \tag{33}$$

237

$$X(\theta, \phi) = \frac{D^2}{4V_s} \frac{j(\theta, \phi, 0)}{\cos^2 \theta \int jt\, dt} \tag{34}$$

Suppose now that a small variation δj will cause variations δe and δx in $e(\theta, \phi)$ and $x(\theta, \phi)$, respectively. Assume these variations are small enough to be linearized. This is essentially a differentiation process on Equations (33) and (34). The result is as follows:

$$\frac{\delta e}{e_o} \cong 2\frac{\int \delta j\, dt}{\int j_o\, dt} - \frac{\int j \delta t\, dt}{\int j_o t\, dt}$$

$$\frac{\delta x}{x_o} \cong -\frac{\int \delta j\, t\, dt}{\int j_o t\, dt}$$

When these are solved for the integrals over current variations, we get

$$\int \delta j\, t^n\, dt \cong 1/2 \left[(1-n)\frac{\delta e}{e_o} - (1+n)\frac{\delta x}{x_o} \right] \int j_o t^n\, dt \tag{35}$$

$$\cong A_n(\theta, \phi) \int j_o t^n\, dt: \quad n = 0, 1$$

In evaluationg (35), the value of j_o to be used in the integrals on the right-hand side is the functional value about which the variation is taken. Referring to Equation (32), the functional to be used in this analysis is

$$j_o(\theta, \phi, t) = I_s f(\theta, \phi) g(t)$$

The fractional deviations $\delta e/e_o$ and $\delta x/x_o$ must be determined from time-of-flight probe data from the beam. The values of e_o and x_o must be calculated from the nominal current, j_o, which may be chosen from some particular direction in the beam. For example

$$j(\theta, \phi, t) = j_o(\theta, \phi, t)$$

$$j(\theta, \phi, t) = 0$$

238

If we now integrate Equation (35) over solid angle, so that

$$\int d\,\Omega \int_\delta j\ t^n\ dt\ =\ \int_\delta i\ t^n dt$$

and the approximate subscript may be chosen depending on whether the integration is done over Ω_B or Ω_C, we get

$$\int dt\ \delta i\ t^n\ dt\ =\ I_s \int fA_n\ d\Omega \int g\ t^n\ dt \tag{36}$$

Retu.. ing to Equation (30), we are ready to make some simplifications. Since the first term in (30) is normally and easily computed, we can make this a factor.

$$W_n\ =\ \int_0^\infty dt\ i_C t^n (1 + \Delta_n) \tag{37}$$

Now Δ_n is ᴧ correction term given as follows:

$$\Delta_n\ =\ \frac{\int dt\ (i_B - i_C) t^n - \int dt\ i_B t^n\ \sin^2 \theta_n}{\int dt\ i_C t^n} \tag{38}$$

To obtain this Equations (30) and (31) were used. The value of θ_n is still defined by Equation (31).

With the aid of Equations (32), (35) and (36), we may rework Equation (38) to obtain:

$$\Delta_n\ =\ \frac{\int_{\Omega_{B-C}} d\Omega\ f(1+A_n)}{\int_{\Omega_C} d\Omega f(1+A_n)}\ \cos^2 \theta_n\ -\ \sin^2 \theta_n \tag{39}$$

239

in which

$$\sin^2 \theta_n = \frac{\int_{\Omega_B} d\Omega \sin^2 \theta \, f(1+A_n)}{\int_{\Omega_B} d\Omega f(1+A_n)} \tag{40}$$

and

$$A_n = 1/2 \left[(1-n)\frac{\delta e}{e_o} - (1+n)\frac{\delta x}{x_o} \right] : n = 0, 1 \tag{41}$$

In order to obtain some idea of how the error terms Δ_n depend on the total beam angle θ_B and the local deviations δe of thrust efficiency and δx of charge-to-mass ratio, a simplified mathematical model was set up and analyzed. The first element of this model is to write

$$A_n = a \sin^2 \theta \tag{42}$$

in which a is the independent variable, and corresponds to the maximum percentage deviation in x if n = 1, or an equal combination of the percentage deviations in x and e if n = 0. Since the model is the same for both n = 0 and n = 1, the subscript n is dropped from the model and from its results. This model gives an axially symmetric deviation, increasing monotonically with θ. If the model were to give an antisymmetric deviation across some plane, there would be, for example, a factor of $\sin\phi$ in Equation (42). Integration of this factor would result in the disappearance of the terms in A_n - a result equivalent to setting a = 0.

The second element of the model is the convenient form of the distribution function, f (unnormalized):

$$f = \cos \theta (\cos^2 \theta - \cos^2 \theta_B) \tag{43}$$

This model of f is symmetric about the thrust axis, $\theta = 0$, and meets the requirement of dropping to zero at the beam angle θ_B. For $\theta > \theta_B$, f is taken to be zero, and no integration is performed. This distribution has a single maximum in the direction of θ equal to zero.

With these simplified models, Equations (39) and (40) are readily integrated. Figure 176 shows the results of this integration, displaying the fractional correction term Δ as a function of beam diverge angle θ_B and the deviation term a. A collector angle θ_c of 15 degrees was chosen.

240
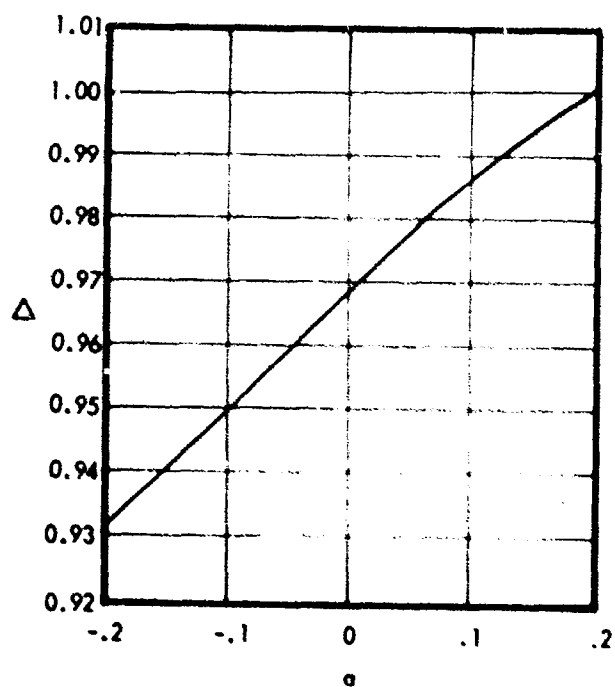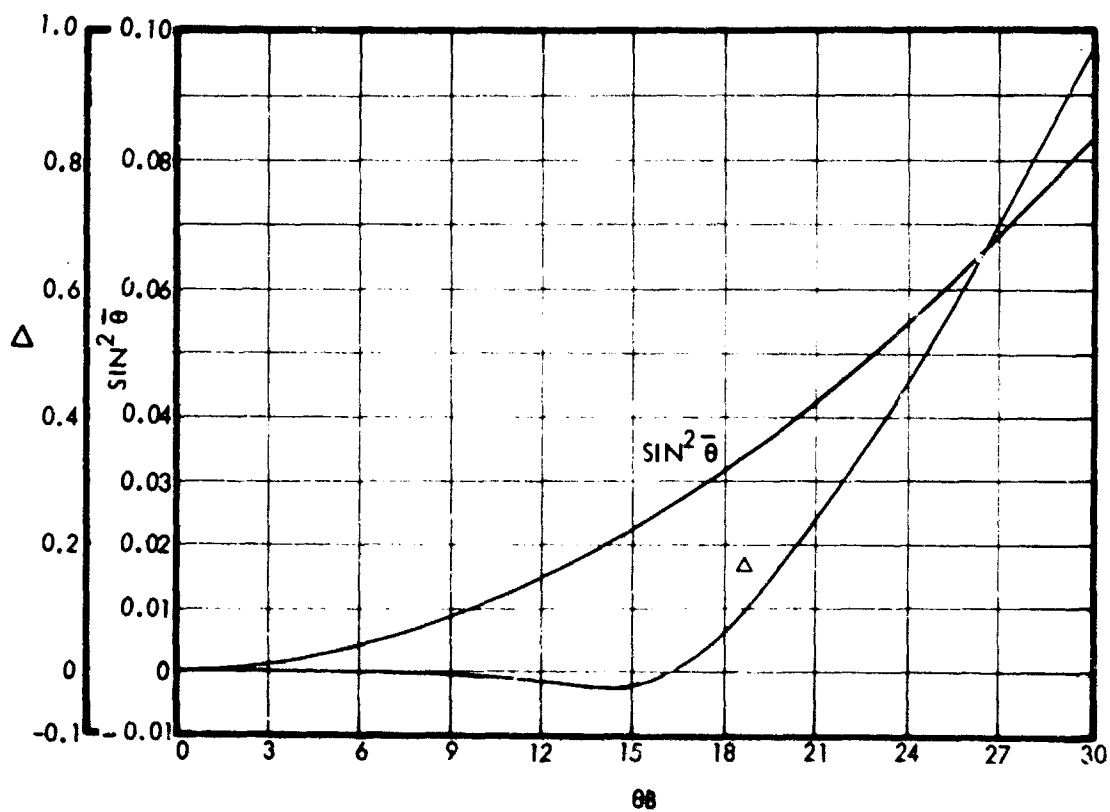
Figure 176. Fractional Correction Term Δ as a Function of Beam Divergence Angle θB, and the <q/m> or Efficiency Deviation Term a

241

In order to incorporate the effects of the Δ_n corrections back into the original time-of-flight equations, we refer to the definitions given by Equations (26), (27) and (37). If a subscript zero is used to designate the uncorrected time-of-flight parameters, the corrected ones are given by the following equations.

$$<v> \;=\; <v>_o \frac{(1+\Delta_o)}{(1+\Delta_1)} \tag{44}$$

$$<v^2> \;=\; <v^2>_o \frac{1}{1+\Delta_1} \tag{45}$$

$$\eta \;=\; \eta_o \frac{(1+\Delta_o)^2}{(1+\Delta_1)} \tag{46}$$

$$F \;=\; F_o\,(1+\Delta_o) \tag{47}$$

$$\dot m \;=\; \dot m_o\,(1+\Delta_1) \tag{48}$$

$$I_{sp} \;=\; I_{sp_o} \frac{1+\Delta_o}{1+\Delta_1} \tag{49}$$

$$<q/m> \;=\; <q/m>_o \frac{1}{1+\Delta_1} \tag{50}$$

For a typical colloid beam of ±15 degrees spread, and a collector subtending a solid angle sector with $\theta = 15$ degrees (3-foot diameter collecting surface at a distance of 1.8 meters), the first term in Equation (39) is negligible. The second term is of order 3 percent and θ_n is approximately 10 degrees. If there is a net thrust vector misalignment the first term can become significant because part of the beam is pushed off the collector preferentially in one direction. In this case, the value of the second term, which is of opposite sign, also increases. The total effect of these two terms has not been evaluated.

242

7.3 DIRECT MASS FLOW MEASUREMENTS

Several experiments to directly measure mass flow rates were performed with both conventional and annular needle geometries. The main objectives were: (1) to provide verification of the accuracy of the time-of-flight technique, and (2) to ider ify whether a significant amount of mass is ejected with no charge. Close agreement between direct and time-of-flight mass flow data would increase confidence in the remainder of the time-of-flight data, such as thrust, specific impulse, and efficiency. Gross differences between the two types of measurement could be indicative of a large neutral fraction.

The variability of the instantaneous time-of-flight data from one measurement to another often made it difficult to establish the true time-of-flight performance values to better than the order of 10 percent. However, within this limitation, reasonably good agreement was attained.

This section first presents a discussion of various alternate approaches which were initially considered. Following this is a detailed discussion of the selected approach, which involves the use of an analytical weight balance to measure the rate of depletion of the propellant reservoir. The measurements that were made, their interpretation, and possible sources of error are then reviewed. A 400-hour life test, during which direct mass flow measurements were made, is also discussed.

7.3.1 Alternate Approaches

Direct mass flow measurement techniques can be classified into two major categories: continuous monitoring and time integrated monitoring. The continuous monitoring method attempts to measure the instantaneous mass flow rate at all times. This, however, is not strictly possible, since the high sensitivity required for these very low mass flow rates forces the devices to have very long time constants.

Continuous flow monitoring devices include those that depend on the pressure drop through a constriction in the propellant flow system and those that depend on the thermal response of the propellant to heat input. The accuracy of these devices depends on the physical properties of the propellant and the thermal control of their operating environment. In addition, these devices must be carefully calibrated in order to infer a mass flow rate from their output signal.

The calibration techniques for continuous flow monitoring devices usually involve the measurement of long-term weight or volume changes. These methods are really time-integrated monitoring techniques which also can be used to monitor thruster mass flow directly. They may involve either volumetric change or weight change measurements. In order to infer a mass flow rate from a volumetric change device, the propellant density must be known to better than the desired flow rate accuracy, and the temperature of the entire propellant system within the monitoring circuit must be uniform and accurately controlled. A weight change monitoring device is the most direct method of measuring flow rate. It does not depend on the physical properties of the propellant; however, it does require control of 's environmental temperature.

Measurement of mass flow rate by monitoring the pressure drop through a flow constriction requires the use of a pressure transducer and the flow constriction. Because of the low flow rates and sensitivity of available pressure transducers, the flow constriction must be a long, small diameter tube, rather than an orifice which is conventionally used for this technqiue. The pressure drop through the tube at a given flow rate is dependent on the viscosity and density of the propellant, both of which are extremely temperature sensitive. Therefore, to achieve the desired flow measuring accuracy, the restriction tube must be maintained within close temperature limits. The pressure drop required to achieve the necessary sensitivity will be equal to or in excess of the pressure drop in the thruster. This condition can cause problems in controlling the propellant flow to the thruster. The propellant specific gravity and viscosity must also be precisely known.

A thermal flow monitoring device consists of a sensor pair and a heat source. One of the sensors monitors the propellant temperature upstream of the point of heat addition; and the other monitors the propellant temperature either downstream of the point of heat addition or out of the flow stream. The mass flow rate is inferred from the signal difference between the two sensors. The temperature can be monitored with thermocouples or thermistors and the heat source can be a resistance element or one of the thermistors. A flow measuring device using this technique is sensitive to propellant properties, especially specific heat and thermal conductivity, and requires thermal control.

Thermal flow monitoring devices are subject to a fundamental limitation in that they rely on convective heat transfer by the flowing fluid as a means of inferring flow rate. Because of the colloid thruster's low flow rate and the finite size of the flow monitoring device, thermal conduction through the propellant and surrounding structure is considerably greater than thermal convection by the propellant. Because of this condition, the response caused by mass flow is a small perturbation to the overall thermal balance of the system. Also, the device's heat capacity, in relation to quantity of heat transferred by the propellant, limits the speed of response that can be attained with this device.

In order to use volumetric change as a means of monitoring propellant flow rate, a relatively small auxiliary propellant supply system must be used in parallel with the main supply. This system would be filled from the main propellant source between flow checks and would be the source of propellant to the thruster during periods of flow check. The change in propellant volume in the auxiliary supply would be measured over a known time period to determine the mass flow rate. The necessity of an auxiliary supply system for this flow measuring technique is to achieve the required measuring sensitivity in a reasonable time period. If the entire propellant supply system is in the monitoring circuit during a measurement, less than 1 percent of the total stored propellant, including line and reserve volume, will be expelled in a 10-hour period. Thus, in order to achieve the necessary accuracy, changes in the total system volume of less than 5×10^{-3} percent would have to be measured. This technique for monitoring mass flow is dependent on the propellant density and requires thermal control of not only the monitored volume, but also the entire propellant distribution system that is in the flow circuit.

244

7.3.2 Selected Approach

The direct mass flow measurement apparatus selected for this task employs an analytical weight balance as shown in Figures 177 and 178. The balance is a Mettler microbalance, type B5H26. This instrument has a total capacity of 200 gms and a sensitivity of 0.1 mgm. This balance is a 0.1-gm-increment null-point device with a factor of 100 additional sensitivity obtainable by using an optical lever to measure very small balance arm deflections. The amount of arm deflection can be reduced by using weights in the sub-100 mgm range.

The propellant supply system is suspended from the balance arm with a glass rod to achieve electrical isolation. The propellant feed and pressurizing lines extend from the propellant supply system on the balance to an electrical isolation feedthrough into the vacuum test chamber. A section of the joined lines is flattened in a horizontal plant to act as a flexure. The lines are separated vertically and symmetrically about a horizontal axis extending from the vacuum system feedthrough to the support point on the balance. The two lines converge at both ends of this axis. The purpose of the flat tube flexural section and the separation and rejoining of the propellant supply and pressurizing tubes is to produce a connection between the propellant supply and the thruster that is compliant in the vertical direction, has negligible Bourdon effect when pressurized, and is rigid in the horizontal direction.

Since the balance is restored to its original position every time the weight changes by 0.1 gm, the balance needed calibration only in the optical lever sub-100 mgm range to establish the influence of the feed and pressure lines on the balance's response to propellant weight changes. This was done by using 10 mgm weights and comparing the balance deflection with the standard.
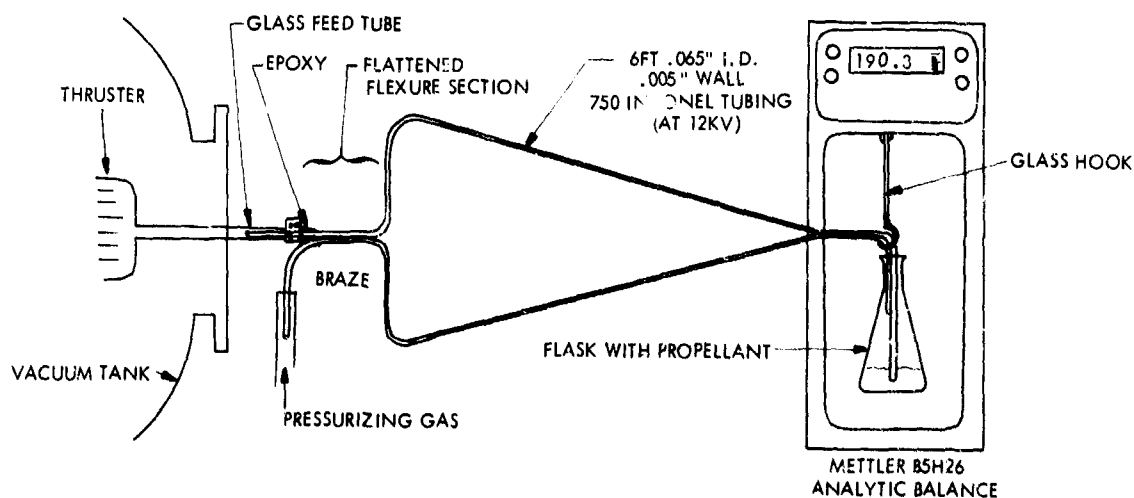
Figure 177. Direct Mass Flow Measurement Schematic

245
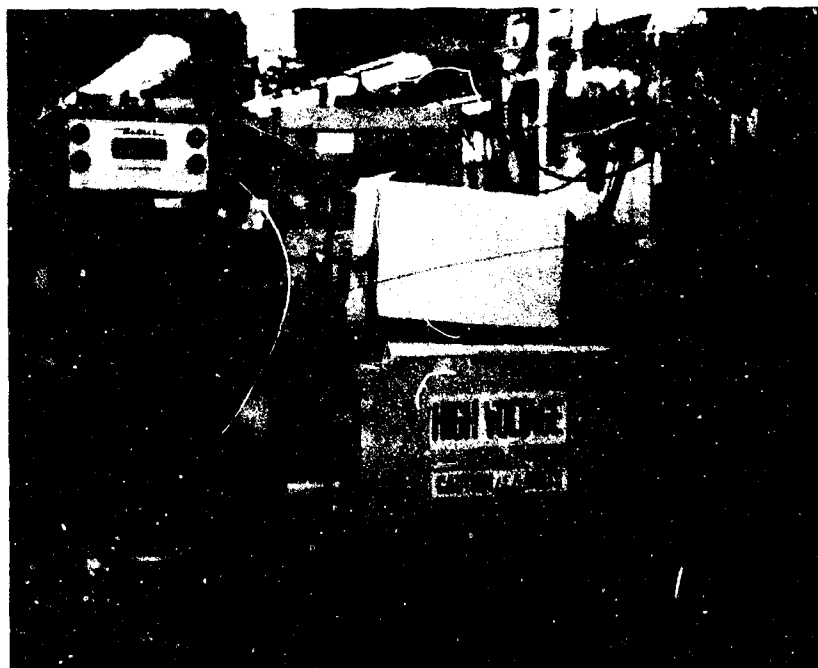
Figure 178.   Direct Mass Flow Experimental
Apparatus

For the system shown in Figures 177 and 178, the effect of the supply and pressurizing lines spring constant is to change the balance sensitivity from 0.1 to 0.17 mgm.   With this mass flow measuring system, only a few hours of operating time is required to obtain a sensitivity of 0.5 percent.   By monitoring the propellant supply system weight at more frequent intervals, and by averaging the data points graphically, it is possible to observe time-averaged thruster operation over time periods of the order of 10 to 15 minutes, which is the range of time constants for continuous monitoring devices.   This technique has the further advantage over continuous devices that as time goes on during the test, the overall accuracy continuously increases.

In order to achieve the desired accuracy with an operational direct weighing technique, several precautions must be observed.   Some of these are inherent to a direct weighing system, but most are inherent to all mass measuring systems.   A major requirement is that the propellant distribution system must be filled void-free.   A void in the propellant system, once formed, will have a tendency to change size.   This size change will displace propellant, causing an erroneous flow reading.   A simple test used to assure a void-free fill with the weighing technique was to make a step change in the propellant supply pressure and to note if there was a step change in the weight of the propellant supply.

Since the propellant supply system is external to the vacuum test facility and is at the operating potential, it is necessary to guard against varying electrostatic forces that could influence the balance reading.   This was done by grounding all permanent surfaces in close proximity to the

246

propellant supply system or using ground shielding where this was not practical. The shielding effectiveness was verified by noting changes in the balance reading caused by movement of grounded objects in the region of the propellant supply system.

Although it is not necessary to control the temperature of the propellant supply system within close limits, the time-averaged temperature over several hours must be constant. This is because of thermometer effects in the propellant distribution line. As an example, if the propellant distribution line contains 5 percent of the total propellant supply, then a 1°C temperature change would cause a transfer of sufficient propellant to maintain a 10 μlb thrust level for approximately 4 minutes. This would make it impossible to obtain a high accuracy within a short measurement time. If the temperature oscillates with a period short compared to the total measurement time, then the effect would automatically average itself out. Room temperature oscillations did not prove detrimental to the tests because the mean temperature was constant. If it had proven necessary, the propellant supply system and b ance could have been surrounded with a thermally controlled shield.

Another environmental condition that affects mass flow measurement is humidity. Changes in atmospheric humidity will change the quantity of adsorbed moisture on the exterior of the propellant supply system and, therefore, its weight. This effect was minim zed by using a drying agent in the balance chamber and minimizing the si e and number of entry ports. The surfaces of the propellant storage vessel were cleaned and polished to reduce their area.

A last, but important, factor is that of dust accumulation. Because the propellant system is at a high positive potential, there can be regions where corona will occur. Although the corona is positive, some negative ions will be produced and these will charge airborne particles in the vicinity of the propellant system. The negatively charged particles will be attracted by, and become attached to, the propellant system. This affect was minimized by ensuring that corona was reduced to a minimum, and controlling the environment around the propellant system.

7.3.3 Experimental Results

Individual experiments were performed with the ADP module, an earlier 36-needle research module, an earlier annular thruster design and, finally, the life test annular thruster. The detailed results are summarized to provide a more complete overview of the actuation and conclusions are made.

For each run the individual balance readings are plotted against time, thus providing a graphical representation of the rate of propellant depletion within the reservoir. The slopes of these graphs are then used to compute the directly measured mass flows which are then tabulated along with the corresponding time-of-flight mass flows. Typical time-of-flight photos are also included.

247

Dec. 9 Run with ADP Module

The first hour was run at a lower mass flow than the rest of the day. Because temperatures were not well established at this time, not much credence is given the value of 12.1 micrograms/sec. Note that if more weight were given the first few points, a closer correlation would have been obtained. The slope shown for the first hour gives a mass flow 10 percent lower than that of the time-of-flight photos. The two points, pictures 9-1 and 9-2, taken during this time are not included in the average. The comparative time-of-flight results are shown in Table 25. The average time-of-flight mass flow is 3 percent higher than the actual mass flow. Corrections were made for meter errors and parallax and time base calibration. Picture 9-4 is shown in Figure 179a. Nominal time base is 50 microseconds/div-tail expansion is a factor of 5.

Dec. 15 Run with Reworked Research Module, Cup-Shielded 36-Needle

Mass flow data are shown in Figure 180. Feed pressure and module temperature were kept accurately constant throughout the day. The average mass flow is 40.4 micrograms/sec — a condition of overfeed. Notice the resulting low specific impulse and good efficiency. The time-of-flight data are shown in the second grouping of Table 25. These numbers represent re-readings to most accurately correct for parallax, etc. A change was made to an oscilloscope with no parallax and very accurate time scale between pictures 6a and 6. Picture 15-7 is shown in Figure 179b. The first part of the ion peak cannot be seen. Zero time is accurately the first grid line. Note the sudden dip in the trace. It is ignored and we extrapolate through it.

Dec. 16 Run, 36-Needle Module at Lower Mass Flow

Mass flow measurements are shown in Figure 181. As in most of these and later runs, although weight readings were started shortly after 8 AM when the engine was restarted, the plot started later at about 10 AM when the operating characteristics stabilized. Improvements in electrostatic shielding caused almost no variation of the analytic balance with voltage. Note also that no change of mass flow can be detected for a change in voltage (i.e., the meniscus curvature change is so slight that it doesn't affect the pressure gradient). The tabulated time-of-flight data are shown in the third group of Table 25. The average time-of-flight $\dot{M}$ is only 90 percent of the $\dot{M}$ as measured on the balance. A rework of picture 16-2 raised the $\dot{M}$ by 3 percent. A slightly better correlation would have resulted if the tail had been expanded. Also, it is noted, upon examining the data fed into the computer, that 0.2 vertical divisions, rather than zero, were fed to the computer as the last point. This is important because the computer subtracts the last point from all the points. Picture 16-6 is shown in Figure 179c.

Dec. 17 Run at 25.2 Micrograms/Second

The mass flow data are shown in Figure 182. Tabulated time-of-flight data in Table 25 show average $\dot{M}$ time-of-flight to be 95 percent of the mass flow from the analytic balance. Picture 17-4a differs from 17-4 by using a 5:1 tail expansion. The effect is negligible in this case. Picture 17-3 is shown in Figure 179d.

248

Table 25. 36-Needle Module Test Results

Picture No.	V_n(KV)	I_n(μa)	T(μlb)	I_{sp}	Eff%	$\dot{M}$(TOF)	$\dot{M}$(BAL)	$\dot{M}_T/\dot{M}_B$
9-1	10.95	180	44.4	1495	73.4	13.5	12.1	1.11*
9-2	10.86	181	46.1	1458	74.5	14.4	12.1	1.19*
9-3	10.87	202	56.4	1344	75.3	19.0	18.4	1.03
9-4	10.88	192	55.2	1328	76.4	18.9	18.4	1.02
9-5	11.9	255.4	67.5	1532	74.1	20.0	18.4	1.08
9-6	11.95	254.5	63.4	1586	74.7	18.1	18.4	0.99
							Average	1.03
15-1	12.1	242.5	91.2	1119	75.8	37.0	40.4	0.92
15-2	12.1	239.6	93	1092	76.3	38.6	40.4	0.96
15-3	12.1	242.5	96.5	1065	76.4	41.1	40.4	1.02
15-4	12.2	242.5	91.7	1120	75.7	37.2	40.4	0.92
15-5	12.15	247.5	93.2	1129	76.3	37.5	40.4	0.93
15-6a	12.2	255	100.6	1100	77.5	41.5	40.4	1.03
15-6	12.2	255	95.5	1152	77.1	37.7	40.4	0.93
15-7	12.2	252	97.6	1121	77.5	39.5	40.4	0.98
							Average	0.98
16-1	12.68	230	62.7	1542	72.4	18.5	21.0	0.88
16-2	12.68	222	62.3	1500	72.3	18.9	21.0	0.90
16-2a	12.68	222.75	63.9	1487	73.3	19.5	21.0	0.93
16-3	13.3	280.2	72.4	1656	70.1	19.8	21.0	0.95
16-4	13.4	279.2	68.2	1769	70.3	17.5	21.0	0.84
16-5	11.6	183.2	53.4	1344	73.6	18.0	21.0	0.86
16-6	11.6	173.3	53.4	1291	74.7	18.8	21.0	0.90
							Average	0.90
17-1	12.01	237.6	70.0	1334	71.3	23.8	25.2	0.95
17-2	12.02	237.6	69.3	1360	71.9	23.1	25.2	0.92
17-3	12.02	237.6	74.3	1325	75.2	25.5	25.2	1.01
17-4	13.03	299	82.9	1574	73	23.9	25.2	0.95
17-4a	13.03	299	83	1575	73.1	23.9	25.2	0.95
							Average	0.95
18-1	12.5	277	83.4	1428	75	26.5	25.4	1.04
18-1a	12.5	277	85.5	1399	75.3	27.8	25.4	1.09*
13-2	12.5	275	75	1515	72.1	22.5	25.4	0.89*
18-3	12.5	275	76.7	1503	73.1	23.2	25.4	0.91*
18-4	12.5	273	75.4	1493	71.1	22.9	25.4	0.90*
18-5	12.95	300	82.1	1575	72.6	23.7	25.4	0.93*
18-6	12.01	249	69.5	1456	73.7	21.7	25.4	0.85*
18-7	12.01	240	72.2	1356	74	24.2	25.4	0.95
18-8	12.5	270	77.7	1437	72.2	24.6	25.4	0.97
18-9	12.5	273	81	1423	73.7	25.9	25.9	1.02
							Average	0.99
							-1% meter correction	0.98
21-1	12.42	270	75.4	1473	72.3	23.2	26.8	0.87
21-2	12.42	270	78.3	1444	73.5	24.6	26.8	0.92
21-3	12.42	270	76.7	1508	75.2	23.1	26.8	0.86*
21-4	12.42	270	75	1512	73.7	22.5	26.8	0.84*
21-5	12.42	270	73.8	1534	73.6	21.9	26.8	0.82*
21-6	12.42	270	76.8	1482	74	23.5	26.8	0.88*
21-7	12.42	269	78.1	1412	72	25.1	26.8	0.93
21-8	12.42	271	77.2	1426	71.3	24.6	26.1	0.94
21-9	12.42	270	78.4	1449	73.8	24.6	26.1	0.94
21-10	12.42	272	79.5	1414	72.5	25.5	26.1	0.98
21-11	11.4	213	65.2	1272	74.5	23.3	26.1	0.89
21-12	13.55	228	94.3	1544	71.4	27.7	26.1	1.01
21-13	11.4	212	67.4	1216	71.9	25.2	26.1	0.97
21-14	12.42	277	79.1	1461	73.2	24.6	26.1	0.94
							Average	0.93
							-1% meter correction	0.94
22-1	12.5	270	87.9	1251	71.1	31.9	31.9	1.00
22-2	12.5	271	88.1	1270	72.2	31.5	31.9	0.97
22-3	11.48	167	62.2	1103	78	25.6	31.9	0.80*
22-4	12.5	265	87.3	1304	75.3	30.4	31.9	0.95
22-5	12.52	265	85.5	1304	73.2	29.8	31.9	0.93
22-6	12.5	259	85.5	1221	70.2	31.8	31.9	1.00
22-7	12.5	259	84.4	1303	74	29.4	31.9	0.92
22-8	12.5	268	87.3	1294	71.5	30.6	32.9	0.94
22-9	13.5	349	103.2	1525	72.8	30.7	32.6	0.94
22-10	13.5	350	104.8	1486	71.8	32.0	32.6	0.99
22-11	13.5	349	100.9	1528	71.3	30.0	32.6	0.92
22-12	13.45	348	102.4	1542	73.5	30.1	32.6	0.92
							Average	0.94
							-1% meter correction	0.94

*Not averaged, see text.

249
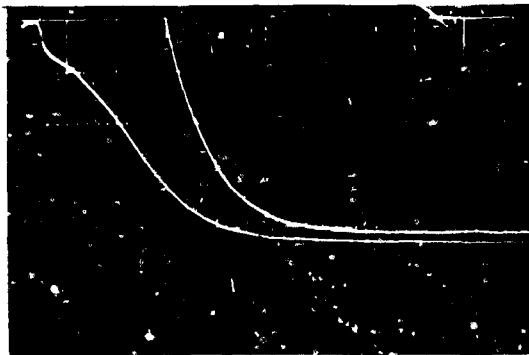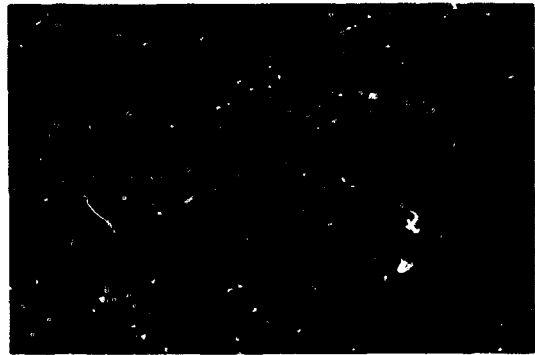
(a) Picture 9-4   (b) Picture 15-7
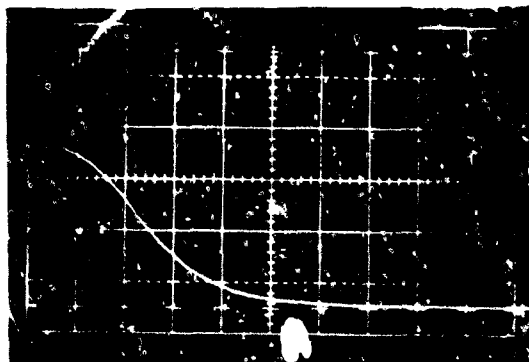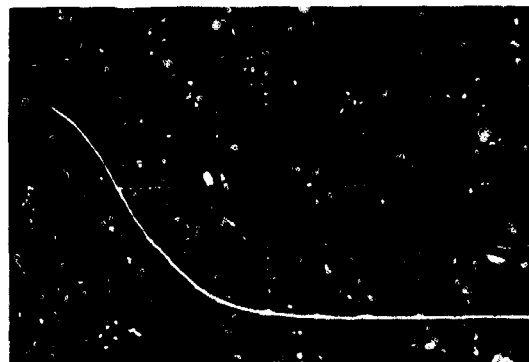
(c) Picture 16-6   (d) Picture 17-3

Figure 179.   Typical Time-of-Flight Photographs
Time scale 50 μs/div.

Dec. 18 Run

To gain insight into and more data pertaining to the previous reading
errors, a day's run similar to the previous day was taken. As seen in
Figure 183 M(bal) was 25.4 μgms/sec. Interestingly, the line was drawn
at time 1300 and all points fell sufficently close so as not to require any
slope revision.   Tabulation of data is in Table 25. Picture 18-1s is a hand
reading of the photo by a different operator and is not averaged because of
personal bias   Picture 18-2 through 18-5 are not averaged because they
are auto-machine taken and are probably about 6 percent low. Pictures
18-4 through 18-6 show a possible nonequilibrium effect of rapidly changing
voltage — i.e., an overfed condition when voltage was first advanced before
the liquid had receded to its new equilibrium position. The average of the
hand-read computations is 99 percent of the balance value of mass flow.
Picture 18-7 is shown in Figure 184.
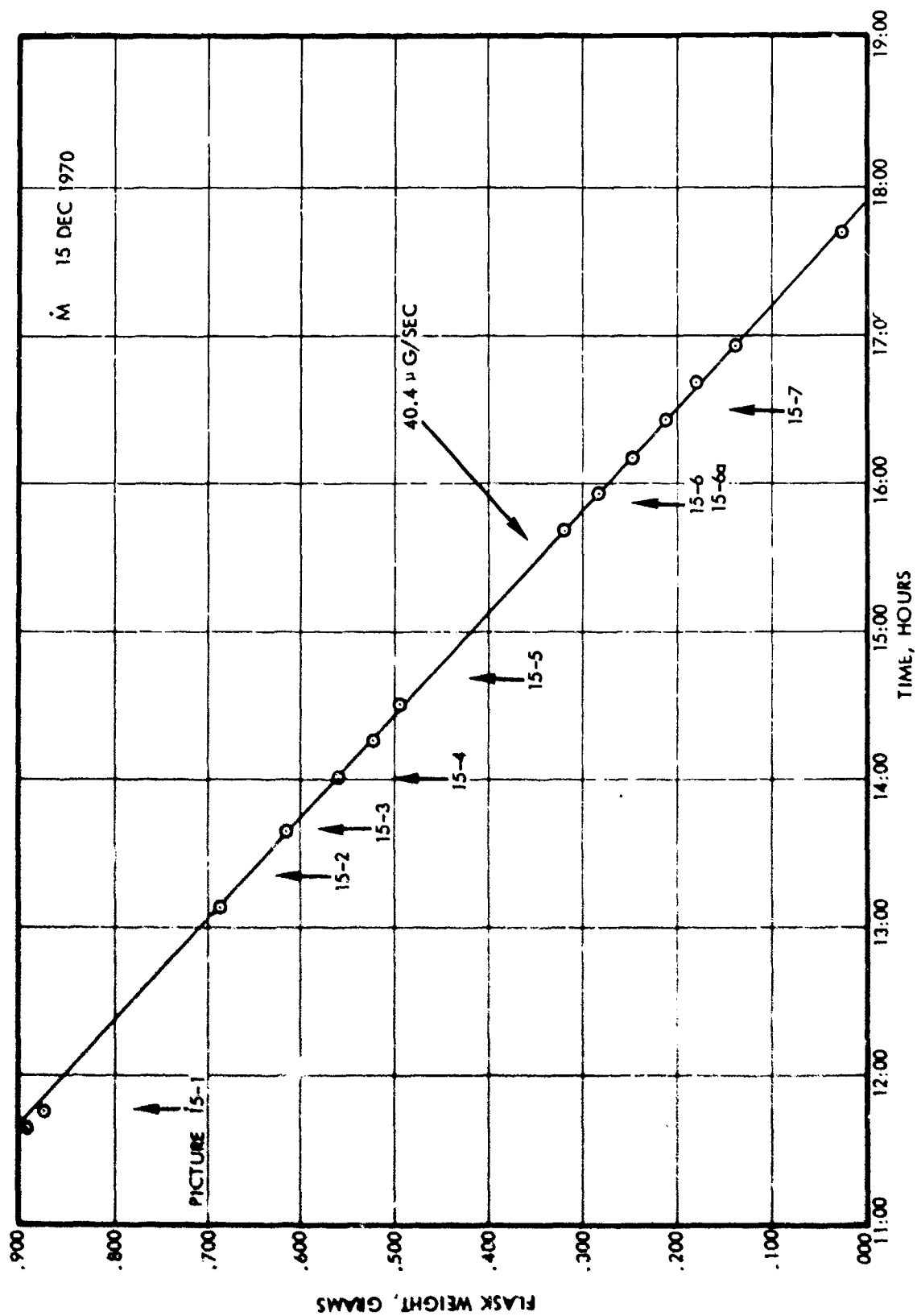
Figure 180. Change of Propellant Flask Weight During Mass Flow Measurement on Research Module with 36 Shielded Needles (Dec. 15)
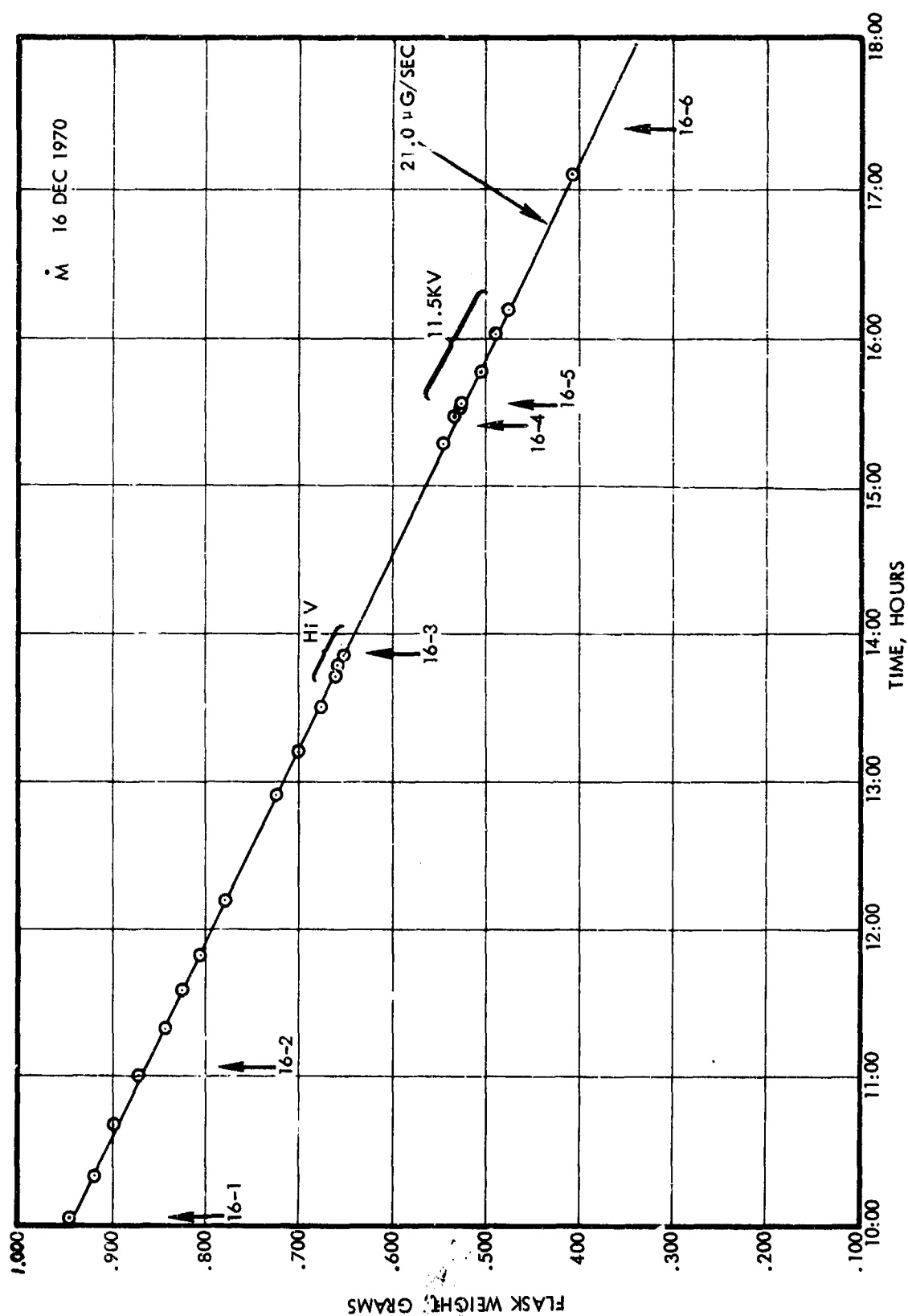
Figure 181. Change of Propellant Flask Weight During Mass Flow Measurement on Research Model with 36 Shielded Needles (Dec. 16)
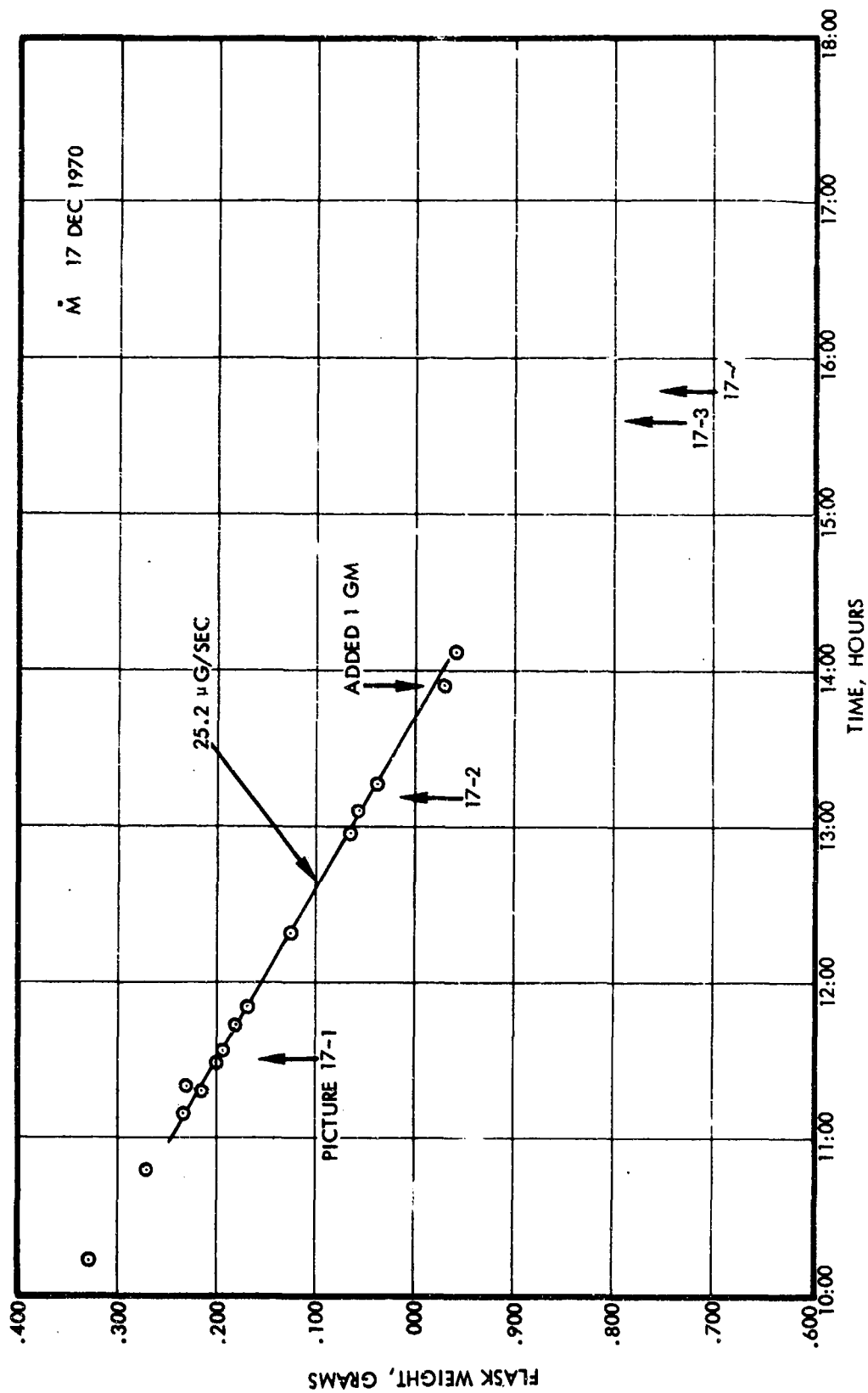
Figure 182. Change of Propellant Flask Weight During Mass Flow Measurement on Research Module with 36 Shielded Needles (Dec. 17)

253
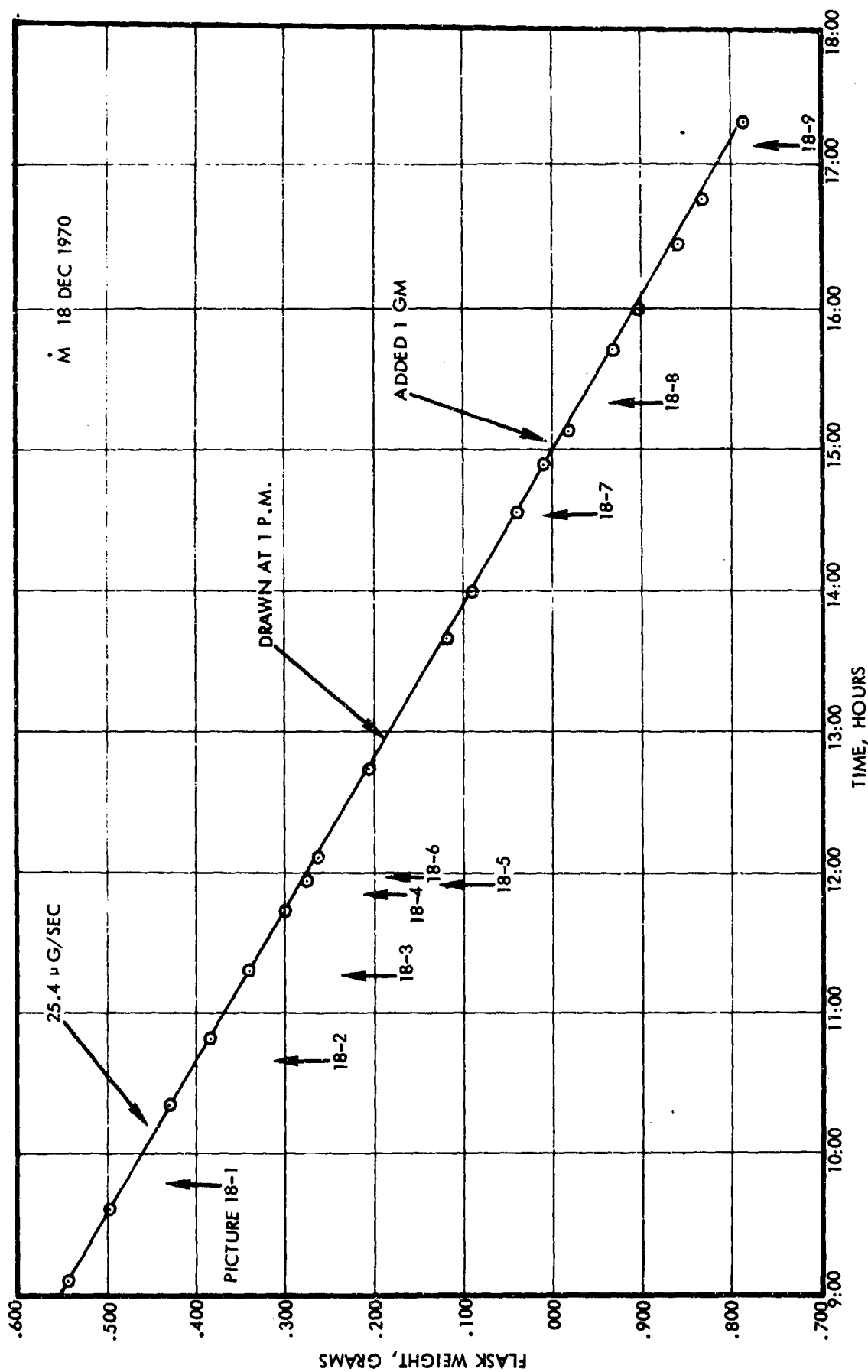
Figure 183. Change of Propellant Flask Weight During Mass Flow Measurement on Research
Module with 36 Shielded Needles (Dec. 18)

(a) Picture 18-7
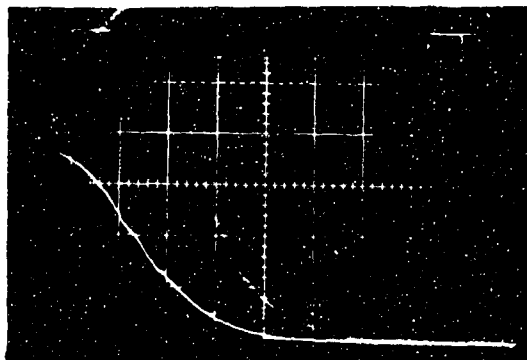
(b) Picture 21-11

(c) Picture 22-3
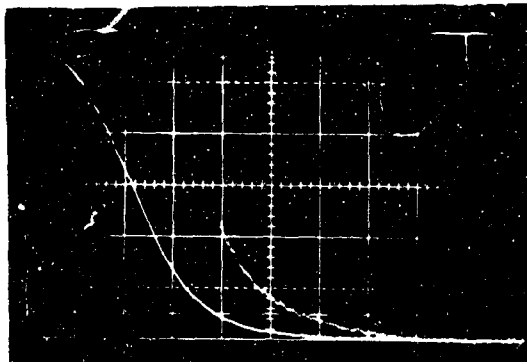
(d) Picture 22-4

Figure 184. Typical Time-of-Flight Photographs Taken During Last Three Runs. Double exposures are x5 tail expansion. Unfortunately, the real tail in Picture 22-3 was not expanded.

Dec. 21 Run

Figure 185 shows the mass flow for this run. In the afternoon a discernable decrease of mass flow (because of a slight drop in feed pressure) was measured — down about 2 percent from 26.8 to 26.1 micrograms/sec. Tabulation of the time-of-flight data in Table 25 shows about the same statistical variation with an average of 94 percent correlation after the automatic values were removed and the 1 percent meter calibration was included. Pictures 10 through 14 were taken at various voltages. Again, the mass flow was low when voltage was first reduced (11), and returned to the average after about 10 minutes (13). However, except for the transient, the M correlation is to first order independent of the voltage. Picture 21-11 is shown in Figure 184b. Discontinuity is evident. It can be suspected that between about 75 and 140 microsecond fast electrons are

255
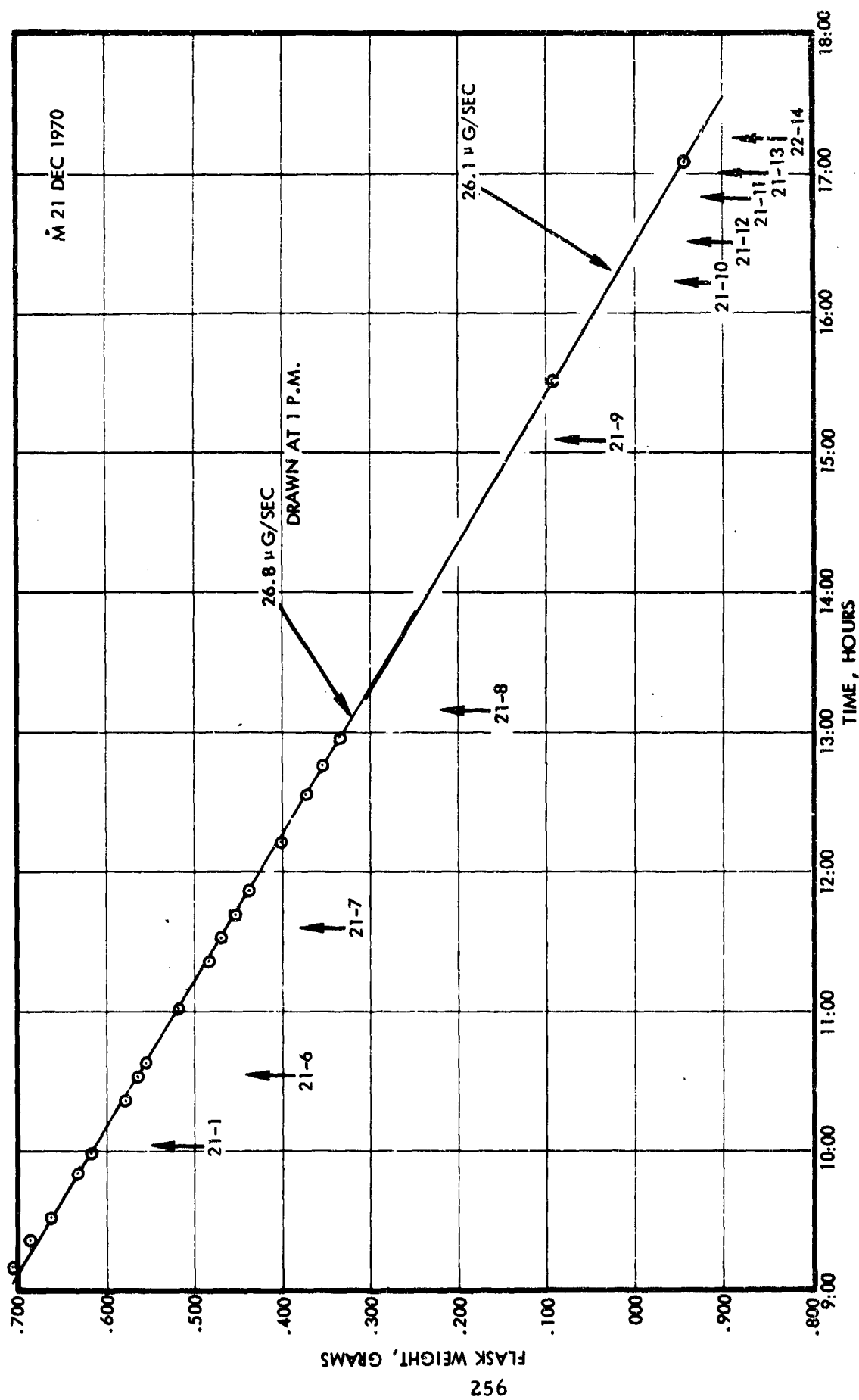
Figure 185. Change of Propellant Flask Weight During Mass Flow Measurement on Research Module with 36 Shielded Needles (Dec. 21)

256

being delivered to the collector. This is despite +150 volts on the screen and -150 volts on the suppressor. If a higher current were received in this interval the mass flow would be higher. This might partially account for the 89 percent correlation on this picture.

Dec. 22 Run

The mass flow for the day is shown in Figure 186. The run was made at a high temperature, 30°C, and a low net feed pressure of 0.7 in. of Hg. This meant the component of feed caused by the concave meniscus was fractionally large, therefore, a measurable reduction in mass flow should result when the voltage is removed. This is seen during the last 1-1/2 hours of the day. The plan had been to turn off the voltage and let the propellant dribble out and flood the engine, but in order not to flood the engine if analysis of the data revealed interesting avenues of pursuit, the needle voltage was lowered to 5 kv in anticipation the liquid would then assume an average zero curvature meniscus and occasionally spurt off the excess propellant and prevent flooding. The reduced slope is clearly seen — 24.8 instead of 32.6 micrograms/sec at high voltage. If the meniscus assisting pressure is X in inches of Hg, then $0.7+X/0.7 = 32.6/24.8 = 1.315$ and $X = 0.7 \times 0.315 = 0.22$. This is the value that was planned on and is the value from $\Delta P = 2\gamma/r$ where a radius of curvature of about 7 mils is assumed using the measured value of propellant surface tension γ.

These data were at the highest temperature of the runs and were taken over a range of voltages. The tabulated data show the same correlation of 0.94 under these conditions. The low value of 0.80 on picture 22-3 is not included in the average because a real tail did exist at this low-voltage, high-feed condition that was not picked up in the picture. The tail had not been expanded, and when the pictures were later taken on a ten times slower speed, a long tail could be clearly seen proceeding to a lower zero current than had been assumed in the picture readout. This 15 percent error shows the effect of neglecting a small (approximately 2 percent) but long (250 microseconds) tail. Picture 22-3 (with the long tail) is shown in Figure 184c. Picture 22-4 is shown in Figure 184d.

Average Correlation of Mass Flow for 0.014-Inch Platinum Needles

When all groups in Table 25 are averaged together giving equal weight to each group, M(TOF) the mass flow from the computer which is fed the reading from the time-of-flight picture is 96 percent of M(bal), the rate of mass reduction from the storage flask which is measured by an accurate (Mettler) analytic balance.

7.3.4 Annular Geometry Mass Flow Measurements

Annular geometry measurements were characterized by poorer time-of-flight data reproducibility than observed with the 36-needle modules. We believe that one reason for this is that the multiple needle modules allow individual needle time variations to mutually cancel when averaged over the entire array. Of course, no such cancellation can occur for a single annular source. A second consideration is that the annular source used for the earlier measurements did not have the operational stability achieved with later models. As with the needles, individual results are presented prior to the final summary.

257
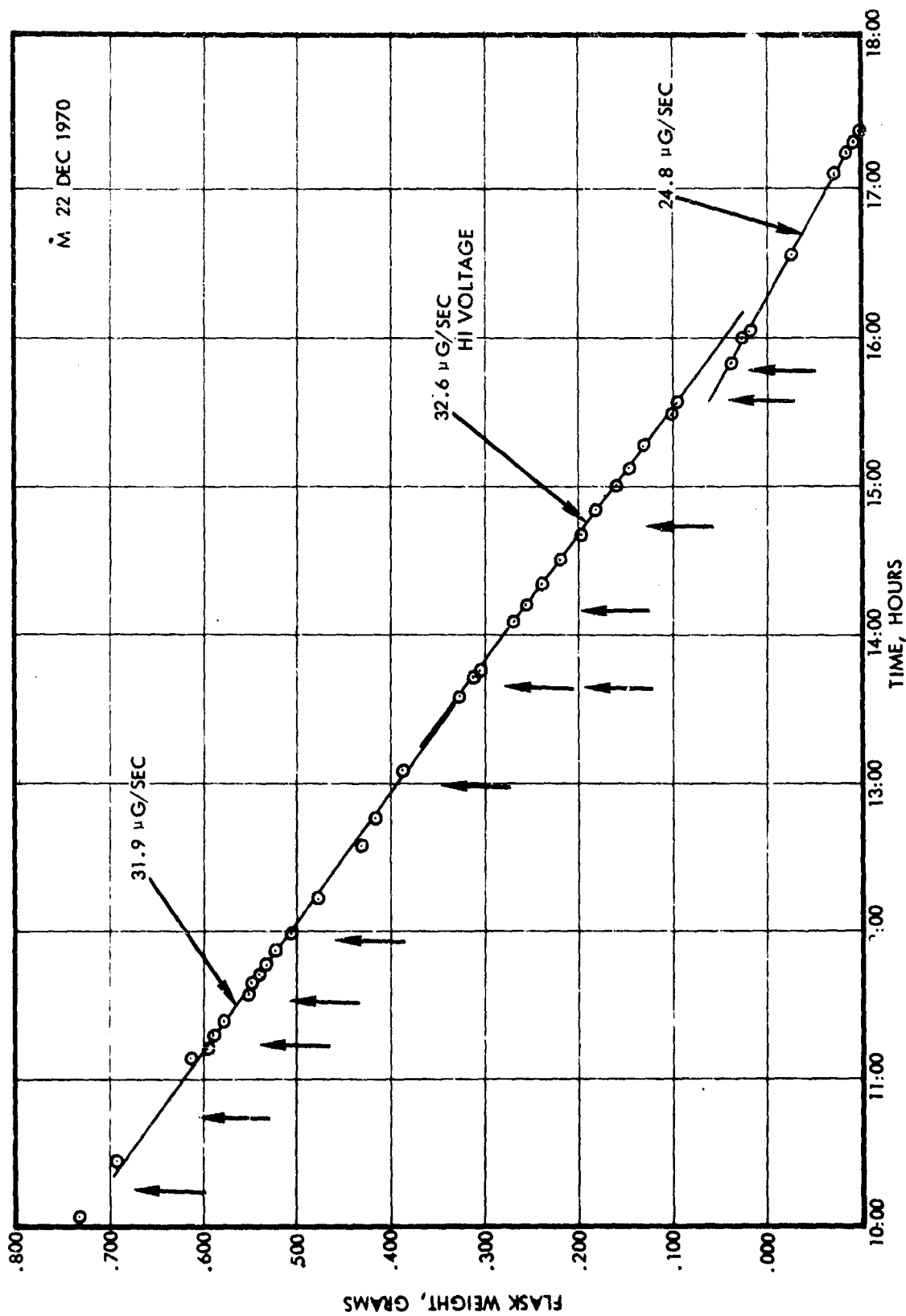
Figure 186. Change of Propellant Flask Weight During Mass Flow Measurement on Research Module with 36 Shielded Needles (Dec. 22)

258

There were two main phases for these experiments: (1) a series of measurements with early experimental thrusters, and (2) later measurements which were intended to be part of the final life test. The earlier series did not have deflector electrodes to shield against electron bombardment from the extractor, a possible source of neutral production.

The earlier data taken over various ranges of temperature, mass flow and voltage are summarized in Table 26. During the course of these runs, the source was run from 12° to 35°C. No basic difference in mode of operation, efficiency, or mass correlation was detected. As the vapor pressure doubles in about 6°C, significant variations in evaporation and their effect on the correlation should have been observed if they were significant enough to escape being obscured by scatter in time-of-flight data. It was noted that with the large needle, operation at low temperatures was not stable. There was a 30 to 40 percent variation in the current. Presuming that this was related to crystal formation from previous long-time low-temperature operation, the needle was temperature cycled three times. Every time the temperature was lowered below about 18°C, the current started varying. The average value of these measurements was $\dot{m}_T/\dot{m}_B$ = 0.90 with a standard deviation of 0.09.

Another series of measurements was then performed with a later model shielded annular source. These produced closer agreement, but it is not known whether this was because of the shielding or because generally more stable performance could be obtained with these later devices.

The time-of-flight parameters during this test were nominally 70 percent efficiency, 1650 seconds specific impulse, 24 μlb thrust, and 90 microamperes source current at 14.2 kv. Table 26 shows a series of 14 time-of-flight measurements taken at 5-minute intervals to test the internal consistency of the time-of-flight measurements and also to compare these results with direct mass flow measurements (Figure 187).

It is apparent from Table 27 that there was considerable spread in the time-of-flight results. The average mass flow for the 14 measurements was 6.76 micrograms per second with a standard deviation of 0.32 (5 percent). The direct mass flow measurements during this period indicated 7.01 micrograms/second, which was 3.7 percent higher than the time-of-flight value. This is better agreement than has been previously attained by this type of comparison. In view of the relatively large deviations, too much significance should not be attached to this agreement. However, it is, of course, encouraging that no great disagreement was found.

A periodic rippling of the propellant meniscus, which might have been caused by gas bubbles, was observed throughout the test. At the beginning of the test, frequencies of the order of 10 per minute were observed. This eventually decreased to 2 per minute. It is quite possible that this surface instability was the cause of the variations in the time-of-flight calculations. The direct mass flow measurements indicated a constant flow when averaged over relatively long time periods. It is safe to assume that the instantaneous flow through the source impedance was also constant, apart from a relatively small variation caused by the temperature control bandwidth within the impedance tube. It is quite probable, however,

Table 26. Unshielded Annular Geometry Mass Flow
Experimental Data

Date	Time	Temperature (°C)	V_N(kv)	I_N(µa)	T(µlb)	Eff. (%)	SI(sec)	$\dot{M}_T$(µg/s)	$\dot{M}_B$	$\dot{M}_T/\dot{M}_B$
1-5	1556	36.1	14	69	28.3	72	1125	11.4	10.9	1.06
1-5	1627	36	14.1	62	23.3	70	1200	8.8	10.9	0.82
1-5	1708	35.7	14.1	60	23.9	70	1140	9.5	10.9	0.88
1-5	1724	35.6	14.1	68	26	70	1185	9.95	10.9	0.92
1-6	0817	34.7	14.1	70	25.8	70	1230	9.5	10.5	0.91
1-6	1026	34.8	14.1	70	27.7	71	1160	10.9	10.5	1.04
1-6	1312	34.6	14.1	70	25.5	70	1240	10.3	10.5	0.99
1-6	1620	34.1	14.1	70	26.9	67	1132	10.8	10.5	1.03
1-6	1622	34.1	14.1	64	24.2	66	1132	9.7	10.5	0.92
1-7	0810	33.8	14.1	70	23.1	68	1331	7.9	9.75	0.81
1-7	0814	33.8	14.1	68	25.3	68	1176	9.8	9.75	1.00
1-7	0825	33.8	14.1	70	24.5	68	1263	8.8	9.75	0.90
1-7	0827	33.8	14.1	70	26.2	70	1210	9.8	9.75	1.00
1-7	0829	33.8	14.1	70	25.2	70	1282	8.9	9.75	0.92
1-7	0830	33.8	14.1	69	25.8	69	1206	9.7	9.75	0.99
1-7	1426	33.8	14.1	71	24.3	69	1297	8.5	9.75	0.87
1-7	1638	33.8	14.1	70	23.8	69	1317	8.2	9.75	0.84
1-8	0745	32.7	14.1	71	23.5	70	1361	7.85	9.38	0.84
1-8	0950	33.2	14.1	70	23.7	67	1274	8.5	9.38	0.91
1-8	1332	33	14.1	68	24.1	65	1191	9.2	9.38	0.98
1-8	1630	33	14.1	72	23.2	67	1343	7.85	9.38	0.84
1-21	1150	33	14.1	82	30.9	74	1269	11.0	10.6	1.04
1-21	1311	33	14.1	82	29.8	73	1296	10.4	10.6	0.98
1-21	1406	32.8	14.1	81	29.3	72	1278	10.4	10.6	0.98
1-21	1445	32.6	14.1	81	27.5	73	1389	9.0	10.6	0.85
1-21	1520	32.6	14.1	82	28.7	73	1346	9.7	10.6	0.92
1-21	1544	32.5	14.1	82	28.5	72	1342	9.6	10.6	0.91
1-21	1618	32.2	14.1	82	23.3	72	1346	9.6	10.6	0.90
1-21	1650	32.2	14.1	84	29.4	72	1320	10.1	10.6	0.95
1-22	0803	31.5	14.1	85	28.9	71	1342	9.8	10.0	0.98
1-22	1155	25	14.1	71	24.3	71	1338	8.2	--	--
1-22	1320	23.7	14.1	70	21.9	70	1431	7.0	7.7	0.91
1-22	1520	24	14.1	70	22.8	69	1370	7.6	7.7	0.99
1-22	1637	24	14.1	70	22.4	70	1407	7.2	7.7	0.94
1-22	1650	24	14.1	70	22.9	69	1365	7.6	7.7	0.99
1-25	0833	23.7	14.1	68	20.8	69	1454	6.5	7.7	0.84
1-25	1038	23.7	14.1	70	20.5	68	1493	6.25	7.7	0.81
1-25	1054	23.7	14.1	70	20.4	69	1523	6.1	7.7	0.79
1-25	1116	23.7	14.1	70	20.4	68	1495	6.2	7.7	0.81
1-25	1150	23.7	14.1	71	20.4	68	1531	6.1	7.7	0.79
1-25	1311	23.7	14.1	70	20.3	68	1488	6.2	7.7	0.80
1-25	1615	29	14.1	80	21.3	67	1611	6.0	--	--
1-25	1650	29.2	14.1	80	21.9	67	1580	6.3	--	--
1-26	0810	29.6	14.1	81	21.5	68	1650	5.9	7.32	0.79
1-26	1041	29.5	14.1	81	21.6	67	1626	6.0	7.32	0.82
1-26	1407	29.3	14.1	80	21.8	68	1620	6.1	7.32	0.83
1-26	1433	29.2	14.1	88	28.8	69	1353	9.7	9.83	0.99
1-26	1515	29.3	14.1	90	28.1	69	1418	9.0	9.83	0.92

Table 26. Unshielded Annular Geometry Mass Flow Experimental Data (Continued)

Date	Time	Temperature °C	V_N(kv)	I_N(μa)	T(μlb)	Eff. %	SI(sec)	$\dot{M}_T$(μg/s)	$\dot{M}_B$	$\dot{M}_T/\dot{M}_B$
1-27	0935	28.5	14.2	82	25	69	1426	8.0	10.2	0.77
1-27	1018	28.5	14.2	81	26.1	71	1422	8.3	10.2	0.81
1-27	1125	28.5	14.2	81	25.6	70	1441	8.1	10.2	0.79
1-27	1320	28.5	14.2	81	24.3	81	1512	7.3	10.2	0.72
1-27	1445	28.2	14.2	80	25.7	67	1362	8.6	10.2	0.84
1-27	1733	28.3	14.2	81	28.1	70	1314	9.7	10.2	0.96
1-28	0806	28.3	14.3	70	20.3	67	1504	6.1	7.8	0.78
1-28	0920	28.3	14.3	70	20.2	68	1536	6.0	7.8	0.77
1-28	1402	28.5	14.2	72	21.3	67	1476	6.5	7.8	0.84
1-28	1545	28.5	14.2	72	21.2	67	1495	6.4	7.8	0.82
1-28	1655	28.5	14.2	71	20.8	69	1523	6.2	7.8	0.79
2-2	0805	31.5	14.2	82	29.7	72	1296	10.4	12.15	0.86
2-2	1004	32	14.2	82	29.3	71	1294	10.3	12.15	0.85
2-2	1042	31.7	14.2	82	30.5	72	1257	11.0	12.15	0.91
2-2	1115	31.7	13.6	75	28.6	71	1158	11.2	12.15	0.92
2-2	1324	31.7	13.6	71	27.0	71	1206	10.1	12.15	0.83
2-2	1342	31.7	13.1	67	26.6	72	1129	10.3	12.15	0.85
2-2	1354	31.7	13.1	68	25.7	72	1147	10.2	12.15	0.84
2-2	1405	31.7	12.6	60	23.2	72	1081	9.7	12.15	0.80
2-2	1429	31.7	12.6	60	24.2	73	1045	10.5	12.15	0.87
2-2	1440	31.7	12.1	51	20.6	74	1012	9.3	12.15	0.77
2-2	1505	31.7	12.1	51	21.6	76	997	9.8	12.15	0.81
2-2	1635	31.7	14	78	32.9	76	1154	12.9	12.15	1.06
2-2	1640	31.7	14	79	30.9	73	1191	11.8	12.15	0.98
2-3	0815	31	14	75	27.9	71	1227	10.3	11.3	0.89
2-3	1334	27.5	14	80	33.3	74	1142	13.2	13.7	0.96
2-3	1512	27.5	14	80	32.5	73	1160	12.7	13.7	0.93
2-3	1635	27.5	14	80	32.5	74	1165	12.7	13.7	0.92
2-4	0810	30	14	78	33.3	73	1103	13.7	14.1	0.97
2-4	1357	30	14	78	32.4	73	1119	13.2	14.1	0.94
2-4	1542	30	14	75	31.5	74	1130	12.6	14.1	0.90
2-4	1616	30	14	75	32.6	73	1083	13.7	14.1	0.97
2-4	1630	30	14	75	30.5	73	1161	11.9	14.1	0.85
2-5	0804	22.5	13.9	59	17.9	71	1480	5.5	8.35	0.66
2-5	0924	22.5	13.9	59	21.3	71	1253	7.7	8.35	0.92
2-5	1016	22.5	13.9	59	21.2	70	1251	7.7	8.35	0.92
2-5	1031	22.5	13.9	59	20.6	70	1286	7.3	8.35	0.88
2-5	1102	22.5	13.8	79	39.3	75	953	18.7	16.6	1.13
2-5	1113	22.5	13.8	78	35.7	75	1040	15.6	16.6	0.94
2-5	1133	22.5	13.8	78	35.2	74	1036	15.4	16.6	0.93
2-5	1146	22.5	13.8	79	32.8	74	1131	13.2	16.6	0.80
2-5	1320	22.5	13.8	78	37.1	75	996	16.9	16.6	1.02
2-5	1442	22.5	14.8	86	34.8	73	1218	13.0	14.2	0.94
2-5	1515	25.5	14.8	82	34.0	72	1173	13.2	14.2	0.93
2-5	1548	22.5	14.8	88	36.9	72	1162	14.4	14.2	1.01
2-5	1636	22.6	14.8	87	36.3	73	1088	16.4	14.2	1.18
2-8	1316	25.3	14.1	68	23.9	70	1294	8.4	9.32	0.88
2-8	1526	25.5	14.1	68	33.7	71	1325	8.1	9.52	0.85
2-8	1630	24.0	14.1	69	24.1	72	1336	8.2	9.52	0.86
2-8	1657	24.0	14.1	62	20.1	70	1403	6.5	7.4	0.88
2-9	0854	24	14.1	68	21.9	70	1406	7.1	7.4	0.95
2-9	1025	24	14.1	62	19.6	70	1432	6.2	7.4	0.84
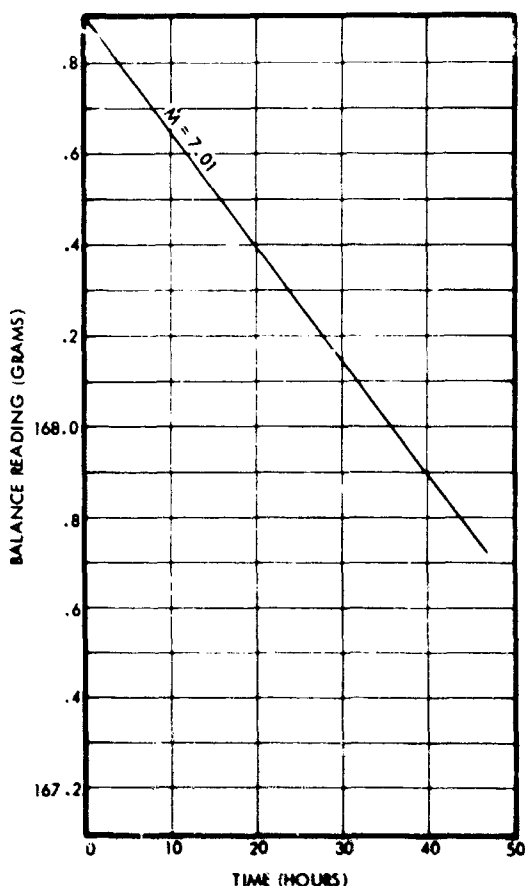
Figure 187. Run 710401 Direct
Mass Flow Readout

that the rippling observed on the fluid surface would result in corresponding changes in the rate at which the electrostatic field removed fluid from the surface. In fact, the changing surface geometry could be both a cause and a result of varying fluid surface emission. Thus the variation in time-of-flight mass flows could be, to a large extent, a real effect, in which the time-of-flight calculations are a true measure of the instantaneous rate of mass expulsion from the fluid surface.

The next measurements were made during an endurance test originally intended to be a 1000-hour life test which also included neutralization, thrust vectoring and beam profile measurements. The run ended after 432.8 hours immediately after deflector drain current developed during a series of vectoring experiments. Although the vectoring experiments were probably a contributory factor, the main cause of the failure is believed to be gas in the propellant caused by problems associated with the direct mass flow measurements. As will be shown later, this part of the experimental setup inadvertently caused electrolytic gas generation within the propellant feed line. Surface instability had been observed during the experiment and the final failure was caused by a sudden surge in needle current and a simultaneous dripping of propellant to the vector electrodes. Even after the feed pressure was removed, there was still a temporary persistence of propellant flow from the source. The most probable cause of this unusual behavior was bubble nucleation caused by electrolytic gas generation within the feed line.

Figure 188 summarizes the direct mass flow measurements during this test and their correlation with time-of-flight calculations. For periods of constant feed pressure the balance readings, which are a measure of the propellant remaining in the reservoir, follow straight lines whose slopes are equal to the rate of propellant utilization. For each period of constant mass flow, the time-of-flight mass flows calculated during that period are also entered. These are four separate "normal" periods during which the average time-of-flights mass flows are in error by 0.4, 16.8, 8.0 and 1.9 percent. The period corresponding to the 16.8 percent differentia includes only two time-of-flight calculations and thus has a high

262

Table 27. Run 710401, Time-of-Flight Test Results at 5-Minute Intervals, April 7, 1971

(Feed Pressure = 7.32 in. Hg, V_n = 14.2 kv, V_{def} = 8 kv Time-of-Flight Distance = 1.88 m, Temperature = 26°C, V_x = -600V, L_x = 0.2 μa)

Time	I_{Source} (μa)	Efficiency (%)	I_{sp} (sec)	$\bar{F}$ (μ/lb)	$\dot{M}$ (μg/sec)	q/m (c/Kg)
1332	90	70	1688	24.31	6.54	13.76
1337	89	69.6	1654	24.38	6.69	13.30
1342	90	69.4	1563	26.03	7.56	11.90
1347	90	69.2	1630	24.89	6.93	12.99
1352	90	68.1	1573	25.37	7.32	12.29
1357	90	70.1	1687	24.35	6.56	13.73
1402	90	69.9	1661	24.66	6.74	13.35
1407	90	69.3	1662	24.43	6.68	13.48
1412	90	68.1	1601	24.94	7.08	12.72
1417	90	69.8	1681	24.34	6.58	13.69
1422	89	69.8	1672	24.20	6.57	13.54
1427	90	69.2	1672	24.27	6.59	13.66
1432	89	71.3	1723	23.99	6.32	14.08
1437	89	69.4	1646	24.45	6.75	13.19
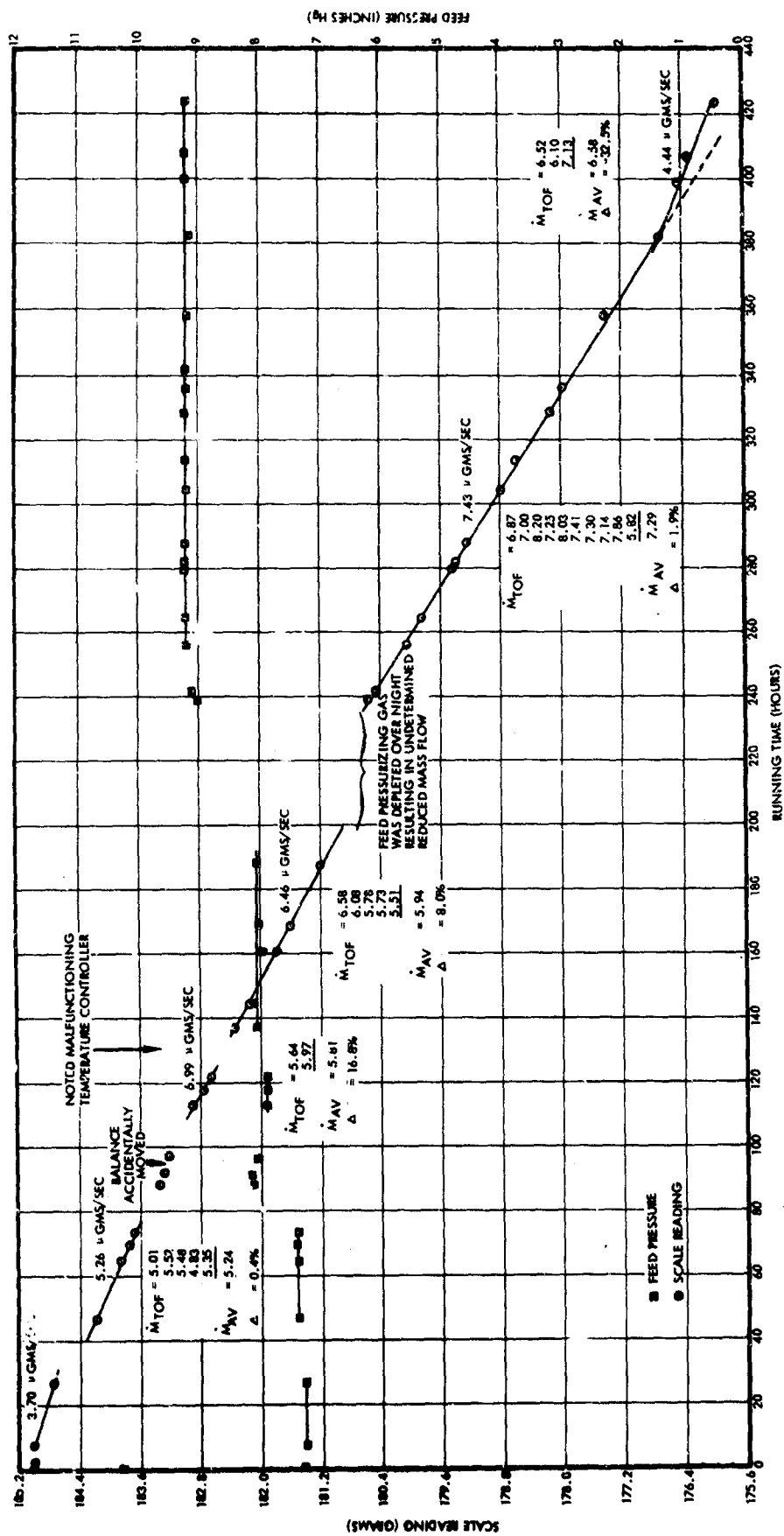
Figure 188. Direct Mass Flow Measurements and Their Correlation with Feed Pressure and Time-of-Flight Calculations. (The scale reading in grams is the combined weight of the propellant reservoir and the fluid within 't.')

264

statistical uncertainty. Also, the time duration for this period is only 10 hours, resulting in some uncertainty in determining the slope of the direct measurements. For the other periods, the agreement is as good as can be expected for these measurements.

Note the "abnormal" period towards the end of the run where the slope of the direct mass flow readings suddenly dropped to 4.44 µgms/sec even though the feed pressure had been held constant. The time-of-flight results, however, did not show any reduction in mass flow. This was probably because of bubble nucleation and expansion in the feed line displacing a measurable propellant volume. This was then the immediate precursor of the thruster failure. The following discussion shows why this happened.

7.3.5 Gas Generation During Mass Flow Measurements

As described earlier, long Monel feed and pressure lines were used outside the vacuum system to minimize external forces on the propellant reservoir suspended from the mass flow balance. This resulted in large areas of exposed high voltage, potential corona, surfaces outside the vacuum system. Figure 188 is a simplified schematic of the arrangement. Since the high voltage is normally applied at the thruster, inside the vacuum chamber, this could result in a drain current through the propellant within the glass feedthrough line which passes through the vacuum chamber wall, connecting the thruster to the external feed system. Since this current would generate gas, it has been standard practice to run a separate high voltage lead to the external feed lines when performing direct mass flow measurements. So that the corona current would not be falsely read as additional needle current, the feed high voltage was tapped off before the needle current meter. This arrangement works quite well as long as there is no appreciable series resistance between the tap point and the source.

For long life tests, when no direct mass flow measurements are made, it is usual practice to have a 10K protective resistor in series with the current meter and also a 100K series resistor attached directly to the source. These resistors are usually removed for direct mass flow measurement. However, in this particular experiment, the direct mass flow apparatus was added as an afterthought to an already existing life test set-up and the resistors were inadvertently allowed to remain.

Because of this, the approximately 10-volt drop across the series resistors during normal operation was imposed across the feed tube line shown in Figure 189. As will now be shown, the resulting electrolytic current generated sufficient gas to cause bubbling at the emitter tip and to eventually abort the test.

The glass feed tube dimensions were 3/32-inch diameter by 2 feet long. For a propellant resistivity of 4500 ohm centimeters, the resulting resistance through the propellant within the tube is 2.3×10^6 ohms. For an imposed potential drop of approximately 10 volts, the resultant leakage current is 4 microamperes. This current results in hydrogen generation at the thruster end of the feed tube. The resulting generation rate of diatomic hydrogen at the thruster end of the feed tube is 4.5×10^{-7} cc/sec

265
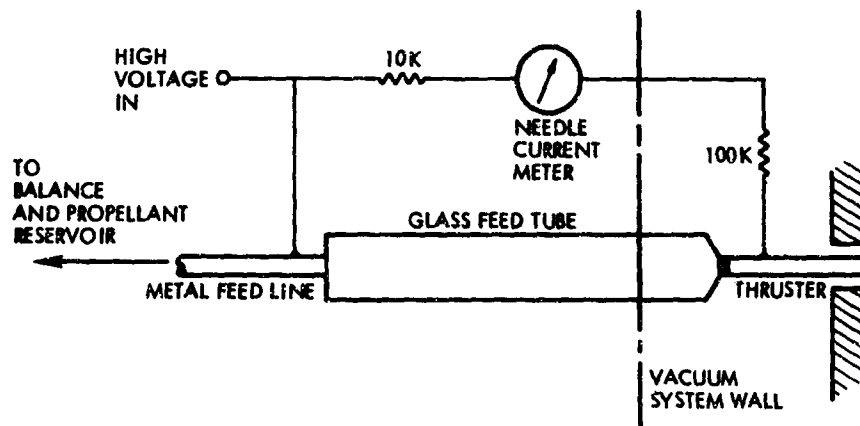
Figure 189. Electrical Connections to Feed Line
and Thruster During Mass Flow
Measurements

at standard temperature and pressure (STP). The propellant volumetric
flow past the gas generation point is approximately 4×10^{-6} cc/sec. Thus,
the steady-state volumetric gas generation (at STP) to propellant flow-by
ratio is 0.1, a factor of 30 higher than the solubility of H_2 in glycerol.
This will obviously cause instability at the needle tip.

An obvious question at this point is the length of time it takes for
enough excess gas to accumulate to nucleate large bubbles within the feed
line. A reasonable criterion for estimating the time scale involved is to
calculate the time required to build up 1 cc of H_2 at the nominal feed line
pressure of approximately 1.3 of an atmosphere. This time is given by:

$$\frac{1 \, cc}{(1/3) \, (4.5 \times 10^{-7} \, cc/sec)} \simeq 7 \times 10^6 \, sec \simeq 200 \, hr$$

Thus, it is not at all surprising that after 400 hours bubbles that
seriously affected the conduct of the experiment developed in the feed line.

7.3.6 Conclusions

The time-of-flight experiments have in general tended to yield too low
a value of the mass flow as determined independently by direct mass flow
measurements. Because of the scatter in the time-of-flight data it is
impossible to precisely state just how much an individual time-of-flight
experiment will be in error. The overall average mass flow disagreement
for the needles and annular geometries was of the order of 5 percent.
Since there was considerable scatter, previous estimates of accuracy to
approximately ± 10 percent in time-of-flight data still appear reasonable.

It had been hoped that these experiments would provide a measure of the neutral fraction in the beam. However, it is now apparent that the scatter in the data precludes this measurement. That is to say, although it is known these are inaccuracies and uncertainties in the time-of-flight technique, there is no way of relating these to any one fundamental effect.

APPENDIX A

THE NUMERICAL SOLUTION OF A TWO POINT
BOUNDARY VALUE PROBLEM

1. INTRODUCTION

A straightforward numerical difference scheme has been instrumented for obtaining the numerical solution to a two point boundary value problem [1, 2, 3].

The purpose of this report is to present:

1. The numerical methods used in obtaining the solution

2. Some of the initial data obtained using the computer program BAMA (small band matrix solver).

Briefly stated, the problem is as follows: Solve the differential equation

$$y'' + \frac{1}{x} y' = 2 \sinh y - Ge^{-(x/w)^2} \tag{A-1}$$

subject to the boundary values

$$y'(0) = 0 \tag{A-2}$$

$$\lim_{x \to +\infty} y(x) = 0 \tag{A-3}$$

The constants G and w are obtained as simple functions of the four parameters D, w_0, Z, Z_0 as follows:

$$w = w_0 \left[1 + (Z/Z_0)^2 \right]^{1/2} \tag{A-4}$$

$$G = D(w_0/w)^2 \tag{A-5}$$

A case of initial interest is the choice

$$D = 529,854.11$$

$$w_0 = 0.03$$

$$Z_0 = 0.17$$

$$Z \geq 0$$

Preceding page blank

269

2. METHOD

The differential equation (A-1) may be replaced with a difference equation, viz:

$$\frac{y_{i+1} - 2y_i + y_{i-1}}{h^2} + \frac{1}{x_i} \frac{y_{i+1} - y_{i-1}}{2h} = 2 \sinh y_i - Ge^{-(x_i/w)^2}$$

$$\text{(A-6)}$$

where

$$h = x_{i+1} - x_i$$

is the common difference between the node points $x_0 = h$, $x_1 = 0$, $x_2 = h$, ... At the origin, symmetry requires that

$$y_2 = y_0 \qquad \text{(A-7)}$$

so that the first equation reduces to

$$2\left(\frac{y_2 - y_1}{h^2}\right) = 2 \sinh y_1 - G \qquad \text{(A-8)}$$

Thereafter, the equations resemble equation (A-6). The final equation, however, is obtained by setting $y_{N+1} = 0$:

$$\frac{-2y_N + y_{N-1}}{h^2} - \frac{1}{x_N} \frac{y_{N-1}}{2h} = 2 \sinh y_N - Ge^{-(x_N/w)^2} \qquad \text{(A-9)}$$

270

written out in matrix notation the system of equations is:

$$
\begin{bmatrix}
-2 & 2 & & & & & \\
1-1/2 & -2 & 1+1/2 & & & & \\
& 1-1/4 & -2 & 1+1/4 & & & \\
& & & \cdot & & & \\
& & & & \cdot & & \\
& & & & & \cdot & \\
& & & 1-\dfrac{1}{2(N-2)} & -2 & 1+\dfrac{1}{2(N-2)} \\
& & & & 1-\dfrac{1}{2(N-1)} & -2
\end{bmatrix}
$$

$$
\begin{bmatrix}
y_1 \\
y_2 \\
\cdot \\
\cdot \\
\cdot \\
y_{N-1} \\
y_N
\end{bmatrix}
= 2h^2
\begin{bmatrix}
\sinh y_1 \\
\cdot \\
\cdot \\
\cdot \\
\cdot \\
\sinh y_N
\end{bmatrix}
- Gh^2
\begin{bmatrix}
1 \\
\cdot \\
\cdot \\
\cdot \\
\cdot \\
e^{-[(N-1)h/w]^2}
\end{bmatrix}
\tag{A-10}
$$

This is a nonlinear system of equations for the quantities $y_1, \ldots, y_N$.

If the step size is to be escalated outward by multiples of two as the difference equations work away from the origin, the matrix in equation (A-10) becomes quadridiagonal with two diagonals below the main diagonal. The fourth diagonal consists of an isolated entry at the equation for which the step size is to be doubled.

Thus, for the nonuniform mesh case, the matrix in equation (A-10) becomes quadridiagonal with two diagonals below the main diagonal. The fourth diagonal consists of an isolated entry at the equation for which the step size is to be doubled.

Let

$$h_i = 2^{i-1}h$$

and suppose there are to be N_i steps of length h_i. The division points will be indexed as follows:

$$x_1, \ldots, x_{N_1}$$

$$x_{N_1 + 1}, \ldots, x_{N_1 + N_2}$$

.

.

$$x_{N_1 + N_2 + 1}, \ldots, x_{N_1 + N_2 + N_3}$$

In matrix form, the equations with three escalations are:

$$Ay = J(2 \sinh y - \rho) \qquad (A-11)$$

where J is a diagonal matrix with the first N_1 diagonal entries equal to

$$h_1^2 = h^2 \, ,$$

the second N_2 entries equal to

$$h_2^2 = (2h)^2 \, ,$$

and the third N_3 entries equal to

$$h_3^2 = (4h)^2 \, .$$

272

For the other quantities appearing in the equation we have

$$
\sinh y = \begin{bmatrix}
\sinh y_1 \\
\cdot \\
\cdot \\
\cdot \\
\sinh y_{N_1} \\
\sinh y_{N_1 + 1} \\
\cdot \\
\cdot \\
\cdot \\
\sinh y_{N_1 + N_2} \\
\sinh y_{N_1 + N_2 + 1} \\
\cdot \\
\cdot \\
\cdot \\
\sinh y_N
\end{bmatrix}
\qquad (A-12)
$$

$$\rho = \begin{bmatrix} 1 \\ \cdot \\ \cdot \\ \cdot \\ \cdot \\ \mathrm{Exp}\left[-\left(x_{N_1}/w\right)^2\right] \\ \mathrm{Exp}\left[-\left(x_{N_1+1}/w\right)^2\right] \\ \cdot \\ \cdot \\ \cdot \\ \mathrm{Exp}\left[-\left(x_{N_1+N_2}/w\right)^2\right] \\ \mathrm{Exp}\left[-\left(x_{N_1+N_2+1}/w\right)^2\right] \\ \cdot \\ \cdot \\ \cdot \\ \mathrm{Exp}\left[-\left(x_N/w\right)^2\right] \end{bmatrix} \qquad (A-13)$$

and finally

$$
A = \begin{bmatrix}
\text{x} & \text{x} & & & & & & & & & & & & & \\
\text{x} & \text{x} & \text{x} & & & & & & & & & & & & \\
& & \cdot & \cdot & & & & & & & & & & & \\
& & \cdot & \cdot & & & & & & & & & & & \\
& & \text{x} & \cdot & & \text{x} & \text{x} & & & & & & & & \\
& & \text{x} & & & \text{x} & \text{x} & \text{x} & & & & & & & \\
& & & & & \text{x} & \text{x} & \text{x} & & & & & & & \\
& & & & & & & \cdot & \cdot & & & & & & \\
& & & & & & & \cdot & \cdot & & & & & & \\
& & & & & & & \text{x} & \text{x} & \text{x} & & & & & \\
& & & & & & & & \text{x} & \text{x} & & & & & \\
& & & & & & & & \text{x} & \text{x} & \cdot & & & & \\
& & & & & & & & & \cdot & \text{x} & & & & \\
& & & & & & & & & \cdot & \cdot & \cdot & & & \\
& & & & & & & & & & \text{x} & & \text{x} & \text{x} \\
& & & & & & & & & & & & \text{x} & \text{x}
\end{bmatrix}
$$

(A-14)

The blocks in this matrix are as follows:

First Block

$$
\begin{bmatrix}
-2 & 2 & & & & & \\
1 - 1/2 & -2 & 1 + 1/2 & & & 0 & \\
& 1 - 1/4 & -2 & 1 + 1/4 & & & \\
& & & \cdot & & & \\
& & & & \cdot & & \\
& 0 & & & \cdot & & \\
& & & & 1 - \dfrac{1}{2(N1 - 1)} & -2 & 1 + \dfrac{1}{2(N1 - 1)}
\end{bmatrix}
$$

(A-15)

275

Second Block

$$\begin{bmatrix}
1 - \dfrac{1}{2N1} & 0 & -2 & 1 + \dfrac{1}{2N1} & & & \\
& 1 - \dfrac{1}{2(N1+1)} & -2 & 1 + \dfrac{1}{2(N1+1)} & 0 & \\
& & \cdot & & & \\
& & & \cdot & & \\
& & & 1 - \dfrac{1}{2(N1+N2-1)} & -2 & 1 + \dfrac{1}{2(N1+N2-1)}
\end{bmatrix}$$

$$(A-16)$$

Third Block

$$\begin{bmatrix}
1 - \dfrac{1}{2(N1+N2)} & 0 & -2 & 1 + \dfrac{1}{2(N1+N2)} & & \\
& & \cdot & & & \\
& 1 - \dfrac{1}{2(N1+N2+N3-2)} & -2 & 1 + \dfrac{1}{2(N1+N2+N3-2)} \\
& & 1 - \dfrac{1}{2(N1+N2+N3-1)} & -2
\end{bmatrix}$$

$$(A-17)$$

Again, equation (A-11) is a nonlinear system of equations for the quantities $y_1, \ldots, y_N$. Newton's method is used to solve them. Suppose we write the system of equation (A-11) as

$$Ay - J(2 \sinh y - \rho) = 0 \qquad (A-18)$$

Assume y_0 is an approximation to the solution, then the true solution may be expanded as

$$y = y_0 + \Delta y_0 + \ldots \qquad (A-19)$$

276

Substituting in equation (A-18) and dropping terms of order higher than two, the correction Δy_0 satisfies the system of linear equations

$$\left(A - J\frac{\partial}{\partial y}2 \sinh y_0\right)\Delta y_0 = -(Ay_0 - 2J\sinh y_0 + J\rho) \qquad (A-20)$$

Solving this system for Δy_0 produces a new approximation to the solution, $y_1 = y_0 + \Delta y_0$. The process is continued until convergence is obtained. "Convergence" in the present case means that the absolute value of the components of

$$Ay_n - 2J\sinh y_n + J\rho \qquad (A-21)$$

where y_n is the nth approximation to y, and all are less than a pre-assigned error bound (called EPS in the program).

A discussion of the theoretical aspects of this procedure can be found in Reference 4, chapter 7.

3. NUMERICAL RESULTS

A selection of solutions to equation (A-1) is shown in Figures 152 through 155. Each corresponds to a choice of the parameter Z. The solutions are believed to be valid to at least three significant figures. The validity of this last statement is based upon multiple runs at increasingly refined step sizes; that is, a solution is sought at step size h and again at step size h/2. If the solution at step size h/2 is assumed to be inherently more accurate than the solution obtained at step size h, comparison of the two solutions reveals the extent to which the figures giving the solution at step size h may be believed.

The validity of this scheme is based upon the convergence of the solutions of the difference equations. In the present case, such an assumption is without doubt warranted, although no attempt has been made to prove the assumption.

4. PROGRAM CONSIDERATIONS

TRW subroutine BAMA is used to solve the system of linear equations (A-20). BAMA requires the storage of the matrix

$$A - 2J\frac{\partial}{\partial y}\sinh y$$

in an N x 4 region, say R, in a particular fashion. This storage is depicted in Figure A-1, without the term

$$-2J\frac{\partial}{\partial y}\sinh y = 2J\cosh y$$

277

R(I, 1)	R(I, 2)	R(I, 3)	R(I, 4)	
0	0	-2	2	$\rightarrow 1$
0	$1 - 1/2$	-2	$1 + 1/2$	$\rightarrow 2$
0	$1 - 1/4$	-2	$1 + 1/4$	$\rightarrow 3$
$\updownarrow$	$\updownarrow$	$\updownarrow$	$\updownarrow$	
0	$1 - \dfrac{1}{2(N1-1)}$	-2	$1 + \dfrac{1}{2(N1-1)}$	$\rightarrow N1$
$1 - \dfrac{1}{2N1}$	0	-2	$1 + \dfrac{1}{2N1}$	$\rightarrow N1+1$
0	$1 - \dfrac{1}{2(N1+1)}$	-2	$1 = \dfrac{1}{2(N1+1)}$	$\rightarrow N1+2$
$\updownarrow$	$\updownarrow$	$\updownarrow$	$\updownarrow$	
0	$1 - \dfrac{1}{2(N1+N2-1)}$	-2	$1 + \dfrac{1}{2(N1+N2-1)}$	$\rightarrow N1+N2$
$1 - \dfrac{1}{2(N1+N2)}$	0	-2	$1 + \dfrac{L}{2(N1+N2)}$	$\rightarrow N1+N2+1$
0	$1 - \dfrac{1}{2(N1+N2+1)}$	-2	$1 + \dfrac{1}{2(N1+N2)}$	$\rightarrow N1+N2+2$
$\updownarrow$	$\updownarrow$	$\updownarrow$	$\updownarrow$	
0	$1 - \dfrac{1}{2(N1+N2+N3-2)}$	-2	$1 + \dfrac{1}{2(N1+N2+N3-2)}$	$\rightarrow N1+N2+N3-1$
0	$1 - \dfrac{1}{2(N1+N2+N3-1)}$	-2	0	$\rightarrow N1+N2+N3$

Figure A-1. Storage for Subroutine BAMA

This term is a diagonal matrix of the form

$$
\begin{bmatrix}
-2h_1^2 \cosh y_1 & & & & \\
& \ddots & & & \\
& & -2h_1^2 \cosh y_{N1} & & \\
& & & -2h_2^2 \cosh y_{N1+1} & \\
& & & & \ddots \\
& & & & & \ddots
\end{bmatrix}
$$

and, as such, is to be added to the column $R(I, 3)$.

The "driver" for BAMA computes and stores the R matrix in accordance with mesh specifications given by the input, sets up the mesh, and computes an initial guess y_0 (see Figure A-2). The solution is achieved by iteration: the addend vector is computed from the current values for y, added to the diagonal of R; and the system is submitted to BAMA. On return, BAMA supplies a Δy function that is added to the previous y to start the next iteration. Once the converged solution is obtained, the driver prints out y values, the residuals ($Ay_n - 2J \sinh y_n + J\rho$), and the net charge density ($2 \sinh y - \rho$) for each mesh point.

279
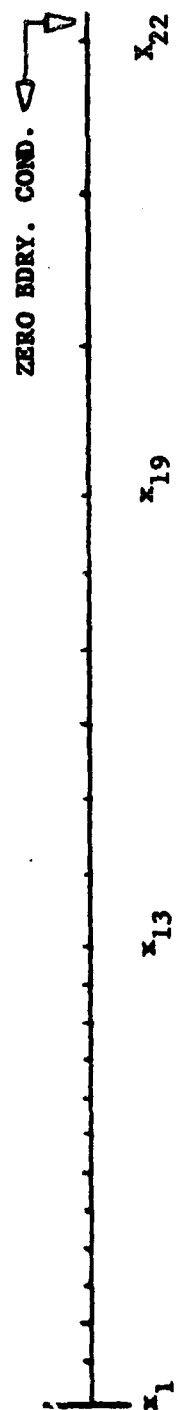
Figure A-2. Example of Variable Mesh Spacing

Meaning of Parameters

Parameter		Nominal Value
(Input) N1	= number of steps at H	50
(Input) N2	= number of steps at 2H	25
(Input) N3	= number of steps at 4H	25
(Input) H	= initial step size	0.1
(Input) D	= parameter	529,854.11
(Input) Z	= distance from spacecraft	17.0
(Input) Z0	= base beam distance	0.17
(Input) W0	= base beam width	0.03
(Input) Alpha	= conversion factor $(Y_{n+1} = Y_n + \alpha * \Delta Y)$	1.0
(Input) M	= maximum number of iterations	20
(Input) ICOMP	= input A, B, or compute	(Compute) = 0
(Either) A	= parameter in initial guess	Alog (G)
(Either) B	= parameter in initial guess	W
(Comp.) W	= mean beam width	$w_0(L = (Z/Z0))^{1/2}$
(Comp.) G	= coefficient in ρ +	D*(w0/w)
(Input) EPS	= error criterion	1.E-8
(Input) NRP	= R matrix print	(no print) 0

REFERENCES

1. R. Kemp, "Neutralization of Colloid Engine Exhaust by the Ambient Plasma," TRW No. 14554-6002-TO-00, March - April 1970.

2. R. Kemp, "Neutralization of Colloid Engine Exhaust by the Ambient Plasma," TRW No. 14554-6003-TO-00, April - May 1970.

3. R. Kemp, "Neutralization of Colloid Engine Exhaust by the Ambient Plasma," TRW No. 14554-6004-TO-00, May - June 1970.

4. P. Henrici, Discrete Variable Methods in Ordinary Differential Equations, John Wiley, 1962.

APPENDIX B

AUTOMATIC DATA ACQUISITION FOR
TIME-OF-FLIGHT MEASUREMENTS AND SAMPLE CASE

1.   A Fortran source listing is shown for the time-of-flight computer program, designated TØF (source deck, FTØ). The program uses a NAMELIST input capability, and is written to accept either hand-written data or data from ADAS.

2.   A sample case is shown using hand read data. The data input appears after the "TAPE, DATA-READY" statement.

3.   A sample case is shown using a paper tape punched by the automated data acquisition system. The tail-off level is 03, corresponding to zero current.

```
      PROGRAM FT0(INPUT,OUTPUT,TAPE5=INPUT,TAPE6=OUTPUT)
      DIMENSION Y(140)
      NAMELIST/IN/V,C,D,H,Y,N
      CALL NMLEOF
      N=127
      T6=1.E+6
 1    DO 5 I=1,8
 5    WRITE(6,109)
      WRITE(6,101)
      DO 6 I=1,8
 6    WRITE(6,109)
      DO 2 I=1,140
 2    Y(I)=0.
      READ(5,100)
      IF(EOF,5)73,75
 75   WRITE(6,100)
      READ(5,IN)
      IF(EOF,5)73,74
 74   IF(Y(1))9,9,10
 9    READ(5,110)(Y(I0),I0=1,127)
      READ(5,IN)
      J=0
 20   J=J+1
      IF(Y(J)-Y(J+1))21,22,22
 21   DO 23 I=1,J
 23   Y(I)=Y(J+1)
      GO TO 20
 22   N=N+1
      W2=Y(1)
      DO 11 I=1,N
      W1=Y(I)
      Y(I)=W2
 11   W2=W1
 10   P=V*C*.001
      WRITE(6,102)V,C,P
      HS=H/T6
      CA=C/T6
      YN=200.
      DO 3 I=1,N
      Y(I)=Y(I)-Y(N)
 3    IF(Y(I).LT.0.)Y(I)=0.
      NN=N-1
      DO 12 I=1,NN
 12   IF((Y(I+1)-Y(I)).GT.0.)Y(I+1)=Y(I)
      O1=(Y(1)+Y(N))*.5
      O2=NN*.5*Y(N)
      DO 4 J=2,NN
      O1=O1+Y(J)
```

```
  4   Q2=(J-1)*Y(J)+Q2
      T1=HS*Q1/Y(1)
      Q1=T1*CA
      Q2=Q2*CA*HS*HS/Y(1)
      T2=(Q2+Q2)/Q1
      ETA=T1/T2
      V1=D/T1
      V2=D/T2
      SPI=V2/9.80665
      F=(P+P)/V1
      DM=F/V2
      F=F*T6
      F1=.22481*F
      XQ1=CA/DM
      XQ2=XQ1*ETA
      T1=T1*T6
      DM=DM*1.E+9
      WRITE(6,103)F,F1
      WRITE(6,104)DM,SPI
      WRITE(6,105)XQ1,XQ2
      WRITE(6,106)V2,ETA
      WRITE(6,107)T1
      GO TO 1
 73   WRITE(6,108)
      STOP
101   FORMAT(*--*)
100   FORMAT(70H
     1                                    )
102   FORMAT(/*   VS = *F5.1* KV     IS =*F7.1* MU-A     P =*
     1F6.3* WATTS*)
103   FORMAT(/*THRUST =*F7.2*E-06 NEWTONS    =   *F7.3* E-06 LBS*)
104   FORMAT(/*MASS FLOW =*F8.3*E-09 KG/SEC    ISP =*F7.1* SEC*)
105   FORMAT(/*AVE Q/M = *F7.0* COUL/KG         SMR Q/M = *F7.0* COUL/KG
     1*)
106   FORMAT(/*AVE VEL = *1PE12.3* M/SEC        THR EFF =*0PF5.3)
107   FORMAT(/*1/<1/TOP> = *F8.3*E-06  SEC*)
108   FORMAT(/*LAST CASE*///////)
109   FORMAT(**)
110   FORMAT(8(F2.0,1X))
      END
```

285

```
0
08/11/71.  16.33.50.
TRW/TSS 6500 - 08/09/71.

USER NUMBER:
JOBNAME - PJG6023.
[ GET, TOF
[ TAPE, DATA
READY.
& SAMPLE CASE FOR HAND READ DATA
PSIN D=.30,H=2,V=12.35,C=5,N=21,Y=24,23.5,21,18.5,17,16,15,14,
  12,10,9,7.5,6,4.5,3,2.2,1.2,.8,.5,.2,0$


[ TOF, DATA


SAMPLE CASE FOR HAND READ DATA
  SIN D=.30,H=2,V=12.35,C=5,N=21,Y=24,23.5,21,18.5,17,16,15,14,
  12,10,9,7.5,6,4.5,3,2.2,1.2,.8,.5,.2,0$

    VS =   12.4 KV     IS =    5.0 MU-A     P = .062 WATTS

THRUST =    6.65E-06 NEWTONS   =    1.495 E-06 LBS

MASS FLOW =    .488E-09 KG/SEC     ISP = 1390.3 SEC

AVE Q/M =   10249 COUL/KG        SMR Q/M =    7526 COUL/KG

AVE VEL =   13.634E+03 M/SEC     THR EFF = .734

1/<1/TOF> =   16.158E-06  SEC

  --


LAST CASE


[ LOG
LOGOFF.

  08/11/71.  16.36.46.PJG6023.
LTIM           2 MIN.
CPU          .229 SEC.
PPU         3.007 SEC.
MUCM         .049 MWD-SEC.
DISK        1.247 KPRUS.
```

```
08/11/71.  16.37.52.
TRW/TSS  6500  -  08/09/71.

USER NUMBER:
JOBNAME - PJID023.
[ GET, TOF
[ TAPE, DATA
READY.
& TEST CASE FOR TOF---ADAS INPUT
PSIN D=1.88,H=5$
59, 59, 59, 57, 51, 45, 41, 39,
37, 36, 35, 34, 33, 32, 30, 28,
27, 25, 24, 22, 21, 19, .8, 17,
16, 15, 13, 12, 11, 10, 09, 08,
08, 07, 07, 06, 05, 05, 05, 04,
04, 04, 04, 04, 04, 03, 03, 03,
03, 03, 03, 03, 03, 03, 03, 03,
03, 03, 03, 03, 03, 03, 03, 03,
03, 03, 03, 03, 03, 03, 03, 03,
03, 03, 03, 03, 03, 03, 03, 03,
03, 03, 03, 03, 03, 03, 03, 03,
03, 03, 03, 03, 03, 03, 03, 03,
03, 03, 03, 03, 03, 03, 03, 03,
03, 03, 03, 03, 03, 03, 03, 03,
03, 03, 03, 03, 03, 03, 03, 03,
03, 03, 03, 03, 03, 03, 03,
PSIN V=14.2, C=90, N=64$


[ TOF, DATA
```

TEST CASE FØR TØF---ADAS INPUT
  SIN D=1.88,H=5S
  SIN V=14.2,C=90,N=64S

  VS = 14.2 KV   IS =   90.0 MU-A   P = 1.278 WATTS

THRUST = 109.49E-06 NEWTØNS   =   24.615 E-06 LBS

MASS FLØW =   6.800E-09 KG/SEC   ISP = 1641.8 SEC

AVE Q/M =   13234 CØUL/KG   SMR Q/M =   9128 CØUL/KG

AVE VEL =   16.101E+03 M/SEC   THR EFF = .690

1/<1/TØF> =   80.536E 06   SEC

  --

LAST CASE

[LØG
LØGØFF.

  08/11/71. 16.41.17.PJID023.
LTIM   3 MIN.
CPU   .305 SEC.
PPU   3.033 SEC.
MUCM   .047 MWD-SEC.
DISK   1.247 KPRUS.

DEPARTMENT OF THE AIR FORCE
AIR FORCE ROCKET PROPULSION LABORATORY (AFSC)
EDWARDS, CALIFORNIA 93523

REPLY TO
ATTN OF: LKDA/Lt Rosen/714-553-2820   17 Jan 1972

SUBJECT: Errata, AFRPL-TR-71-128, "Exploratory Development of Advanced
          Colloid Thrusters"

TO: All Recipients of AFRPL-TR-71-128

The following items and attachment are to be included in the subject
report:

   a. Item One - To be included on inside front cover:

"When U.S. Government drawings, specifications, or other data are used
for any purpose other than a definitely related Government procurement
operation, the Government thereby incurs no responsibility nor any
obligation whatsoever, and the fact that the Government may have
formultated, furnished, or in any way supplied the said drawings,
specifications or other data, is not to be regarded by implication or
otherwise, or in any manner licensing the holder or any other person
or corporation, or conveying any rights or permission to manufacture,
use, or sell any patented invention that may in any way be related
thereto."

   b. Item Two - To be included on cover and title page:

"Approved for public release; distribution unlimited."

   c. Item Three - All references to AFRPL-TR-128 should be changed
to "AFRPL-TR-71-128".

   d. Item Four - Attached DD Form 1473 to be included.

WALTER A. DETJEN, Chief   1 Atch
Engine Development Branch   DD Form 1473

3

DOCUMENT CONTROL DATA - R & D

(Security classification of title, body of abstract and indexing annotation must be entered when the overall report is classified)

1. ORIGINATING ACTIVITY *(Corporate author)*	2a. REPORT SECURITY CLASSIFICATION
TRW Systems Group One Space Park Redondo Beach CA 90278	UNCLASSIFIED
	2b. GROUP N/A

3. REPORT TITLE

(U) Exploratory Development of Advanced Colloid Thrusters

4. DESCRIPTIVE NOTES *(Type of report and inclusive dates)*

Technical Report, 15 May 1970 to 15 September 1971

5. AUTHOR(S) *(First name, middle initial, last name)*

M. Huberman, C. Lear, H. Shelton, W. Krieve, R. Kemp

6. REPORT DATE	7a. TOTAL NO. OF PAGES	7b. NO. OF REFS
November 1971	293	4

8a. CONTRACT OR GRANT NO. F33615-70-C-1405	9a. ORIGINATOR'S REPORT NUMBER(S)
b. PROJECT NO. 3141	AFRPL-TR-71-128
c.	9b. OTHER REPORT NO(S) *(Any other numbers that may be assigned this report)*
d.	

10. DISTRIBUTION STATEMENT

Distribution of this document is unlimited.

11. SUPPLEMENTARY NOTES	12. SPONSORING MILITARY ACTIVITY
	Department of the Air Force AF Rocket Propulsion Laboratory Edwards CA 93523

13. ABSTRACT

This report describes a program to develop high performance colloid thruster systems. An electrostatically vectorable high thrust-density colloid source was developed and endurance tested for periods up to 2000 hours. The investigation of pulsed colloid thruster technology resulted in a demonstration of a feasible concept. Also, a breadboard high voltage supply for a pulsed thruster was built and demonstrated as well as a high voltage isolation valve to electrically decouple the propellant storage system from an individual thruster. Theoretical neutralization investigations evaluated the feasibility of utilizing the electrons in the ambient space plasma at synchronous altitudes to provide colloid thruster exhaust space charge neutralization. An electron gun type neutralizer for colloid engines was developed and life tested for more than 10,000 hours. Diagnostic investigations were directed toward analytically evaluating colloid thruster performance and its interaction with the laboratory test environment.

DD FORM 1473
1 NOV 65

14. KEY WORDS	LINK A		LINK B		LINK C	
	ROLE	WT	ROLE	WT	ROLE	WT
Colloid Propulsion						
Electrostatic Propulsion						
Electric Propulsion						